Extending the Optical Properties of Cesium Lead Halide Perovskite Nanocrystals through Lanthanide Functionalization

Dissertation submitted in fulfillment of the requirement for the degree of Doctor of Science: Chemistry

By
Min Zeng

Department of Chemistry
Faculty of Sciences
2020

Promoter: Prof. Dr. Rik Van Deun	Ghent University
Copromotor: Prof. Dr. Zeger Hens	Ghent University
Copromotor: Dr. Flavia Artizzu	Ghent University

Members of the Examination Committee

Prof. Dr. Kristof Van Hecke	Ghent University (Chairman)
Prof. Dr. Philippe Smet	Ghent University
Prof. Dr. Pieter Geiregat	Ghent University
Prof. Dr. Prof. Andrea Falqui	King Abdullah University of Science and Technology (KAUST)
Prof. Dr. Carlo Maria Carbonaro	Cagliari State University
Dr. Federico Locardi	Ghent University

This work was funded by China Scholarship Council (CSC) and Special Research Fund (BOF) CSC-Cofunding Scholarship.
Grant Number: 201607565018

Acknowledgements

My four-year PhD studying experience is a very special and precious gift for my whole life. I will remember and benefit from it forever. I won’t finish my PhD on time without the help of my great promoter and copromotors, kind colleagues, friends and family. Here, I cannot express how grateful I am to all of you who have helped me during my PhD studies.

First of all, I would like to express my sincere gratitude to my country, China, for the financial support: China Scholarship Council (CSC). Therefore, I have the opportunity to go out to pursue my doctoral degree and have a look at this interesting world. I also would like to thank the Embassy of the People’s Republic of China in the Kingdom of Belgium for giving us warm tips and timely face masks. I also would like to acknowledge the financial support from Special Research Fund (BOF) CSC-Cofunding Scholarship from Gent University.

I sincerely thank my promoter Prof. Rik Van Deun. Thank you for offering me this opportunity to be your PhD student and meet a lot of friendly people in our department. You are always here to help me and support me. I am really impressed by your rigorous attitude towards research and friendly attitude towards people. I wish L^3 better and better.

I am very grateful to my copromoter Prof. Zeger Hens for introducing me to this exciting nanostructure world. Thank you for designating PCN members as my advisors to teach me the new synthesis every time I need. Your instructional suggestions and decisions are very important for my scientific research.

I would like to express my heartfelt appreciation to my copromotor, Dr. Flavia Artizzu. I cannot run smoothly without your unselfish dedication and kind encouragement. Whenever I come across some scientific questions out of my understanding, you are always here to patiently explain the underlying principles to me and make me understood. I have learnt a lot from you, not only for science but also for the life. Sometimes you look like my old sister. You really care about me and protect me. Thanks for sharing delicious Italian food with me. In total, you are very special for me.

Jing, you are one of the most important people in my life. I would not come here without your help. Sometimes, you are my dear friend. I feel very happy to be with you whenever we go shopping or travelling. Sometimes, you look like my teacher. You always give me very useful advices when I feel depressed and confused.

Thank you Shalini for teaching me everything in the PCN lab at the first year of my PhD studies. Thanks you for make explanations to Prof. Zeger Hens in the group meeting due to my poor English at the beginning. You have given me a lot of useful instructions on experimental design, synthesis and analysis. I also thank you for doing TEM measurements for me. I felt very warm every time I saw your smile. Now I miss you!

Thank you Dr. Federico Locardi for introducing me to the lead-free perovskites world. It is very lucky to meet you at the last year of my PhD studies. You are very cautious about the experimental synthesis. You even show me how to efficiently and correctly label the samples. Such small details really impressed me. You always reply me very quickly, including synthesis design and manuscript correction. I will cherish the remaining time with you for the new synthesis.

I would like to acknowledge my kind and upright colleague Dimitrije. You are a very helpful person. You can fix everything in the lab. Thank you for making four-year chemical orders for our group and discussing the science with me. Thank you Prof. Anna Kaczmarek for well understanding my English and teaching me to use the PL setup.

Thanks for all PCN members. Igor, thank you for helping me in the PCN lab and showing me how to measure the relative quantum yield and calculate the quantum dot size. Jorick and Valeriia, thank you for teaching me how to synthesize the quantum dots. I also would like to thank the other members: Prof. Pieter Geiregat, Willem, Dorian, Mickäel, Hannes, Jari, Emile, Margarita, Natalia, Pieter, Kim, Alessio, etc.

I would like to thank our warm-hearted Pierre, Kathleen, Pat, Bart, Tom, Funda and Katrien. Thank you our secretaries, Pierre and Kathleen for dealing with our administrative documents. I would like to acknowledge the technical staff, Bart, Pat, Tom, Funda and Katrien. Thank you Bart for fixing every broken device in the L^3 lab and carrying the nitrogen gas cylinder for me. Thank you Tom and Funda for dealing with the lab safety stuffs. I am also grateful to Funda for teaching me to use the XRF setup and performing measurements for me. Katrien, thank you very much for performing TEM measurements and bringing mulberry fruits for me.

I would like to acknowledge the other people in S3 building. Prof. Kristof Van Hecke, I really appreciate your frequent interactions with your students. Tim, Laurens, Marina, Marek, Jonas, Hannes, Himanshu, Chidharth, Norini, Sara and Parviz, etc. You are very nice persons. Thank our department leaders Prof. Patrick Bultinck and Prof. Isabel Van Driessche for creating a good environment for us.

It is very lucky to meet the Chinese family in Gent. Sisi, Xiaoxuxu&Dazeze, Hui, Pengshang&Jiaren, Jieqi, Guangbo, Xiao, Shuna, Kai, small Min, Xinyuan, Wanlu, Chaoqing, Dahang, Zhenmin, Minglun, Jiyu, Liao, Chunhui and Jiamin, thank all of you for making me feel at home and sharing interesting things and delicious Chinese food with me.

Here, I also would like to thank my parents and boyfriend. You are my spiritual support!

Min Zeng (曾敏)

Department of Chemistry

Ghent University

Sept, 2020

List of Acronyms

AFM	atomic force microscopy
CB	conduction band
CIE	Commission Internationale de L’Eclairage
CW	continuous-wave
DMF	*N*,*N*-Dimethylformamide
DMSO	dimethyl sulfoxide
EDS	energy-dispersive X-ray spectrometry
ET	energy transfer
FRET	Förster resonance energy transfer
HRTEM	high resolution transmission electron microscopy
LEDs	light-emitting diodes
LHPs	cesium lead halide perovskites
Ln	lanthanide
Ln^{3+}	lanthanide ions
LSC	luminescent solar concentrator
NCs	nanocrystals
NIR	near-infrared
OA	oleic acid
ODE	1-octadecene
OLA	oleylamine
PCE	power conversion efficiency
PL	photoluminescence
PR	photon reabsorption
QDs	quantum dots
QC	quantum cutting
QY	quantum yield
SEM	scanning electron microscopy
SSCs	silicon solar cells

TEM	transmission electron microscopy
XRD	X-ray diffraction
XRF	X-ray fluorescence
UC	upconversion
UCL	upconversion luminescence
UCNPs	upconversion nanoparticles
UV	ultraviolet
VB	valence band

English Summary

All-inorganic cesium lead halide perovskites $CsPbX_3$ ($X = Cl^-, Br^-, I^-$) nanocrystals have emerged as a new generation of semiconducting materials due to their superior optical and electronic properties, such as ultrahigh molar extinction coefficient, tunable bandgap, long charge diffusion length, high carrier mobility, and high photoluminescence quantum yield in the green and red region. Owing to the direct bandgap semiconductor properties of $CsPbX_3$ with a bandgap ranging between ~3.1 – 1.8 eV, the band-edge emission wavelength is limited in the visible region (~410 – 700 nm), which hampers their wider application in near-infrared (NIR) range to some extent, such as optical telecommunication (which requires longer wavelength).

In contrast to $CsPbX_3$ perovskites, the photoluminescence emission of most trivalent lanthanide ions (Ln^{3+}), except for La^{3+} and Lu^{3+}, covers the entire spectral range from UV to visible and NIR (up to 3 μm) depending on the nature of the Ln^{3+} ion. Meanwhile, the ionic radius of Ln^{3+} ion is routinely smaller than Pb^{2+}. Therefore, partial replacement of Pb^{2+} by Ln^{3+} ions may have an effect on the perovksite structure and thus on its optoelectronic and optical properties. Importantly, due to the shielding of 4f orbitals by the outer filled 5s and 5p shells, the sharp bands in the Ln^{3+} absorption and emission spectra, corresponding to 4f–4f transitions, are virtually insensitive to the external environment (e.g., pH, temperature), which allows sensitive detection above background noise in some applications (e.g., bioprobes). In the past three years, Ln^{3+}-doped $CsPbX_3$ perovskites have received significant attention due to the novel functionalities endowed by the combination of Ln^{3+} ions with the $CsPbX_3$ material, which opens novel perspectives for applications in solar cells, luminescent solar concentrators and light-emitting diodes. Yb^{3+}-doped $CsPbCl_3$ or mixed-halide $CsPb(Cl/Br)_3$ perovskites have demonstrated exceptionally high photoluminescence quantum yield exceeding unity of Yb^{3+} NIR emission at ~1.0 μm as a result of the

one-to-two photons emission process. Nonetheless, Er^{3+}, also a well-known NIR-emitting Ln^{3+} ion at ~1.5 μm, which is more interesting than 1.0 μm for optical telecommunication, has received much less attention than Yb^{3+}.

While the $CsPbX_3$ perovskites require photoexcitation in the UV or visible spectral region, their nonlinear photon upconversion (UC) ability to convert two or more NIR photons to a single, shorter-wavelength photon, is very limited. The limited UC ability arises from the low efficiency ($<10^{-8}$) of multiphoton absorption by $CsPbX_3$ perovskites. Photon UC of NIR photons is highly desirable for a wide range of applications in solar cells, photocatalysis, photodetection, anti-counterfeiting, etc. Fortunately, Ln^{3+}-doped UC materials pumped by a low-cost NIR laser are capable of generating efficient ($>10^{-3}$) UC luminescence via a multistep photon absorption. Therefore, combining Ln^{3+}-doped UC nanoparticles (UCNPs) with $CsPbX_3$ perovskites has been recognized as a promising route to overcoming the inherent limits of $CsPbX_3$; that is, the UCNPs serve as NIR antennas for improving the UC luminescence brightness of $CsPbX_3$.

Inspired by these exciting perspectives, research efforts are being made to functionalize highly performing $CsPbX_3$ perovskites with luminescent Ln^{3+} ions. Two strategies can be followed in this regard, that have been also pursued in this doctoral work: i) decoration of $CsPbX_3$ with Ln^{3+}-based UCNPs and ii) Ln^{3+} doping into $CsPbX_3$. These two approaches allow adding different optical functionalities to $CsPbX_3$. In particular, the first one allows for the extension of the optical absorption to the NIR region to achieve NIR-to-visible photon UC while the second one opens novel possibilities for the tuning of the spectral emission range.

Chapter 1 gives an introduction to $CsPbX_3$ perovskites, lanthanides, UCNPs-sensitized $CsPbX_3$, and Ln^{3+}-doped $CsPbX_3$. Firstly, the crystal structures and optical properties of $CsPbX_3$ perovskites are presented, followed by an introduction to lanthanides, including their electronic configurations and luminescence mechanisms. Afterwards, UCNPs-sensitized $CsPbX_3$ is overviewed, including synthetic methods and UC luminescence properties. Finally, the doping principles, synthesis and optical performance of Ln^{3+}-doped $CsPbX_3$ perovskites are summarized.

Chapter 2 describes the synthesis and characterization of the Ln^{3+}-based UCNPs-sensitized $CsPbBr_3$ system. Firstly, a comparison between physical mixing and *in situ* growth methods for assembling $CsPbBr_3$ with UCNPs is presented. The results suggest that a hybrid system with short-separation distance between the UCNPs and $CsPbBr_3$ can be obtained by *in situ* growth. Next, energy transfer mechanisms in the hybrid system are also investigated in detail. The thermal and photostability of the system is further explored.

Chapter 3 describes a strategy to boost the Er^{3+} 1.5 μm luminescence in $CsPbCl_3$ nanocrystals through Yb^{3+} sensitization. Firstly, Yb^{3+} and Er^{3+}-singly doped $CsPbCl_3$ are explored. Afterwards, Yb^{3+}/Er^{3+} codoped $CsPbX_3$ with different doping ratios is presented. Importantly, a transient internal redox mechanism is proposed to rationalize the anomalous different behavior of Yb^{3+} and Er^{3+} emitters in singly doped $CsPbX_3$.

Chapter 4 demonstrates the sensitization of Er^{3+} 1.5 μm luminescence in $CsPbCl_3$ nanocrystals through an alternative sensitizer: the Mn^{2+} ion. Firstly, synthesis and characterization of Mn^{2+}-doped $CsPbCl_3$ nanocrystals are investigated. Next, synthesis and characterization of Mn^{2+}/Er^{3+} codoped $CsPbCl_3$ with different doping ratios are explored. The energy transfer mechanism in Mn^{2+}/Er^{3+} codoped $CsPbCl_3$ is additionally discussed.

Chapter 5 summarizes the conclusions of this PhD thesis and gives an outlook based on the results that have been obtained.

Nederlandstalige samenvatting

Geheel anorganische cesium-lood halide perovskiet $CsPbX_3$ ($X = Cl^-$, Br^-, I^-) nanokristallenzijn naar voren gekomen als een nieuwe generatie halfgeleidende materialen, vanwege hun superieureoptische en elektronische eigenschappen, zoals ultrahoge absorptiedoorsnede, afstembare bandgap, lange ladingsdiffusie-lengte, hoge dragermobiliteit en hoge fotoluminescentie kwantumopbrengst in het groene en rode gebied. Vanwege de directe bandgap halfgeleider eigenschappen van $CsPbX_3$ met een bandgap tussen ~3.1 – 1.8 eV, is de bandrand emissiegolflengte beperkt tot het zichtbare gebied (~410 – 700 nm), wat hun bredere toepassing tot op zekere hoogte belemmert, zoals voor wat betreft optische telecommunicatie (waarvoor langere golflengten nodig zijn).

In tegenstelling tot $CsPbX_3$ perovskieten, dekt de fotoluminescentie-emissie van de meeste driewaardige lanthanide-ionen (Ln^{3+}) het volledige spectrale bereik van UV tot zichtbaar en nabij-infrarood (NIR) (tot 3 μm), afhankelijk van de aard van het Ln^{3+} -ion. Terzelfder tijd is de ionstraal van Ln^{3+}-ionen kleiner dan deze van Pb^{2+}. Daarom kan gedeeltelijke substitutie van Pb^{2+} door Ln^{3+}-ionen een effect hebben op de perovskiet-structuur en dus op de opto-elektronische en optische eigenschappen. Belangrijk is dat vanwege de afscherming van de 4f-orbitalen door de meer naar buiten gelegen, gevulde 5s- en 5p-schillen de scherpe banden in de Ln^{3+}-absorptie- en –emissie spectra, die overeenkomen met 4f-4f overgangen, vrijwel ongevoelig zijn voor de omgeving (vb. pH, temperatuur), wat in sommige toepassingen (vb. bioprobes) gevoelige detectie boven het achtergrondniveau mogelijk maakt. In de afgelopen drie jaar zijn Ln^{3+}-gedoteerde $CsPbX_3$ perovskieten veel aandacht beginnen krijgen vanwege de nieuwe eigenschappen die ontstaan door combinatie van Ln^{3+}-ionen met het $CsPbX_3$ perovskiet-materiaal, wat nieuwe perspectieven biedt voor toepassingen in zonnecellen, zonlichtconcentratoren en LEDs. Er is aangetoond dat de Yb^{3+}-emissie bij ~1.0 μm van Yb^{3+}-gedoteerde $CsPbCl_3$ of gemengde halide $CsPb(Cl/Br)_3$-perovskieten een uitzonderlijk hoge fotoluminescentie- kwantumopbrengst heeft, boven 1, wat het resultaat is van het één-op-twee fotonenemissieproces. Niettemin, Er^{3+}, ook een bekend NIR-emitterend Ln^{3+}-ion bij ~1.5 µm, dat interessanter is dan 1.0 µm voor optische telecommunicatie, heeft veel minder aandacht gekregen dan Yb^{3+}.

Doordat $CsPbX_3$ perovskietenfoto-excitering in het UV of zichtbare spectrale gebied vereisen, is hun niet-lineaire opconversie-vermogen om twee of meer NIR-fotonen om te zetten in een enkel foton met kortere golflengte, erg beperkt. Het beperkte opconversie-vermogen komt voort uit het lage rendement ($<10^{-8}$) van multifotonabsorptie door $CsPbX_3$ perovskieten. Foton-opconversie van NIR-fotonen is erg wenselijk voor een breed scala aan toepassingen, zoals in zonnecellen, fotokatalyse, fotodetectie, namaakbestrijding, enz. Gelukkig vertonen Ln^{3+}-gedoteerde opconversie-materialen die geëxciteerd kunnen worden door een goedkope NIR-laser, efficiënte ($>10^{-3}$) opconversie-luminescentie via een meerstaps-fotonabsorptie. Daarom wordt het combineren van Ln^{3+}-gedoteerde opconversie-nanodeeltjes (UCNPs) met $CsPbX_3$ perovskieten erkend als een veelbelovende route om de inherente beperkingen van $CsPbX_3$ te overwinnen; dat wil zeggen dat de UCNPs dienen als NIR-antennes voor het verbeteren van de opconversie-luminescentie van $CsPbX_3$.

Geïnspireerd door deze veelbelovende perspectieven wordt er onderzoek verricht om goed presterende $CsPbX_3$ perovskieten te functionaliseren met luminescerende Ln^{3+}-ionen. In dit opzicht kunnen twee strategieën worden gevolgd, die ook in dit doctoraatswerk aan bod zijn gekomen: i) het decoreren van $CsPbX_3$ met Ln^{3+}-gedoteerde UCNPs en ii) Ln^{3+}-dotering in $CsPbX_3$. Deze twee benaderingen maken het mogelijk om verschillende optische funcionaliteiten aan $CsPbX_3$ toe te voegen. Meer specifiek maakt de eerste benadering het mogelijk om de lichtabsorptie naar het NIR-gebied uit te breiden, om zo tot NIR-naar-zichtbare foton-opconversie te komen, terwijl de tweede benadering nieuwe mogelijkheden biedt voor het afstemmen van het spectrale emissiebereik.

Hoofdstuk 1 geeft een inleiding tot $CsPbX_3$ perovskieten, lanthaniden, UCNPs-gesensiteerde $CsPbX_3$, en Ln^{3+}-gedoteerde $CsPbX_3$. Allereerst worden de kristalstructuren en optische eigenschappen van $CsPbX_3$ perovskietengepresenteerd, gevolgd door een inleiding tot de lanthaniden, waaronder ook hun elektronische configuraties en luminescentiemechanismen. Vervolgens wordt UCNPs-gesensiteerd $CsPbX_3$ bekeken, inclusief synthesemethoden en opconversie-luminescentie eigenschappen. Ten slotte worden de dotering sprincipes, synthese en optische performantie van Ln^{3+}-gedoteerde $CsPbX_3$ perovskietensamengevat.

Hoofdstuk 2 beschrijft de synthese en karakterisering van het Ln^{3+}-UCNPs-gesensiteerde $CsPbBr_3$ systeem. In eerste instantie wordt een vergelijking gemaakt tussen fysieke menging enerzijds en *in-situ* groeimethoden anderzijds, voor het combineren van $CsPbBr_3$ met UCNPs. De resultaten suggereren dat een hybride systeem met een kleine afstand tussen de UCNPs en het $CsPbBr_3$ kan worden bekomen door *in-situ* groei. Vervolgens worden de energietransfer mechanismen in het hybride systeem in detail onderzocht. De thermisch en fotostabiliteit van het systeem wordt ook van naderbij bekeken.

Hoofdstuk 3 beschrijft een strategie omde Er^{3+} 1.5 μm luminescentie in $CsPbCl_3$ nanokristallen te versterkendoor middel van Yb^{3+}-sensitering. Ten eerste wordt Yb^{3+}- en Er^{3+}-enkelvoudig gedoteerd $CsPbCl_3$ onderzocht. Daarna wordt Yb^{3+}/Er^{3+} gecodoteerd $CsPbX_3$ met verschillende doteringsgehaltes gepresenteerd. Belangrijk is dat een transient intern redox-mechanisme wordt voorgesteld om het afwijkende gedrag van de Yb^{3+}- en Er^{3+}-emitters te verklaren in enkelvoudig gedoteerd $CsPbX_3$.

Hoofdstuk 4 demonstreertde sensiteringvan de Er^{3+} 1.5 μm luminescentie in $CsPbCl_3$ nanokristallendoor een alternatieve sensiteerder: het Mn^{2+} ion. Ten eerste worden de syntheseen karakterisering van Mn^{2+}-gedoteerde $CsPbCl_3$ nanokristallen onderzocht. Vervolgens worden de synthese en karakterisering van Mn^{2+}/Er^{3+}

gecodoteerd $CsPbCl_3$ met verschillende doteringsgehaltes bekeken. Hetenergie-overdrachtsmechanisme in Mn^{2+}/Er^{3+} gecodoteerd $CsPbCl_3$ wordt vervolgens besproken.

Hoofdstuk 5 vat de conclusies van deze doctoraatsthesis samen en geeft een vooruitblik op basis van de behaalde resultaten.

Contents

Chapter 1 Introduction

This thesis deals with luminescent lanthanide-functionalized all-inorganic cesium lead halide perovskites (LHPs) $CsPbX_3$ ($X = Cl^-, Br^-, I^-$). The two components of these materials, namely LHPs and lanthanide ions, bring special characteristics that are worth summarizing before entering more in-depth into the discussion of their combined properties.

1.1 $CsPbX_3$ Perovskite

The discovery of bulk all-inorganic $CsPbX_3$ LHPs dates back to 1893,[1] whereas their perovskite crystal structure and optical properties were not revealed until the 1950s.[2] Although LHPs have been studied for more than 60 years, they have been gaining intense interest since the first perovskite photovoltaic cell based on organic-inorganic hybrid perovskites $CH_3NH_3PbI_3$ with a power conversion efficiency (PCE) of 3.8% came out in 2009.[3] The PCE of these perovskites-based single-junction solar cells has rapidly increased to >25% over the past decade,[4] which is comparable to Si-based solar cells. Despite the great progress in efficiency, such hybrid perovskites suffer from poor thermal stability because of the volatile and hygroscopic organic A-site cation, i.e., methylammonium ($MA = CH_3NH_3^+$) or formamidinium ($FA = NH_2CH = NH_2^+$).[5] The phase instability has become a bottleneck for their commercial applications. Replacement of the organic cation with inorganic Cs^+ has been proved successful to solve this problem.[6] It was not until 2015 when all-inorganic perovskites also gained tremendous attention after the first demonstration of nanometer-scale colloidal nanocrystals (NCs), also known as quantum dots (QDs), using a hot-injection (HI) route by Protesescu et al.[7] Since then, $CsPbX_3$ LHPs became an emerging branch in the emissive nanomaterials family.

Over the past several years, $CsPbX_3$ NCs have been widely applied in photovoltaic and optoelectronic devices, including solar cells, lasers, photodetectors, and light-emitting diodes (LEDs).[8-16] All these applications benefit from their superior optical and electronic properties, such as extremely high molar extinction coefficient, tunable emission wavelength, high color purity, high carrier mobility.[7,17-19] An in-depth understanding of the structure is essential to reveal these electrical and optical properties.

1.1.1 Crystal and Electronic Structure

Crystal structure

The general chemical formula of the perovskites is ABX_3. In the case of $CsPbX_3$ LHPs, A is a large monovalent cation (Cs^+), B is a divalent cation (Pb^{2+}), and X is a monovalent halide anion (Cl^-, Br^-, I^-). In an ideal cubic structure of LHPs, the Cs^+ cations are situated at the cube vertices, and X^- anions are located at the face centers of the cube. The Pb^{2+} ion is instead located at the body center of the cube. The central Pb^{2+} cation coordinates with 6 X^- anions, forming an octahedral structure (Figure 1.1a). The stability of the perovskite crystal structure can be predicted by the semiempirical geometric Goldschmidt's tolerance factor ($t = (r_A + r_B)/[\sqrt{2}(r_B + r_X)]$), along with the octahedral factor ($\mu = r_B/r_X$); r_A, r_B, and r_X refer to the ionic radii of A, B and X, respectively.[20]

To obtain a perovskite structure, the tolerance factor requires to be roughly in the range of $0.8< t <1.0$, and the octahedral factor in the range of $0.44< \mu <0.90$.[10] An ideal cubic perovskite structure is favored in the range $0.9< t <1$, while a distorted perovskite structure of tetragonal/orthorhombic is formed in the range $0.8< \tau <0. 9$. For the values of $\tau <0.8$ and $\tau >1$, non-perovskite structure will be formed. For the case of $CsPbX_3$ perovskites, the t values are calculated to be 0.87, 0.86 and 0.85 for $CsPbCl_3$, $CsPbBr_3$ and $CsPbI_3$, respectively. Obviously, all of the t values for

$CsPbX_3$ are near the lower boundary for perovskite structures, indicating that the perovskite structures are prone to distortion. Among the series of $CsPbX_3$ perovskites, the tolerance factor value of $CsPbI_3$ is the smallest, which favors its transformation from the cubic black phase (α-$CsPbI_3$) to an orthorhombic yellow phase (δ-$CsPbI_3$) at room temperature (Figure 1.1b,c).[10] Partial substitution of Pb^{2+} with smaller metal ions (e.g., Bi^{3+}, Ca^{2+}, transition metal ions, lanthanide ions) in the $CsPbX_3$ LHPs has been regarded as an attractive strategy for stabilizing the perovskite structure as discussed further in the following section.[21-26]

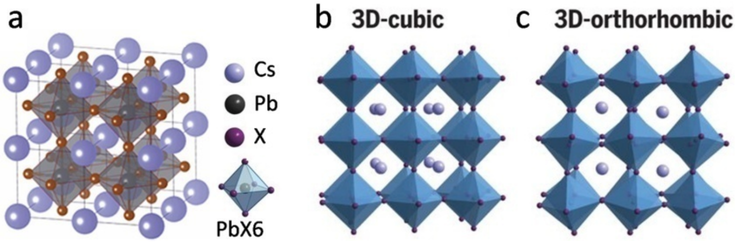

Figure 1.1 Schematic representations of (a) $CsPbX_3$ perovskites with cubic structure. Adapted from ref 7. Crystal structures of lead halide perovskites with (b) cubic and (c) orthorhombic phase. Adapted from ref 27.

Electronic structure

Theoretical calculations and experimental measurements have consistently shown that the conduction band minimum (CBM) of $CsPbX_3$ is predominantly composed of antibonding mixing of Pb 6p and X np orbitals with dominant contributions from Pb 6p, while the valence band maximum (VBM) results from antibonding hybridization of Pb 6s and X np orbitals, with major contribution from X np (Figure 1.2a).[18,28] When the X ions cross from Cl^- to Br^- to I^-, the VBM is found to shift prominently toward higher energies (less positive potentials), while the CBM shifts slightly towards lower energies (less negative potentials), yielding a systematic decrease in the bandgap for $CsPbX_3$ (Figure 1.2b).[18] Correspondingly, the molar extinction coefficient (ε, calculated based on Beer−Lambert law, $A(\lambda)$ =

$\varepsilon(\lambda)\times C\times L$; here A is the absorbance at the wavelength λ, C is the molar concentration of $CsPbX_3$ NCs, and L is the optical path length as determined by the dimension of the cuvette) or the absorption cross section (σ, calculated from the equation, $\sigma(E) = 1000\times\varepsilon(E)\times\text{In}(10)/N_A$; here E is the energy of absorbed light corresponding to the respective lowest-energy excitonic transition, and N_A (mol^{-1}) is Avogadro's number) of $CsPbX_3$ also exhibits a systematic decrease from $X^- = Cl^-$ to Br^- to I^- (Figure 1.2c). The observed change in ε with halide composition can be explained by the decrease in the dielectric constant (ε_{eff}) from $CsPbI_3$ to $CsPbBr_3$ to $CsPbCl_3$.[7,29] Although the physical parameters of $CsPbCl_3$ are not shown in Figure 1.2d, the values of the exciton binding energy (R^*) and the reduced effective mass (μ) are considered to be larger than those of the bromide and iodide analogs with smaller bandgaps; while the ε_{eff} value is in the opposite case. The smaller the ε_{eff}, the larger the R^*, which in turn gets reflected in the stronger excitonic absorption (Figure 1.2c,d).[18]

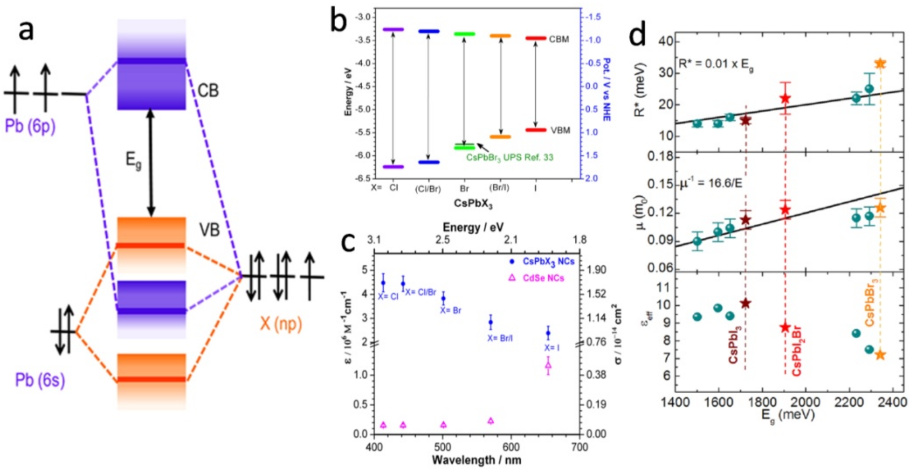

Figure 1.2 (a) Schematic representation of bonding/antibonding orbitals of $APbX_3$ showing the formation of the VB and CB. (b) Band edge energies of $CsPbX_3$ NCs. (c) Molar extinction coefficient (ε) and absorption cross section (σ) of $CsPbX_3$ NCs. Please note that the pink triangles corresponding to CdSe NCs are used to indicate the stronger absorption

of $CsPbX_3$ than CdSe with a similar optical gap. Adapted from ref 18. (d) Exciton binding energy (R*), effective mass (μ), and dielectric constant (ε_{eff}) of $CsPbX_3$ as a function of the bandgap (Eg). Brown, red, and yellow stars indicate the results for $CsPbI_3$, $CsPbI_2Br$, and $CsPbBr_3$, respectively. Green balls reprensent the results for different hybrid organic−inorganic materials for comparison. Adapted from ref 29.

1.1.2 Optical Properties

The optical properties of $CsPbX_3$ LHPs are dependent on their electronic structures. It has been reported that the optical transition energy is decreased from $CsPbCl_3$ to $CsPbI_3$; thereby the resulting absorption and photoluminescence (PL) emission spectra exhibit a red shift (Figure 1.3a-c).[7] One of the greatest advantages of LHPs is the ease with which the individual components can be exchanged to tailor the bandgap of the resulting material, enabling tunable emission wavelength in the entire visible spectrum (Figure 1.3d).[19] The PL emission bandwidth (full width at half-maximum, fwhm) of the perovskite NCs is narrower (12 – 42 nm) than that for most of the other types of quantum dots (QDs), thereby placing the PL color coordinates of LHPs more toward the curved edge of the CIE chromaticity space (e.g., CIE 1931 standard).[30]

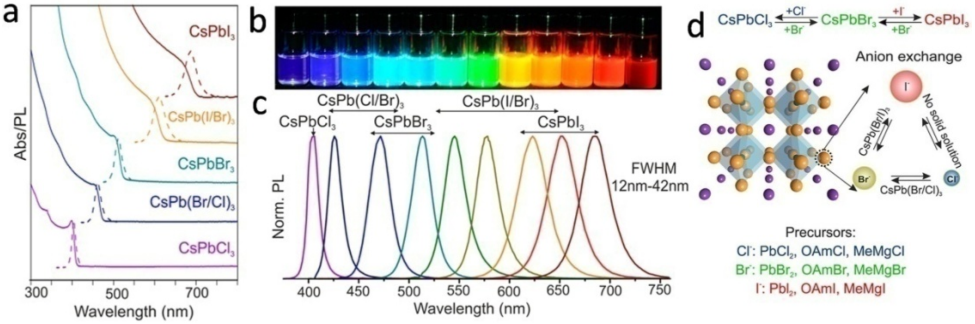

Figure 1.3 (a) Typical optical absorption and PL spectra of $CsPbX_3$ NCs. (b) Colloidal solutions in toluene under UV lamp (λ = 365 nm). (c) Representative PL spectra. Adapted from ref 7. (d) Schematic of the anion exchange within the cubic perovskite crystal

structure of $CsPbX_3$ along with a list of suitable reagents for each reaction when performed in organic media. Adapted from ref 19.

As can be seen from the above figures, the absorption and emission performance of the $CsPbX_3$ LHPs are limited to the visible spectral regions. It has been reported that the optical properities of $CsPbX_3$ can be extended to the near-infrared (NIR) range by pairing the energy transfer (ET) system of trivalent lanthanide ions (Ln^{3+}) doped upconversion nanoparticles (UCNPs) with LHPs and Ln^{3+}-doped LHPs.

1.2 Ln^{3+}

Generally, the term lanthanide (Ln) is associated with the group of elements in the periodic table (sixth period in periodic table) from lanthanum (Z = 57) to lutetium (Z = 71) with similar physical and chemical properties, particularly oxidation states.[31]

1.2.1 Electron Configurations

Ln can occur as divalent (Ln^{2+}) or trivalent (Ln^{3+}), but the latter state is more stable considering the electron configurations. Ln^{3+} ions in the Ln series have unique electron configurations ($[Xe]4f^n$, n = 0 – 14) with a gradual filling of the 4f orbitals from $4f^0$ (La^{3+}) to $4f^{14}$ (Lu^{3+}), which are shielded by the outer filled $5s^25p^6$ shells (Table 1.1).[32] The 4f–4f intraconfigurational transition of free Ln^{3+} ion is parity forbidden, which can be broken by the mixing of certain odd-parity configurations once the Ln^{3+} ion is inserted into a matrix lattice (usually inorganic materials) with a wide range of coordination numbers (CN >6).[33]

Table 1.1 Electron configuration of Ln and Ln^{3+} ions, and ground state energy level of Ln^{3+} ions.[34]

Element	Atomic number (Z)	Configuration Ln	Configuration Ln^{3+}	Ground state Ln^{3+}
La	57	$5d^16s^2$	$4f^0$	$^1S_0$
Ce	58	$4f^15d^16s^2$	$4f^1$	$^2F_{5/2}$
Pr	59	$4f^36s^2$	$4f^2$	$^3H_4$
Nd	60	$4f^46s^2$	$4f^3$	$^4I_{9/2}$
Pm	61	$4f^56s^2$	$4f^4$	$^5I_4$
Sm	62	$4f^66s^2$	$4f^5$	$^6H_{5/2}$
Eu	63	$4f^76s^2$	$4f^6$	$^7F_0$
Gd	64	$4f^75d^16s^2$	$4f^7$	$^8S_{7/2}$
Tb	65	$4f^96s^2$	$4f^8$	$^7H_6$
Dy	66	$4f^{10}6s^2$	$4f^9$	$^6H_{15/2}$
Ho	67	$4f^{11}6s^2$	$4f^{10}$	$^5I_8$
Er	68	$4f^{12}6s^2$	$4f^{11}$	$^4I_{15/2}$
Tm	67	$4f^{13}6s^2$	$4f^{12}$	$^3H_6$
Yb	70	$4f^{14}6s^2$	$4f^{13}$	$^2F_{7/2}$
Lu	71	$4f^{14}5d^16s^2$	$4f^{14}$	$^1S_0$

1.2.2 Luminescence Mechanisms

The history of light emission from Ln dates back to the 19th century.[35] Since then, different types of Ln-containing light-emitting materials have been developed for applications in light-emitting devices. Notably, one of the most interesting features of the Ln^{3+} ions with the exception of La^{3+} and Lu^{3+} is their luminescence emission spanning from UV, visible, to NIR spectral regions because of their intraconfigurational transitions and rich energy levels (Figure 1.4).[36-38] Owing to the shielding of the 4f orbitals from the environment by outer filled $5s^2$ and $5p^6$ shells, the emission originating from inner-shell 4f–4f transitions is characterized by sharp bands and long lifetimes (up to tens of milliseconds).[32,38] Ce^{3+} is a special case in view of its intense broadband emission due to parity-allowed f–d transition. The color of the emitted light depends on the Ln^{3+}. For instance, Gd^{3+} emits UV light, Eu^{3+} red, Tb^{3+} green, Sm^{3+} orange, and Tm^{3+} blue light. Yb^{3+}, Nd^{3+}, and Er^{3+} are well-known for their NIR luminescence, but other Ln^{3+} ions (Pr^{3+}, Sm^{3+}, Dy^{3+}, Ho^{3+}, and Tm^{3+}) also show transitions in the NIR region (Figure 1.4c).[39]

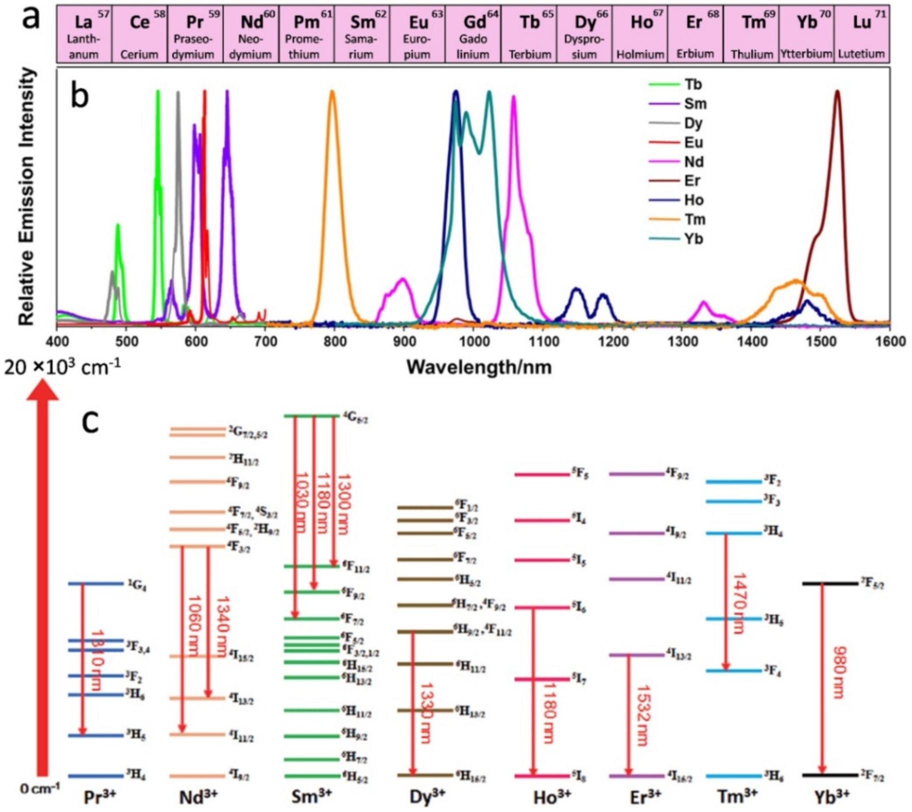

Figure 1.4 (a) The fifteen Ln^{3+} ions with atomic numbers from 57 to 71. (b) Normalized emission bands of Ln^{3+} complexes in solution: illustration of sharp emission spectra. Adapted from ref 36. (c) Energy level diagrams of Ln^{3+} ions with typical emissions within the NIR region. Adapted from ref 39.

In general, the Ln^{3+} luminescence mechanisms consist of three models of spectral conversion: downshifting (DS), downconversion (DC) and upconversion (UC).[40] The simplified schematic diagram of these three processes is presented in Scheme 1.1, where the blue arrows represent a higher-energy photon, and the green, yellow and red arrows lower-energy photons.[41] DS luminescence is a Stokes process, in which one shorter-wavelength photon with higher energy is converted to one longer-wavelength photon with lower energy. The most widely reported visible Ln^{3+} activators are Tb^{3+}, Eu^{3+}, Sm^{3+}, Dy^{3+} ions.[42] DC (also known as quantum cutting QC or quantum splitting) luminescence is able to cut one higher-energy photon into at least two lower-energy photons.[43] UC luminescence (UCL) is a nonlinear optical anti-Stokes process, where the sequential absorption of two or more low-energy photons (e.g., NIR photons) gives rise to one high-energy photon.[44] The UCL typically takes place in a sensitizer (usually Nd^{3+} or Yb^{3+})-activator (usually Ho^{3+}, Er^{3+} or Tm^{3+}) codoped inorganic host materials.

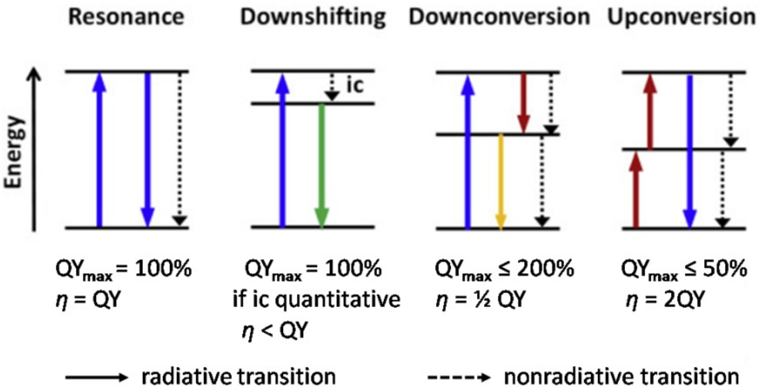

Scheme 1.1 The schematic representation of resonant emission, DS, DC and UC mechanisms; QY is the quantum yield and η the quantum effiiency; ic means internal conversion. Modified from ref 41.

It is well known that quantum efficiency (η, refers to energy output/energy input) or quantum yield (QY, refers to events/absorbed photon or emitted photons/absorbed photons depending on the processes),[41] is the most important factor for luminescent materials. Quantum efficiency (η) is only equal to quantum yield (QY) for a primary photochemical process, i.e. resonant luminescence from a two-level system (Scheme 1.1). According to ref 41, the η for DS is lower than QY (usually smaller than 100%) because it is a one-photon to one-photon conversion, along with nonradiative relaxation processes[43] and 100% can only be achieved in a resonance situation. While the η for DC is <100% and the QY is above 100% because it is a two-photon emission mechanism. Instead, for UC, the η and QY will not exceed 100% and 50%, respectively, because it is a two-photon absorption mechanism.

Quantum cutting

The term QC describes the phenomenon that one absorbed high-energy photon is transformed into two or more emitted lower-energy photons, with a QY theoretically larger than 100%.[45] The discovery of the QC effect observed in Pr^{3+}-doped YF_3 with a QY of about 140% under the excitation of 185 nm dates back to 1970s.[45,46]

The concept is illustrated in Figure 1.5 with two types of ions, I and II, with hypothetical energy level schemes. Type I is an ion for which emission from a high energy level can occur. Type II is an ion to which ET takes place.[47] The first mechanism is based on a single ion with three energy levels (Figure 1.5a). NIR QC by a two-photon emission from a high energy level by absorption of one UV or visible photon is theoretically possible for a single Ln^{3+} ion. Representative examples have been reported for single Ln^{3+}-doped fluorides capable of a cascade emission from ions such as Ho^{3+}, Tm^{3+}, or Er^{3+}. However, competing emission in the UV regions and nonradiative recombination that compete with the desired emission of two NIR photons are the major problems presented by single ion-based QC.

The use of a second type of Ln^{3+} ion (type II ion) can prevent losses in the UV regions. The mechanisms involving type I ion (energy donor) and type II ion (energy acceptor) for NIR QC are summarized in Figure 1.5b-e. Two NIR photons emission can be achieved by QC involving a two-step (Figure 1.5b) or one-step ET between two Ln^{3+} ions (Figure 1.5c,d). These three QC mechanisms require resonance ET between two Ln^{3+} ions in close proximity. The ET can be described as a first-order rate process, governed by the degree of spectral overlap between the donor emission and the acceptor absorption. A second-order cooperative sensitization may dominate the relaxation process if there is no spectral overlap, which results in simultaneous excitation of two energy acceptors and subsequent emission of two NIR photons (Figure 1.5e). In this case, the energy of the emitted photons from the donor must equal the energy of the absorption transitions of the two acceptors. It should be noted that the possibility of the second-order cooperative ET process is about 1000 times lower than that of the first-order resonant ET process.[47]

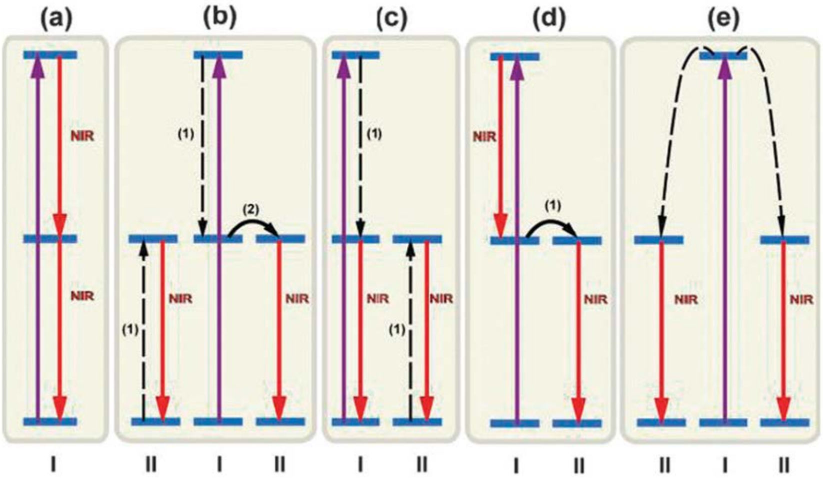

Figure 1.5 Summary of typical mechanisms of NIR QC. Simplified energy level diagrams for types I and II ions are given to illustrate the concept of NIR QC. (a) NIR QC on a single ion by the sequential emission of two NIR photons. (b-d) NIR QC due to resonant ET from ion I to ion II. (e) NIR QC due to cooperative ET from ion I to ion II. Note that two type II ions simultaneously emit two photons in the NIR spectral region. The purple solid, red solid, and dashed arrows represent excitation, emission, and ET processes (cross relaxation for b,c and cooperative ET for e), respectively. Adapted from ref 47.

Dorenbos and coworkers predicted that hosts with weak crystal field, low phonon energy, large bandgap, large cation-anion distance, and large coordination number for the substitution site were considered important to favor the QC phenomenon.[48] Fluorides and oxides with wide bandgap and low phonon energy have been accepted as potential hosts for QC to achieve 200% QY. Up to now, QC has been reported in a variety of Pr^{3+}-doped fluorides and several oxides.

Upconversion

Ln^{3+}-doped UCNPs are a promising new generation of imaging agents for bioimaging, taking advantage of their zero autofluorescence background, large anti-Stokes shifts, narrow emission bandwidths, high resistance to photobleaching.[49,50] In the most efficient UC mechanism system, two different types of ions, namely a sensitizer and an activator, are embedded in the unit of UCNP. Yb^{3+} has been reported to be the best sensitizer, due to its larger molar aborption coefficient (2.4 M^{-1} cm^{-1}) at 980 nm for the $^2F_{7/2} \rightarrow {}^2F_{5/2}$ transition among Ln^{3+} ions.[40] While the most common activators in UCNPs are generally restricted to Er^{3+}, Tm^{3+}, and Ho^{3+} ions, thanks to their ladder-like energy levels.[49] Yb^{3+}/Tm^{3+}, Yb^{3+}/Er^{3+}, and Yb^{3+}/Ho^{3+} pairs are the ideal sensitizer/activator pairs in UCNPs for enhanced excitation at 975 nm.

It has been reported that the phonon-induced nonradiative process is the main loss mechanism for UC emissions.[49] Hence, selection of a low phonon-energy matrix for Ln^{3+} has been one of the most efficient strategies to realize an efficient UC process in UCNPs.[39] Among investigated hosts, fluoride materials (e.g., $NaLnF_4$, $BaLnF_5$, CaF_2, etc.) have been proven to be optimal due to their relative low phonon energy (~500 cm^{-1}) and excellent chemical stability. The color output in UCNPs can be finely tuned by variation of the concentrations of Yb^{3+}/Er^{3+}, Yb^{3+}/Tm^{3+} or Yb^{3+}/Ho^{3+} pairs, along with combinations of two or more Ln^{3+} dopants with desirable concentrations (Figure 1.6).[51-53]

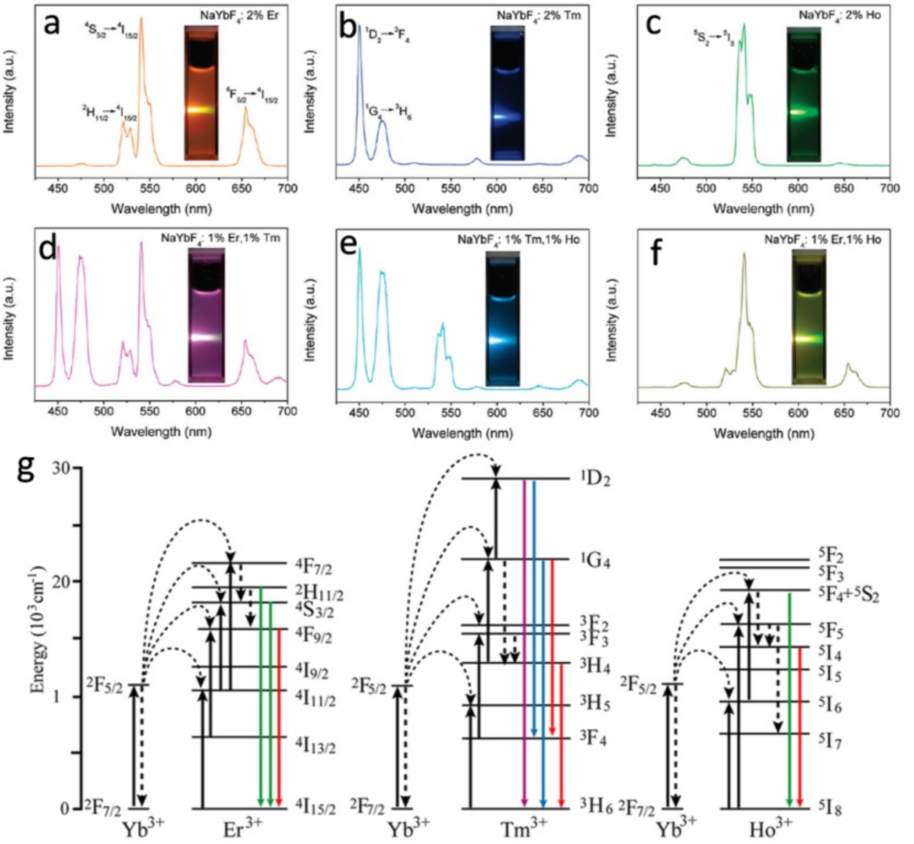

Figure 1.6 UC spectra of NaYbF$_4$:Ln@SiO$_2$ UCNPs (Ln = Er, Tm, Ho) colloidal solutions excited with a 980 nm laser. (a) Ln = 2%Er, (b) 2%Tm, (c) 2%Ho, (d) 1%Er,1%Tm, (e) 1%Tm,1%Ho, (f) 1%Er,1%Ho. Insets are the digital photographs of the corresponding UCNPs colloidal solutions, excited with a 980 nm laser. Adapted from ref 51. (g) UC mechanism in Yb^{3+}/Ln^{3+} codoped UC materials. Adapted from ref 54.

1.2.3 Near-Infrared Light-Based Applications

NIR light in the spectral region of 800 – 1600 nm has attracted great interest for potential applications in photovoltaic cells, lasers, telecommunications and so forth.[32] NIR-emitting trivalent Ln^{3+} ions, such as Yb^{3+} emits at about 1.0 μm, Nd^{3+}

at 1.06 μm, Tm^{3+} at 1.47 μm, and Er^{3+} at 1.5 μm, are ideally suitable candidates for the above applications.

Photovoltaic cells

Energy loss stems from the spectral mismatch of incident solar photon energies to the energy gap of a solar cell is the main factor limiting its efficiency. The Ln^{3+}-doped luminescent materials as spectral convertors have shown great promise in improving the photovoltaic conversion of c-Si or Ge solar cells. This is due to the spectral match between Ln^{3+} ions and semiconducting Si or Ge; for example, Yb^{3+} emission at ~1.0 μm and Er^{3+} emission at ~1.5 μm are in line with the absorption bands of Si (~1.1 eV) and Ge (0.7 eV) solar cells, respectively.

Lasers

NIR-luminescent Ln^{3+} ions have been regarded as active materials for solid-state lasers. YAG:Nd (III) with the emission line at 1.06 μm is one of the most widely used lasers; multi-line lasers can be easily obtained from doubled (532 nm), tripled (355 nm), or quadrupled (266 nm) frequency.[31,32] High-power YAG:Nd lasers can find applications in manufacturing, while low-power lasers emitting at long wavelengths are very interesting in medical applications. In addition, NIR-emitting lasers are one of the major components in telecommunication systems.[31]

Telecommunications

Telecommunications and high-speed internet are usually dependent on silica optical fibers, but signal attenuation occurs after 50 or 100 km and need amplification in spite of their excellent transparency in the visible and NIR range.[31] One of the solutions is to use the ideal waveguide amplifiers: Er-doped silica which emits light at 1.5 μm located in the main telecommunication window (C band, 1.5 μm). An alternative way could be doping Er^{3+} into different hosts.

1.3 UCNPs-Sensitized $CsPbX_3$

Despite the fact that $CsPbX_3$ LHPs exhibit superb linear optical properties under UV or visible light excitation, their nonlinear optical properties, i.e. NIR-triggered photon UC, are limited because of the low efficiency of multiphoton absorption and the requirement of expensive pulsed lasers for excitation.[55,56] In contrast to linear optical luminescence, the nonlinear UCL features several merits including a large penetration depth, high spatial resolution, and little damage to the targeted samples, which are desired in effective solar spectrum conversion, multiplexed optical encoding, three-dimensional displays, and bioimaging.[57,58]

1.3.1 Construction of UCNPs-Sensitized LHPs

The integration of UCNPs with LHP NCs can be mainly pursued by two routes, namely physical mixing and *in situ* growth. The physical mixing method relies on the simple mixing of preformed UCNPs and LHPs with the desired ratio under the assistance of grinding, magnetic stirring or spin-coating depending on the phase of the starting materials (powders or suspensions, respectively).[55,59-62] On the other hand, *in situ* growth consists in the nucleation and growth of LHPs NCs on the surface of preformed UCNPs which serve as seed for the growth of the LHPs NCs as the LHPs precusors are injected. The organic ligand plays a key role as structure-directing agent for obtaining hybrids of UCNPs and LHPs in both mixing and *in situ* growth methods. Simple mixing of UCNPs and LHPs without extra addition of organic ligands was found to yield isolated phases (Figure 1.7a),[60] while a more homogenous hybrid system can be achieved if proper ligands which can anchor to the surfaces of both UCNPs and LHPs NCs are added (Figure 1.7 d).[63,64] On the other hand, the *in situ* growth approach generates a hybrid heterostructure with shorter distance between UCNPs and LHPs, which are more homogeneously distributed, resulting in a higher probability of interactions in the composite.[65]

In addition to direct interactions between UCNPs and LHPs, these two components can also be coinserted into a matrix. Recently, Li and coworkers developed an *in situ* melt-quenching technique to prepare a dual-phase glass containing $NaYbF_4$:Tm UCNPs (the doping concentration is not clear) and $CsPbBr_3$ NCs, which were simultaneously precipitated inside the same glass matrix (Figure 1.7e,f).[61] In the glass, $NaYbF_4$:Tm and $CsPbBr_3$ NCs phases were not closely packed, due to the fact that no organic ligands were introduced. However, even if organic ligands were added, the high-temperature (1000 °C) required for glass fabrication would have decomposed them. Although no hybrid structure was obtained, the glass matrix can solve the issue of the poor long-term stability of LHPs.

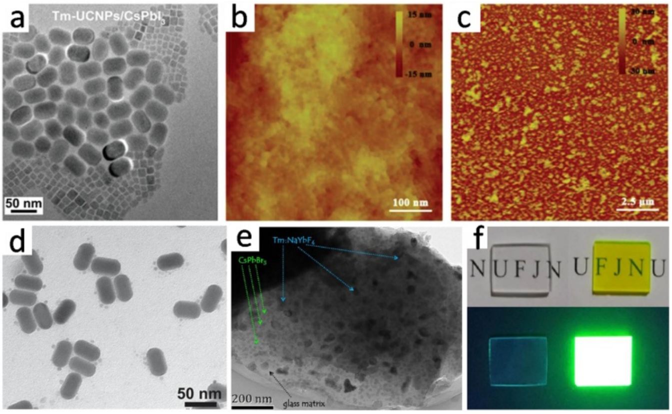

Figure 1.7 (a) TEM image of a composite constituted by $CsPbI_3$ NCs and $NaYF_4$:20%Yb,0.5%Tm UCNPs through physical mixing approach. Adapted from ref 60. (b) Atomic force microscopy (AFM) image of the as prepared α-$CsPbI_3$ film on a quartz substrate; (c) AFM image of the $NaYF_4$:20%Yb,2%Er film fabricated on top of the α-$CsPbI_3$ film via spin-coating technique. Adapted from ref 62. (d) Transmission electron microscopy (TEM) image of nanohybrids obtained from the physical mixing of

$NaYF_4$:22%Yb,1.2%Tm UCNPs and $CH_3NH_3PbBr_3$ NCs. Adapted from ref 63. (e) TEM image of a typical $CsPbBr_3$ and $NaYbF_4$:Tm dual-phase glass; (f) Photographs of the precursor glass (left) and dual-phase glass (right) under the irradiation of a daylight (top) and UV lamp (bottom). Adapted from ref 62.

1.3.2 Optical Properties of UCNPs-Sensitized LHPs

The realization of nonlinear UCL for $CsPbX_3$ LHPs is based on multistep ET processes through Yb^{3+} → Tm^{3+} (or Er^{3+}, Ho^{3+}) → $CsPbX_3$ under NIR excitation. Namely, the NIR photons are firstly captured by the Yb^{3+} sensitizer and then the energy is transferred to the luminescent activator (e.g., Tm^{3+}, Er^{3+}, Ho^{3+}) which emits upconverted light in the UV/visible range. These high-energy photons can reach the $CsPbX_3$ LHPs and thus triggering the band-edge emission. There are two primary ET mechanisms in the UCNPs sensitized-LHPs system, radiative photon reabsorption (PR) and nonradiative Förster resonance energy transfer (FRET), as it will be further described in Chapter 2 of this thesis. Spectral overlap between the energy donor (UCNPs) emission and the acceptor (LHPs) absorption is the prerequisite for both PR and FRET, which also benefit from the high molar extinction coefficient of the LHPs. Radiative PR is a photon-mediated process where the acceptor is excited via the absorption of photons emitted by the donor. Such ET can occur over a very long distance in some cases without the change in the donor luminescence lifetime due to no interactions between the donor and accepor. However, nonradiative FRET requires short separation distances ($R < 10$ nm) between donor-acceptor pairs as the efficiency of FRET scales with R^{-6}, and energy is transferred between the resonant electronic excited states resulting in significantly more efficient ET compared to the PR.[66-68] Tm^{3+}-based UCNP is the most efficient energy donor for LHPs due to the intense UV UCL at ~360 nm and (or) blue emission at ~450/480 nm (whose relative intensity depends on the environment of the Tm^{3+} ions), which effectively overlaps with the absorption of wide-bandgap LHPs. Therefore, the whole series of the $CsPbX_3$ LHPs can be excited by Tm^{3+}-based UCNPs.[55] Instead, the absorption spectrum of the narrow-bandgap $CsPbI_3$ matches all of the emission spectra of UCNPs, including Er-, Ho-, and Tm-based UCNPs, resulting in efficient UCL sensitization for $CsPbI_3$.

In 2018, Zheng et al. firstly assembled a series of all-inorganic $CsPbX_3$ (X = Cl^-, Br^-, I^-) NCs with $LiYbF_4$:0.5%Tm@$LiYF_4$ UCNPs by a simple mixing route.[55] Under a low-cost continuous-wave (CW) diode laser excitation (980 nm), the UCNPs-sensitized $CsPbX_3$ NCs showed full-color UCL arising from the perovskite structure through tuning the halide cations (Figure 1.8). Strikingly, the UCL lifetimes of the excitons were found abnormally lengthened from ns to ms. The authors proposed that the ET from UCNPs to LHPs was radiative PR rather than nonradiative FRET in view of the donor core/shell structure disfavoring distance-dependent FRET. The reported ET efficiency from UCNPs to LHPs varied from 65.5 to 96.6 and 99.9% as the halide composition changed from Cl^- to Br^- to I^-. They attributed the lower ET efficiency from UCNPs to $CsPbCl_3$ to the weaker absorption of $CsPbCl_3$ in the UV range than the other halide analogs. However, the ET system containing $CsPbBr_3$ exhibited the highest UC photoluminescence quantum yield (PLQY) of 0.36% for the band-edge emission. They noted that the UC PLQY of $CsPbX_3$ NCs could be boosted by enhancing both the UC PLQYs of the UCNPs and the PLQYs of $CsPbX_3$. Alternative to this work, an *in situ* growth approach affording close-contact hybrid structures consisting of $BaYF_5$:20%Yb,x%Ln (x%Ln = 1%Tm, 2%Er, 2%Ho) UCNPs and $CsPbBr_3$ NCs is presented in Chapter 2 of this thesis. The sensitized $CsPbBr_3$ NCs in three assemblies ($BaYF_5$:20%Yb,1%Tm/$CsPbBr_3$, $BaYF_5$:20%Yb,2%Er/$CsPbBr_3$ and $BaYF_5$:20%Yb,2%Ho/$CsPbBr_3$) all showed bright green UCL emissions from the band-edge carriers recombination under NIR excitation (see Chapter 2).

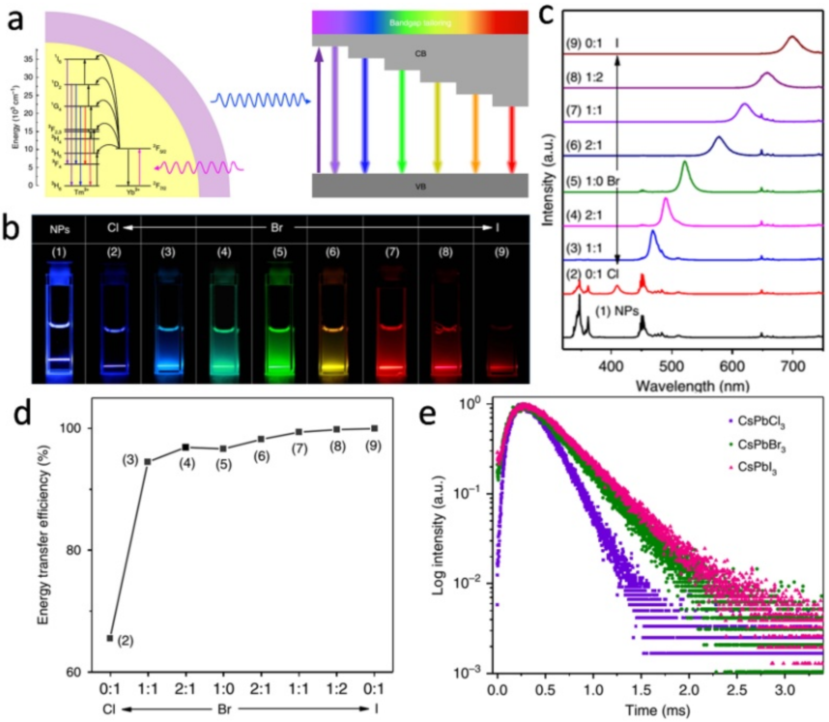

Figure 1.8 (a) Schematic illustration of full-color UCL tuning in $CsPbX_3$ NCs through sensitization by $LiYbF_4$:0.5%Tm@$LiYF_4$ UCNPs. (b) Digital photographs of samples with varying halide compositions under 980 nm illumination, showing color tuning through bandgap tailoring of LHPs. (c) UCL spectra of $LiYbF_4$:0.5%Tm@$LiYF_4$ UCNPs and UCNPs-sensitized $CsPbX_3$ NCs under 980 nm laser excitation. (d) Calculated ET efficiency in UCNPs-sensitized LHPs, as obtained from (c). (e) UCL decays from the band-edge emission in UCNPs-sensitized $CsPbCl_3$, $CsPbBr_3$, and $CsPbI_3$ NCs by monitoring their emissions at 410, 520, and 700 nm, respectively, under 980 nm excitation. Adapted from ref 55.

Obviously, the attractive optical properties of the UCNPs-sensitized LHPs in suspensions are counterbalanced by severe long-term instability, because of the ionic nature and low formation energy of LHPs.[30,69] To overcome the stability issue of LHPs, Lin et al. prepared a novel dual-phase glass containing $NaYbF_4$:Tm UCNPs and $CsPbBr_3$ NCs in the form of powder instead of suspension, and the

$CsPbBr_3$ was protected by the glass host encapsulation.[61] In addition to the UCL bands from Tm^{3+} characteristic 4f–4f transitions, an extra band at 523 nm belonging to the band-edge emission of $CsPbBr_3$ appeared under 980 nm laser excitation. The ET mechanism in $NaYbF_4$:Tm and $CsPbBr_3$ dual-glass was evidenced to be radiative PR from the Tm^{3+} $^1G_4$ state to $CsPbBr_3$ NCs. They found that the emitting color of $CsPbBr_3$ NCs in the glass was tunable by modifying the pumping light power under simultaneous excitation at 365 nm and 980 nm or by changing the measurement temperature (Figure 1.9a-e). Importantly, the $CsPbBr_3$ NC under the protection of solid inorganic oxide glass did not show any PL attenuation after immersion in water for 30 days, indicating superior long-term stability (Figure 1.9f).

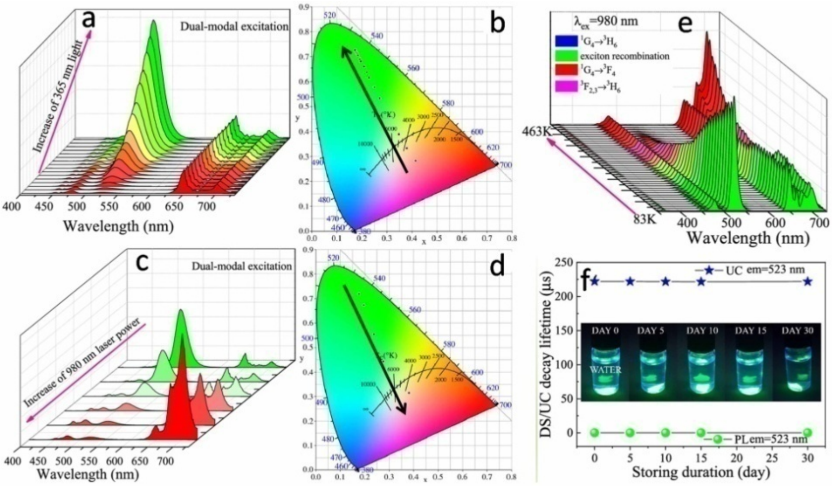

Figure 1.9 (a, c) UCL spectra and (b, d) Color coordinates in the CIE diagrams for the $NaYbF_4$:Tm and $CsPbBr_3$ dual-phase glass under simultaneous excitation at 365 nm and 980 nm: (a, b) the 980 nm NIR laser power is fixed and UV light power gradually increases; (c, d) the 365 nm UV light power is fixed and NIR laser power monotonically enhances. The arrows represent an increase of the excitation light power. (e) Temperature-sensitive UCL spectra for the dual-phase glass under 980 nm laser excitation. (f) Long-term stability test by directly immersing the dual-phase glass in water for 30 days: UCL and PL decay

lifetimes of band-edge emission versus storage time. Insets are the corresponding luminescent photographs of the dual-phase glass in water. Adapted from ref 61.

In comparison with nonradiative FRET, researchers pay more attention to the radiative PR system, probably due to the fact that the PR system can break the distance restriction, which imparts more flexibility for this system. However, PR process only works for acceptors, such as QDs and organic dyes featuring broad and intense absorptions, and not effective for the majority of lanthanide acceptors because of the narrow absorption bands and low molar extinction coefficients (<10 M^{-1} cm^{-1}). On the other hand, FRET can endow the system more efficient ET efficiency and is less sensitive to the competitive concentration quenching effect than PR.

1.4 Ln^{3+}-Doped LHPs

As mentioned before, the Pb 6p orbital contributes more to the CBM of $CsPbX_3$.[18] Therefore, B-site doping with smaller luminescent Ln^{3+} ions has been widely accepted as an attractive approach not only for modulating the optical and optoelectronic properties, but also imparting novel functionalities to LHPs.[70-79] In the case of Ln^{3+} doping, there are two possible circumstances that can be summoned to elaborate the subsequent perovskite structure:[80] i) dopants may modify the perovskite crystal surface. ii) The dopants are substitutionally exposed while replacing the Pb^{2+} component. In the first case, the modification of the crystal surface can affect the growth rate and surface passivation. The second case seems feasible as it increases the overall entropy of the perovskite lattice, thereby stabilizing it thermodynamically. These two cases may endow different optical and optoelectric properties of Ln^{3+}-doped LHPs.

Song's group has systematically studied a series of Ln^{3+}-doped $CsPbCl_3$ and $CsPb(Cl/Br)_3$ NCs. They first reported Ln^{3+} (Ce^{3+}, Yb^{3+}, Er^{3+}) doping into mixed-halide $CsPb(Cl/Br)_3$ NCs by a hot-injection (HI) method. In Ln^{3+}-doped $CsPb(Cl/Br)_3$ NCs, characteristic Ce^{3+} and Yb^{3+} emissions were observed and the power conversion efficiency (PCE) of silicon solar cells was improved from 18.1% to 21.5% because of the energy match between Yb^{3+} and silicon.

However, Ln^{3+} doping into such semiconducting matrixes is particularly challenging and deserves some considerations. First, it has to be reminded that, as known, Ln^{3+} incorporation into traditional QDs, such as CdS, CdSe, GaAs, InP, etc. is highly inefficient, owing to the fact that Ln^{3+} prefers sites with high CN ($\geq$6) and is not easily substituted in tetrahedral sites (CN = 4) typical of CdS or CdSe.[81] On the other hand, compared to traditional QDs, the LHPs can provide an octahedral coordination environment (CN = 6) for Ln^{3+}, which can be beneficial for doping. However, similarly to the Mn^{2+} case that doping into CdSe QDs is more difficult than CdS analogs,[82] doping Ln^{3+} into narrow-bandgap LHPs, i.e., $CsPbBr_3$ and $CsPbI_3$ NCs by the popular HI method that has been used for chloride analogs remains challenging. Therefore, it is highly desired to rationalize the different behavior among the class of LHPs with different halides.

1.4.1 Doping Principle and Mechanism

Since the first demonstration of the $CsPbX_3$ NCs synthesis by Protesescu and coworkers in 2015,[7] scientific researchers have made enormous efforts towards metal ions doping into LHPs for high-performance devices. However, there was no report on Ln^{3+} doping into LHP host until two years later. This observation highlights that Ln^{3+} doping into LHPs by the popular HI method below 200 °C is particularly challenging. Some chemistry principles and guidelines need to be taken into careful consideration when designing a procedure for Ln^{3+} doping, which may be also applied for the incorporation of other metal ions.

Goldschmidt's rules

As discussed before, a perovskite structure should meet the requirements of the tolerance factor 0.8< t <1.0, and the octahedral factor 0.44< μ <0.90. Figure 1.10 shows the plotted values for the tolerance against the octahedral factor for $CsMX_3$ (M = Pb^{2+}, Ln^{3+} and Mn^{2+}) structures by only taking into consideration the ionic radii, in which the grey areas (I and II) stand for the perovskite region, and the dark grey shading indicates the area of ideal cubic perovskite structure II (0.9< t <1). When the radius of B-cation is decreased from Pb^{2+} (119 pm) to Mn^{2+} (83 pm), all of chloride perovskites with listed B-cations fall in area II because of the increased tolerance factor, indicating that B-site doping with smaller cation makes the 3D cubic structure more stable.[83] On the contrary, the iodide perovskites fall out of the perovskite area after complete substitution of Pb^{2+} by smaller Ln^{3+} or Mn^{2+}, resulting in the tilting or rotation of the octahedron leading eventually to the collapse of the perovskite structure. For B-site doping, the charge state should also be taken into consideration to avoid dopant segregation in the host crystal lattice. Despite the simplicity of this rule, it has proven to be a useful tool for predicting the characteristics of the perovskites structures.[84]

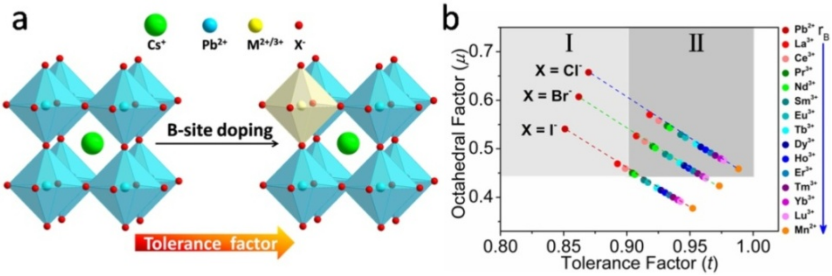

Figure 1.10 (a) Schematic illustration of the B-site doping in $CsPbCl_3$ cubic structure. (b) Tolerance factor t versus μ of $CsMX_3$. I and II indicate the area for the perovskite structure, and II designates the area for the ideal cubic perovskite structure. The ionic radius is reduced from Pb^{2+} to Mn^{2+} ions as indicated by the blue arrow.

Hard and soft acids and bases principle

The chemical species that constitute the lattice of a semiconducting material can be subdivided into two categories of different chemical-physical characteristics, according to a concept theory first proposed by Pearson. “Hard” species are denoted by small size, high charge and weak polarizing ability.[85] In contrast, “soft” species are characterized by a large radius and low charge, which can be delocalized (polarizability). These characteristics are often associated to Lewis acids, which are electron acceptor species without unshared pairs of electrons in their valence shell, and Lewis bases, which are electron donor species. It has to be underlined that these concepts are qualitative, and different intermediate degrees of “hardness” and “softness” can characterize Lewis acids and bases. A typical example is the series of halide bases Cl^-, Br^-, I^-, where the increasing radius and decreased electronegativity increases the “softness” (or decreases the “hardness”) of the species, meaning that chloride is harder than bromide, which in turn is harder than iodide. According to the empirical principle of “hard and soft acids and bases” (HSAB principle), hard acids prefer to bind to hard bases and soft acids prefer to bind to soft bases. Therefore, soft Lewis acids will form more stable complexes with I^-, and hard Lewis acids with Cl^-.[85] Consequently, Ln^{3+} ions, as very hard Lewis acids, prefer to coordinate with harder bases such as Cl^- rather than Br^- or I^-. Compared to Ln^{3+} ions, where outer-shell electrons are buried in the core, d-transition metals, such as Mn^{2+}, which has a d^5 configuration, is considerably softer.[85] Therefore, the Mn^{2+} ion has a stronger tendency to be incorporated into soft LHPs with respect to Ln^{3+} ion. Despite the qualitative nature of the HSAB principle, it can be a useful guideline to predict the feasibility of impurity incorporation into LHPs.

Doping mechanism

The major obstacle for impurity doping arises from the inherent tendency of the system to expel impurity atoms to minimize the energy of the system. Hence, until now, Ln^{3+} doping in traditional QDs has remained a challenge, as well as in LHPs.

On the other hand, Mn^{2+} doping into II-VI QDs has been extensively studied over the last two decades, and the doping mechanism can be tuned among nucleation-doping, growth-doping to diffusion doping by changing the reaction conditions, such as surfactant, precursor source and concentration, reaction temperature and annealing time.[82,86]

According to the different literature reports on Ln^{3+} doping into LHPs, the resulting LHPs exhibit different structure phase, size and morphology depending on the synthetic protocols used ranging from room temperature to high temperature (260 °C). Different doping mechanism may be involved for varied synthetic approaches and even within the same approach. To date, synthetic conditions, i. e., dopant source, surfactants, reaction temperature and time, electronic structures and optical properties of Ln^{3+}-doped LHPs have not been systematically investigated. Correspondingly, the Ln^{3+} doping mechanism, which is crucial for understanding the optical behavior of Ln^{3+} in LHPs, remains unclear. Lignos et al. investigated the LHPs growth kinetics reporting that the nucleation and growth of LHPs NCs occurred within 1 – 5 s,[87] which is much faster than traditional QDs, likely due to the extreme ease by which these crystals with high degree of ionic character are formed in solution.[9] Therefore, it is very difficult to separate the nucleation and growth processes, which might be an intrinsic issue that hampers further study on the doping mechanism.

It has been reported that the NCs size and shape can be controlled mainly by varying the ligand combinations and ratios as well as the reaction temperature.[88] However, up to now, no systematic studies on size and shape effect as well as the ligand-binding effect on Ln^{3+} doping exist. However, careful control of synthetic parameters, such as precursor source, surfactant and reaction temperature, may lead to effective doping.

1.4.2 Synthesis of Ln^{3+}-Doped LHPs

In 2015, Protesescu et al. firstly reported the successful synthesis of colloidal LHPs NCs emitting in the entire visible light spectrum via a HI method.[7] This method can produce uniform sizes, controllable morphologies and good dispersibility of the NCs where surfactants play a key role in growth process. However, the HI method requires high temperature and an inert atmosphere, and the production output is in small scale, which increases the costs and limits the implementation of such materials in devices.[9] Since then, several novel synthetic methods have been established for preparing LHPs either in the form of thin films or colloidal NCs. It has been reported that doping Ln^{3+} into narrow-bandgap bromide and iodide LHPs by the popular HI method is more difficult than chloride analogs. However, the narrowest-bandgap composition of $CsPbI_3$ with cubic phase is the most prominent candidate for photovoltaic light harvesters among LHPs.[80] Therefore, other approaches have been developed. In general, high-temperature HI, solution-processing and alternative synthesis methods have become the three main effective strategies for the successful preparation of Ln^{3+}-doped LHPs. All these synthetic protocols may give rise to different formation and doping mechanism of Ln^{3+}-doped LHPs, which are very vital for the further optimization of the synthesis. Thereby, an in-depth understanding of the synthesis chemistry is required. The comparison of different reports on Ln^{3+}-doped LHPs shows that the synthetic parameters, like precursor source and concentration, halide-to-cation ratio, organic ligand, reaction temperature, affect the phase, size, composition and thus the optical and optoelectronic performance.

Regardless of the specific method used, all of the synthetic processes involve two steps of nucleation and growth. During the nucleation process, the raw materials release free atoms or ions, and these free ions accumulate into small aggregates. The continuously released free atoms or ions bond or assemble on the surface of the nucleus, corresponding to the NCs growth process.[78,89] This section will summarize different synthetic approaches with advantages and disadvantages, and rationalize the key synthetic parameters that lead to the successful Ln^{3+} doping into LHPs.

1.4.2.1 Hot-Injection

The HI method was first developed for the synthesis of cadmium chalcogenide QDs in the 1990s.[90] This method is based on the rapid injection of a precursor into a mixed hot solution composed of the remaining precursors, surfactants, and a high boiling solvent. In 2015, Protesescu et al. firstly synthesized $CsPbX_3$ NCs in an organic high-boiling-point solvent via this HI approach.[7] As shown in Figure 1.11a, the PbX_2 salt is first dissolved in a high-boiling point solution containing 1-octadecene (ODE) solvent, oleic acid (OA) and oleylamine (OLA) surfactants in a three-neck flask. Preheated Cs-oleate (~100 °C) is then swiftly injected into PbX_2 precursor solution to ignite the NCs nucleation and growth at 140 − 200 °C. Immediately after Cs-oleate injection, a rapid nucleation burst occurs with a simultaneous formation of small nuclei. A rapid depletion of monomers terminates the nucleation stage, after which the nuclei continue growing (with ideally no new nuclei forming). Over time, this leads to the evolution of a NCs' population, which is characterized by a narrow size distribution.[91] However, unlike metal chalcogenides QDs forming covalent materials with the increase of the reaction time, the nucleation and growth steps of LHPs NCs are completed within a few seconds forming ionic compounds. The different ionic and covalent structures indicate very different nucleation processes and surface engineerings. The HI method for LHPs has seen tremendous progress over the past five years on size and shape control (nanocubes, nanowires, nanoplatelets quantum-confined NCs), thus allowing the tuning of the optoelectrical and optical performance. The key parameters of the HI method that enable to control the size, and shape of LHP NCs are i) the chain length of the surfactant ligands; ii) the concentration of the Pb precursor (such as 0.02 M); iii) the injection temperature of the cation or anion precursor; and iv) the reaction time.[9]

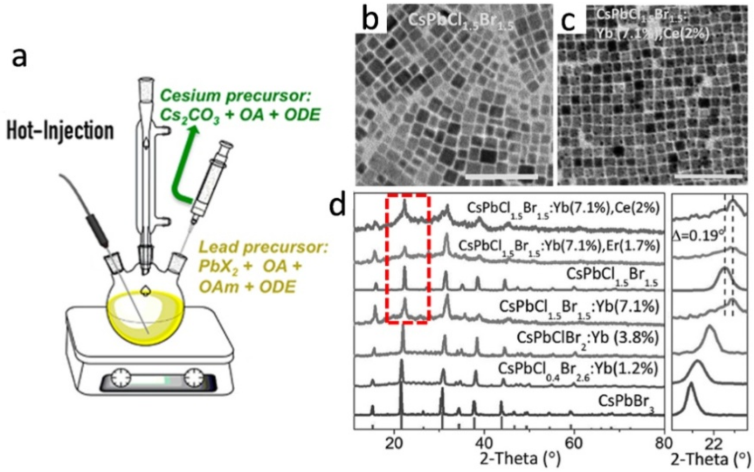

Figure 1.11 (a) Schematic illustration of the HI method for the synthesis of LHP NCs. Adapted from ref 92. TEM images of (b) undoped $CsPbCl_{1.5}Br_{1.5}$ NCs and (c) Yb^{3+}-doped $CsPbCl_{1.5}Br_{1.5}$ NCs. (d) XRD patterns of undoped and doped NCs. Adapted from ref 70.

The HI approach was further extended by Zhou and coworkers to synthesize Ln^{3+} (Ce^{3+}, Yb^{3+}, Er^{3+}) doped mixed halide $CsPb(Cl/Br)_3$ NCs with some modifications, in which Ln^{3+} halide salts were mixed with PbX_2 salts in ODE, OA and OLA solution.[70] The reaction was ignited by the rapid injection of Cs-oleate at 200 °C. The cubic morphology of mixed-halide $CsPbCl_{1.5}Br_{1.5}$ NCs retained after Ce^{3+}/Yb^{3+} codoping, and the average size decreased from 7.7 nm for undoped NCs to 6.8 nm for doped NCs (Figure 1.11b,c). This behavior was attributed to the lattice contraction of NCs induced by the replacement of Pb^{2+} (119 pm) with smaller Ln^{3+} ions (Yb^{3+}: 87 pm, Er^{3+}: 89 pm, Ce^{3+}: 101 pm), as supported by the observed shift of powder X-ray diffraction (XRD) patterns toward large angles as displayed in the red rectangle in Figure 1.11d.

Due to the limited solubility of metal-halide salts serving as both cation and anion sources most commonly used in LHPs synthesis, metal-acetate salts with higher solubility in high-boiling-point organic solvents were introduced by Milstein et al.[93] In the optimized HI protocols, metal-acetate salts and chlorotrimethylsilane (TMS-Cl) provide cation and halide sources, respectively. Interestingly, the replacement of metal-halide salts by metal-acetate salts can also avoid the introduction of a preexisting Pb-Cl bond, which is not beneficial for some B-site doping.[94] On the other hand, the separation of cation and anion sources enables one to easily control the cation/anion ratio and reach a halide-rich environment to reduce nonradiative carrier recombinations. Contrary to ref 70, the 6.0% Yb^{3+}-doped $CsPbCl_3$ NCs did not exhibit reduction of the NCs size after Yb^{3+} doping, and no obvious XRD patterns shift correlating with doping was observed by the authors (Figure 1.12).

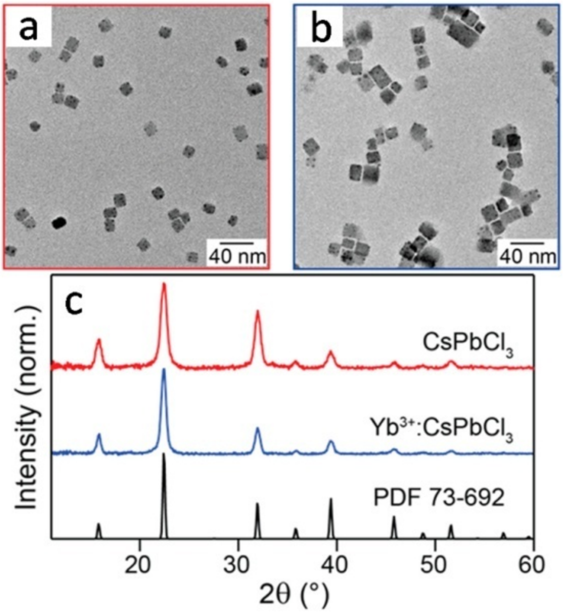

Figure 1.12 (a, b) TEM and (c) XRD data for undoped d = 13 nm $CsPbCl_3$ NCs (red) and d = 16 nm 6.0% Yb^{3+}-doped NCs (blue). Adapted from ref 93.

Although remarkable success has been achieved with the HI approach, the growth kinetics of $CsPbX_3$ NCs prepared via this method is not yet fully understood by research communities, unlike the case of traditional QDs. The main difference between traditional QDs and $CsPbX_3$ is that the nucleation and growth steps of $CsPbX_3$ NCs are fast and hardly separable in time, likely due to the extreme ease by which these crystals with high degree of ionic character are formed in solution.[9] Ln^{3+} doping into narrow-bandgap $CsPbX_3$ NCs, like pure $CsPbBr_3$, $CsPbI_3$ or mixed $CsPb(Br/I)_3$ NCs has not yet been reported by using this HI method. In addition, HI route always faces two main drawbacks: the use of nitrogen or expensive argon and small-scale production, which hampers commercialization. Therefore, some other effective synthetic protocols (e.g., solution-processing, postsythesis, ultrasonication) for preparing Ln^{3+}-doped $CsPbX_3$ are under investigation.

1.4.2.2 Solution-Processing

Compared to the popular and shape-controllable HI method, the solution-processing approach is more facile, energy saving and thus enabling large-scale production. The current highest-performing organic-inorganic perovskite thin-film photovoltaics have been prepared from solution.[4,22,95-97] However, solution-based processing also reveals a number of hurdles: lower size and shape control, inhomogeneous coating, and inefficient charge collection in films with variable thickness.[4] This approach also reveals the solubility problems of some metal-halide salts (e.g., CsCl), hampering the control of accessible compositions, film thicknesses, and morphologies.[98]

Spin-coating technique

In comparison with other approaches for preparing LHPs, the spin-coating technique is relatively simple, and is widely used to prepare LHP films. The thickness of the LHP film can be easily tuned by adjusting the rotational speed, deposition time and precursor concentration. The film quality depends on the solvent volatilization speed, determined by the heating temperature and heating rate. Duan et al. fabricated Ln^{3+}-doped $CsPbBr_3$ films (Ln = La, Ce, Nd, Sm, Eu, Gd, Tb, Ho, Er, Yb, and Lu) through a multi-step solution-processing spin-coating technique.[99] First, a 1 M $PbBr_2$ in *N*,*N*-dimethylformamide (DMF) solution containing various Ln^{3+} ions sources in the stoichiometric range 1% – 5% was spin coated onto a FTO/c-TiO_2/m-TiO_2 glass substrate at 2000 rpm for 30 s at 90 °C and kept for 1 h. Afterwards, a 0.07 M CsBr methanol solution was then spin coated onto the $PbBr_2$ film at 2000 rpm for 30 s and continuingly heated at 250 °C for 5 min. This process was repeated for several times to obtain a pure $CsPbBr_3$ phase with a film thickness of 400 nm (Figure 1.13). Upon doping with Ln^{3+} ions, the grain size of the $CsPbBr_3$ film gradually increased and became more and more compact with the decrease of the atomic number of the dopant Ln^{3+} ions. Correspondingly, the diffraction peak intensity of the $CsPbBr_3$ film doped with different Ln^{3+} was dramatically enhanced by obeying an order of $Sm^{3+} > Tb^{3+} > Ho^{3+} > Er^{3+} > Yb^{3+}$, evidencing the role of the Ln^{3+} dopant for optimizing the grain crystallinity. Characteristic peaks shift to higher angles and variation range obeyed an opposite order, and further suggested partial substitution of Pb^{2+} sites by Ln^{3+}. The Ln^{3+} dosage was reported to be around 2% with respect to Pb^{2+} (3% in precursors). Ishii et al. also fabricated a Yb^{3+}-doped $CsPbCl_3$ crystalline film on a quartz substrate using a similar approach to refs 99,100 They obtained a 120 nm-thick Yb^{3+}-doped $CsPbCl_3$ film after five repetitions of the spin coating-heating procedures, however, the actual Yb^{3+} concentration was unclear.

Almost at the same time with Duan, Kroupa et al. demonstrated a two-step solution-deposited protocol to prepare bulk Yb^{3+}-doped $CsPb(Cl/Br)_3$ polycrystalline films with 150 ± 31 nm thickness.[101] A 0.86 M mixed $PbCl_2$/$PbBr_2$ phase from dimethyl sulfoxide (DMSO) solution was firstly deposited onto a glass substrate at 6000 rpm for 35 s and the obtained film was annealed at 100 °C for 5 min. After this step, a 0.25 M CsCl/CsBr ($YbCl_3$/$YbBr_3$) methanol solution was then spin coated onto the $PbCl_2$/$PbBr_2$ film at 6000 rpm for 35 s, followed by annealing at 250 °C for 10 min to promote crystallization. The Yb^{3+} concentration in the $CsPb(Cl/Br)_3$ polycrystalline film was found to be extremely high, reaching 48%. Up to now, the role of precursor concentration and spin coating speed on the Ln^{3+} incorporation leading to such high values of Yb^{3+} concentration with respect to the report in ref 99, remains however unclear.

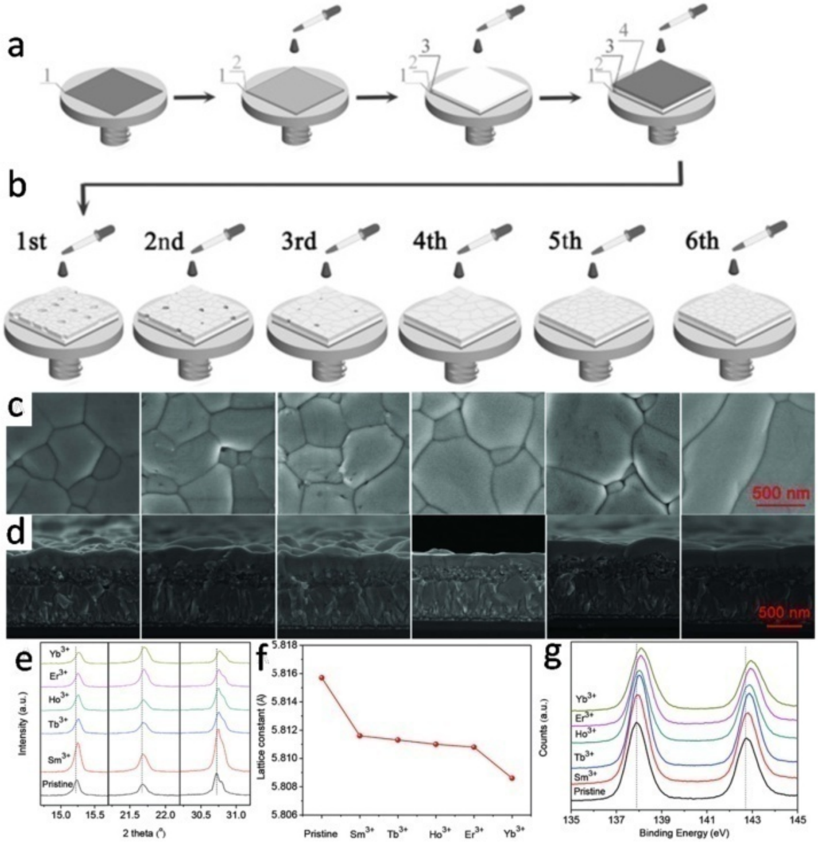

Figure 1.13 (a) Illustration of the deposition process on 1) FTO with 2) c-TiO_2, 3) m-TiO_2, and 4) $PbBr_2$. (b) Multistep solution-processing deposition of CsBr. Adapted from ref 102. (c) The top and (d) cross-sectional scanning electron microscope (SEM) images of the as-prepared perovskite films on FTO/c-TiO_2/m-TiO_2 substrates (left to right: $CsPbBr_3$,

Yb^{3+}-$CsPbBr_3$, Er^{3+}-$CsPbBr_3$, Ho^{3+}-$CsPbBr_3$, Tb^{3+}-$CsPbBr_3$, Sm^{3+}-$CsPbBr_3$). (e) XRD profiles of various perovskite films. (f) Lattice constant evolution of perovskite crystals on dependence of the nature of the dopant. (g) High-resolution X-ray photoelectron spectroscopy (XPS) spectra of Pb 4f for various perovskite films. Adapted from ref 99.

Xiang et al. employed a one-step spin-coating technique to deposit perovskite films from $CsPb_{1-x}Eu_xI_2Br$ ($0 \leq x \leq 1$) precursor solutions, which were composed of 1 M $CsPbI_2Br$ DMSO solution, 1 M CsBr formamide solution and 1 M EuI_2 DMF: DMSO solution.[103] A 150 nm-thick perovskite film was prepared by spin-coating the precursor solutions onto a FTO/c-TiO_2/m-TiO_2 glass substrate in a two steps program at 1000 rpm and 3000 rpm for 10 s and 30 s in dry air box, respectively. The films were then left for 5 min and annealed at 280 °C for 10 min. The undoped $CsPbI_2Br$ film showed crystal domains and clear pinholes (Figure 1.14). Upon incorporation of 5 mol% Eu, the $CsPb_{0.95}Eu_{0.05}I_2Br$ film was fully uniform and became smoother, and the grain size decreased.

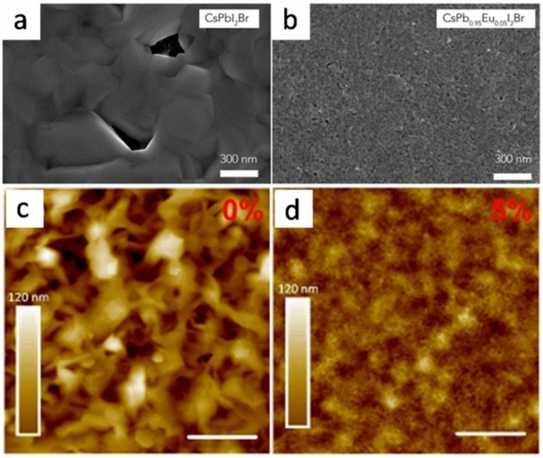

Figure 1.14 SEM images of (a) $CsPbI_2Br$ and (b) $CsPb_{0.95}Eu_{0.05}I_2Br$ perovskite thin films. Scale bar, 300 nm. AFM images of (c) $CsPbI_2Br$ and (d) $CsPb_{0.95}Eu_{0.05}I_2Br$ perovskite thin films. Scale bar, 2 µm. Adapted from ref 103.

One-pot ultrasonication

As mentioned before, Ln^{3+} ions cannot be doped into $CsPbBr_3$ NCs by using the typical HI approach, whereas the ultrasonic method has been recently proved successful. One-pot ultrasonication can produce acoustic cavitation, which then creates bubbles. The collapse of these bubbles releases a transient ultrahigh energy that overcomes the nucleation barrier and initiates the growth of NCs simultaneously. In 2018, Eu^{3+} and Tb^{3+} doping into $CsPbBr_3$ NCs was realized using this protocol for the first time.[72] CsBr and $PbBr_2$ powders were loaded into a DMF solution containing a proper amount of Ln^{3+} ions, and then the solution was subjected to ultrasonication with the assistance of water cooling (Figure 1.15a). Ln^{3+}-doped $CsPbBr_3$ NCs were collected after centrifugation. TEM images showed that both undoped and doped NCs exhibited cubic shapes, but with a rather inhomogeneous distribution with different levels of aggregation and slight truncations caused by the ultrasonication synthesis procedure. It was found that the average sizes of the NCs decreased from 42.9 nm to 30.0, and 34.1 nm after Eu^{3+} and Tb^{3+} doping, respectively. XRD patterns were consistent with the standard pattern of $CsPbBr_3$ (PDF#18-0364) except for a small amount of a secondary $PbBr_2$ phase, and the (110) peak at ~21.5° shifted toward higher angles upon Ln^{3+} doping.

In this synthetic approach, the main driving force for facilitating Ln^{3+} incorporation into the NC lattices is likely from a transient ultrahigh energy provided by the high temperature (>5000 K) and pressure (>1000 bar) on hot spots.

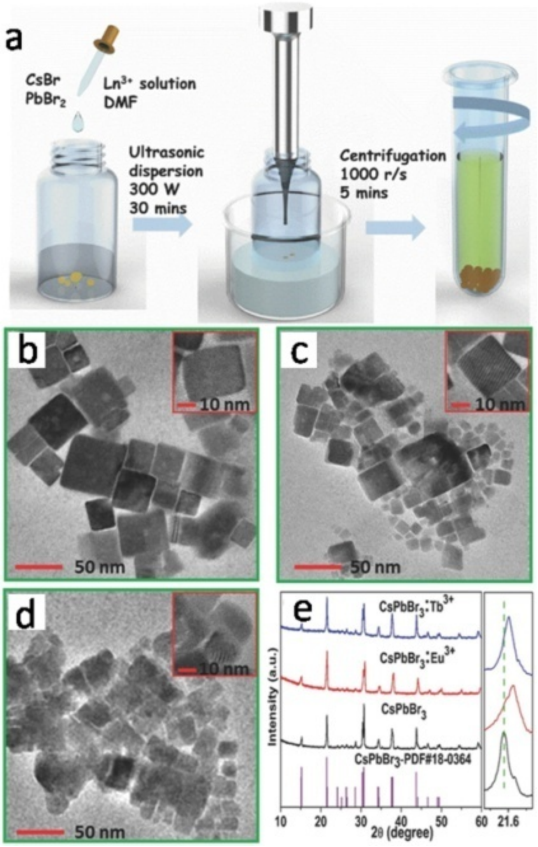

Figure 1.15 (a) Flow diagram of the synthetic procedure. The yellow solids at the bottom of the bottle represent CsBr and $PbBr_2$, which are slightly soluble in DMF. Water cooling was supplied to avoid the overheating of the solution. TEM images of (b) $CsPbBr_3$, (c) Eu^{3+}-doped $CsPbBr_3$, and (d) Tb^{3+}-doped $CsPbBr_3$ NCs. (e) XRD results of the three samples and the enlarged XRD patterns of the samples at 20.5° – 22.5°. Adapted from ref 72.

1.4.2.3 Postsynthetic Anion/Cation Exchange

Anion exchange

The major contribution to the VBM of LHP materials comes from the halide orbitals.[18] Thus, a systematic halide composition exchange (Cl → Br → I or I → Br

→ Cl) of such compounds allows for a fine adjustment of the VBM. The narrow-bandgap $CsPbBr_3$ (2.39 eV) and $CsPbI_3$ (1.8 eV) LHPs are the most promising materials for applications in photovoltaic/optoelectronic devices since they enable a wider absorption of the solar spectrum with respect to the chloride counterparts. In principle, the bandgap of $CsPbI_3$ should be sufficiently wide to sensitize Yb^{3+} emission (1.25 eV); therefore, it will be very interesting to dope Yb^{3+} into the narrow-bandgap hosts for potential applications in silicon solar cells (SSCs). Unfortunately, it has been shown that Ln^{3+} doping into $CsPbBr_3$ and $CsPbI_3$ by the direct HI method remains challenging. Milstein et al. prepared Yb^{3+}-doped $CsPbBr_3$ NCs by the postsynthetic anion exchange of Cl^- with Br^- from doped chloride NCs (Figure 1.16a-c).[104] While the bandgap of the LHP could be continuously tuned by anion exchange, the QC effect yielding two-photon emission at ~1000 nm was deactivated in Yb^{3+}-doped $CsPb(Cl/Br)_3$ NCs at values down to the energy threshold of ~2.53 eV (~490 nm).

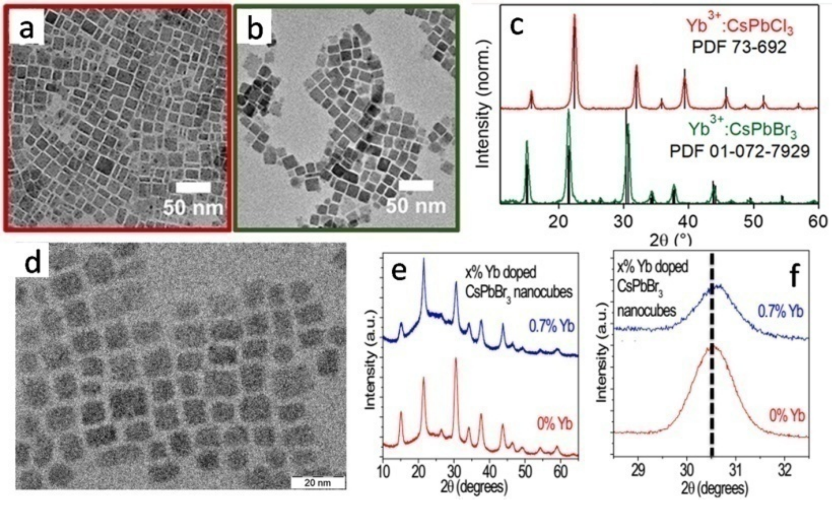

Figure 1.16 TEM images of 7.7% Yb^{3+}-doped $CsPbCl_3$ NCs collected (a) before and (b) after anaerobic anion exchange with trimethylsilyl bromide (TMS-Br) in dry hexane, which converts Yb^{3+}-doped $CsPbCl_3$ NCs into Yb^{3+}-doped $CsPbBr_3$ NCs. (c) Representative XRD data for the same NCs from panel a,b. Reference diffraction patterns are included for

comparison, confirming essentially complete anion exchange. Adapted from ref 104. (d) TEM image of 0.7% Yb^{3+}-doped $CsPbBr_3$ nanocubes. (e) XRD patterns and (f) shows magnified view of the most intense peak at 2θ ~30.6° for undoped and 0.7% Yb^{3+}-doped $CsPbBr_3$ nanocubes. Adapted from ref 74.

Cation exchange

Cation exchange is a well-established synthesis method for metal ions doping in semiconducting NCs with unchanged morphology and structure. Typically, the host NCs is first prepared and the dopants source with desired amount is then introduced into the host NCs solution at room temperature promoting cation exchange. Mir et al. extended this postsynthesis cation exchange route for doping Yb^{3+} into $CsPbX_3$ (X = Cl^-, Br^-, or I^-) nanocubes and $CsPbBr_3$ nanoplatelets (Figure 1.16d-f).[74] Simply, a Yb^{3+} precursor source was prepared by dissolving $Yb(NO_3)_3$ in a mixture of methyl acetate and toluene. The Yb^{3+} doping concentration was controlled by adding different amounts of Yb^{3+} precursor solution to the NCs dispersion under continuous stirring for 1 min. Interestingly, Yb^{3+} doping into the narrowest-bandgap host of $CsPbI_3$ NCs achieved the highest Yb^{3+} concentration among the whole class of Ln^{3+}-doped LHPs, reaching up to 3.7%. This phenomenon seems at odds with the HSAB principle. The authors mentioned that the complete mechanistic insights into the postsynthesis doping reaction were not yet available, but they believed that ligand binding adsorption of dopants on the surface of NCs followed by fast halide migration to incorporate dopants into the host matrix was beneficial for the successful doping.

1.4.2.4 Alternative Methods

In addition to the above HI, solution-processing, postsynthetic methods, some other effective synthetic protocols, such as chemical vapor deposition (CVD) and melt-quenching are also developed. High temperature is required for these two approaches. The CVD technique can afford large-size plates or bulk films of LHP. The melt-quenching method is used to precipitate LHPs in a glass matrix.

Chemical vapor deposition

As mentioned before, solution-based processing for film preparation may actually impose limitations, such as precursor solubility and uniform coating. On the other hand, CVD method may be able to meet these needs. This method is already widely used in the optoelectronics industry, making it particularly attractive for integration with existing manufacturing.[98] Jing et al. prepared Er^{3+}-doped mixed-halide $CsPb(Cl/Br)_3$ microplates via a CVD method (Figure 1.17a-c).[105] Two alumina boats containing a mixture of CsX and PbX_2 (X= Cl^-, Br^-) and $ErCl_3$ powders were placed at the heating zone. The furnace was then heated to 775 − 785 °C with high-purity Ar as a carrier gas. The resulting microplates displayed a lateral dimension in the range of 5 − 30 μm and a thickness from several atomic layers to several 100 nm. The Er^{3+} concentration was reported to be 1.57%; however, the nominal concentration was unclear. The authors claimed that the formed structural defects created by the dopants during the growth of the nanomaterials and the high temperature might further trigger the adsorption and then incorporation of the dopants.

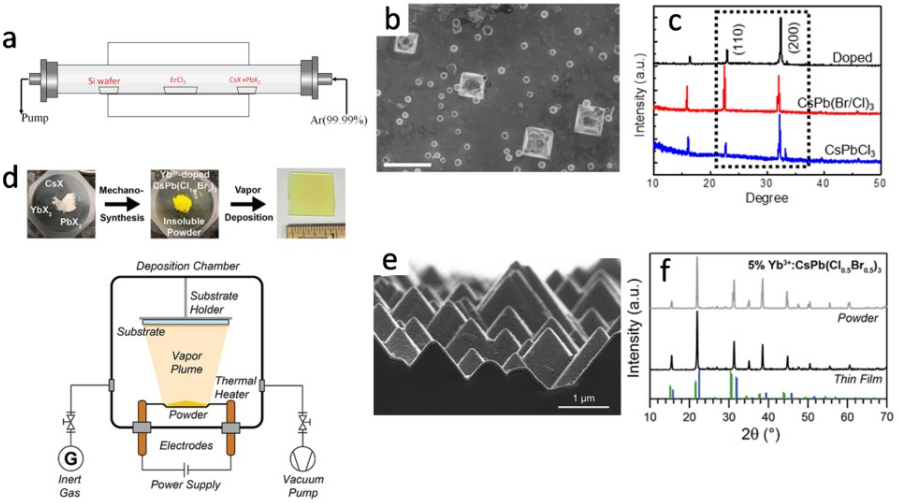

Figure 1.17 (a) Setup schematic for the growth of Er^{3+}-doped $CsPb(Cl/Br)_3$ microplates by an *in situ* source changing CVD route. (b) Top-view SEM images of the as-grown microplates. (c) XRD patterns of the doped and undoped $CsPb(Cl/Br)_3$ microplates. Adapted from ref 105. (d) Processing of complex perovskite films involves grinding ionic precursors into single-source powders, followed by SSVD of the ground powders. (e) Cross-sectional SEM image of an Yb^{3+}-doped $CsPbCl_3$ film deposited by SSVD onto a textured silicon solar cell. (f) Yb^{3+}-doped $CsPb(Cl_{0.5}Br_{0.5})_3$ powder (gray) and thin film (black). Adapted from ref 98.

Among the possible CVD methods, the single-source vapor deposition (SSVD), which makes use of a solid-state form of the desired material (typically a powder) as the source material, is one of the most popular CVD methods. Even more commonly used is the multi-source coevaporation approach, as it allows the control of the film stoichiometry and thickness by tuning the evaporation rate of each precursor individually. However, this approach is time-consuming and requires frequent optimization of the deposition conditions.[98]

Between these two approaches, SSVD is generally simpler and thus enables higher throughput than multi-source coevaporation. Crane et al. adopted a SSVD method for depositing high quality conformal Yb^{3+}-doped $CsPb(Cl/Br)_3$ thin films (Figure

1.17 d-f).[98] The evaporator chamber was maintained at a pressure varying between 10^{-2} and 10^{-6} torr, and a high current was passed through the boat holding the precursor, causing sublimation followed by film deposition. A conformal 130 nm-thick Yb^{3+}-doped $CsPbCl_3$ film evenly coating the textured silicon surface was obtained. The authors claimed that these conformal perovskite coatings contrasted with those produced from solution, which are thick in the troughs and thin at the peaks due to solvent pooling and nonuniform evaporation. The other advantage of this SSVD method is the ultraeffective Yb^{3+} ions doping; that is, the thin films contained almost the same concentration of Yb^{3+} (4.7% of total B-site cations) as the single-source precursor (5.0%).

Melt-quenching

Cheng et al. adopted a conventional melt-quenching approach to fabricate Tb^{3+}, Eu^{3+} and Tb^{3+}/Eu^{3+} codoped $CsPbBr_3$ NCs glass.[106] In their synthesis, Cs_2CO_3, $PbBr_2$, Ln^{3+} oxides serving as the $CsPbBr_3$ precursors together with some other oxide precursors for preparing borosilicate glass, were first mixed in an agate mortar and then dissolved in a crucible at 1100 °C for 30 min in ambient air, followed by a heat treatment at 450 °C to release the pressure. The as-prepared Tb^{3+}-doped $CsPbBr_3$ NCs (black spots) of average diameter of approximately 5.73 nm were uniformly distributed inside the glass matrix (Figure 1.18). The physical adsorption of Ln^{3+} cations on the surface of the prepared NCs was reported to be ruled out following the evidence of the XRD peak shift toward higher angles after Ln^{3+} doping. The successful Ln^{3+} doping into the soft $CsPbBr_3$ matrix is probably ascribed to the slower growth steps in the solid state and the broken energy barrier at the ultrahigh temperature reached during the synthesis.

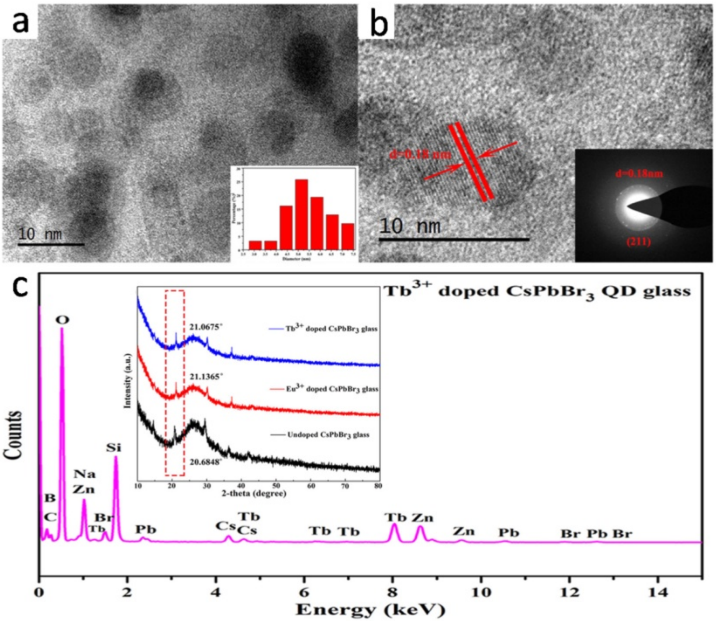

Figure 1.18 (a) TEM image of Tb^{3+}-doped $CsPbBr_3$ glass. (b) HRTEM image of Tb^{3+}-doped $CsPbBr_3$ glass (illustration: selected area electron diffraction (SAED) pattern of Tb^{3+}-doped $CsPbBr_3$ glass). (c) Energy-dispersive X-ray spectrometry (EDS) graph of the Tb^{3+}-doped $CsPbBr_3$ QDs glass. Insert in panel (c) is the comparison of XRD patterns of different Ln^{3+}-doped $CsPbBr_3$ QDs glasses. Adapted from ref 106.

1.4.3 Optical Properties

It has been reported that the PL emission of LHPs can be easily tuned by anion exchange, or by controlling their size and shape through the quantum confinement effect. As said, another effective strategy to control the optical properties is doping with luminescent Ln^{3+} ions substituting Pb^{2+} at B-sites of LHPs. Ln^{3+} ions enable emission across a wide spectral range from UV to visible light to the NIR region due to 4f–4f transitions.

Modulation of LHPs emission in the visible spectral region has been obtained by Ln^{3+} ions doping, such as green-emitting Tb^{3+} ions and red-emitting Eu^{3+} ions doping, or Tb^{3+}/Eu^{3+} codoping (Figure 1.19).[106] Importantly, they also observed that the stability of the $CsPbBr_3$ glass was also improved by Ln^{3+} doping.

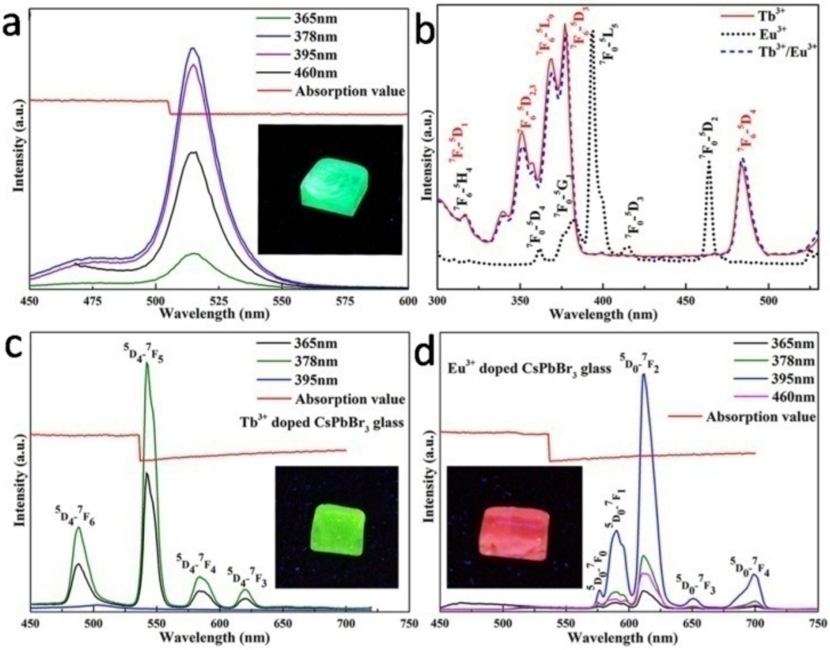

Figure 1.19 (a) Emission curves of the $CsPbBr_3$ NCs glass at various excitation wavelengths (illustration: appearance of the corresponding glass sample under UV light). (b) Excitation spectra of Tb^{3+}-doped $CsPbBr_3$ glass, Eu^{3+}-doped $CsPbBr_3$ glass, and Tb^{3+}/Eu^{3+} codoped $CsPbBr_3$ glass. (c) Emission curves of the Tb^{3+}-doped $CsPbBr_3$ glass with various energies of excitation (illustration: appearance of the corresponding glass sample under UV light). (d) Emission curves of the Eu^{3+}-doped $CsPbBr_3$ glass with various energies of excitation (illustration: appearance of the corresponding glass sample under UV light); the red solid lines are the absorption spectra. Adapted from ref 106.

The PL emission of LHP NCs can be further expanded to the otherwise inaccessible NIR spectral region by the incorporation of NIR-emitting Ln^{3+} ions. Zhou et al. reported Ce^{3+}/Yb^{3+} codoped mixed-halide $CsPbCl_{1.5}Br_{1.5}$ NCs, which exhibited an intense Yb^{3+} emission band centered at 988 nm with total PLQY of 146% (Figure 1.20).[70] The lengthened lifetime of the Yb^{3+} emission in Ce^{3+}/Yb^{3+}

codoped $CsPbCl_{1.5}Br_{1.5}$ NCs was attributed to the Ce^{3+} assistance in the population of the upper $^2F_{7/2}$ state of Yb^{3+} ions, resulting in an apparent QC effect, i.e., single photon excitation of the perovskite host gives rise to two photons emitted by Yb^{3+} ions (Figure 1.20b,c). Soon after, the same group systematically studied a series of Ln^{3+}-doped $CsPbCl_3$ NCs (Ln = Ce, Sm, Eu, Tb, Dy, Er, and Yb), which displays widely tunable multicolor emissions (Figure 1.20d).[71] Intriguingly, the $CsPbCl_3$ NCs doped with 9.1% Yb^{3+} showed unprecedentedly high PLQY of 143%. Meanwhile, the Yb^{3+} PL decay curve monitored at 1000 nm presented a single exponential behavior (Figure 1.20e). The authors argued that such high PLQY may result from the QC of the excitonic transition of the $CsPbCl_3$ NC host, which was assisted by an intermediate energy level associated with defect states (Figure 1.20f). Moreover, the authors also found that the colloidal stability of the LHP NCs was slightly enhanced by the introduction of Ln^{3+} ions. Zhang et al. also reported Yb^{3+}-doped and Yb^{3+}/Er^{3+} codoped $CsPbCl_3$ NCs using a HI method.[107] In Er^{3+}-doped $CsPbCl_3$ NCs, a wide peak at 591 nm appeared, instead of an Er^{3+} NIR emission peak (Figure 1.21a). They assumed this wide peak might have been related to defect states in the bandgap of the $CsPbCl_3$ NCs caused by Er^{3+}. Importantly, a NIR emission peak at 1533 nm originated from the Er^{3+} $^4I_{13/2}\rightarrow{}^4I_{15/2}$ transition appeared after the introduction of Yb^{3+}, and the lifetime of this transition was 868 μs (Figure 1.21b,c). Furthermore, the authors found that the photostability of the NCs host was improved by Yb^{3+} doping (Figure 1.21d).

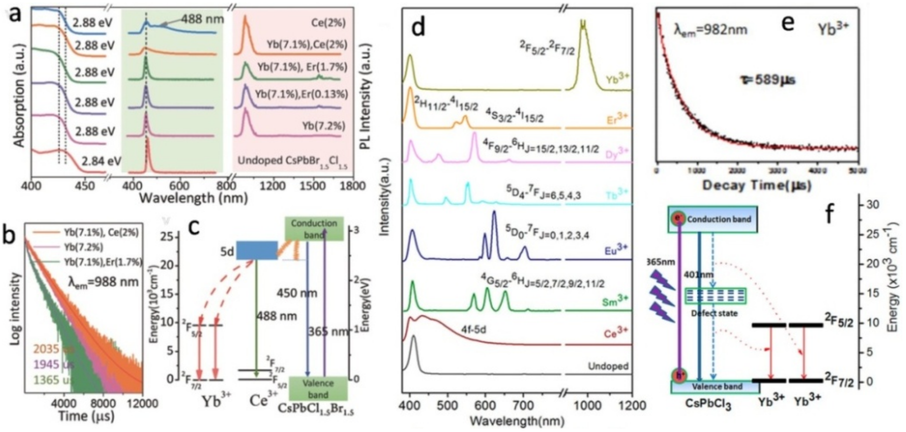

Figure 1.20 (a) Absorption spectra (left), visible emission spectra (middle), and NIR emission spectra (right, excited by 365 nm light) of $CsPbCl_{1.5}Br_{1.5}$ NCs codoped with different Ln^{3+} ions. (b) Dynamics of Yb^{3+} emission in doped $CsPbCl_{1.5}Br_{1.5}$ NCs monitored at 988 nm. (c) Schematic diagram of the proposed ET mechanism in the Yb^{3+}/Ce^{3+} codoped $CsPbCl_{1.5}Br_{1.5}$ NCs. Adapted from ref 70. (d) PL spectra of undoped and 7.2% Ce^{3+}, 7.3% Sm^{3+}, 7.9% Eu^{3+}, 7.6% Tb^{3+}, 7.4% Dy^{3+}, 7.8% Er^{3+}, and 9.1% Yb^{3+}-doped $CsPbCl_3$ NCs. (e) Dynamics of Yb^{3+}-doped $CsPbCl_3$ NCs monitored at 1000 nm. (f) Energy level diagram of Yb^{3+}-doped $CsPbCl_3$ NCs and the possible QC mechanisms. Adapted from ref 71.

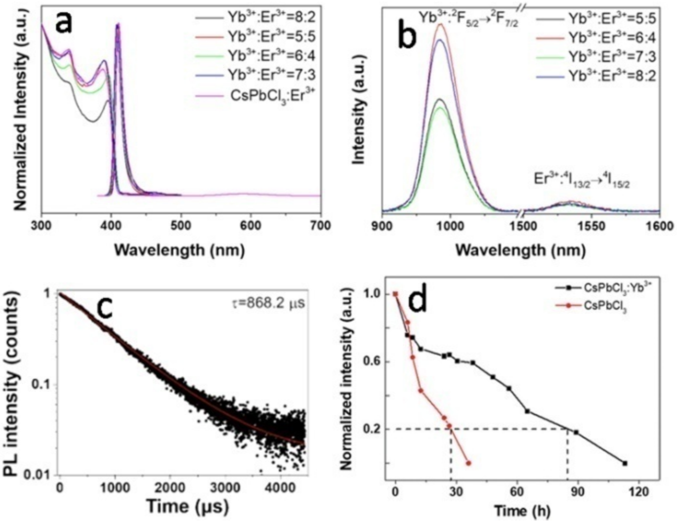

Figure 1.21 (a) Absorption and visible emission spectra of Er^{3+}-doped and Yb^{3+}/Er^{3+} codoped $CsPbCl_3$ NCs. (b) NIR emission spectra of Yb^{3+}/Er^{3+} codoped $CsPbCl_3$ NCs excited at 365 nm. (c) Time-resolved PL decay profile of the $^4I_{13/2} \rightarrow {}^4I_{15/2}$ transition of Er^{3+} ions in Yb^{3+}/Er^{3+} codoped $CsPbCl_3$ NCs fitted by a single-exponential function. (d) PL decrease of the $CsPbCl_3$ and Yb^{3+}-doped $CsPbCl_3$ NCs under 365 nm UV light irradiation. Adapted from ref 107.

Milstein and coworkers also reported an ultra-high PLQY (170%) of Yb^{3+} NIR emission in Yb^{3+}-doped $CsPbCl_3$ NCs.[93] The PL intensity of the Yb^{3+} NIR emission increased with increasing Yb^{3+} incorporation contents (Figure 1.22a). In addition, the average lifetime of this Yb^{3+} emission in $CsPbCl_3$ NCs doped with different concentrations was found to be over 2 ms (Figure 1.22b). The authors proposed a charge neutral Yb^{3+}-V_{Pb}-Yb^{3+} defect model, instead of an intermediate energy level associated with defect states in the bandgap, to explain the extremely efficient Yb^{3+} sensitization through an apparent picosecond QC mechanism. Such model was further supported by Li and coworkers using theoretical calculations.[108]

Later, an energy threshold for Yb^{3+} QC emission in mixed-halide $CsPb(Cl/Br)_3$ NCs was found by the same group via a continuous tuning of the bandgap through an anion exchange approach.[104] They reported that the NCs energy gaps can be tuned continuously from Eg ≈ 3.06 eV (405 nm) in $CsPbCl_3$ down to $E_g \approx 2.53$ eV (~490 nm) in $CsPb(Cl_{0.25}Br_{0.75})_3$ while retaining a constant PLQY above 100% (Figure 1.22d,e). The same group further investigated the optical properties of Yb^{3+}-doped $CsPb(Cl/Br)_3$ polycrystalline films with ~150 nm thickness prepared by a two-step solution deposition protocol (Figure 1.22f).[101] A maximum Yb^{3+} NIR PLQY of bulk mix-halide $CsPb(Cl/Br)_3$ films was reported to be 193%, which was comparable to Yb^{3+}-doped $CsPb(Cl/Br)_3$ NCs (~200%).[104] Therefore, the authors claimed that the extremely efficient QC mechanism was intrinsic to the Yb^{3+}-doped $CsPb(Cl/Br)_3$ composition itself. Furthermore, they also observed that the photoinduced halide segregation was strongly suppressed by Yb^{3+} doping. These two works shed detailed lights on a fundamental understanding of the role of the bandgap and the host composition itself in QC and possible applications requiring relevant visible light absorption.

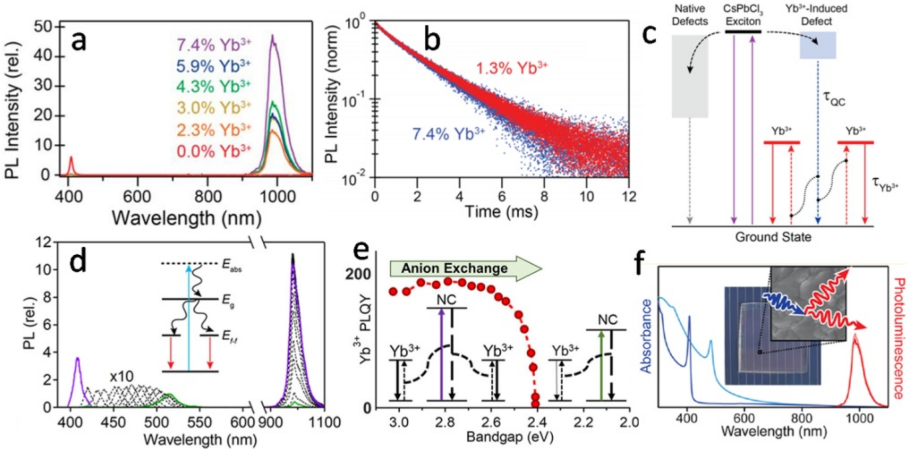

Figure 1.22 (a) PL spectra of undoped and Yb^{3+}-doped NCs with different concentrations. (b) Time-resolved PL of the NIR emission for 1.3% Yb^{3+} and 7.4% Yb^{3+}-doped NCs. (c) Proposed Yb^{3+}-sensitization mechanism involving an Yb^{3+}-induced defect state. Adapted from ref 93. (d) PL spectra of Yb^{3+}-doped $CsPb(Cl/Br)_3$ NCs collected *in situ* during anion exchange from Yb^{3+}-doped $CsPbCl_3$ (purple) to Yb^{3+}-doped $CsPbBr_3$ (green). (e) Plot of the Yb^{3+} $^2F_{5/2} \rightarrow {}^2F_{7/2}$ PLQY versus the excitonic PL energy. The red dotted line marks approximately twice the Yb^{3+} ($^2F_{7/2} \rightarrow {}^2F_{5/2}$) absorption onset ($2\times E_{f\text{–}f}$); that is, the anticipated energy threshold for QC in these materials below which energy conservation cannot be maintained. Adapted from ref 104. (f) Absorption and PL spectra of Yb^{3+}-doped $CsPb(Cl/Br)_3$ thin films. The insert shows the corresponding SEM image. Adapted from ref 101.

Mir et al. further extended the host of Yb^{3+} dopant to the narrow-bandgap compositions of $CsPbI_3$ nanocubes and $CsPbBr_3$ nanoplatelets (NPLs).[74] Notably, the relative intensity of the NIR Yb^{3+} emission is significantly decreased for $CsPbBr_3$ and $CsPbI_3$ NCs although the Yb^{3+} concentration was higher compared to chloride analogs (Figure 1.23). However, the PLQYs of Yb^{3+} emission are unknown. This work is helpful for the fundamental understanding about the role of the bandgap and morphology in the QC mechanism.

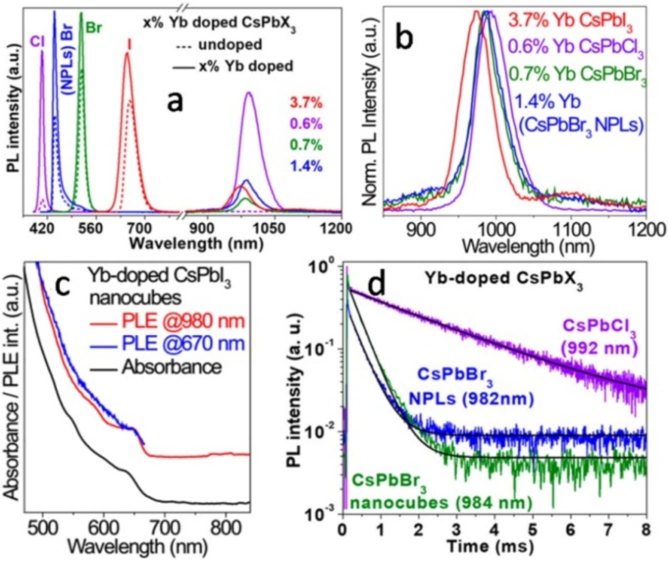

Figure 1.23 (a) PL spectra of undoped and Yb^{3+}-doped $CsPbX_3$ nanocubes and $CsPbBr_3$ NPLs. Dotted lines are for undoped samples, and solid lines of the same color are for Yb^{3+}-doped samples. (b) Normalized PL spectra of dopant emission in Yb^{3+}-doped $CsPbX_3$ (X = Cl^-, Br^-, I^-) nanocubes and $CsPbBr_3$ NPLs. This Yb^{3+}-emission undergoes a blue shift by ~20 nm as the halide composition is varied from Cl^- to Br^- to I^- of the host $CsPbX_3$ nanocubes. (c) Comparison of absorbance spectra and PL excitation spectra collected at both excitonic emission and Yb^{3+} emission in Yb^{3+}-doped $CsPbI_3$ nanocubes. (d) PL decay dynamics of Yb^{3+} emission from $CsPbX_3$ nanocubes and NPLs are fitted with a single-exponential decay function. Adapted from ref 74.

1.5 Aim of This Thesis

Over the last five years, tremendous success has been achieved in $CsPbX_3$ LHPs due to their excellent optical and electrical properties, which has allowed applications in solar energy conversion, lighting and displaying. However, these perovskite materials are strongly limited by two main shortcomings, which are the poor absorption and negligible emission properties in the NIR region.

Extending the absorption range of LHPs to the NIR range is a crucial change for the development of efficient solar energy converters as only a small fraction of the incident sunlight can be absorbed by the LHPs due to the wide-bandgap (~3.1 – 1.8 eV). This means that the photons with energy lower than the bandgap are lost in the form of thermalization energy. One of the most successful strategies to extend the optical response of LHPs to the NIR region is their combination with Ln^{3+}-doped UCNPs. The UCNPs can absorb and convert NIR photons to short-wavelength photons. These short-wavelength photons can be transferred to the LHPs either through radiative PR or nonradiative FRET or both. Compared to the simple PR process, FRET is faster and more efficient. Therefore it can overcome the detrimental concentration quenching phenomenon, which is likely to occur in devices where LHPs are deposited as films with severe aggregation. So far, physical mixing without introduction of binding surfactants has been the most popular approach to combine the UCNPs and LHPs. However, this method affords assemblies that are overall inhomogeneously distributed and show phase segregation, thus only allowing PR as long-range ET processs.

On the other hand, interesting results have been obtained in enabling NIR emission in LHPs. Impressively, the PLQYs of Yb^{3+} emission at ~1.0 μm in Yb^{3+}-doped $CsPbCl_3$ have been reported to be extremely high, reaching up to 170%. Two different models have been proposed to account for such over-unity PLQYs, involving an intermediate energy level associated with defect states or a charge neutral Yb^{3+}-V_{Pb}-Yb^{3+} defect mediating Yb^{3+} sensitization through QC. Nonetheless, Er^{3+}, also a well-known NIR-emitting Ln^{3+} ion at ~1.5 μm, of particular interest in optical telecommunication and silicon-integrated devices, has received much less attention than Yb^{3+} likely due to the weak or negligible emission properties so far displayed by Er^{3+}-doped LHPs. The abnormal behavior of Er^{3+} seems at odds with the case of Yb^{3+}, in view of the similarity of the energy levels configuration of these ions having resonant energy levels yielding emission at ~1.0 μm in both ions. These observations suggest that a mechanism other than ET by QC may account for the lanthanide sensitization. On the other hand, by taking advantage of the energy levels resonance between these two ions, Yb^{3+} has been accepted as a good sensitizer for Er^{3+} to improve the 1.5 μm luminescence. However, in the few published literature reports, only a broad and weak band with short lifetime (with respect to Yb^{3+}) was detected, suggesting that large amount of Er^{3+} ions were most probably located at the surface (or near the surface) due to an ineffective synthetic method.

Besides these shortcomings, Yb^{3+} also remains the only sensitizer so far reported for Er^{3+} in LHPs. Alternative low-cost and more universal sensitizer potentially enabling the emission of other lanthanide ions are highly desired.

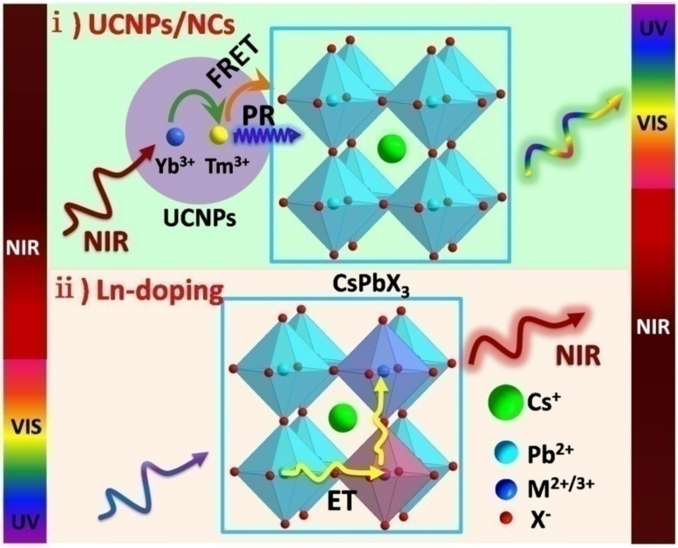

The aim of this PhD therefore is to extend the optical properties of LHPs through Ln^{3+} functionalization. To break through the inherent optical absorption and emission limitations of LHPs in the NIR region, different materials have been investigated in this doctoral work as shown in the figure above: i) hybrid composites of LHPs NCs and Ln^{3+}-doped UCNPs obtained through an improved *in situ* method; ii) Yb^{3+}/Er^{3+} codoped LHPs and Ln^{3+} singly doped LHPs and iii) Mn^{2+}/Er^{3+} codoped LHPs. These three materials allow adding different optical functionalities to LHPs. In particular, the first one allows for the extension of the optical absorption to the NIR to achieve NIR-to visible photon UC through enhanced FRET. In the second work, an optimized synthesis for Ln^{3+} doping into LHPs was adopted, allowing the dopant to be deeply buried into the perovskite lattice. Therefore, enhanced Er^{3+} emission at ~1.5 μm and long lifetime are achieved. Furthermore, a transient internal redox mechanism was proposed based on the luminescence properties of several representative Ln^{3+} (Yb^{3+}, Er^{3+}, Eu^{3+}, Nd^{3+}) doped $CsPbCl_3$ LHPs. The proposed mechanism can suitably account for the extremely intense Yb^{3+} luminescence at 1.0 μm compared to the weak emission output of the corresponding Er^{3+}-doped $CsPbCl_3$ NCs at 1.5 μm. In the third work, the low-cost Mn^{2+} ion was employed as an alternative and efficient sensitizer for Er^{3+}. These latter results undoubtedly open novel possibilities for the tuning of the spectral emission range for example by enabling the efficient sensitization of other lanthanide ions.

References

(1) Wells, H. L. On the Caesium- and the Potassium-Lead Halides. *Am. J. Sci.* **1893**, *45*, 121-134.

(2) Møller, C. K. Crystal Structure and Photoconductivity of Cæsium Plumbohalides. *Nature* **1958**, *182*, 1436-1436.

(3) Kojima, A.; Teshima, K.; Shirai, Y.; Miyasaka, T. Organometal Halide Perovskites as Visible-Light Sensitizers for Photovoltaic Cells. *J. Am. Chem. Soc.* **2009**, *131*, 6050-6051.

(4) Best Research-Cell Efficiencies (Rev. 04-06-2020). National Renewable Energy Laboratory (NREL), https://www.nrel.gov/pv/cell-efficiency.html.

(5) Juarez-Perez, E. J.; Hawash, Z.; Raga, S. R.; Ono, L. K.; Qi, Y. Thermal Degradation of $CH_3NH_3PbI_3$ Perovskite into NH_3 and CH_3I Gases Observed by Coupled Thermogravimetry–Mass Spectrometry Analysis. *Energy Environ. Sci.* **2016**, *9*, 3406-3410.

(6) Kulbak, M.; Gupta, S.; Kedem, N.; Levine, I.; Bendikov, T.; Hodes, G.; Cahen, D. Cesium Enhances Long-Term Stability of Lead Bromide Perovskite-Based Solar Cells. *J. Phys. Chem. Lett.* **2016**, *7*, 167-172.

(7) Protesescu, L.; Yakunin, S.; Bodnarchuk, M. I.; Krieg, F.; Caputo, R.; Hendon, C. H.; Yang, R. X.; Walsh, A.; Kovalenko, M. V. Nanocrystals of Cesium Lead Halide Perovskites ($CsPbX_3$, X= Cl, Br, and I): Novel Optoelectronic Materials Showing Bright Emission with Wide Color Gamut. *Nano Lett.* **2015**, *15*, 3692-3696.

(8) Wang, Y.; Dar, M. I.; Ono, L. K.; Zhang, T.; Kan, M.; Li, Y.; Zhang, L.; Wang, X.; Yang, Y.; Gao, X.; Qi, Y.; Grätzel, M.; Zhao, Y. Thermodynamically Stabilized β-$CsPbI_3$-based Perovskite Solar Cells with Efficiencies >18%. *Science* **2019**, *365*, 591-595.

(9) Shamsi, J.; Urban, A. S.; Imran, M.; De Trizio, L.; Manna, L. Metal Halide Perovskite Nanocrystals: Synthesis, Post-Synthesis Modifications, and Their Optical Properties. *Chem. Rev.* **2019**, *119*, 3296-3348.

(10) Jena, A. K.; Kulkarni, A.; Miyasaka, T. Halide Perovskite Photovoltaics: Background, Status, and Future Prospects. *Chem. Rev.* **2019**, *119*, 3036-3103.

(11) Quan, L. N.; Rand, B. P.; Friend, R. H.; Mhaisalkar, S. G.; Lee, T.-W.; Sargent, E. H. Perovskites for Next-Generation Optical Sources. *Chem. Rev.* **2019**, *119*, 7444-7477.

(12) Wei, Y.; Cheng, Z.; Lin, J. An Overview on Enhancing the Stability of Lead Halide Perovskite Quantum Dots and Their Applications in Phosphor-Converted Leds. *Chem. Soc. Rev.* **2019**, *48*, 310-350.

(13) Shoaib, M.; Zhang, X.; Wang, X.; Zhou, H.; Xu, T.; Wang, X.; Hu, X.; Liu, H.; Fan, X.; Zheng, W.; Yang, T.; Yang, S.; Zhang, Q.; Zhu, X.; Sun, L.; Pan, A. Directional Growth of Ultralong $CsPbBr_3$ Perovskite Nanowires for High-Performance Photodetectors. *J. Am. Chem. Soc.* **2017**, *139*, 15592-15595.

(14) Yuan, S.; Wang, Z.-K.; Zhuo, M.-P.; Tian, Q.-S.; Jin, Y.; Liao, L.-S. Self-Assembled High Quality $CsPbBr_3$ Quantum Dot Films toward Highly Efficient Light-Emitting Diodes. *ACS Nano* **2018**, *12*, 9541-9548.

(15) Shen, K.; Xu, H.; Li, X.; Guo, J.; Sathasivam, S.; Wang, M.; Ren, A.; Choy, K. L.; Parkin, I. P.; Guo, Z.; Wu, J. Flexible and Self-Powered Photodetector Arrays Based on All-Inorganic $CsPbBr_3$ Quantum Dots. *Adv. Mater.* **2020**, *32*, 2000004.

(16) Dong, H.; Zhang, C.; Liu, X.; Yao, J.; Zhao, Y. S. Materials Chemistry and Engineering in Metal Halide Perovskite Lasers. *Chem. Soc. Rev.* **2020**, *49*, 951-982.

(17) Geiregat, P.; Maes, J.; Chen, K.; Drijvers, E.; De Roo, J.; Hodgkiss, J. M.; Hens, Z. Using Bulk-Like Nanocrystals to Probe Intrinsic Optical Gain Characteristics of Inorganic Lead Halide Perovskites. *ACS Nano* **2018**, *12*, 10178-10188.

(18) Ravi, V. K.; Markad, G. B.; Nag, A. Band Edge Energies and Excitonic Transition Probabilities of Colloidal $CsPbX_3$ (X = Cl, Br, I) Perovskite Nanocrystals. *ACS Energy Lett.* **2016**, *1*, 665-671.

(19) Nedelcu, G.; Protesescu, L.; Yakunin, S.; Bodnarchuk, M. I.; Grotevent, M. J.; Kovalenko, M. V. Fast Anion-Exchange in Highly Luminescent Nanocrystals of Cesium Lead Halide Perovskites ($CsPbX_3$, X = Cl, Br, I). *Nano Lett.* **2015**, *15*, 5635-5640.

(20) Goldschmidt, V. M. Die Gesetze Der Krystallochemie. *Naturwissenschaften* **1926**, *14*, 477-485.

(21) Hu, Y.; Bai, F.; Liu, X.; Ji, Q.; Miao, X.; Qiu, T.; Zhang, S. Bismuth Incorporation Stabilized A- $CsPbI_3$ for Fully Inorganic Perovskite Solar Cells. *ACS Energy Lett.* **2017**, *2*, 2219-2227.

(22) Wang, L.; Zhou, H.; Hu, J.; Huang, B.; Sun, M.; Dong, B.; Zheng, G.; Huang, Y.; Chen, Y.; Li, L.; Xu, Z.; Li, N.; Liu, Z.; Chen, Q.; Sun, L.-D.; Yan, C.-H. A Eu^{3+}-Eu^{2+} Ion Redox Shuttle Imparts Operational Durability to Pb-I Perovskite Solar Cells. *Science* **2019**, *363*, 265-270.

(23) Zhou, Y.; Chen, J.; Bakr, O. M.; Sun, H.-T. Metal-Doped Lead Halide Perovskites: Synthesis, Properties, and Optoelectronic Applications. *Chem. Mater.* **2018**, *30*, 6589-6613.

(24) Swarnkar, A.; Mir, W. J.; Nag, A. Can B-Site Doping or Alloying Improve Thermal- and Phase-Stability of All-Inorganic $CsPbX_3$ (X = Cl, Br, I) Perovskites? *ACS Energy Lett.* **2018**, *3*, 286-289.

(25) Akkerman, Q. A.; Meggiolaro, D.; Dang, Z.; De Angelis, F.; Manna, L. Fluorescent Alloy $CsPb_xMn_{1-x}I_3$ Perovskite Nanocrystals with High Structural and Optical Stability. *ACS Energy Lett.* **2017**, *2*, 2183-2186.

(26) Luo, B.; Li, F.; Xu, K.; Guo, Y.; Liu, Y.; Xia, Z.; Zhang, J. Z. B-Site Doped Lead Halide Perovskites: Synthesis, Band Engineering, Photophysics, and Light Emission Applications. *J. Mater. Chem. C* **2019**, *7*, 2781-2808.

(27) Kovalenko, M. V.; Protesescu, L.; Bodnarchuk, M. I. Properties and Potential Optoelectronic Applications of Lead Halide Perovskite Nanocrystals. *Science* **2017**, *358*, 745-750.

(28) Brandt, R. E.; Stevanović, V.; Ginley, D. S.; Buonassisi, T. Identifying Defect-Tolerant Semiconductors with High Minority-Carrier Lifetimes: Beyond Hybrid Lead Halide Perovskites. *MRS Commun.* **2015**, *5*, 265-275.

(29) Yang, Z.; Surrente, A.; Galkowski, K.; Miyata, A.; Portugall, O.; Sutton, R. J.; Haghighirad, A. A.; Snaith, H. J.; Maude, D. K.; Plochocka, P.; Nicholas, R. J. Impact of the Halide Cage on the Electronic Properties of Fully Inorganic Cesium Lead Halide Perovskites. *ACS Energy Lett.* **2017**, *2*, 1621-1627.

(30) Huang, H.; Bodnarchuk, M. I.; Kershaw, S. V.; Kovalenko, M. V.; Rogach, A. L. Lead Halide Perovskite Nanocrystals in the Research Spotlight: Stability and Defect Tolerance. *ACS Energy Lett.* **2017**, *2*, 2071-2083.

(31) Bünzli, J.-C. G. Lanthanide Luminescence: From a Mystery to Rationalization, Understanding, and Applications. In *Handbook on the Physics and Chemistry of Rare Earths*; Bünzli, J.-C. G.; Pecharsky, V. K., Eds.; Elsevier, **2016**; Vol. *50*, pp 141-176.

(32) Binnemans, K. Lanthanide-Based Luminescent Hybrid Materials. *Chem. Rev.* **2009**, *109*, 4283-4374.

(33) Kumar, V.; Ntwaeaborwa, O. M.; Soga, T.; Dutta, V.; Swart, H. C. Rare Earth Doped Zinc Oxide Nanophosphor Powder: A Future Material for Solid State Lighting and Solar Cells. *ACS Photonics* **2017**, *4*, 2613-2637.

(34) Cotton, S., *Lanthanide and Actinide Chemistry*. John Wiley & Sons: 2013.

(35) Sousa Filho, P. C. d.; Lima, J. F.; Serra, O. A. From Lighting to Photoprotection: Fundamentals and Applications of Rare Earth Materials. *J. Braz. Chem. Soc.* **2015**, *26*, 2471-2495.

(36) Martinić, I.; Eliseeva, S. V.; Petoud, S. Near-Infrared Emitting Probes for Biological Imaging: Organic Fluorophores, Quantum Dots, Fluorescent Proteins, Lanthanide (III) Complexes and Nanomaterials. *J. Lumin.* **2017**, *189*, 19-43.

(37) Auzel, F. Upconversion and Anti-Stokes Processes with F and D Ions in Solids. *Chem. Rev.* **2004**, *104*, 139-174.

(38) Eliseeva, S. V.; Bünzli, J.-C. G. Lanthanide Luminescence for Functional Materials and Bio-Sciences. *Chem. Soc. Rev.* **2010**, *39*, 189-227.

(39) Yu, S.; Tu, D.; Lian, W.; Xu, J.; Chen, X. Lanthanide-Doped Near-Infrared-II Luminescent Nanoprobes for Bioapplications. *Sci. China Mater.* **2019**, *62*, 1071-1086.

(40) Balabhadra, S.; Debasu, M. L.; Brites, C. D. S.; Ferreira, R. A. S.; Carlos, L. D. Radiation-to-Heat Conversion Efficiency in SrF_2:Yb^{3+}/Er^{3+} Upconverting Nanoparticles. *Opt. Mater.* 2018, 83, 1-6.

(41) Wong, K.-L.; Bünzli, J.-C. G.; Tanner, P. A. Quantum Yield and Brightness. *J. Lumin.* **2020,** 117256.

(42) Xu, J.; Zhou, J.; Chen, Y.; Yang, P.; Lin, J. Lanthanide-Activated Nanoconstructs for Optical Multiplexing. *Coord. Chem. Rev.* **2020**, *415*, 213328.

(43) Wegh, R. T.; Donker, H.; Oskam, K. D.; Meijerink, A. Visible Quantum Cutting in $LiGdF_4$: Eu^{3+} through Downconversion. *Science* **1999**, *283*, 663-666.

(44) Zhou, B.; Shi, B.; Jin, D.; Liu, X. Controlling Upconversion Nanocrystals for Emerging Applications. *Nat. Nanotechnol.* **2015**, *10*, 924.

(45) Sommerdijk, J. L.; Bril, A.; de Jager, A. W. Two Photon Luminescence with Ultraviolet Excitation of Trivalent Praseodymium. *J. Lumin.* **1974**, *8*, 341-343.

(46) Piper, W. W.; DeLuca, J. A.; Ham, F. S. Cascade Fluorescent Decay in Pr^{3+}-Doped Fluorides: Achievement of a Quantum Yield Greater Than Unity for Emission of Visible Light. *J. Lumin.* **1974**, *8*, 344-348.

(47) Huang, X.; Han, S.; Huang, W.; Liu, X. Enhancing Solar Cell Efficiency: the Search for Luminescent Materials as Spectral Converters. *Chem. Soc. Rev.* **2013,** *42*, 173-201.

(48) Dorenbos, P. The 5d Level Positions of the Trivalent Lanthanides in Inorganic Compounds. *J. Lumin.* **2000**, *91*, 155-176.

(49) Chen, G.; Qiu, H.; Prasad, P. N.; Chen, X. Upconversion Nanoparticles: Design, Nanochemistry, and Applications in Theranostics. *Chem. Rev.* **2014**, *114*, 5161-5214.

(50) Hudry, D.; Howard, I. A.; Popescu, R.; Gerthsen, D.; Richards, B. S. Structure-Property Relationships in Lanthanide-Doped Upconverting Nanocrystals: Recent Advances in Understanding Core-Shell Structures. *Adv. Mater.* **2019**.

(51) Wang, M.; Mi, C.; Zhang, Y.; Liu, J.; Li, F.; Mao, C.; Xu, S. NIR-Responsive Silica-Coated $NaYbF_4$:Er/Tm/Ho Upconversion Fluorescent Nanoparticles with Tunable Emission Colors and Their Applications in Immunolabeling and Fluorescent Imaging of Cancer Cells. *J. Phys. Chem. C* **2009**, *113*, 19021-19027.

(52) Wang, F.; Liu, X. G. Upconversion Multicolor Fine-Tuning: Visible to Near-Infrared Emission from Lanthanide-Doped $NaYF_4$ Nanoparticles. *J. Am. Chem. Soc.* **2008**, *130*.

(53) Su, Q.; Han, S.; Xie, X.; Zhu, H.; Chen, H.; Chen, C.-K.; Liu, R.-S.; Chen, X.; Wang, F.; Liu, X. The Effect of Surface Coating on Energy Migration-Mediated Upconversion. *J. Am. Chem. Soc.* **2012**, *134*, 20849-20857.

(54) Zhou, J.; Liu, Q.; Feng, W.; Sun, Y.; Li, F. Upconversion Luminescent Materials: Advances and Applications. *Chem. Rev.* **2015**, *115*, 395-465.

(55) Zheng, W.; Huang, P.; Gong, Z.; Tu, D.; Xu, J.; Zou, Q.; Li, R.; You, W.; Bünzli, J.-C. G.; Chen, X. Near-Infrared-Triggered Photon Upconversion Tuning in All-Inorganic Cesium Lead Halide Perovskite Quantum Dots. *Nat. Commun.* **2018**, *9*, 3462.

(56) Wang, Y.; Li, X.; Zhao, X.; Xiao, L.; Zeng, H.; Sun, H. Nonlinear Absorption and Low-Threshold Multiphoton Pumped Stimulated Emission from All-Inorganic Perovskite Nanocrystals. *Nano Lett.* **2016**, *16*, 448-453.

(57) Wang, J.; Ming, T.; Jin, Z.; Wang, J.; Sun, L.-D.; Yan, C.-H. Photon Energy Upconversion through Thermal Radiation with the Power Efficiency Reaching 16%. *Nat. Commun.* **2014**, *5*, 5669.

(58) Zou, W.; Visser, C.; Maduro, J. A.; Pshenichnikov, M. S.; Hummelen, J. C. Broadband Dye-Sensitized Upconversion of Near-Infrared Light. *Nat. Photonics* **2012**, *6*, 560.

(59) Lin, J.; Yang, C.; Huang, P.; Wang, S.; Liu, M.; Jiang, N.; Chen, D. Photoluminescence Tuning from Glass-Stabilized $CsPbX_3$ (X = Cl, Br, I) Perovskite Nanocrystals Triggered by Upconverting $Tm:KYb_2F_7$ Nanoparticles for High-Level Anti-Counterfeiting. *Chem. Eng. J.* **2020**, *395*, 125214.

(60) Rao, M.; Fu, J.; Wen, X.; Sun, B.; Wu, J.; Liu, X.-H.; Dong, X. Near-Infrared-Excitable Perovskite Quantum Dots via Coupling with Upconversion Nanoparticles for Dual-Model Anti-Counterfeiting. *New J. Chem.* **2018**, *42*, 12353-12356.

(61) Li, X.; Yang, C.; Yu, Y.; Li, Z.; Lin, J.; Guan, X.; Zheng, Z.; Chen, D. Dual-Modal Photon Upconverting and Downshifting Emissions from Ultra-Stable $CsPbBr_3$ Perovskite Nanocrystals Triggered by Co-Growth of $Tm:NaYbF_4$ Nanocrystals in Glass. *ACS Appl. Mat. Interfaces* **2020**, *12*, 18705-18714.

(62) Zhang, X.; Wang, Q.; Jin, Z.; Zhang, J.; Liu, S. Stable Ultra-Fast Broad-Bandwidth Photodetectors Based on α-$CsPbI_3$ Perovskite and $NaYF_4$:Yb,Er Quantum Dots. *Nanoscale* **2017**, *9*, 6278-6285.

(63) Francés-Soriano, L.; Gonzalez-Carrero, S.; Navarro-Raga, E.; Galian, R. E.; González-Béjar, M.; Pérez-Prieto, J. Efficient Cementing of $CH_3NH_3PbBr_3$ Nanoparticles to Upconversion Nanoparticles Visualized by Confocal Microscopy. *Adv. Funct. Mater.* **2016**, *26*, 5131-5138.

(64) Zhang, W.; Chen, T.; Su, L.; Ge, X.; Chen, X.; Song, J.; Yang, H. Quantum Dot-Based Sensitization System for Boosted Photon Absorption and Enhanced Second Near-Infrared Luminescence of Lanthanide-Doped Nanoparticle. *Anal. Chem.* **2020**, *92*, 6094-6102.

(65) Zeng, M.; Singh, S.; Hens, Z.; Liu, J.; Artizzu, F.; Van Deun, R. Strong Upconversion Emission in $CsPbBr_3$ Perovskite Quantum Dots through Efficient $BaYF_5$:Yb,Ln Sensitization. *J. Mater. Chem. C* **2019**, *7*, 2014-2021.

(66) Cardoso Dos Santos, M.; Hildebrandt, N. Recent Developments in Lanthanide-to-Quantum Dot FRET Using Time-Gated Fluorescence Detection and Photon Upconversion. *TrAC, Trends Anal. Chem.* **2016**, *84*, 60-71.

(67) Muhr, V.; Würth, C.; Kraft, M.; Buchner, M.; Baeumner, A. J.; Resch-Genger, U.; Hirsch, T. Particle-Size-Dependent Förster Resonance Energy Transfer from Upconversion Nanoparticles to Organic Dyes. *Anal. Chem.* **2017**, *89*, 4868-4874.
(68) Wang, Z.; Meijerink, A. Dye-Sensitized Downconversion. *J. Phys. Chem. Lett.* **2018**, *9*, 1522-1526.
(69) Zou, S.; Liu, Y.; Li, J.; Liu, C.; Feng, R.; Jiang, F.; Li, Y.; Song, J.; Zeng, H.; Hong, M.; Chen, X. Stabilizing Cesium Lead Halide Perovskite Lattice through Mn (II) Substitution for Air-Stable Light-Emitting Diodes. *J. Am. Chem. Soc.* **2017**, *139*, 11443-11450.
(70) Zhou, D.; Liu, D.; Pan, G.; Chen, X.; Li, D.; Xu, W.; Bai, X.; Song, H. Cerium and Ytterbium Codoped Halide Perovskite Quantum Dots: A Novel and Efficient Downconverter for Improving the Performance of Silicon Solar Cells. *Adv. Mater.* **2017**, *29*.
(71) Pan, G.; Bai, X.; Yang, D.; Chen, X.; Jing, P.; Qu, S.; Zhang, L.; Zhou, D.; Zhu, J.; Xu, W.; Dong, B.; Song, H. Doping Lanthanide into Perovskite Nanocrystals: Highly Improved and Expanded Optical Properties. *Nano Lett.* **2017**, *17*, 8005-8011.
(72) Hu, Q.; Li, Z.; Tan, Z.; Song, H.; Ge, C.; Niu, G.; Han, J.; Tang, J. Rare Earth Ion-Doped $CsPbBr_3$ Nanocrystals. *Adv. Opt. Mater.* **2018**, *6*, 1700864.
(73) Erickson, C. S.; Crane, M. J.; Milstein, T. J.; Gamelin, D. R. Photoluminescence Saturation in Quantum-Cutting Yb^{3+}-Doped $Cspb(Cl_{1-x}/Br_x)_3$ Perovskite Nanocrystals: Implications for Solar Downconversion. *J. Phys. Chem. C* **2019,** *123*, 12474-12484.
(74) Mir, W. J.; Mahor, Y.; Lohar, A.; Jagadeeswararao, M.; Das, S.; Mahamuni, S.; Nag, A. Postsynthesis Doping of Mn and Yb into $CsPbX_3$ (X = Cl, Br, or I) Perovskite Nanocrystals for Downconversion Emission. *Chem. Mater.* **2018**, *30*, 8170-8178.
(75) Zhou, D.; Sun, R.; Xu, W.; Ding, N.; Li, D.; Chen, X.; Pan, G.; Bai, X.; Song, H. Impact of Host Composition, Codoping, or Tridoping on Quantum-Cutting Emission of Ytterbium in Halide Perovskite Quantum Dots and Solar Cell Applications. *Nano Lette.* **2019**, *19*, 6904-6913.
(76) Ma, J.-P.; Chen, Y.-M.; Zhang, L.-M.; Guo, S.-Q.; Liu, J.-D.; Li, H.; Ye, B.-J.; Li, Z.-Y.; Zhou, Y.; Zhang, B.-B.; Bakr, O. M.; Zhang, J.-Y.; Sun, H.-T. Insights into the Local Structure of Dopants, Doping Efficiency, and Luminescence Properties of Lanthanide-Doped $CsPbCl_3$ Perovskite Nanocrystals. *J. Mater. Chem. C* **2019**, *7*, 3037-3048.
(77) Mir, W. J.; Sheikh, T.; Arfin, H.; Xia, Z.; Nag, A. Lanthanide Doping in Metal Halide Perovskite Nanocrystals: Spectral Shifting, Quantum Cutting and Optoelectronic Applications. NPG Asia Mater. **2020**, *12*, 9.
(78) Zeng, Z.; Xu, Y.; Zhang, Z.; Gao, Z.; Luo, M.; Yin, Z.; Zhang, C.; Xu, J.; Huang, B.; Luo, F.; Du, Y.; Yan, C. Rare-Earth-Containing Perovskite Nanomaterials: Design, Synthesis, Properties and Applications. *Chem. Soc. Rev.* **2020**, *49*, 1109-1143.
(79) Song, Z.; Zhao, J.; Liu, Q. Luminescent Perovskites: Recent Advances in Theory and Experiments. *Inorg. Chem. Front.* **2019**, *6*, 2969-3011.
(80) Faheem, M. B.; Khan, B.; Feng, C.; Farooq, M. U.; Raziq, F.; Xiao, Y.; Li, Y. All-Inorganic Perovskite Solar Cells: Energetics, Key Challenges, and Strategies toward Commercialization. *ACS Energy Lett.* **2020**, *5*, 290-320.
(81) Martín-Rodríguez, R.; Geitenbeek, R.; Meijerink, A. Incorporation and Luminescence of Yb^{3+} in Cdse Nanocrystals. *J. Am. Chem. Soc.* **2013**, *135*, 13668-13671.

(82) Erwin, S. C.; Zu, L.; Haftel, M. I.; Efros, A. L.; Kennedy, T. A.; Norris, D. J. Doping Semiconductor Nanocrystals. *Nature* **2005**, *436*, 91-94.

(83) Swarnkar, A.; Mir, W. J.; Nag, A. Can B-Site Doping or Alloying Improve Thermal-and Phase-Stability of All-Inorganic $CsPbX_3$ (X= Cl, Br, I) Perovskites? *ACS Energy Lett.* **2018**, *3*, 286-289.

(84) Linaburg, M. R.; McClure, E. T.; Majher, J. D.; Woodward, P. M. $Cs_{1-x}Rb_xPbCl_3$ and $Cs_{1-x}Rb_xPbBr_3$ Solid Solutions: Understanding Octahedral Tilting in Lead Halide Perovskites. *Chem. Mater.* **2017**, *29*, 3507-3514.

(85) Pearson, R. G. Hard and Soft Acids and Bases, HSAB, Part 1: Fundamental Principles. *J. Chem. Educ.* **1968**, *45*, 581.

(86) Deng, Z.; Tong, L.; Flores, M.; Lin, S.; Cheng, J.-X.; Yan, H.; Liu, Y. High-Quality Manganese-Doped Zinc Sulfide Quantum Rods with Tunable Dual-Color and Multiphoton Emissions. *J. Am. Chem. Soc.* **2011**, *133*, 5389-5396.

(87) Lignos, I.; Stavrakis, S.; Nedelcu, G.; Protesescu, L.; deMello, A. J.; Kovalenko, M. V. Synthesis of Cesium Lead Halide Perovskite Nanocrystals in a Droplet-Based Microfluidic Platform: Fast Parametric Space Mapping. *Nano Lett.* **2016**, *16*, 1869-1877.

(88) Pan, A.; He, B.; Fan, X.; Liu, Z.; Urban, J. J.; Alivisatos, A. P.; He, L.; Liu, Y. Insight into the Ligand-Mediated Synthesis of Colloidal $CsPbBr_3$ Perovskite Nanocrystals: The Role of Organic Acid, Base, and Cesium Precursors. *ACS Nano* **2016**, *10*, 7943-7954.

(89) Heuer-Jungemann, A.; Feliu, N.; Bakaimi, I.; Hamaly, M.; Alkilany, A.; Chakraborty, I.; Masood, A.; Casula, M. F.; Kostopoulou, A.; Oh, E.; Susumu, K.; Stewart, M. H.; Medintz, I. L.; Stratakis, E.; Parak, W. J.; Kanaras, A. G. The Role of Ligands in the Chemical Synthesis and Applications of Inorganic Nanoparticles. *Chem. Rev.* **2019**, *119*, 4819-4880.

(90) Murray, C. B.; Norris, D. J.; Bawendi, M. G. Synthesis and Characterization of Nearly Monodisperse CdE (E = Sulfur, Selenium, Tellurium) Semiconductor Nanocrystallites. *J. Am. Chem. Soc.* **1993**, *115*, 8706-8715.

(91) Manna, L.; Milliron, D. J.; Meisel, A.; Scher, E. C.; Alivisatos, A. P. Controlled Growth of Tetrapod-Branched Inorganic Nanocrystals. *Nat. Mater.* **2003**, *2*, 382-385.

(92) El-Ballouli, A. a. O.; Bakr, O. M.; Mohammed, O. F. Compositional, Processing, and Interfacial Engineering of Nanocrystal- and Quantum-Dot-Based Perovskite Solar Cells. *Chem. Mater.* **2019**, *31*, 6387-6411.

(93) Milstein, T. J.; Kroupa, D. M.; Gamelin, D. R. Picosecond Quantum Cutting Generates Photoluminescence Quantum Yields over 100% in Ytterbium-Doped $CsPbCl_3$ Nanocrystals. *Nano Lett.* **2018**, *18*, 3792-3799.

(94) Cai, T.; Yang, H.; Hills-Kimball, K.; Song, J.-P.; Zhu, H.; Hofman, E.; Zheng, W.; Rubenstein, B. M.; Chen, O. Synthesis of All-Inorganic Cd-Doped $CsPbCl_3$ Perovskite Nanocrystals with Dual-Wavelength Emission. *J. Phys. Chem. Lett.* **2018**, *9*, 7079-7084.

(95) Saliba, M.; Matsui, T.; Domanski, K.; Seo, J.-Y.; Ummadisingu, A.; Zakeeruddin, S. M.; Correa-Baena, J.-P.; Tress, W. R.; Abate, A.; Hagfeldt, A.; Grätzel, M. Incorporation of Rubidium Cations into Perovskite Solar Cells Improves Photovoltaic Performance. *Science* **2016**, *354*, 206-209.

(96) Yang, W. S.; Park, B.-W.; Jung, E. H.; Jeon, N. J.; Kim, Y. C.; Lee, D. U.; Shin, S. S.; Seo, J.; Kim, E. K.; Noh, J. H.; Seok, S. I. Iodide Management in Formamidinium-Lead-Halide-Based Perovskite Layers for Efficient Solar Cells. *Science* **2017**, *356*, 1376-1379.

(97) Jeon, N. J.; Na, H.; Jung, E. H.; Yang, T.-Y.; Lee, Y. G.; Kim, G.; Shin, H.-W.; Il Seok, S.; Lee, J.; Seo, J. A Fluorene-Terminated Hole-Transporting Material for Highly Efficient and Stable Perovskite Solar Cells. *Nat. Energy* **2018**, *3*, 682-689.
(98) Crane, M. J.; Kroupa, D. M.; Roh, J. Y.; Anderson, R. T.; Smith, M. D.; Gamelin, D. R. Single-Source Vapor Deposition of Quantum-Cutting Yb^{3+}:$CsPb(Cl_{1-x}Br_x)_3$ and Other Complex Metal-Halide Perovskites. *ACS Appl. Energy Mater.* **2019**, *2*, 4560-4565.
(99) Duan, J.; Zhao, Y.; Yang, X.; Wang, Y.; He, B.; Tang, Q. Lanthanide Ions Doped $CsPbBr_3$ Halides for HTM-Free 10.14%-Efficiency Inorganic Perovskite Solar Cell with an Ultrahigh Open-Circuit Voltage of 1.594 V. *Adv. Energy Mater.* **2018**, *8*, 1802346.
(100) Ishii, A.; Miyasaka, T. Sensitized Yb^{3+} Luminescence in $CsPbCl_3$ Film for Highly Efficient Near-Infrared Light-Emitting Diodes. *Adv. Sci.* **2020**, *7*, 1903142.
(101) Kroupa, D. M.; Roh, J. Y.; Milstein, T. J.; Creutz, S. E.; Gamelin, D. R. Quantum-Cutting Ytterbium-Doped $CsPb(Cl_{1-x}Br_x)_3$ Perovskite Thin Films with Photoluminescence Quantum Yields over 190%. *ACS Energy Lett.* **2018**, *3*, 2390-2395.
(102) Duan, J.; Zhao, Y.; He, B.; Tang, Q. High-Purity Inorganic Perovskite Films for Solar Cells with 9.72 % Efficiency. *Angew. Chem. Int. Ed*. **2018**, *57*, 3787-3791.
(103) Xiang, W.; Wang, Z.; Kubicki, D. J.; Tress, W.; Luo, J.; Prochowicz, D.; Akin, S.; Emsley, L.; Zhou, J.; Dietler, G.; Grätzel, M.; Hagfeldt, A. Europium-Doped $CsPbI_2Br$ for Stable and Highly Efficient Inorganic Perovskite Solar Cells. *Joule* **2019**, *3*, 205-214.
(104) Milstein, T. J.; Kluherz, K. T.; Kroupa, D. M.; Erickson, C. S.; De Yoreo, J. J.; Gamelin, D. R. Anion Exchange and the Quantum-Cutting Energy Threshold in Ytterbium-Doped $CsPb(Cl_{1-x}Br_x)_3$ Perovskite Nanocrystals. *Nano Lett.* **2019**, *19*, 1931-1937.
(105) Jiang, F.; Zheng, W.; Jiang, Y.; Li, Y.; Fan, P.; Huang, W.; Fu, X.; Li, L.; Ouyang, Y.; Zhu, X.; Zhuang, X.; Pan, A. Trap-Mediated Energy Transfer in Er-Doped Cesium Lead Halide Perovskite. *J. Phys. Chem. Lett.* **2020**, *11*, 9, 3320-3326.
(106) Cheng, Y.; Shen, C.; Shen, L.; Xiang, W.; Liang, X. Tb^{3+}, Eu^{3+} Co-Doped $CsPbBr_3$ QDs Glass with Highly Stable and Luminous Adjustable for White Leds. *ACS Appl. Mat. Interfaces* **2018**, *10*, 21434-21444.
(107) Zhang, X.; Zhang, Y.; Zhang, X.; Yin, W.; Wang, Y.; Wang, H.; Lu, M.; Li, Z.; Gu, Z.; Yu, W. W. Yb^{3+} and Yb^{3+}/Er^{3+} Doping for Near-Infrared Emission and Improved Stability of $CsPbCl_3$ Nanocrystals. *J. Mater. Chem. C* **2018**, *6*, 10101-10105.
(108) Li, X.; Duan, S.; Liu, H.; Chen, G.; Luo, Y.; Ågren, H. Mechanism for the Extremely Efficient Sensitization of Yb^{3+}Luminescence in $CsPbCl_3$ Nanocrystals. *J. Phys. Chem. Lett.* **2019**, *10*, 487-492.

Chapter 2 Strong Upconversion Emission in $CsPbBr_3$ Perovskite Quantum Dots through Efficient $BaYF_5$:Yb,Ln Sensitization

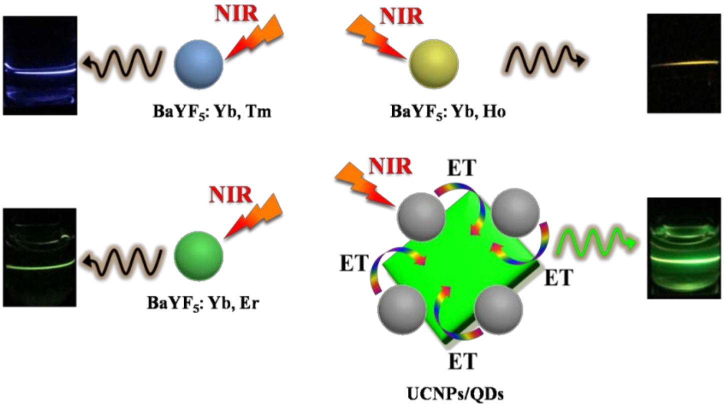

The results of this chapter were published in:

Zeng, M.; Singh, S.; Hens, Z.; Liu, J.; Artizzu, F.; Van Deun, R. Strong Upconversion Emission in $CsPbBr_3$ Perovskite Quantum Dots through Efficient $BaYF_5$:Yb,Ln Sensitization. *J. Mater. Chem. C* **2019,** *7*, 2014-2021.

Abstract

Owing to their remarkable optical properties, all-inorganic cesium lead halide perovskite $CsPbX_3$ ($X = Cl^-, Br^-, I^-$) quantum dots (QDs) have emerged as promising materials for a variety of applications, such as solar cells and light-emitting diodes. However, these perovskite QDs can only be excited under short-wavelength light with high power below 600 nm, which limits their applications. Herein, we demonstrate an effective strategy to realize near-infrared (NIR) pumping for $CsPbBr_3$ QDs through energy transfer from lanthanide-doped upconversion nanoparticles (UCNPs). UCNPs/QDs pairs with different molar ratios were synthesized by an *in situ* growth method. Transmission electron microscopy images show that the configuration of the assembly is dependent on the molar ratio of the two units which are distributed homogenously with high surface contact. High energy transfer efficiency ~100% from the UCNPs donors to the QDs acceptors is achieved, leading to intense green emission from the perovskite $CsPbBr_3$ QDs under NIR laser light even in liquid suspension. Additionally, the high photostability of $CsPbBr_3$ QDs under NIR irradiation suggests that this strategy can be a critical point for the development of perovskite-based functional emitters or devices with long-term operational stability.

2.1 Introduction

Benefiting from their high photoluminescence quantum yields (PLQY), extremely large molar extinction coefficients and tunable color output throughout the entire visible spectrum, colloidal $CsPbX_3$ ($X = Cl^-, Br^-, I^-$) perovskite quantum dots (QDs) are promising optically active materials for light-emitting diodes (LEDs),[1,2] photovoltaics,[3,4] and photodetectors.[5,6] The above applications prove successful under short-wavelength light excitation, whereas the near-infrared (NIR)-triggered photon upconversion is not possible for the original perovskite QDs, which limits their potential applications, such as deep-tissue bioimaging and photodynamic therapy. In contrast to perovskite QDs, lanthanide-doped upconversion nanoparticles (UCNPs) offer the opportunity to convert low-energy NIR photons into higher energy UV-visible light by using easily accessible and low-cost continuous-wave (CW) diode lasers at relatively low excitation power. The limitation of perovskite QDs can be overcome by integration with UCNPs, which can serve as NIR sensitizers by acting as donors in an energy transfer (ET) process, either through nonradiative Förster resonance energy transfer (FRET) or radiative photon reabsorption (PR). UCNPs have already been shown to be excellent energy transfer donors for a variety of acceptors (such as gold nanoparticles,[7] organic dyes,[8] and QDs[9]) through FRET and (or) PR.

Among the ET systems hitherto reported, $NaYF_4$ UCNPs assembled with traditional QDs (such as CdS, CdSe, CdTe)[9-15] and semiconductors (such as TiO_2, ZnO)[16-21] have been explored. However, these systems typically display broad or weak emission peaks of the sensitized QDs. Recently, Marin et al. used ternary $CuInS_2$ QDs as energy transfer acceptors in the $LiYF_4$:25%Yb,0.5%Tm/QDs system, obtaining up to 32% FRET efficiency in solid state sample with the appearance of very weak QD emission.[22]

Nonetheless, lead-halide perovskite QDs seem more promising for these applications since they possess outstanding advantages over traditional QDs.[23] Francés-Soriano and co-workers combined $NaYF_4$:22%Yb,1.2%Tm UCNPs with $CH_3NH_3PbBr_3$ QDs by direct physical stirring, and were able to observe detectable emission from $CH_3NH_3PbBr_3$ QDs under UCNPs irradiation.[24] Compared to hybrid organometallic halide perovskite QDs, all-inorganic $CsPbX_3$ perovskite QDs have higher compositional tunability, lower sensitivity to oxygen, moisture, temperature, and light and very high PLQY up to 90%.[23,25,26] Zhang et al. assembled $NaYF_4$:20%Yb,2%Er UCNPs with all-inorganic $CsPbI_3$ perovskite QDs by a spin-coating method to fabricate a photodetector device. However, despite the evidence of optical response of the perovskite-based device under NIR irradiation, the upconversion luminescence (UCL) properties of the hybrid assembly were not studied.[27] Only very recently, Zheng and coworkers succeeded in obtaining strong emissions from $CsPbX_3$ QDs combined with $LiYbF_4$:0.5%Tm UCNPs with color-tunability by tailoring the perovskite QD bandgap.[25] Thanks to the much larger molar extinction coefficient of the perovskite material, this system showed better performances than the other energy transfer systems where traditional QDs were used as the acceptors. However, the $CsPbX_3$ QDs and $LiYbF_4$:0.5%Tm UCNPs were simply combined by physical mixing, which affords a highly inhomogeneous material and is not preferable for distance-dependent ET processes. The excitons from the UCNPs will migrate to the lowest energy states and be trapped if no nearby molecules are accessible for energy transfer.[28] Consequently, only PR process was involved in the energy transfer mechanism in the above system, which was more easily subjected to competitive quenching and less efficient compared to FRET.[29]

In this framework, we addressed the design of a UCNPs/QDs nanoassembly where high UCL performances of QDs are triggered by efficient NIR sensitization through optimized donor-acceptor ET. To realize such efficient converter, two main guidelines are to be taken into consideration: i) spectral resonance between the donor emission and the acceptor absorption, and ii) short donor-acceptor spatial separation. While the first requirement can be easily achieved by proper selection of the donor-acceptor pair, the latter is less obvious in such a heterogeneous nanoassembly. In this regard, small-sized UCNPs as energy transfer donors[6,22] and enhanced surface contact between the UCNPs and QDs in the assembly are expected to favor distance-dependent ET processes, both radiative (PR) and non-radiative (FRET).[22] Moreover, small nanoparticle sizing is indeed preferred for biological applications.[30-32] In light of these considerations, we studied a novel ET system based on sub-10 nm $BaYF_5$:20%Yb,x%Ln (x%Ln= 1%Tm, 2%Ho, 2%Er) UCNPs combined with $CsPbBr_3$ QDs (PLQY: 64%), whose bandgap matches the wavelength of the light emitted by UCNPs, this pair enabling low energy NIR excitation and high energy visible-light emission. In our design strategy, we resorted to the use of $CsPbBr_3$ QDs around 13 nm of diameter, larger than traditional QDs. The relatively large surface allows for conjugating multiple donors,[33] assumed to improve the ability for NIR photons harvesting. Herein, $BaYF_5$:20%Yb,1%Tm, $BaYF_5$:20%Yb,2%Ho and $BaYF_5$:20%Yb,2%Er were selected as the ET donors, and were coupled with $CsPbBr_3$ QDs by an *in situ* growth method in a mixture of oleic acid (OA) and oleylamine (OLA) to obtain a close-contact assembly of donor and acceptor units. The UCL performance of the ET system with different molar ratios of UCNPs to $CsPbBr_3$ QDs (1: 0.125, 1: 0.25, 1: 1, 1: 4, 1: 8) was investigated to gain insight into the influence of the detected emission intensity on the relative number of donor/acceptor units.

2.2 Experimental Section

2.2.1 Sample Preparation

Materials and chemicals. $YCl_3·6H_2O$ (99.99%), $YbCl_3·6H_2O$ (99.9%), $ErCl_3·6H_2O$ (99.9%), oleic acid (OA, 90%), oleylamine (OLA, 70%) were purchased from Sigma-Aldrich. $TmCl_3·6H_2O$ (99.9%), Cs_2CO_3 (99.5%) and acetone were purchased from Acros Organics. $HoCl_3·6H_2O$ (99.9%), $PbBr_2$ (99.999%) and 1-octadecene (ODE, 90%) were purchased from Alfa Aesar. $Ba(OH)_2·8H_2O$ (98%) was purchased from Janssen Chimica. NH_4F (≥98.0 %) was purchased from Merck. Cyclohexane and methanol were purchased from Fisher Scientific. All chemicals were used as received.

Synthesis of $BaYF_5$:20%Yb,x%Ln (x%Ln = 2%Er, 2%Ho, 1%Tm) upconversion nanoparticles (UCNPs). The $BaYF_5$:20%Yb,x%Ln (x%Ln = 2%Er, 2%Ho, 1%Tm) UCNPs were prepared using a high-temperature coprecipitation method. In a typical procedure for the synthesis of 0.5 mmol of $BaYF_5$:20%Yb,1%Tm, 119.83 mg (0.395 mmol) of $YCl_3·6H_2O$, 38.75 mg (0.1 mmol) of $YbCl_3·6H_2O$ and 1.38 mg (0.005 mmol) of $TmCl_3·6H_2O$ were mixed with 10 mL of ODE and 6 mL of OA in a three-neck flask. The mixture was heated to 120 °C for 1 h under vacuum to remove moisture and oxygen. The reaction vessel was filled with N_2 and heated to 160 °C for 30 min to form a transparent solution, and then cooled down to room temperature. A mixture of 6.25 mL of methanol solution containing 2.5 mmol NH_4F and 1.5 mL of methanol solution containing 0.5 mmol $Ba(OH)_2$ $·8H_2O$ was injected into the reaction flask, and heated at 45 °C for 30 min. Subsequently, the temperature was raised to 100 °C and maintained for 30 min to remove methanol. Finally, the solution was heated to 300 °C and kept for 1 h under N_2 flow, then let cooling down to room temperature naturally. The as-synthesized UCNPs were precipitated by acetone, collected by centrifugation at 5000 rpm for 5 min, and washed three times with acetone. The obtained UCNPs were dispersed in 4 mL of cyclohexane and stored in a refrigerator (4 °C) for the subsequent step.

Synthesis of perovskite $CsPbBr_3$ quantum dots (QDs). $CsPbBr_3$ QDs were synthesized according to a previously reported procedure.[34] Briefly, 34.5 mg of $PbBr_2$, 4 mL of ODE, 0.4 mL of OA and 0.4 mL of OLA were loaded into a three-neck flask, evacuated and refilled with N_2 and kept at 120 °C for 1 h. Then the temperature was raised to 185 °C and 0.2 mL of Cs-oleate (407 mg of Cs_2CO_3 dissolved in 20 mL of ODE and 1.55 mL of OA at 150 °C) were swiftly injected. After 40 s, the reaction was quenched by immersion in an ice-bath. The crude solution was first centrifuged at 5000 rpm for 10 min and the coloured supernatant was discarded. Subsequently, 1 mL of cyclohexane was added, followed by centrifugation for 5 min at 4500 rpm. The resulting yellow precipitate, containing larger particles and agglomerates, was discarded, and the supernatant was diluted to 3 mL with cyclohexane, forming a long-term stable dispersion.

Synthesis of $BaYF_5$:20%Yb,x%Ln (x%Ln = 2%Er, 2%Ho, 1%Tm)/$CsPbBr_3$ composites. To investigate the photoluminescence properties of different component concentrations, a set of molar ratios of $BaYF_5$:20%Yb,x%Ln to $CsPbBr_3$ (1: 0.125, 1: 0.25, 1: 1, 1: 4, 1: 8) were chosen. The ET pairs were assembled together by an *in situ* growth method. In a typical synthesis of $BaYF_5$:20%Yb,x%Ln/$CsPbBr_3$ composite with 1: 1 ratio, 34.5 mg of $PbBr_2$, 4 mL of ODE, 0.4 mL of OA and 0.4 mL of OLA were added into a three-neck flask, dried under vacuum for 1 h at 120 °C and refilled with N_2. Then 0.023 mmol of UCNPs in cyclohexane were added into the solution and the cyclohexane was removed by evacuation. The flask was then backfilled with N_2 and heated to 185 °C. At this temperature, 0.2 mL of Cs-oleate (0.023mmol) was swiftly injected into the reaction system. After 40 s, the reaction was ceased by immersing in an ice-bath. The obtained suspension was centrifuged and the supernatant liquid, containing smaller-sized QDs and isolated UCNPs, was discarded. Subsequently, 1 mL of cyclohexane was added, followed by centrifugation for 5 min at 4500 rpm to remove the yellow agglomerates, keeping the supernatant. The resulting supernatant constituted by UCPNs/QDs nanocomposites and pure QDs was diluted to 3 mL with cyclohexane.

Preparation of the physical mixture of $BaYF_5$:20%Yb,1%Tm and $CsPbBr_3$. The mixtures containing $BaYF_5$:20%Yb,1%Tm UCNPs and $CsPbBr_3$ QDs were mixed in cyclohexane by vigorous magnetic stirring for 1 h.

2.2.2 Characterization

Powder X-ray diffraction (XRD) patterns were recorded on a Thermo Scientific ARLX’TRA diffractometer equipped with a CuKα (λ= 1.5405 Å) source, at a scanning rate of 1.2° (2θ)/min from 10° to 80°. Transmission electron microscopy (TEM) and energy-dispersive X-ray spectroscopy (EDS) measurements were made using a Cs-corrected JEOL 2200FS microscope. Fourier Transform Infrared (FT-IR) spectra in the range of 1000-4000 cm^{-1} were acquired on a Thermo Nicolet 6700 FT-IR spectrometer equipped with a nitrogen-cooled MCT detector and a KBr beam splitter. UV-Vis absorption spectra were collected using a Perkin Elmer Lambda 950 spectrometer. Photoluminescence (PL) spectra were obtained on an Edinburgh Instruments FLSP920 spectrofluorimeter. The absolute PL quantum yield (PLQY) of QDs was measured using an integrating sphere (Edinburgh Instruments), coated on the inside with BENFLEC, and connected to the FLSP920 spectrofluorimeter. A 450 W xenon lamp and a 975 nm CW laser diode with maximum power of 400 mW were used as the steady-state excitation sources for QDs and UCNPs, respectively. The time-resolved PL measurements for QDs were performed using a Fianium Supercontinuum white light laser (100 ps pulses) as the excitation source. For time-resolved UCL, a Continuum Surelite I-10 Nd: YAG pumped OPO Plus laser with a pulse rate of 10 Hz, operating at a wavelength of 975 nm, was used as the excitation source.

2.3 Results and Discussion

Sub-10 nm $BaYF_5$:20%Yb,x%Ln (x%Ln = 2%Er, 2%Ho, 1%Tm) UCNPs were first synthesized using a high-temperature coprecipitation method as described in the Experimental Section. The so-obtained nanoparticles were subsequently directly injected into the precursors' mixture for the formation of the perovskite $CsPbBr_3$ QDs, which were synthesized through standard procedures. This *in situ* growth routine afforded a highly homogeneous material constituted by tightly assembled UCNPs/QDs particles. Powder X-ray diffraction (XRD) patterns were recorded to characterize the crystal structure of the sample. Diffractograms for the $BaYF_5$:20%Yb,1%Tm/$CsPbBr_3$ pair as a representative example, are reported in Figure 2.1. As seen from Figure 2.1a, the diffraction peaks of $BaYF_5$:20%Yb,1%Tm UCNPs are in good agreement with the tetragonal $BaYF_5$ phase (JCPDS No.46-0039). No other impurity peaks were detected, indicating that the as-synthesized $BaYF_5$:20%Yb,1%Tm nanoparticles are pure-phased. Figure 2.1b depicts the XRD pattern of $CsPbBr_3$ QDs, wherein the diffraction peaks are consistent with the cubic phase of $CsPbBr_3$ (JCPDS No.54-0752). It was found that the pattern of the UCNPs/QDs pair is still dominated by the peaks of the cubic $CsPbBr_3$ QDs phase, while a weak peak at 26.26° associated with UCNPs is appearing when the ratio of UCNPs/$CsPbBr_3$ is up to 1: 0.25 as shown in Figure 2.1c.

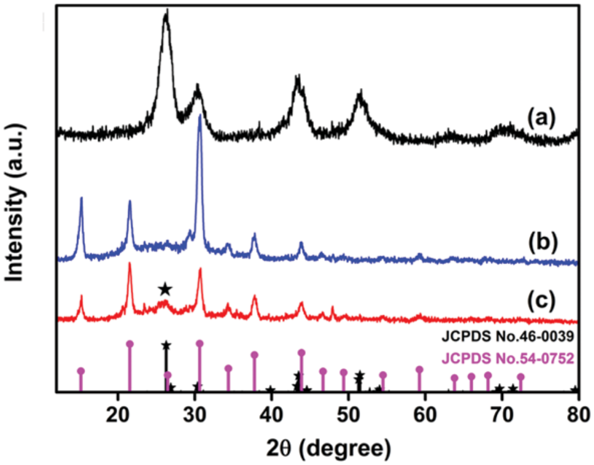

Figure 2.1 XRD patterns of (a) $BaYF_5$:20%Yb,1%Tm UCNPs, (b) $CsPbBr_3$ QDs, (c) $BaYF_5$:20%Yb,1%Tm/$CsPbBr_3$ composite with a ratio of 1: 0.25. The standard data of $BaYF_5$ (JCPDS No. 46-0039) and $CsPbBr_3$ (JCPDS No. 54-0752) are given as references.

Transmission electron microscopy (TEM) images for the system with different densities of $CsPbBr_3$ QDs are displayed in Figure 2.2. According to the TEM image in Figure 2.2a, the as-prepared UCNPs are roughly spherical in shape with an average diameter of about 6 nm (Figure S2.1a). The high-resolution transmission electron microscopy (HRTEM) image shown in the inset of Figure 2.2a highlights that the UCNPs possess a well-defined crystalline structure with lattice fringes of 2.9 Å, which is consistent with the distance of the (330) plane in tetragonal $BaYF_5$. Figure 2.2b shows that the average edge length of $CsPbBr_3$ cube is ~13 nm (Figure S2.1b), and the HRTEM investigation (Figure 2.2b, inset) reveals that the interplanar distance of $CsPbBr_3$ QD is 4.1 Å, corresponding to the (110) crystal facet of the cubic $CsPbBr_3$ phase. These results are in accordance with the XRD patterns.

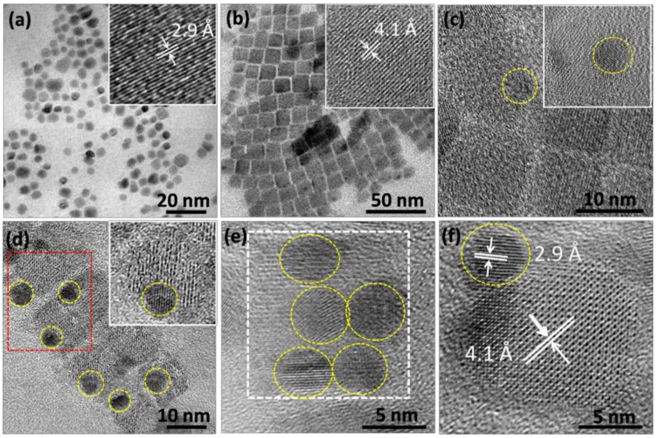

Figure 2.2 TEM images as a function of molar ratios of $BaYF_5$:20%Yb,1%Tm UCNPs to $CsPbBr_3$ QDs; (a) pure $BaYF_5$:20%Yb,1%Tm UCNPs, (b) pure $CsPbBr_3$ QDs, (c)-(e) $BaYF_5$:20%Yb,1%Tm/$CsPbBr_3$ pairs with 1: 8, 1: 1 and 1: 0.125 ratio, respectively, (f) HRTEM image of $BaYF_5$:20%Yb,1%Tm/$CsPbBr_3$ with 1: 1 ratio showing the lattice spacing of both the tetragonal fluoride and cubic perovskite phases. The inserts are the corresponding HRTEM images. The UCNPs are outlined with yellow circles. The corresponding EDS analysis of the red rectangle region is shown in Figure S2.2.

In Figure 2.2c-e, the presence of highly contrasted spots (yellow circles) over the surface of the QD in the composite material can be observed. The reliable attribution of these features to UCPNs rather than lead bromide nanoparticles coexisting along the $CsPbBr_3$ perovskites (Figure S2.4) is supported by the appearance of two different overlapping lattice fringes, which are assigned to the (330) plane of the tetragonal $BaYF_5$ phase and the (110) plane of the cubic $CsPbBr_3$ phase, evidencing the presence of two distinct phases in a single nanocrystalline assembly (Figure 2.2f). Energy-dispersive X-ray (EDS) analysis further reveals the Ba, Y, F, Yb, Tm, Cs, Pb and Br elements are present and assigned to $BaYF_5$:20%Yb,1%Tm UCNPs and $CsPbBr_3$ QDs. (Figure S2.2 and Table S2.1)

The configuration of the composite varies according to the UCNPs/QDs ratio, from multiple UCNPs/single QD for the highest 1: 0.125 ratio to single UCNP/multiple QDs in the case of the lowest 1: 8 ratio. The successful attachment of the UCNP to the surface of the QD may be driven by the electrostatic attraction between oppositely charged (oleate capped UCNPs and oleylammonium capped QDs) nanoparticles (Figure S2.3).[12,34,35] No segregation of phases and a high homogeneity of the UCNPs distribution over the surfaces of the QDs particles are observed in the *in situ* prepared samples, confirming the tight interactions between the UCNPs and the QDs in the formed assemblies (see Figure S2.4a). In contrast, a reference sample obtained by simple physical mixing of $CsPbBr_3$ QDs with UCNPs, showed an inhomogeneous distribution of the UCNPs over the $CsPbBr_3$ QDs and most of the two phases are not closely coupled (Figure S2.4b). The low yield of the UCNPs/$CsPbBr_3$ QDs composite may be due to the surfactants losses after the purifying procedure, which hampers the establishment of strong electrostatic interactions between the two phases.

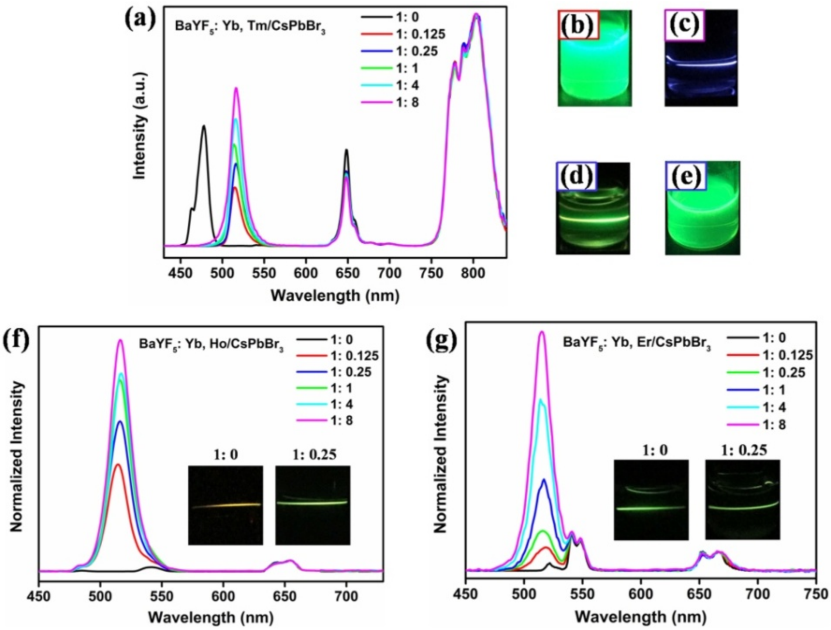

Figure 2.3 Normalized UCL emission spectra of UCNPs/QDs pairs with varying density of $CsPbBr_3$ QDs excited at 975 nm and digital images. (a) $BaYF_5$:20%Yb,1%Tm/$CsPbBr_3$, (b) $CsPbBr_3$ QDs under UV lamp, (c) $BaYF_5$:20%Yb,1%Tm UCNPs under 975 nm laser excitation, (d-e) $BaYF_5$:20%Yb,1%Tm/$CsPbBr_3$ composite with 1: 0.25 ratio under 975 nm laser and UV lamp excitation, respectively, (f-g) $BaYF_5$:20%Yb,2%Ho/$CsPbBr_3$ and $BaYF_5$:20%Yb,2%Er/$CsPbBr_3$ composites, the insets are the digital images.

The UCL spectra of the three UCNPs/QDs pairs under 975 nm laser irradiation are shown in Figure 2.3. To investigate the influence of the donor/acceptor density on the UCL properties, UCNPs/QDs pairs with different molar ratios were synthesized and studied. For the sake of comparison between varying ratios, the UCL spectra of UCNPs/QDs pairs have been normalized to the UCNPs emission peaks which are out of resonance with the QDs absorption bands and therefore related to excited levels not involved in the energy transfer process (803 nm, 654 nm and 666 nm for $BaYF_5$:20%Yb,1%Tm/$CsPbBr_3$, $BaYF_5$:20%Yb,2%Ho/$CsPbBr_3$ and $BaYF_5$:20%Yb,2%Er/$CsPbBr_3$, respectively). As expected, all of the UCL spectra of the UCNPs were significantly altered upon integration with the $CsPbBr_3$ QDs. The intensity of the blue emission band at 478 nm associated with the $^1G_4 \rightarrow {}^3H_6$ transition of Tm^{3+} is dramatically quenched, and this change is accompanied by the appearance of an intense and narrow emission band (full width at half maximum, fwhm, ~19 nm) at ~516 nm, relatable to $CsPbBr_3$ QD emission. The emission spectrum of the $CsPbBr_3$ QD in the composite structure excited at 975 nm almost remained the same with that of the pristine $CsPbBr_3$ QD excited at 466 nm, except for ~1 nm wavelength shift (Figure S2.5). Furthermore, the red emission band of the $^1G_4 \rightarrow {}^3F_4$ transition (Tm^{3+}) is also slightly attenuated (Figure 2.3a). A control experiment on the bare $CsPbBr_3$ QDs confirmed that no green emission could be triggered by NIR excitation. Therefore, the new emission band originates from the $CsPbBr_3$ QDs excited radiatively through PR or nonradiatively through FRET from the UCNPs donors. Similar conclusions can be drawn for the $BaYF_5$:20%Yb,2%Ho/$CsPbBr_3$ and $BaYF_5$:20%Yb,2%Er/$CsPbBr_3$ composites, although the spectral overlap between the blue Ho^{3+}emission band of the $^5F_3 \rightarrow {}^5I_8$ transition at 485 nm (Figure 2.3f) and the Er^{3+} emission band of the $^2H_{11/2} \rightarrow {}^4I_{15/2}$ transition at 522 nm (Figure 2.3g) with the $CsPbBr_3$ QDs luminescence band hampers direct observation of the UCNPs' peak attenuation. Additionally, the relative intensities of $CsPbBr_3$ QDs to UCNPs (acceptors to donors) emission peaks improved substantially as the amount of acceptors was increased.

The most intuitive phenomenon that reflects the difference of the optical properties between the UCNPs and the UCNPs/QDs composites is the UCL colour change. As displayed in Figure 2.3b-e, the UCL colour of the bare

$BaYF_5$:20%Yb,1%Tm is blue (Figure 2.3c), and then changes to intense green for the $BaYF_5$:20%Yb,1%Tm/$CsPbBr_3$ pair under NIR laser excitation (Figure 2.3d), which matches the colour of $CsPbBr_3$ QDs under UV lamp (Figure 2.3b). Similarly, the UCL colour output changed from yellow-green for the pristine $BaYF_5$:20%Yb,2%Ho UCNPs to green for their assembly with $CsPbBr_3$ QDs (Figure 2.3f, insert). From the insert in Figure 2.3g, no change in the colour output between the bare $BaYF_5$:20%Yb,2%Er UCNPs and the $BaYF_5$:20%Yb,2%Er/$CsPbBr_3$ pair under 975 nm irradiation could be observed due to close spectral match between the emission band of $CsPbBr_3$ QDs and the green UCL from $BaYF_5$:20%Yb,2%Er UCNPs.

Figure 2.4 shows the energy level diagrams illustrating the upconversion processes and ET phenomena that may take place in the studied assemblies. As shown, the $^5F_3$ energy level of Ho^{3+}, and the $^1D_2$ and $^1G_4$ energy levels of Tm^{3+} are higher in energy than the conduction band of the $CsPbBr_3$ QDs, thus enabling efficient ET from Ho^{3+} and Tm^{3+} to the QD. On the other hand, while the bandgap (2.4 eV) of $CsPbBr_3$ QDs is very similar in energy to the $^2H_{11/2} \rightarrow {}^4I_{15/2}$ transition of Er^{3+}, ET from the $^2H_{11/2}$ energy level of Er^{3+} to the conduction band of the $CsPbBr_3$ QDs can nonetheless explain the observed QD emission upon NIR excitation.

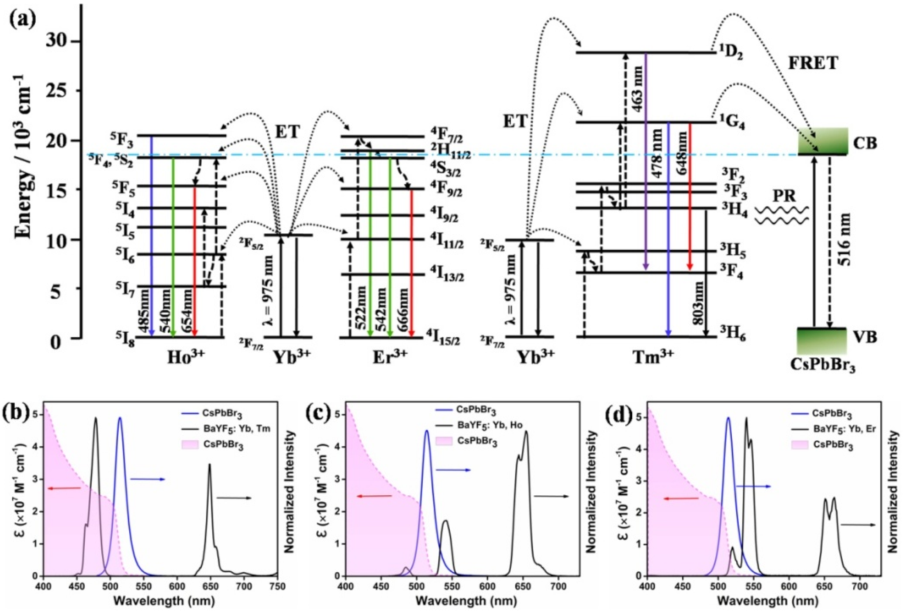

Figure 2.4 (a) Schematic diagrams of energy levels for upconversion processes and the proposed ET mechanism in the BaYF$_5$:20%Yb,x%Ln/CsPbBr$_3$ composites excited at 975 nm: PR and FRET process, (b-d) UCL emission spectra of UCNPs excited at 975 nm, absorption and emission spectra of CsPbBr$_3$ QDs excited at 466 nm.

The high sensitization ability of UCNPs towards CsPbBr$_3$ QDs is attributed to the very high molar extinction coefficient of the QDs (~10^7 M^{-1} cm^{-1}) over a broad wavelength range, leading to a good spectral overlap between the absorption spectra of the QDs acceptors and the emission spectra of the UCNPs donors (Figure 2.4b-4d and Figure S2.6).[34] The close contact of the QDs emitters with the UCNPs sensitizers because of the *in situ* growth method is also beneficial for the sensitization process. These factors enable efficient energy transfer from the UCNPs to the CsPbBr$_3$ QDs either through PR or FRET, which are both dependent on the donor-acceptor resonance and their relative distance according to a squared power or sixth power law, respectively.[22]

The ET efficiency in the UCNPs/QDs pair can be defined as the ratio of the number of emitted photons from UCNPs that are captured by $CsPbBr_3$ QDs to the number of emitted photons from UCNPs with frequencies above the band edges of $CsPbBr_3$ QDs in the bare UCNPs excited at 975 nm under identical conditions.[25] Assuming that the oscillator strength of the lanthanide emitters does not change upon assembly of the UCNPs with the QDs particles and that sensitization of $CsPbBr_3$ QDs is the only additional deactivation channel with respect to the bare donors, the energy transfer efficiency (E) can be estimated based on the quenching of the Ln^{3+} UCL intensity by Eq. (1):

$$E = \frac{I_D - I_{DA}}{I_D}$$

where I_D and I_{DA} are the integrated emissions of UCNPs with frequencies above the band edges of $CsPbBr_3$ QDs in the absence and presence of QDs, respectively. Here, we report the case of the $BaYF_5$:20%Yb,1%Tm/$CsPbBr_3$ pair as the large spectral overlaps of the Ho^{3+} and Er^{3+} emissions with the emission of the $CsPbBr_3$ QDs hamper this quantitative analysis.

As can be found in Figure 2.5, the integrated intensity of the $^1G_4 \rightarrow {}^3H_6$ transition of Tm^{3+} in the presence of $CsPbBr_3$ QDs in the 1: 0.125 ratio drops by ~98%, and is completely lost for the sample with the highest acceptor density, suggesting that the energy transfer efficiency in the $BaYF_5$:20%Yb,1%Tm/$CsPbBr_3$ pair is ~100%. The integrated intensity of the emission band of $CsPbBr_3$ QD showed a roughly linearly increasing trend as the amount of $CsPbBr_3$ QD was increased, as expected when taking into account that thousands of lanthanide donor emitters embedded into UCPNs exist per single semiconductor QD acceptor in such assembly. The almost unitary efficiency of the ET process allows multiple acceptors to be activated simultaneously either radiatively and nonradiatively and the related emission intensity is therefore enhanced according to the total number of emitters. Interestingly, there is a small attenuation for the integrated intensity of the $^1G_4 \rightarrow {}^3F_3$ transition of Tm^{3+}. Since this transition shares the same excited level as the quenched $^1G_4 \rightarrow {}^3H_6$ transition and red light cannot be absorbed by $CsPbBr_3$ QDs, this observation supports the occurrence of FRET in the composite. It is worth mentioning that, the physical mixture of $BaYF_5$:20%Yb,1%Tm UCNPs and $CsPbBr_3$ QDs shows lower ET efficiency than that of the composite as the blue emission of Tm^{3+} does not drop completely and the emission band of $CsPbBr_3$ QD is comparably weaker (Figure S2.7). Additionally, the red emission band of the physical mixture remained nearly unchanged, meaning that the energy transfer is totally dominated by the PR process, in agreement with the results reported by Zheng et al.[25] The difference can be likely related to the more homogenous distribution, the enhanced surface contact and tight assembly between the donor and acceptor units in the composite synthesized by the *in situ* method favouring distance-dependent ET even in solvent dispersion.

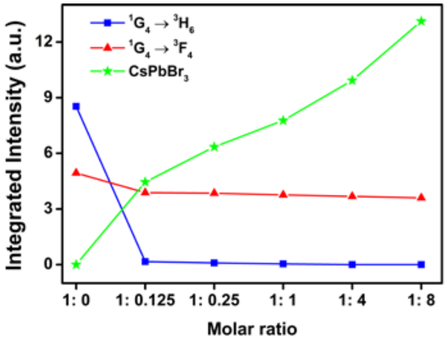

Figure 2.5 Integrated UCL intensities based on Figure 2.3a as a function of the ratio of $BaYF_5$:20%Yb,1%Tm UCNPs to $CsPbBr_3$ QDs in the system under 975 nm laser excitation.

On the basis of these observations, the $CsPbBr_3$ QDs sensitization process is assumed to involve both radiative transfer (PR) and nonradiative transfer (FRET) of excitation energy from the UCNPs. To discriminate the contributions of these two processes, time-resolved photoluminescence measurements have been performed taking into account that only the nonradiative Förster's mechanism will affect the donor decay dynamics, while simple photon emission followed by subsequent reabsorption will not. The FRET efficiency can then be directly experimentally quantified by the lifetimes of the donor in the absence (τ_D) and presence (τ_{DA}) of the acceptor (Eq. S1, Supporting Information), and the results are listed in Table 2.1. The FRET efficiency for the $BaYF_5$:20%Yb,1%Tm/$CsPbBr_3$ pair with 1: 0.25 ratio is calculated to be 35%, which is lower than the overall ET efficiency (~100%) estimated on the basis of steady-state spectral data (Eq. 1 and Figure 2.5) for the blue Tm^{3+} emission band, which is fully resonant with the QD absorption. Assuming that the integrated intensity of the Tm^{3+} red emission is only affected by quenching through FRET (as no photon at 648 nm can be reabsorbed by the QDs), the degree of its decrease (~22%) with respect to the initial signal (Figure 2.5) can be considered to be proportional to the FRET efficiency and is comparable to the 35% value retrieved through temporal dynamics, taking into account experimental errors. The above considerations confirm that both PR and FRET are occurring in the system of the $BaYF_5$:20%Yb,1%Tm/$CsPbBr_3$ composite, while PR dominates. Similar considerations can be done for the other composites with $BaYF_5$:20%Yb,2%Ho and $BaYF_5$:20%Yb,2%Er on the basis of the donor decay dynamics. The lower FRET efficiency of Er^{3+} to QDs in the composite can be explained on the basis of the lower value of the overlap integral J between the emission band of the donor and the absorption band of the acceptor, as reported in Table 2.1 (see SI for details).

Table 2.1 Lifetime values of the donor in the absence (τ_D) and presence (τ_{DA}) of the acceptor and retrieved values of FRET efficiency (η). The lifetimes were measured for the

$^1G_4 \rightarrow {}^3H_6$ transition in Tm^{3+}, the $^5F_3 \rightarrow {}^5I_8$ transition in Ho^{3+} and the $^2H_{11/2} \rightarrow {}^4I_{15/2}$ transition in Er^{3+} for the composites with 1: 0.25 ratio, to ensure acceptable signal to noise ratios for the attenuated transitions. Overlap integrals J (λ) and Förster radii (R_0) of the FRET systems are also reported (assuming a random orientation of donor and acceptor dipoles, κ^2 was set to 2/3, while κ^2 = 4 was also used to allow comparison across the literature).

Donor	τ_D (μs)	τ_{DA} (μs)	η (%)	J (M^{-1} cm^{-1} nm^4)	R_0 (nm) κ^2 = 2/3	R_0 (nm) κ^2=4
$BaYF_5$:20%Yb,1%Tm	9.4	6.1	35	1.34×10^{18}	3.50	4.71
$BaYF_5$:20%Yb,2%Ho	9.0	7.2	20	1.41×10^{18}	3.52	4.75
$BaYF_5$: 20%Yb,2%Er	28.9	24.5	15	5.30×10^{17}	2.99	4.04

The FRET efficiency is directly dependent on the relative spatial coordinates of the donor and the acceptor, in particular the distance r and the relative orientation of the associated oscillating dipoles.[36] The latter parameter is expressed by the variable κ^2 which may assume values from 0 to 4 on going from fully orthogonal to collinear donor and acceptor dipoles, respectively. Since a definite orientation of the emitting and accepting oscillators in the studied system cannot be established, we take the average κ^2 = 2/3, referred to a random spatial distribution of dipoles, as the most reliable value to calculate the Förster radius (R_0), that is, the distance at which energy transfer efficiency is 50% (Eq. S2, see Supporting Information for a detailed discussion). Overestimated R_0 values for κ^2 = 4 have also been calculated for comparison with literature reports (*vide infra*). It can be seen in Table 2.1 that the three pairs have relatively high R_0 values, which are consistent with typical values for FRET pairs when QDs act as FRET acceptors.[31] The R_0 value of the $BaYF_5$:20%Yb,2%Er/$CsPbBr_3$ pair is the lowest, as a consequence of the lower value of the spectral overlap integral J (see Figure S2.6 for details). For the $BaYF_5$:20%Yb,1%Tm/$CsPbBr_3$ FRET pair, the Förster distance is up to 4.71 nm, which is considerably larger than that of the $NaYF_4$:20%Yb,2%Er/CdSe pair (1.5 nm) reported by Bednarkiewicz et al.,[13] and of the $LiYF_4$:25%Yb,0.5%Tm/$CuInS_2$ pair (1.92 nm) by Marin et al.,[22] calculated by taking into account the maximum κ^2 value of 4. The remarkably larger Förster distances calculated here are a result of the much higher molar extinction coefficient of the $CsPbBr_3$ QDs (ε_{478} = ~2×10^7 M^{-1} cm^{-1}) as compared to CdSe QDs (ε_{478} = ~1.0×10^6 M^{-1} cm^{-1}) and $CuInS_2$ QDs (ε_{478} = ~1.0×10^5 M^{-1} cm^{-1}), thus contributing to a larger overlap integral. The Förster energy transfer rate constants (κ_T) of the three studied pairs $BaYF_5$:20%Yb,1%Tm/$CsPbBr_3$, $BaYF_5$:20%Yb,2%Ho/$CsPbBr_3$ and $BaYF_5$:20%Yb,2%Er/$CsPbBr_3$ are estimated to be 2.7×10^5 s^{-1}, 2.9×10^5 s^{-1} and 3.4×10^4 s^{-1}, respectively, based on the donor lifetime in the absence of an acceptor, the Förster distance, and the average donor/acceptor separation taken as the distance from the centre of the UCNPs to the surface of the QDs (Eq. S4, Supporting Information). The three FRET rates are significantly slower than the excited-state decay rate of $CsPbBr_3$ QDs ($1/\tau = 1.2 \times 10^8\,s^{-1}$, τ = 8.6 ns).[37] Therefore, the energy can be repeatedly transferred from nearby UCNPs donors to $CsPbBr_3$ QDs acceptors which then relax to the ground state during the decay time of the Ln^{3+} emission.[38] This dynamics leads to apparent QDs' exciton lifetimes much longer than usual for bare QDs as a result of the slow feeding process through the long-lived lanthanide emitters.[25]

Beyond the assessment of FRET average parameters as reported in Table 2.1, it has to be remarked that these are the result of the combination of the ET dynamics of multiple non-equal donor-acceptor pairs in the assembly. As a matter of fact, in the studied systems, the donor units are the emitting lanthanide ions (Tm^{3+}, Ho^{3+} and Er^{3+}) that are supposedly homogeneously distributed into the UCNPs and therefore lie at various distances from the surface of the QD acceptor depending on the size of the nanoparticle. Predictions of the FRET efficiency on the dependence of the distance r between the donor/acceptor pair according to the Förster's model (Eq. S5) are reported in Figure S2.8. It can be deducted that FRET efficiency values can reach ~70% for the Tm^{3+} and Ho^{3+} to $CsPbBr_3$ QDs, and ~50% for Er^{3+} to $CsPbBr_3$ QDs when the lanthanide ions are located in the centre of the UCNPs, while lanthanide ions closer to the acceptors will exhibit higher FRET efficiencies. These results suggest that higher nonradiative energy transfer from the UCNPs to $CsPbBr_3$ QDs can be achieved for smaller donor sizes.

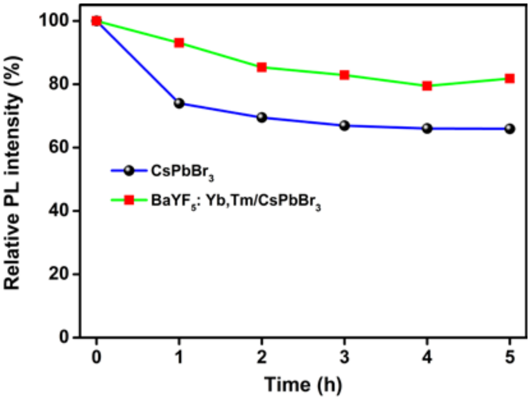

Figure 2.6 Photostability tests of the $CsPbBr_3$ QDs under a 365 nm UV lamp (8 W) and $BaYF_5$:20%Yb,1%Tm/$CsPbBr_3$ pair under a 975 nm diode laser (400 mW) in ambient conditions. Time interval: 1 hour. The emission intensities were normalized to 100% at t = 0 h.

In addition to the high ET efficiency, stability of the system is also an important factor. The photostabilities of the bare $CsPbBr_3$ QDs and the

$BaYF_5$:20%Yb,1%Tm/$CsPbBr_3$ composite solutions in terms of their photoluminescence (PL) quenching were measured under exposure to UV lamp light and 975 nm laser light, respectively (Figure 2.6). The PL intensity of the $CsPbBr_3$ QDs under UV light exposure decayed seriously in the first hour and then experienced a steady output with 65.9% of the initial PL intensity after 5 h irradiation. In contrast, after the $CsPbBr_3$ QDs were conjugated to UCNPs, the sample showed a much less steep PL intensity drop during 5 h illumination period with lower energy NIR photons at 975 nm and more than 80% of its original PL intensity was preserved. Furthermore, the $BaYF_5$:20%Yb,1%Tm/$CsPbBr_3$ composite film also exhibited excellent thermal stability (Figure S2.9a). After 5 h of thermal treatment at 80 °C, the PL intensity was enhanced by 42%. Conversely, low PL intensity (68%) was left in the pristine $CsPbBr_3$ QDs. However, both the pristine $CsPbBr_3$ QDs and the $BaYF_5$:20%Yb,1%Tm/$CsPbBr_3$ composite showed poor humidity stability, while more than 80% of the initial PL intensities can recover after drying in the air (Figure S2.9b). The results suggest that the studied nanocomposites are promising candidates for the fabrication of photonic devices.

2.4 Conclusions

In summary, we have studied three fascinating nanoheterostructures ($BaYF_5$:20%Yb,1%Tm/$CsPbBr_3$, $BaYF_5$:20%Yb,2%Ho/$CsPbBr_3$, $BaYF_5$:20%Yb,2%Er/$CsPbBr_3$) prepared by an *in situ* growth method, where highly intense green emission from all-inorganic perovskite QDs can be triggered by NIR irradiation thanks to efficient sensitization from lanthanide-based UCNPs. The small-sized UCNPs donors tightly assembled onto the surface of $CsPbBr_3$ QD can ensure efficient donor properties in the composite. On the other hand, the extremely high molar extinction coefficients and the large spectral overlap with UCNPs emission make $CsPbBr_3$ QDs perfect candidates as ET acceptors. As a result, both PR and FRET processes are involved in the energy transfer mechanisms, contributing to an overall 100% energy transfer efficiency and allowing the intensity of the emission to increase almost linearly with the amount of acceptor emitters in the system. Photoluminescence steady-state and time-resolved studies indicate that the contribution of the FRET mechanism to the sensitization process is relevant and in the range 15 – 35% for the three investigated systems. These results are consistent with estimations made by implementing the Forster's model, which allowed to retrieve R_0 values (ranging from 3.52 to 2.99 nm) considerably larger than those so far reported for similar UCNPs/QDs donors/acceptors pairs. The FRET efficiency in the composite material is limited by the spatial distribution of donor units (i.e. the lanthanide ions) within the hosting UCNPs. This suggests that further improvements to the structural design of this system are still needed to achieve control of the donor/acceptor separation distance and ultimately favor sensitization via FRET than via PR as the latter can be more easily subjected to competitive quenching phenomena. To this end we will address the synthesis of core/shell structures or resort to the use of short-length organic linkers to enhance the FRET efficiency. Nonetheless, the investigated UCNPs/$CsPbBr_3$ QDs ET assembly, which shows high thermal and photostability, opens new opportunities toward the development of efficient donor/acceptor pairs for wide applications in areas such as bioimaging, photodynamic therapy and photovoltaics.

References

(1) Cho, H.; Wolf, C.; Kim, J. S.; Yun, H. J.; Bae, J. S.; Kim, H.; Heo, J. M.; Ahn, S.; Lee, T. W. High-Efficiency Solution-Processed Inorganic Metal Halide Perovskite Light-Emitting Diodes. *Adv. Mater.* **2017**, *29*, 1700579.
(2) Pan, G.; Bai, X.; Yang, D.; Chen, X.; Jing, P.; Qu, S.; Zhang, L.; Zhou, D.; Zhu, J.; Xu, W.; Dong, B.; Song, H. Doping Lanthanide into Perovskite Nanocrystals: Highly Improved and Expanded Optical Properties. *Nano Lett.* **2017**, *17*, 8005-8011.
(3) Yadav, P.; Alotaibi, M. H.; Arora, N.; Dar, M. I.; Zakeeruddin, S. M.; Grätzel, M. Influence of the Nature of A Cation on Dynamics of Charge Transfer Processes in Perovskite Solar Cells. *Adv. Funct. Mater.* **2018**, *28*, 1706073.
(4) Mariotti, S.; Hutter, O. S.; Phillips, L. J.; Yates, P. J.; Kundu, B.; Durose, K. Stability and Performance of $CsPbI_2Br$ Thin Films and Solar Cell Devices. *ACS Appl. Mat. Interfaces.* **2018**, *10*, 3750-3760.
(5) Shoaib, M.; Zhang, X.; Wang, X.; Zhou, H.; Xu, T.; Wang, X.; Hu, X.; Liu, H.; Fan, X.; Zheng, W.; Yang, T.; Yang, S.; Zhang, Q.; Zhu, X.; Sun, L.; Pan, A. Directional Growth of Ultralong $CsPbBr_3$ Perovskite Nanowires for High-Performance Photodetectors. *J. Am. Chem. Soc.* **2017**, *139*, 15592-15595.
(6) Ramasamy, P.; Lim, D.-H.; Kim, B.; Lee, S.-H.; Lee, M.-S.; Lee, J.-S. All-Inorganic Cesium Lead Halide Perovskite Nanocrystals for Photodetector Applications. *Chem. Commun.* **2016**, *52*, 2067-2070.
(7) Clarke, C.; Liu, D.; Wang, F.; Liu, Y.; Chen, C.; Ton-That, C.; Xu, X.; Jin, D. Large-Scale Dewetting Assembly of Gold Nanoparticles for Plasmonic Enhanced Upconversion Nanoparticles. *Nanoscale* **2018**, *10*, 6270-6276.
(8) Wisser, M. D.; Fischer, S.; Siefe, C.; Alivisatos, A. P.; Salleo, A.; Dionne, J. A. Improving Quantum Yield of Upconverting Nanoparticles in Aqueous Media via Emission Sensitization. *Nano Lett.* **2018**, *18*, 2689-2695.
(9) Wang, Y.; Si, B.; Lu, S.; Liu, E.; Hu, X.; Fan, J. Near-Infrared Excitation of CdTe Quantum Dots Based on Fluorescence Resonance Energy Transfer and Their Use as Fluorescent Sensors. *Sens. Actuators B, Chem.* **2017**, *246*, 127-135.
(10) Balaji, R.; Kumar, S.; Reddy, K. L.; Sharma, V.; Bhattacharyya, K.; Krishnan, V. Near-Infrared Driven Photocatalytic Performance of Lanthanide-Doped $NaYF_4$@CdS Core-Shell Nanostructures with Enhanced Upconversion Properties. *J. Alloy. Compd.* **2017**, *724*, 481-491.
(11) Tou, M.; Mei, Y.; Bai, S.; Luo, Z.; Zhang, Y.; Li, Z. Depositing CdS Nanoclusters on Carbon-Modified $NaYF_4$:Yb,Tm Upconversion Nanocrystals for NIR-Light Enhanced Photocatalysis. *Nanoscale* **2016**, *8*, 553-562.
(12) Yan, C.; Dadvand, A.; Rosei, F.; Perepichka, D. F. Near-IR Photoresponse in New Up-Converting CdSe/$NaYF_4$:Yb,Er Nanoheterostructures. *J. Am. Chem. Soc.* **2010**, *132*, 8868-8869.
(13) Bednarkiewicz, A.; Nyk, M.; Samoc, M.; Strek, W. Up-conversion FRET from Er^{3+},Yb^{3+}:$NaYF_4$ Nanophosphor to CdSe Quantum Dots. *J. Phys. Chem. C* **2010**, *114*, 17535-17541.

(14) Xu, S.; Xu, S.; Zhu, Y.; Xu, W.; Zhou, P.; Zhou, C.; Dong, B.; Song, H. A Novel Upconversion, Fluorescence Resonance Energy Transfer Biosensor (FRET) for Sensitive Detection of Lead Ions in Human Serum. *Nanoscale* **2014**, *6*, 12573-12579.
(15) Antoniak, M.; Wawrzynczyk, D.; Zareba, J. K.; Samoc, M.; Nyk, M. Spectrally Resolved Two-photon Absorption Properties and Switching of Multi-Modal Luminescence of $NaYF_4$:Yb,Er/CdSe Hybrid Nanostructures. *J. Mater. Chem. C.* **2018**, *6*, 5949-5956.
(16) Wang, W.; Li, Y.; Kang, Z.; Wang, F.; Jimmy, C. Y. A NIR-Driven Photocatalyst Based on α-$NaYF_4$:Yb,Tm@TiO_2 Core-Shell Structure Supported on Reduced Graphene Oxide. *Appl. Catal. B: Environ.* **2016**, *182*, 184-192.
(17) Braz, A. K.; Moura, D. S.; Gomes, A. S.; Ohulchanskyy, T. Y.; Chen, G.; Liu, M.; Damasco, J.; de Araujo, R. E.; Prasad, P. N. TiO_2-Coated Fluoride Nanoparticles for Dental Multimodal Optical Imaging. *J. Biophotonics* **2018**, *11*, e201700029
(18) Wang, M.; Hou, Z.; Al Kheraif, A. A.; Xing, B.; Lin, J. Mini Review of TiO_2-Based Multifunctional Nanocomposites for Near-Infrared Light-Responsive Phototherapy. *Adv. Healthcare Mater.* **2018**, *7*, 1800351.
(19) Guo, X.; Song, W.; Chen, C.; Di, W.; Qin, W. Near-Infrared Photocatalysis of β-$NaYF_4$:Yb^{3+},Tm^{3+}@ZnO Composites. *Phys. Chem. Chem. Phys.* **2013**, *15*, 14681-14688.
(20) Guo, X.; Chen, C.; Yin, S.; Song, W.; Shi, F.; Qin, W. The Effect of Phase Structures on the Near-Infrared Photocatalytic Activity of $NaYF_4$:Yb^{3+},Tm^{3+}/ZnO Nanocomposites. *J. Photochem. Photobiol. A: Chem.* **2015**, *297*, 14-19.
(21) Tou, M.; Luo, Z.; Bai, S.; Liu, F.; Chai, Q.; Li, S.; Li, Z. Sequential Coating Upconversion $NaYF_4$:Yb,Tm Nanocrystals with SiO_2 and ZnO Layers for NIR-Driven Photocatalytic and Antibacterial Applications. *Mater. Sci. Eng., C.* **2017**, *70*, 1141-1148.
(22) Marin, R.; Labrador-Paéz, L.; Skripka, A.; Haro-González, P.; Benayas, A.; Canton, P.; Jaque, D.; Vetrone, F. Upconverting Nanoparticle to Quantum Dot Förster Resonance Energy Transfer: Increasing the Efficiency through Donor Design. *ACS Photonics* **2018**, *5*, 2261-2270.
(23) Swarnkar, A.; Chulliyil, R.; Ravi, V. K.; Irfanullah, M.; Chowdhury, A.; Nag, A. Colloidal $CsPbBr_3$ Perovskite Nanocrystals: Luminescence Beyond Traditional Quantum Dots. *Angew. Chem. Int. Ed.* **2015**, *127*, 15644-15648.
(24) Francés-Soriano, L.; Gonzalez-Carrero, S.; Navarro-Raga, E.; Galian, R. E.; González-Béjar, M.; Pérez-Prieto, J. Efficient Cementing of $CH_3NH_3PbBr_3$ Nanoparticles to Upconversion Nanoparticles Visualized by Confocal Microscopy. *Adv. Funct. Mater.* **2016**, *26*, 5131-5138.
(25) Zheng, W.; Huang, P.; Gong, Z.; Tu, D.; Xu, J.; Zou, Q.; Li, R.; You, W.; Bünzli, J.-C. G.; Chen, X. Near-Infrared-Triggered Photon Upconversion Tuning in All-Inorganic Cesium Lead Halide Perovskite Quantum Dots. *Nat. Commun.* **2018**, *9*, 3462.
(26) Protesescu, L.; Yakunin, S.; Bodnarchuk, M. I.; Krieg, F.; Caputo, R.; Hendon, C. H.; Yang, R. X.; Walsh, A.; Kovalenko, M. V. Nanocrystals of Cesium Lead Halide Perovskites ($CsPbX_3$, X= Cl, Br, and I): Novel Optoelectronic Materials Showing Bright Emission with Wide Color Gamut. *Nano Lett.* **2015**, *15*, 3692-3696.
(27) Zhang, X.; Wang, Q.; Jin, Z.; Zhang, J.; Liu, S. F. Stable Ultra-Fast Broad-Bandwidth Photodetectors Based on α-$CsPbI_3$ Perovskite and $NaYF_4$:Yb,Er Quantum Dots. *Nanoscale* **2017**, *9*, 6278-6285.

(28) Menke, S. M.; Holmes, R. J. Exciton Diffusion in Organic Photovoltaic Cells. *Energy Environ. Sci.* **2014,** *7*, 499-512.

(29) Riuttamäki, T.; Hyppänen, I.; Kankare, J.; Soukka, T. Decrease in Luminescence Lifetime Indicating Nonradiative Energy Transfer from Upconverting Phosphors to Fluorescent Acceptors in Aqueous Suspensions. *J. Phys. Chem. C* **2011**, *115*, 17736−17742.

(30) Zhao, J.; Lu, Z.; Yin, Y.; McRae, C.; Piper, J. A.; Dawes, J. M.; Jin, D.; Goldys, E. M. Upconversion Luminescence with Tunable Lifetime in $NaYF_4$:Yb,Er Nanocrystals: Role of Nanocrystal Size. *Nanoscale* **2013**, *5*, 944-952.

(31) Liu, J.; Chen, G.; Hao, S.; Yang, C. Sub-6 nm Monodisperse Hexagonal Core/Shell $NaGdF_4$ Nanocrystals with Enhanced Upconversion Photoluminescence. *Nanoscale* **2017**, *9*, 91-98.

(32) Gargas, D. J.; Chan, E. M.; Ostrowski, A. D.; Aloni, S.; Altoe, M. V. P.; Barnard, E. S.; Sanii, B.; Urban, J. J.; Milliron, D. J.; Cohen, B. E. Engineering Bright Sub-10-nm Upconverting Nanocrystals for Single-Molecule Imaging. *Nat. Nanotechnol.* **2014**, *9*, 300-305.

(33) Geißler, D.; Hildebrandt, N. Recent Developments in Förster Resonance Energy Transfer (FRET) Diagnostics Using Quantum Dots. *Anal. Bioanal. Chem.* **2016**, *408*, 4475-4483.

(34) De Roo, J.; Ibáñez, M.; Geiregat, P.; Nedelcu, G.; Walravens, W.; Maes, J.; Martins, J. C.; Van Driessche, I.; Kovalenko, M. V.; Hens, Z. Highly Dynamic Ligand Binding and Light Absorption Coefficient of Cesium Lead Bromide Perovskite Nanocrystals. *ACS Nano* **2016**, *10*, 2071-2081.

(35) Reineck, P.; Gibson, B. C. Near-Infrared Fluorescent Nanomaterials for Bioimaging and Sensing. *Adv. Opt. Mater.* **2017**, *5*, 1600446

(36) Hildebrandt, N.; Spillmann, C. M.; Algar, W. R.; Pons, T.; Stewart, M. H.; Oh, E.; Susumu, K.; Diaz, S. A.; Delehanty, J. B.; Medintz, I. L. Energy Transfer with Semiconductor Quantum Dot Bioconjugates: A Versatile Platform for Biosensing, Energy Harvesting, and Other Developing Applications. *Chem. Rev.* **2016**, *117*, 536-711.

(37) Deng, R.; Wang, J.; Chen, R.; Huang, W.; Liu, X. Enabling Förster Resonance Energy Transfer from Large Nanocrystals through Energy Migration. *J. Am. Chem. Soc.* **2016**, *138*, 15972-15979.

(38) Algar, W. R.; Wegner, D.; Huston, A. L.; Blanco-Canosa, J. B.; Stewart, M. H.; Armstrong, A.; Dawson, P. E.; Hildebrandt, N.; Medintz, I. L. Quantum Dots as Simultaneous Acceptors and Donors in Time-Gated Förster Resonance Energy Transfer Relays: Characterization and Biosensing. *J. Am. Chem. Soc.* **2012**, *134*, 1876-1891

.

Supporting Information for Chapter 2

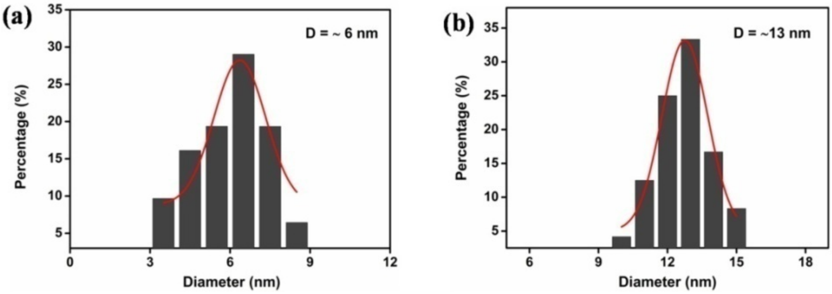

Figure S2.1 Size distribution histograms of (a) $BaYF_5$:20%Yb,1%Tm UCNPs and (b) $CsPbBr_3$ QDs.

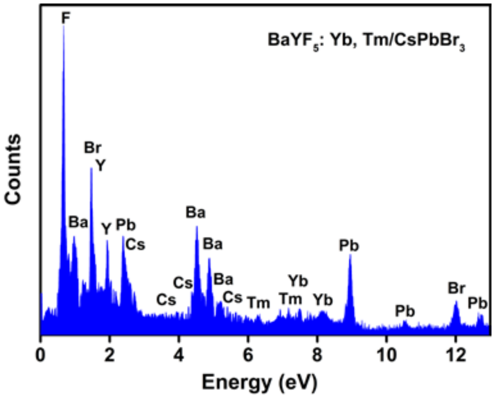

Figure S2.2 EDS spectrum of the $BaYF_5$:20%Yb,1%Tm/$CsPbBr_3$ composite with 1: 1 ratio. The results are summarized in the following Table.

Table S2.1 EDS elemental analysis of the $BaYF_5$:20%Yb,1%Tm/$CsPbBr_3$ composite with 1: 1 ratio, indicating the existence of Ba, Y, F, Yb, Tm, Cs, Pb and Br elements which are assigned to $BaYF_5$:20%Yb,1%Tm UCNPs and $CsPbBr_3$ QDs. The value of lanthanide does not represent the actual composition because of instrument limitations.

Element	Ba	Y	F	Yb	Tm	Cs	Pb	Br
At %	8.02	6.4	35.45	0.95	0.42	8.26	9.88	30.63

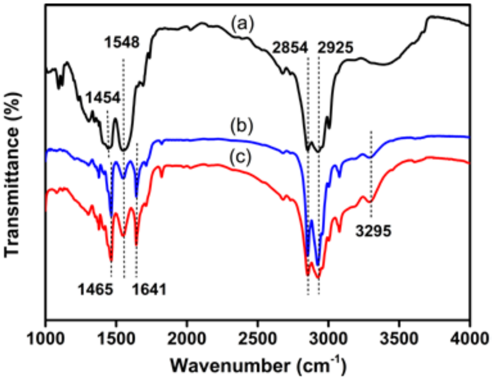

Figure S2.3 FT-IR spectra of (a) $BaYF_5$:20%Yb,1%Tm UCNPs, (b) $CsPbBr_3$ QDs and (c) $BaYF_5$:20%Yb,1%Tm/$CsPbBr_3$ composite with 1: 0.25 ratio.

FT-IR spectra evidence a strong resemblance of the transmission bands appearing at 2925 and 2854 cm^{-1}, which are assigned to the asymmetric and symmetric stretching vibrations of methylene groups (–CH_2), respectively.[1] The bands at 1454 cm^{-1} in the spectrum of UCNPs (a) and 1548 cm^{-1} in the three spectra are attributed to the symmetric and antisymmetric stretching of the carboxylate (COO–), respectively. The result indicates that OA molecules were chemisorbed onto the UCNPs as a carboxylate.[2] In the spectra of $CsPbBr_3$ QDs (b) and $BaYF_5$:20%Yb,1%Tm/$CsPbBr_3$ composite (c), the characteristic peaks of OLA are observed at 1465, 1641, and 3295 cm^{-1}, which are associated with –C–H bending, C=O stretching and N–H stretching, respectively.[3–4] It is interesting to notice that the very broad shoulder at around 3400 cm^{-1}, related to the OH groups of OA in the spectrum of UCNPs (a), completely disappeared in the spectrum of the composite (c), indicating a thoroughly deprotonation of the carboxylic group in the presence of OLA, to form oleate.

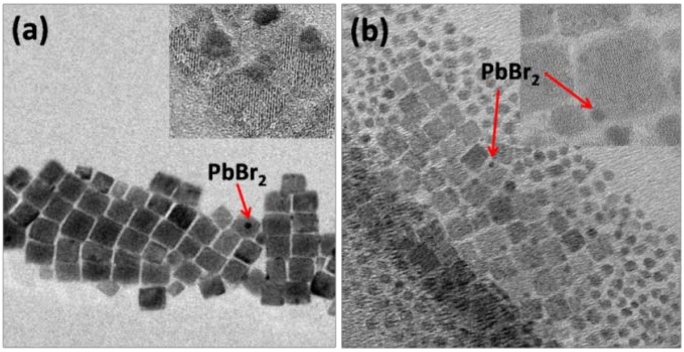

Figure S2.4 TEM images of (a) $BaYF_5$:20%Yb,1%Tm/$CsPbBr_3$ composite with 1: 1 ratio synthesized through the *in situ* growth method, (b) mixture of $BaYF_5$:20%Yb,1%Tm UCNPs and $CsPbBr_3$ QDs with 1: 1 ratio assembled by physical mixing. The red arrows indicate small black dots with poor crystallinity of about 2 nm which are attributed to $PbBr_2$ nanoparticles (coexisting along the $CsPbBr_3$ QDs),[5] which can be easily distinguished from UCNPs by different sizes and crystallinity.

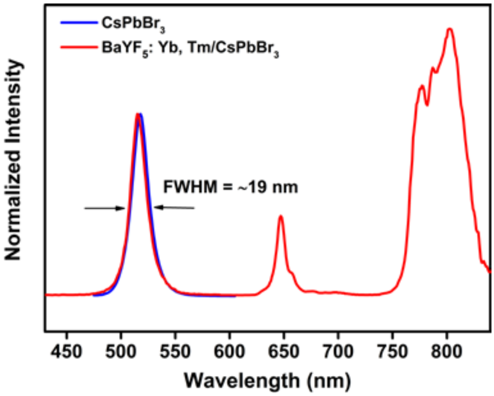

Figure S2.5 Emission spectrum of the pristine $CsPbBr_3$ QDs excited at 466 nm (blue line), UCL emission spectrum of the $BaYF_5$:20%Yb,1%Tm/$CsPbBr_3$ QDs composite (red line) excited at 975 nm.

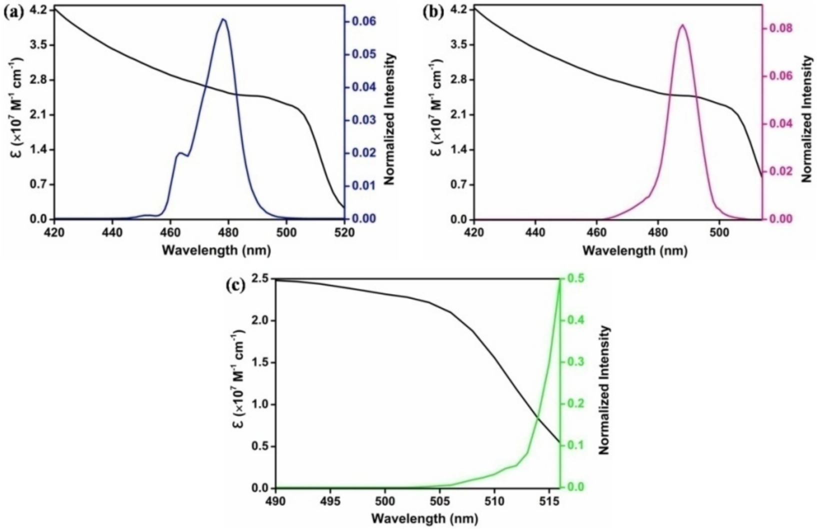

Figure S2.6 Absorption spectra of $CsPbBr_3$ QDs (black line) and normalized UCL emission spectra of (a) $BaYF_5$:20%Yb,1%Tm (blue line), (b) $BaYF_5$:20%Yb,2%Ho (pink line), and (c) $BaYF_5$:20%Yb,2%Er (green line), which are used to calculate the overlap integral (J). There is partial spectral overlap between the $BaYF_5$:20%Yb,2%Er FRET donor and the $CsPbBr_3$ acceptor.

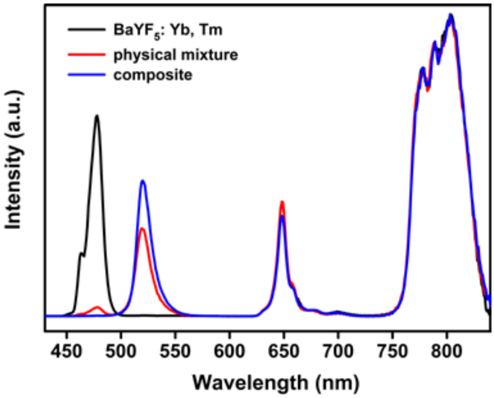

Figure S2.7 UCL emission spectra of $BaYF_5$:20%Yb,1%Tm UCNPs (black line), $BaYF_5$:Yb,Tm/$CsPbBr_3$ QDs composite with 1: 1 ratio (blue line), physical mixture of $BaYF_5$:Yb,Tm and $CsPbBr_3$ QDs with the same composite ratio (red line).

Förster resonance energy transfer

The FRET efficiency can be experimentally estimated based on the corresponding decay lifetimes:[6]

$$\eta = 1 - \frac{\tau_{DA}}{\tau_D} \qquad \text{(S2.1)}$$

where τ_D and τ_{DA} are the luminescence lifetimes of the donor in the absence and presence of the acceptor, respectively.

Efficient FRET between UCNPs donors and $CsPbBr_3$ QDs acceptors will only take place at short distances.[7] The distance at which energy transfer efficiency is 50%, defined as the Förster radius (R_0), is given by:[8]

$$R_0 = \left[\frac{9(In10)\kappa^2 \phi_D}{128\pi^5 N_A n^4} J \right]^{1/6} \qquad \text{(S2.2)}$$

where κ^2 is the orientation factor of the interacting dipoles, Φ_D is the luminescence quantum yield of the donor in the absence of the acceptor, n is the average refractive index of the medium, N_A is the Avogadro constant, and J is a spectral overlap integral (M^{-1} cm^{-1} nm^4). The integral J can be defined as:[8]

$$J(\lambda) = \int F_D(\lambda)\varepsilon_A \lambda^4 \mathrm{d}\lambda \tag{S2.3}$$

where $F_D(\lambda)$ is the UCL spectrum of the donor normalized to unit area ($\int F_D(\lambda)\, d\lambda = 1$), and $\mathcal{E}_A$ is the acceptor's molar extinction coefficient (M^{-1} cm^{-1}) as a function of the wavelength λ (nm), as shown in Figure S2.4. Herein, the value of 2/3 was used for κ^2 (assuming a random orientation of donor and acceptor dipoles), while $\kappa^2 = 4$ was also used to allow comparison across the literature. The refractive index of the medium was taken as 1.44, an average value between 1.427 (cyclohexane) and 1.459 (OA). The reported PLQY of the UCNPs donor (Φ_D) was in the range of 0.005 – 0.1%,[9] while Φ_D = 0.01% was also assumed for the UCNPs to allow comparison across the literature.[10,11]

The rate of FRET (κ_T) is calculated from the lifetime of the donor in absence of the acceptor, Förster distance, and the average UCNPs-QDs separation distance, according to Eq. (S4):[12]

$$\kappa_T = \frac{1}{\tau_D} \times \left(\frac{R_0}{\mathrm{r}}\right)^6 \tag{S2.4}$$

Taking into account an average separation distance between the donor and the acceptor of 3 nm (Ln ions in the center of the particle) and τ_D values reported in Table 2.1 in the manuscript (9.4 µs, 9.0 µs and 28.9 µs for Tm^{3+}, Ho^{3+} and Er^{3+}, respectively), it is possible to retrieve κ_T values of 2.7×10^5 s^{-1}, 2.9×10^5 s^{-1} and 3.4×10^4 s^{-1} for the FRET processes from the Tm^{3+}, Ho^{3+} and Er^{3+} donors, respectively.

It has however to be remarked that in the studied systems the donor units are the emitting lanthanide ions (Tm^{3+}, Ho^{3+} and Er^{3+}) that are homogeneously distributed into the UCNPs and therefore lie at various distances from the surface of the QDs acceptor depending on the size of the nanoparticle. According to the Förster's model, predictions of the FRET efficiency on dependence of the distance r between the donor/acceptor pair, can be quantified by the following equation:[7]

$$\eta = \frac{R_0^6}{R_0^6 + \mathrm{r}^6} \tag{S2.5}$$

As shown in Figure S2.6, the FRET efficiencies estimated by the Förster model (taking the reliable value of $\kappa^2 = 2/3$) can reach ~70% for the Tm^{3+} and Ho^{3+} to $CsPbBr_3$ QDs, and ~50% for Er^{3+} to $CsPbBr_3$ QDs when the Ln^{3+} are located in the center of the UCNPs. Ln^{3+} closer to the acceptors will exhibit higher FRET efficiencies. These results suggest that higher energy transfer from the UCNPs to the $CsPbBr_3$ QDs may be achieved for smaller donor sizes.

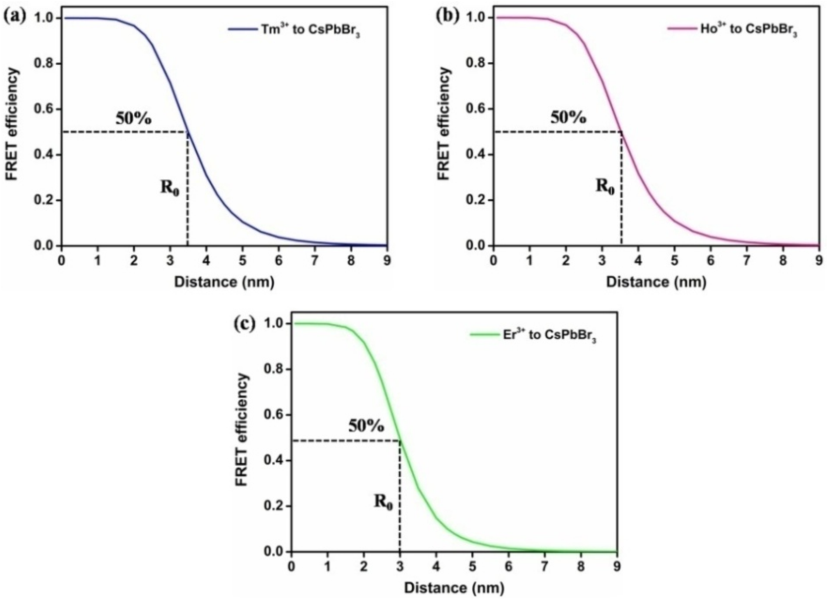

Figure S2.8 FRET efficiency as a function of separation distance between the donor/acceptor pair: (a) Tm^{3+} to $CsPbBr_3$ QDs, (b) Ho^{3+} to $CsPbBr_3$ QDs and (c) Er^{3+} to $CsPbBr_3$ QDs.

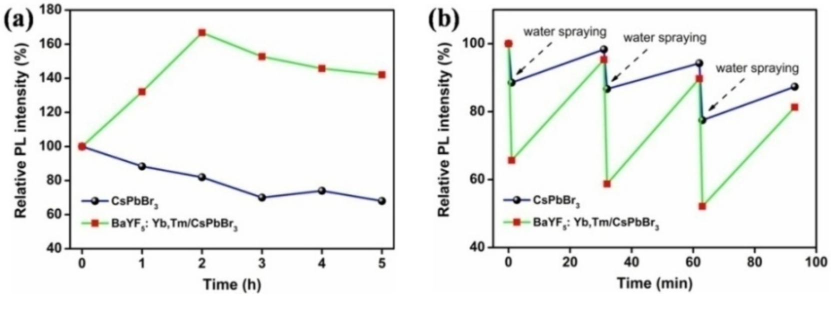

Figure S2.9 (a) Thermal stability tests of the $CsPbBr_3$ QDs and $BaYF_5$:20%Yb,1%Tm/$CsPbBr_3$ composite films versus thermal treatment time at 80 °C under ambient pressure, (b) humidity stability tests. Exposure to moisture was realized by spraying deionized water onto the sample' surface.

Interestingly, the $BaYF_5$:20%Yb,1%Tm/$CsPbBr_3$ composite sample exhibited a sharp increase in PL intensity in the first two hours upon thermal annealing at 80 °C followed by a decrease, while the PL intensity was still enhanced by 42% after 5 h thermal treatment. On the contrary, an obvious thermal quenching of PL intensity was observed in the pristine $CsPbBr_3$ QDs sample and only 68% of the initial signal was left. It was also found that both the pristine $CsPbBr_3$ QDs and the $BaYF_5$:20%Yb,1%Tm/$CsPbBr_3$ composite displayed a slight red shift (1 – 2 nm) of emission, suggesting that the $CsPbBr_3$ QDs were growing during the thermal annealing process. Similar PL phenomena were also observed in the bare $CsPbBr_3$ QDs by Yuan et al.[13]

The PL changes observed in the $BaYF_5$:20%Yb,1%Tm/$CsPbBr_3$ composite are probably a result of the two competing processes: the increase of nonradiative recombination centers and the shortening of the distance between the energy donors and acceptors, which will lead to PL quenching and enhancement, respectively. Only the first process occurred in the pristine $CsPbBr_3$ QDs. The increase of the nonradiative recombination centers is likely arising from the partial loss of surface bonding ligands during the thermal treatment, followed by the formation of surface energy states and subsequent PLquenching.[13] On the other hand, the evaporation of cyclohexane is likely to favor a shorter distance between the energy donors and acceptors which will improve the FRET efficiency. Therefore, the PL intensity of the $BaYF_5$:20%Yb,1%Tm/$CsPbBr_3$ composite was enhanced due to the increased energy transfer efficiency from the energy donors to the acceptors. In the $BaYF_5$:20%Yb,1%Tm/$CsPbBr_3$ composite, the latter process dominated in the first two hours and then became weaker, accompanied with the PL enhancement and subsequent quenching.

The pristine $CsPbBr_3$ QDs and $BaYF_5$:20%Yb,1%Tm/$CsPbBr_3$ composite films were subjected to cycles of water spraying followed by natural drying (30 min in air) to investigate the stability to humidity of the materials and their PL performances. As shown in Figure S2.9b, the $BaYF_5$:20%Yb,1%Tm/$CsPbBr_3$ composite showed a serious PL intensity drop compared with the pristine $CsPbBr_3$ QDs upon water exposure. However, after 30 min drying, 87% and 81% of the original intensities were recovered after three cycles for the pristine $CsPbBr_3$ QDs and the $BaYF_5$:20%Yb,1%Tm/$CsPbBr_3$ composite, respectively. Further, the exciton peak positions of the two samples stayed the same. The PL quenching is probably associated with the desorption of the capping ligands on the surface of the nanoparticles or surface decomposition, followed by the occurrence of new surface trap states.[14] The $BaYF_5$:20%Yb,1%Tm/$CsPbBr_3$ composite is more sensitive to moisture compared with the pristine $CsPbBr_3$ QDs. In the $BaYF_5$:20%Yb,1%Tm/$CsPbBr_3$ composite, partial UCNPs detachment from the surface of the $CsPbBr_3$ QDs, owing to the desorption of the surface bonding ligands, or enhanced lanthanide vibrational quenching, could related to the reduced FRET efficiency and PL intensity in the presence of water.

References

(S1) Zhai, X.; Liu, S.; Liu, X.; Wang, F.; Zhang, D.; Qin, G.; Qin, W. Sub-10 nm $BaYF_5$: Yb^{3+},Er^{3+} Core–Shell Nanoparticles with Intense 1.53 μm Fluorescence for Polymer-Based Waveguide Amplifiers. *J. Mater. Chem. C*, **2013**, *1*, 1525-1530.

(S2) De Berti, I. P.; Cagnoli, M. V.; Pecchi, G.; Alessandrini, J. L.; Stewart, S. J.; Bengoa, J. F.; Marchetti, S. G. Alternative Low-Cost Approach to the Synthesis of Magnetic Iron Oxide Nanoparticles by Thermal Decomposition of Organic Precursors. *Nanotechnology*, **2013**, *24*, 175601.

(S3) Lin, Y.; Jin, J.; Song, M. Preparation and Characterisation of Covalent Polymer Functionalized Graphene Oxide. *J. Mater. Chem. C*, **2011**, *21*, 3455-3461.

(S4) Liu, M.; Zhang, L.; Wang, K.; Zheng, Z. Low Temperature Synthesis of δ-Bi_2O_3 Solid Spheres and Their Conversion to Hierarchical Bioi Nests Via the Kirkendall Effect. *CrystEngComm*, **2011**, *13*, 5460-5466.

(S5) Zhang, M.; Li, H.; Jing, Q.; Lu, Z.; Wang, P. Atomic Characterization of Byproduct Nanoparticles on Cesium Lead Halide Nanocrystals Using High-Resolution Scanning Transmission Electron Microscopy. Crystals **2018**, *8*, 2

(S6) Prevo, B.; Peterman, E. J. Förster Resonance Energy Transfer and Kinesin Motor Proteins. *Chem. Soc. Rev.*, **2014**, *43*, 1144-1155.

(S7) Hildebrandt, N.; Spillmann, C. M.; Algar, W. R.; Pons, T.; Stewart, M. H.; Oh, E.; Susumu, K.; Diaz, S. A.; Delehanty, J. B.; Medintz, I. L. Energy Transfer with Semiconductor Quantum Dot Bioconjugates: A Versatile Platform for Biosensing, Energy Harvesting, and Other Developing Applications. *Chem. Rev.* **2017**, *117*, 536-711.

(S8) Algar, W. R.; Wegner, D.; Huston, A. L.; Blanco-Canosa, J. B.; Stewart, M. H.; Armstrong, A.; Dawson, P. E.; Hildebrandt, N.; Medintz, I. L. Quantum Dots as Simultaneous Acceptors and Donors in Time-Gated Förster Resonance Energy Transfer Relays: Characterization and Biosensing. *J. Am. Chem. Soc.*, **2012**, *134*, 1876-1891.

(S9) Boyer, J.-C.; Van Veggel, F. C. Absolute Quantum Yield Measurements of Colloidal $NaYF_4$:Er^{3+},Yb^{3+} Upconverting Nanoparticles. *Nanoscale* **2010**, *2*, 1417-1419.

(S10) Bednarkiewicz, A.; Nyk, M.; Samoc, M.; Strek, W. Up-conversion FRET from Er^{3+}/Yb^{3+}:$NaYF_4$ Nanophosphor to CdSe Quantum Dots. *J. Phys. Chem. C*, **2010**, *114*, 17535-17541.

(S11) Marin, R.; Labrador-Paéz, L.; Skripka, A.; Haro-González, P.; Benayas, A.; Canton, P.; Jaque, D.; Vetrone, F. Upconverting Nanoparticle to Quantum Dot Förster Resonance Energy Transfer: Increasing the Efficiency through Donor Design. *ACS Photonics*, **2018**, *5*, 2261-2270.

(S12) Artizzu, F.; Serpe, A.; Marchiò, L.; Saba, M.; Mura, A.; Mercuri, M. L.; Bongiovanni, G.; Deplano, P.; Quochi, F. Controlling Nd-to-Yb Energy Transfer through a Molecular Approach. *J. Mater. Chem. C*, **2015**, *3*, 11524-11530.

(S13) Yuan, X.; Hou, X.; Li, J.; Qu, C.; Zhang, W.; Zhao, J.; Li, H. Thermal Degradation of Luminescence in Inorganic Perovskite $CsPbBr_3$ Nanocrystals. *Phys. Chem. Chem. Phys.*, **2017**, *19*, 8934-8940.

(S14) Huang, S.; Li, Z.; Wang, B.; Zhu, N.; Zhang, C.; Kong, L.; Zhang, Q.; Shan, A.; Li, L. Morphology Evolution and Degradation of $CsPbBr_3$ Nanocrystals under Blue Light-Emitting Diode Illumination. *ACS Appl. Mater. Interfaces*, **2017**, *9*, 7249-7258.

Chapter 3 Boosting the Er^{3+} 1.5 μm Luminescence in $CsPbCl_3$ Perovskite Nanocrystals for Photonic Devices Operating at Telecommunication Wavelengths

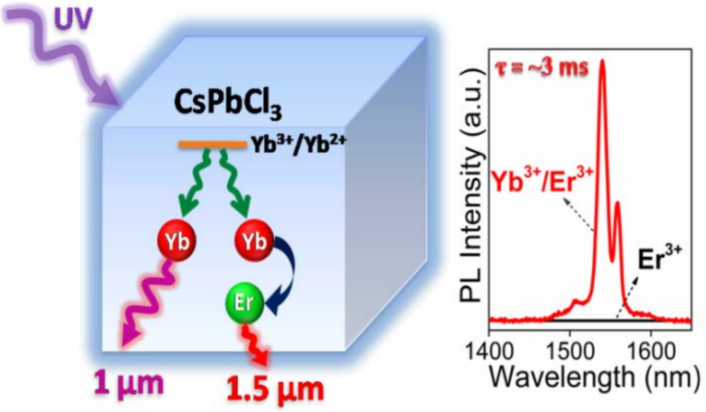

The results of this chapter were published in:

Zeng, M.; Artizzu, F.; Liu, J.; Singh, S.; Locardi, F.; Mara, D.; Hens, Z.; Van Deun, R. Boosting the Er^{3+} 1.5 μm Luminescence in $CsPbCl_3$ Perovskite Nanocrystals for Photonic Devices Operating at Telecommunication Wavelengths. *ACS Appl. Nano Mater*. **2020**, *3*, 4699-4707.

Abastract

$CsPb(Cl/Br)_3$ perovskite nanocrystals (NCs) doped with Yb^{3+} ions have recently attracted large attention for their applications in photovoltaics in view of the high quantum yield, exceeding 100% of Yb^{3+} emission at ~1.0 µm. In contrast, the particularly relevant Er^{3+} emission at 1.5 µm in the third telecommunication window, of high interest in silicon integrated photonics, has been so far largely neglected also in view of the weak emission performance displayed by Er^{3+} doped NCs. Comprehensive steady-state and time-resolved spectroscopic measurements provide insights into the underlying mechanisms of Yb^{3+} and Er^{3+} sensitization to rationalize the anomalous different behavior of these two emitters in singly-doped NCs. We propose that single-photon excitation of two Yb^{3+} ions possibly occurs through a transient internal redox mechanism in the perovskite host, while this pathway is unviable for Er^{3+}. In turn, Yb^{3+}-bridged Er^{3+} sensitization, boosts the Er^{3+} luminescence at ~1.5 µm by 10^4-fold compared to Er^{3+} singly-doped NCs, and a relative high quantum yield of ~6% and long lifetime (~3.0 ms) are obtained. The resulting high Er^{3+} excited state densities, combined with the large molar extinction coefficient of the semiconducting $CsPbCl_3$ matrix make Er^{3+} doped perovskite promising innovative materials to realize photonic devices operating at telecommunication wavelengths.

3.1 Introduction

All inorganic cesium lead halide perovskite (LHP) $CsPbX_3$ (X = Cl^-, Br^- and I^-) nanocrystals (NCs) have been widely studied in the last decade due to their appealing optical and electrical properties, which are highly suitable for optoelectronics,[1,2] solar energy conversion,[3,4] photodetection,[5,6] lighting and lasing.[7–10] By adjusting the halide composition, the emission range of LHPs can be tuned from the blue to the red part of electromagnetic spectrum, and LHP NCs often routinely reach >90% photoluminescence quantum yields (PLQYs).[11] The emission wavelength can be changed further by the incorporation of optically-active dopants, such as lanthanide (Ln^{3+})[12–18] and transition metal ions (Mn^{2+}, Fe^{2+}, Cd^{2+}).[19–21] In such systems, the large molar extinction coefficient (~10^7 M^{-1} cm^{-1}) of the NCs for light with a photon energy above the LHP band gap,[22] greatly facilitates the harvesting of the energy needed to excite the dopants. In particular, Ln^{3+}-doped LHP NCs currently attract considerable interest in view of the unique optical properties that arise from sensitized intra-atomic f–f transitions, whose long-lived and narrow-band emission can find applications in solar cells and light-emitting diodes.[8,14,23] Recently, extremely high PLQYs, exceeding 100% at ~1 μm, were reported for Yb^{3+} doped $CsPbCl_3$ NCs;[15,16] a finding attributed to a highly efficient picosecond two-photon quantum cutting (QC) process from the perovskite host to the Yb^{3+} $^2F_{5/2}$ excited level. Clearly, the underlying demonstration of the work on Yb^{3+} doped $CsPbCl_3$ NCs that LHP NCs can trigger highly efficient Ln^{3+} emission, creates novel perspectives for developing Ln-based optical devices operating in the near-infrared (NIR) window. Applications such as solar energy conversion, lasing and optical amplification would all greatly benefit from the enhanced molar extinction coefficient, the high excitation densities and the semiconducting properties delivered by the LHP matrix.[24] However, for emerging silicon integrated photonics technologies, NIR emission at around 1.5 μm, as provided by Er^{3+} $^4I_{13/2} \rightarrow {}^4I_{15/2}$ transition,[25] is more attractive than the 1 μm emission characteristic of Yb^{3+}. Interestingly, Er^{3+} has a $^4I_{11/2}$ upper level that is resonant with the Yb^{3+} $^2F_{5/2}$ level. Hence, one could expect that Er^{3+} doped $CsPbCl_3$ NCs exhibit a similar two-photon QC from the $CsPbCl_3$ host (~24000 cm^{-1}) that leads to emission at 1.5 μm after internal relaxation to the emissive $^4I_{13/2}$ level (~6500 cm^{-1}) or, possibly, a direct three-photon QC to this $^4I_{13/2}$ level.[26]

Despite the prospects of Er^{3+} doped LHP NCs, the few pioneering studies that have addressed this system reported Er^{3+} emission performance that is not comparable with the Yb^{3+} case,[27,28] and the underlying reason is not yet known. Such results could reflect the ineffective doping of Er^{3+} ions, which would lead to quenched emitters at the surface of the NCs, or the inefficient energy transfer from LHP NCs to Er^{3+}. Given the outlined analogy between Yb^{3+} and Er^{3+}, the latter explanation seems at odds with the highly efficientsensitization of Yb^{3+} by LHP NCs. Even so, a drastic improvement of the luminescence of LHP NCs at 1.5 μm by Er^{3+} doping will require the combination of better synthetic protocols that achieve deeply buried Er^{3+} ions in the LHP NCs, and a better insight in the underlying mechanism of Ln^{3+} sensitization in doped LHP NCs.

Following these considerations, we report here on a strategy to achieve intense and long-lived Er^{3+} emission at ~1.5 μm in doped $CsPbCl_3$ NCs. We first introduce an optimized synthetic method[15] to ensure the homogeneous incorporation of Er^{3+} into the NCs. However, rather than accelerating the quenching of band-edge charge carriers by energy transfer, we find that Er^{3+} doping merely suppresses the carriers trapping without inducing any noticeable emission at ~1.5 μm. Interestingly, we observe the same behavior after Nd^{3+} doping, whereas Eu^{3+} doping does induce a rapid loss of band-edge carriers, similarly to Yb^{3+}, a difference suggesting that electron transfer to the most readily reduced Yb^{3+} and Eu^{3+} ions is an essential step of the sensitization process. Following this observation, we introduce Yb^{3+} ions as co-dopants to obtain Yb^{3+}/Er^{3+} doped $CsPbCl_3$ NCs. We show that once Yb^{3+} ions are present, a rapid loss of band-edge carriers occurs and that Yb^{3+}/Er^{3+} co-doped NCs exhibit intense Er^{3+} emission at ~1.5 μm with long lifetime (~3.0 ms) and relatively high PLQY (~6%), stemming from efficient Yb^{3+}-bridged Er^{3+} sensitization through the highly absorbing LHP host. This result provides the guidelines for the future design of Ln^{3+}-functionalized doped perovskite NCs and brings new opportunities for the development of photonic devices operating at telecommunication wavelengths.[25]

3.2 Experimental Section

3.2.1 Sample Preparation

Synthesis of $CsPbCl_3$ NCs. The $CsPbCl_3$ NCs were synthesized following the method reported by Milstein et al. with minor changes.[15] Typically, 0.2 mmol of $Pb(CH_3CO_2)_2{\cdot}3H_2O$ and 0.28 mL of 1 M $CsCH_3CO_2$ ethanol solution were loaded into a three-neck flask containing 5 mL ODE, 1 mL OA and 0.5 mL OLA. This mixture was heated to 120 °C under vacuum for 1 h. Then it was placed under N_2 atmosphere and heated to 240 °C. At this temperature, the Cl precursor containing 0.2 mL of TMS-Cl diluted with 0.5 mL ODE solution was swiftly injected into the reaction mixture and immediately quenched by immersion in a room-temperature water bath. The crude solution was centrifuged at 3500 rpm for 15 min and the supernatant was discarded. The residue was dispersed in cyclohexane and washed by ethyl acetate as antisolvent, followed by centrifugation at 3500 rpm for 15 min. This washing step was repeated twice. The obtained pellet was redispersed in cyclohexane and allowed to settle down overnight and again centrifuged at 3000 rpm for 15 s. Finally, the NCs were obtained by filtering the supernatant with a 0.2 μm PTFE filter and suspended in cyclohexane.

Synthesis of Ln^{3+}-doped $CsPbCl_3$ NCs. The above procedure was also applied for the Ln^{3+} doped $CsPbCl_3$ NCs, except the addition of corresponding lanthanide acetate to the original reaction mixture. The Yb^{3+}/Er^{3+} codoped $CsPbCl_3$ NCs with varying relative doping concentrations of Er^{3+} to Yb^{3+} were synthesized by varying the Er^{3+} concentration, and keeping fixed concentration of 40% Yb^{3+} with respect to Pb^{2+}. The starting amounts for synthesizing different dopant concentrations in $CsPbCl_3$ NCs are listed in Table S3.1.

3.2.2 Characterization

Structural characterization was performed using a Thermo Scientific ARL X'TRA X-ray diffraction (XRD) diffractometer with Cu K_α (λ = 1.5406 Å) radiation over the range of $2\theta = 10 - 50°$. The samples were made by drop casting colloidal $CsPbCl_3$ NCs onto glass substrates. Doping concentrations of the NCs were determined using X-ray fluorescence (XRF) spectrometer (Rigaku NEX-CG). Transmission electron microscope (TEM) images were collected on a Cs-corrected JEOL 2200FS microscope operated at 200 kV. UV−vis absorption spectra were recorded with a Perkin Elmer Lambda 950 spectrometer. Steady-state and time-resolved photoluminescence (PL) were obtained on a FLS920 spectrofluorometer (Edinburgh Instruments) equipped with a 450 W xenon lamp. The luminescence signals in the VIS and NIR spectral range were detected using a photomultiplier (PMT) (Hamamatsu, R928P) and a liquid N_2 cooled PMT (Hamamatsu, R5509-72), respectively. A pulsed xenon microsecond flash lamp μF900H (pulse frequency 0.1 – 100 Hz, 60 W) and a hydrogen-filled nanosecond flash lamp nF900 (pulse frequency 40 kHz, 150W) were employed as the excitation sources for slow decay process and fast decay process, respectively. The instrument response function(IRF) was obtained from a nonfluorescing suspension of colloidal silica LUDOX. Absolute PLQY of the NCs band-edge emission was determined using an integrating sphere (Edinburgh Instruments) connected to the

FLSP920 spectrofluorometer. Relative NIR PLQYs of Yb^{3+} and Er^{3+} emission were measured using $[Ru(bpy)_3]^{2+}$ ($C_{30}H_{24}Cl_2N_6Ru\cdot6H_2O$) dissolved in water as reference standard ($\Phi = 0.04$), according to the protocol described in ref 54. An uncertainty of 10% is estimated on the retrieved values. Unless specified, the optical density (OD) at the first exciton of $CsPbCl_3$ NCs for optical measurements is below 0.3 (OD <0.3).

3.3 Results and Discussion

3.3.1 Synthesis and Characterization of Doped NCs

The main challenge in the synthesis of Ln^{3+} doped LHP NCs is to achieve doping into the LHP lattice. This is intrinsically difficult given the mismatch between the chemically soft LHP matrix and the Ln^{3+} ions, which are typically hard acids. This limitation can be partly overcome by using $CsPbCl_3$ LHP instead of the typically softer bromide compounds. However, even in that case, the pre-existing Pb−Cl bonds in the $PbCl_2$ precursor that is often used to synthesize $CsPbCl_3$ NCs are not favorable for specific kinds of B-site doping.[21] To avoid such issues, we extended the synthetic approach reported by Milstein and coworkers,[15] in which lead, cesium and ytterbium acetates and chlorotrimethylsilane are used as the precursors to form Yb^{3+} doped $CsPbCl_3$, to the formation of Er^{3+} doped and Yb^{3+}/Er^{3+} codoped $CsPbCl_3$ NCs. We first envisaged the synthesis of Er^{3+} and Yb^{3+} singly-doped $CsPbCl_3$ NCs by using varying amounts of erbium and ytterbium acetates, while keeping the amount of lead acetate fixed (see Experimental Section and Table S3.1 for details). Following the same synthetic approach, Yb^{3+}/Er^{3+} codoped NCs were also prepared by varying the Er^{3+}: Yb^{3+} molar ratio, while keeping the Yb^{3+}: Pb^{2+} ratio fixed at 1: 2.5. The successful incorporation of Er^{3+} and Yb^{3+} in these NCs was verified by X-ray fluorescence (XRF). As shown in Table S3.1, this analysis indicates that the doping concentration by means of the Ln^{3+} molar fraction with respect to Pb^{2+} increases with increasing the nominal molar ratio [Ln]/([Ln] + [Pb]).

Figure 3.1a-d represents a set of bright field transmission electron microscopy (TEM) images, which show that both undoped and doped $CsPbCl_3$ NCs exhibit a cubic shape. Doped NCs exhibit a slightly larger average edge length, which increases from 11.0 ± 1.7 nm for undoped NCs to 14.5 ± 1.4 nm, 13.4 ± 1.9 nm and 13.6 ± 1.7 nm for NCs doped with 2.4% Er^{3+}, 2.7% Yb^{3+} and co-doped with 1.8%/1.8% Yb^{3+}/Er^{3+}, respectively. Contrary to ref 16, the average size is increased upon Ln^{3+} incorporation, but this observation is nonetheless consistent with ref 15. The apparent anomaly may be the result of different synthetic protocols. In this case, the cation and anion are supplied by separate sources, unlike the $PbCl_2$ and $LnCl_3$ salts used in ref 16 that provide both cation and anion source. Furthermore, in our synthetic approach, the much higher Cl^- rich reaction environment can provide extra Cl^- ions, which can introduce into the NCs lattice or on the surface for charge compensation because of the substitution of divalent Pb^{2+} by trivalent Ln^{3+}. Consequently, the NC size increases. As shown in Figure S3.1, doping does not induce a notable shift of the diffraction peaks in the XRD patterns, similarly to ref 15, but contrary to the more significant shift reported in ref 16. The reason for this behavior is not yet clear. It may be influenced by the synthetic approach. Moreover, the experimental setup used in this work is not able to distinguish a faint shift due to low amount of dopant incorporated. Based on the observed Ln^{3+} photoluminescence (see later), we conclude that the synthetic protocol used here effectively leads to Ln^{3+} doped $CsPbCl_3$ NCs, as further supported by the characterization on Ln^{3+} doping concentration as deduced from XRF measurements.

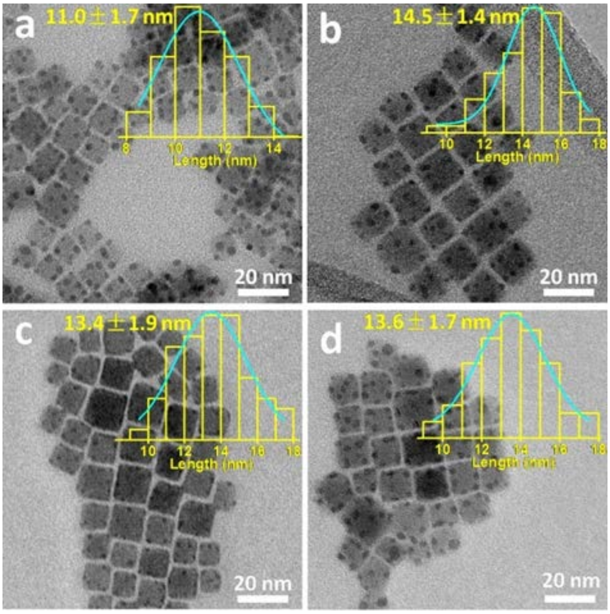

Figure 3.1 TEM images of (a) undoped $CsPbCl_3$ NCs, (b) 2.4% Er^{3+} doped NCs, (c) 2.7% Yb^{3+} doped NCs, and (d) 1.8%/1.8% Yb^{3+}/Er^{3+} codoped NCs. The insets are the corresponding size distribution histograms. The black dots appearing in bright field image at the edges of the NCs are attributed to Pb metallic aggregates formed by the electron beam.[29]

3.3.2 Optical Properties of Er^{3+}-Doped NCs

Figure 3.2a,b shows the absorption and photoluminescence (PL) spectra of the blank and Er^{3+} doped $CsPbCl_3$ NCs with different doping concentrations. Clearly, doping with Er^{3+} does not induce a significant shift of the band-edge absorption of $CsPbCl_3$ NCs. Note that with NCs diameters ranging from 11.0 to 14.5 nm, sizes well above the exciton Bohr radius of $CsPbCl_3$ (5 nm),[11] quantum confinement will have little effect on the band-edge transition of these NCs. Hence, we conclude that Er^{3+} doping hardly affects the band gap of $CsPbCl_3$. In line with this conclusion, the band-edge PL of $CsPbCl_3$ NCs does not shift upon doping. On the other hand,

Figure 3.2b shows that the introduction of 0.6% Er^{3+} strongly raises the intensity of the band-edge emission. More quantitatively, we measure an increase of the PLQY of the band-edge emission from 1.2% for the undoped NCs to 6.8% for the 0.6% Er^{3+} doped NCs (see Table S3.2). A further increase of the Er^{3+} doping again reduces the PLQY to 2.9% and 1.7% for the 2.4% Er^{3+} and the 3.5% Er^{3+} doped samples, respectively. While we detected Er^{3+} ions in purified $CsPbCl_3$ NCs, Er^{3+} doped NCs exhibit only a faint Er^{3+} emission at ~1.54 μm in concentrated samples (see Figure S3.2), which suggest a weak Er^{3+} sensitization. For both undoped and Er^{3+} doped $CsPbCl_3$ NCs, we observed a NIR emission feature centered at 994 nm with a full width at half-maximum (fwhm) of ~55 nm, while a defect-related visible emission around 600 nm was observed by Watanabe et al.[30] This 994 nm emission has a broad excitation profile that closely resembles the excitation profile of the $CsPbCl_3$ band-edge emission (see Figure S3.3). The above result indicates that the 994 nm emission band originates from a state directly fed by the band-edge electron-hole pairs. It should be pointed out that Yb^{3+} contamination can be excluded for this emission band owing to the absence of such peak after Lu^{3+} doping (see Figure S3.4). Interestingly, increasing the Er^{3+} concentration leads to a progressive suppression of this emission band (see Figure S3.2), which may be related to intrinsic deep traps in $CsPbCl_3$ NCs, such as Cl vacancies or undercoordinated Pb atoms.[31,32] A similar NIR emission at 930 nm assigned to the defective states of oxygen vacancies in Fe doped $SrSnO_3$ perovskite was also noticed by Muralidharan et al.[33] Cl vacancies are commonly observed in perovskite materials and seen as a predominant source of electron trapping.[34,35] However, such vacancies can be removed by B-site doping with divalent metal ions,[36–38] or trivalent lanthanide ions which favor the introduction of negatively charged Cl^{-} ions for charge compensation.[30] To verify that the quenching of the 994 nm emission band by Er^{3+} incorporation can be ascribed to the removal of defects rather than to the activation of additional energy transfer pathways, we extended our analysis to Lu^{3+} doped CsPbCl$_3$ NCs as reference. Lu^{3+} ions (r = 86 pm),[39] are optically silent and have a smaller ionic radius than Yb^{3+} (87 pm)[39] and Er^{3+} (89 pm),[39] so they can be favorably doped into the CsPbCl$_3$ matrix without affecting its optical properties. As shown in Figure S3.4, we find also for this system that doping strongly quenches the 994 nm emission, an observation that corroborates the hypothesis that Ln^{3+} doping helps removing trap states in the LHP host.

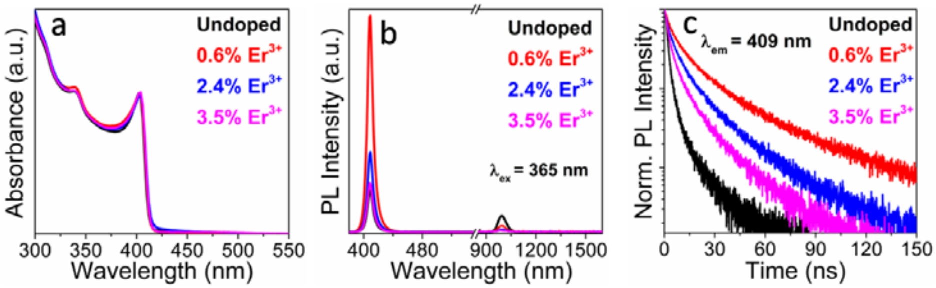

Figure 3.2 Optical properties of undoped and Er^{3+}-doped CsPbCl$_3$ NCs as a function of Er^{3+} doping concentration. (a) Absorption spectra (OD <0.3 at first exciton) and corresponding (b) PL spectra, (c) PL decay curves monitored at 409 nm (λ_{ex} = 350 nm).

To unveil the effect of Er^{3+} doping on the charge carrier dynamics, time-resolved PL measurements at the band-edge emission were performed. Analysis of the data reveals a biexponential decay in undoped CsPbCl$_3$ NCs. The shortest component constitutes the majority of the overall signal (~96%) and its decay time constant (τ_1 ~2.0 – 3.0 ns) differs by about one order of magnitude with respect to the long-lived component (see Table S3.2), revealing the existence of two different deactivation channels, likely related to the carrier trapping (τ_1) and the radiative carrier recombination (τ_2), respectively. Upon Er^{3+} doping, the carrier lifetime increases significantly and the overall temporal dynamics is fully in agreement with the observed trends of emission intensity (Figure 3.2b) and PLQY (see Table S3.2). The nonradiative decay rate constant as calculated by using the measured PLQY and PL lifetime[40] drops from 380.0 µs^{-1} for the undoped NCs to 69.5 µs^{-1} for the 0.6% Er^{3+} doped NCs (see Table S3.2), further supporting the effect of Er^{3+} doping in the passivation of nonradiative trap centers. Decay curves of the doped NCs can be well fitted with a triexponential function, but differently to the case of Yb^{3+} inducing a picosecond decay component,[15] no ultrafast component below 2.0 ns is found to significantly contribute to the dynamics, indicating that the carrier-Er^{3+} exchange coupling is negligible. The absence of any detectable Er^{3+} NIR emission in Lu^{3+}/Er^{3+} codoped $CsPbCl_3$ NCs, where Lu^{3+} is expected to largely remove Cl vacancies, rules out the role of deep trap states in the competitive depopulation of the band-edge electron-hole pairs (see Figure S3.4). Hence, the feeble Er^{3+} emission observed in the concentrated $CsPbCl_3$ NCs (see Figure S3.2) could be ascribed to an inefficient Förster resonance energy transfer (FRET) or simple photon reabsorption as a result of the spectral overlap between the band-edge emission at 409 nm and the Er^{3+} $^2H_{9/2} \rightarrow {}^4I_{15/2}$ transition at ~410 nm, while this process is limited by the low Er^{3+} doping concentration and small molar extinction coefficient (<10 M^{-1} cm^{-1}) of Er^{3+}.[41]

On the other hand, as the Er^{3+} doping concentration increases from 0.6% to 3.5%, the contribution of the shortest decay component (τ_1 ~3.0 – 2.3 ns) to the overall signal increases and accounts for the observed decrease in PLQY and emission intensity. These data point out the role of Er^{3+} in introducing new deactivation channels for the charge carriers. Taking into consideration that the direct transfer of excitation to Er^{3+} is deemed to be highly inefficient, as discussed above, the perceived behavior is compatible with the presence of shallow traps which lead to photogenerated carriers depopulation. The formation of Ln^{3+}-induced shallow trap states has been previously proposed in ref 15 and ref 42. In Yb^{3+}-doped $CsPbCl_3$ NCs, these states are likely to account for a highly efficient process of activation of Yb^{3+} emission following a supposed QC and nonradiative energy transfer, agreeing with the observed ultrafast ns charge carrier decay dynamics (see Figure S3.5) and the high PLQY above unity (~150%) that we observed in the Yb^{3+} singly doped sample, in accordance with the reported works.[15] In contrast, the much slower carrier dynamics observed in Er^{3+} singly doped NCs indicates that this mechanism is unexpectedly not active in the sole presence of Er^{3+}. This may seem in contrast with the fact that Er^{3+} possesses an upper energy level $^4I_{11/2}$ which is fully resonant with the Yb^{3+} $^2F_{5/2}$ level, and is known to be suitably fed by nonradiative energy transfer from a donor. This observation makes Yb^{3+} a special case among the possible Ln^{3+} emission activators in doped $CsPbCl_3$ NCs. We hypothesize that the principal parameter affecting the charge carrier-dopant interaction is the electronic configuration difference between Yb^{3+} ($4f^{13}$) and Er^{3+} ($4f^{11}$) ions resulting in a remarkably higher reduction potential to divalent state for the former (–1.05 V vs NHE, corresponding to 3.45 eV below vacuum level) than for the latter (–3.00 V vs NHE, corresponding to 1.5 eV below vacuum level).[43] Therefore, Yb^{3+} can be suitable to act as an electron trap for the $CsPbCl_3$ conduction band (3.26 eV below vacuum level)[44] that is energetically located above the Yb^{3+}/Yb^{2+} couple reduction potential, likely through the induced shallow trap states localized in the vicinity of the dopant ion as shown in Figure 3.3 (see Supporting Information for details). This process generates a transient Yb^{2+} species which can subsequently undergo hole recombination with the LHP valence band (6.24 eV below vacuum level).[44] According to the mechanism proposed by Horrocks,[45] this transient internal redox process releases sufficient energy to leave two Yb^{3+} ions in the excited state and accounts for an apparent QC effect. This conjecture is further supported by observations made in Eu^{3+} ($4f^6$, 4.14 eV below vacuum level) and Nd^{3+} ($4f^3$, 1.8 eV below vacuum level)[43] singly doped $CsPbCl_3$ NCs, where the band-edge carrier lifetime of Eu^{3+}-doped NCs is extensively decreased due to electron depletion by Eu^{3+} ions (similarly to Yb^{3+} doped NCs), while the opposite trend is observed for Nd^{3+}-doped NCs (similarly to Er^{3+}-doped NCs) (see Figure S3.10). As expected, the Eu^{3+}-doped NCs do not show any characteristic Eu^{3+}

emission, unlike Yb^{3+}, since the electron transfer from Eu^{2+} to the LHP valence band does not yield sufficient energy to excite Eu^{3+}. The mechanism of Ln^{3+} sensitization is further discussed in the text. On the basis of the above conjecture and discussion in Supporting Information, we can expect that the QC process can still exist in Yb^{3+}-doped mixed halide $CsPb(Cl/Br)_3$ and it might be possible in $CsPbBr_3$ if the band gap is finely controlled, but probably not the lower-band gap $CsPbI_3$.[46]

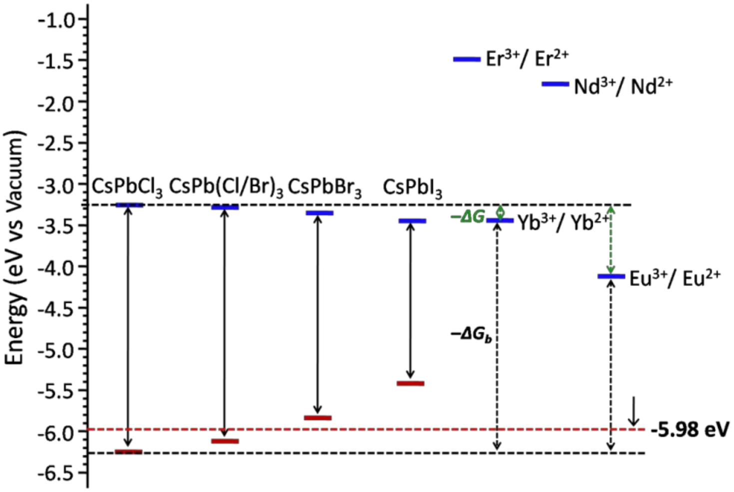

Figure 3.3 Energy level diagram of $CsPbX_3$ NCs[44] with respect to the reduction potential of Ln^{3+}/Ln^{2+} couple[43].

3.3.3 Yb^{3+}-Bridged Enhancement of Er^{3+} 1.5 μm Luminescence

The unviable mechanism of transient internal redox poses severe limitations to the sensitization of Er^{3+} and the optical output achievable at 1.5 μm. Fortunately, Yb^{3+} is a well-known sensitizer for Er^{3+},[47] so it is expected to be an energy bridge for triggering the Er^{3+} 1.5 μm emission. Figure 3.4 plots the absorption and PL spectra of the undoped and Yb^{3+}/Er^{3+} co-doped $CsPbCl_3$ NCs with various Er^{3+} concentrations (from Er^{3+}: Yb^{3+} ratio 0: 1 to 3: 1, which is used to denote the respective codoped samples) under fixed Yb^{3+} and Pb^{2+} content (see Methods and Table S3.1 for details). The absorption spectra of the samples are nearly the same, displaying a peak at ~403 nm. On the other hand, the band-edge emission is dramatically quenched after Yb^{3+} doping or Yb^{3+}/Er^{3+} codoping (Figure 3.4b), likely due to the activation of efficient band-edge carrier-to-Yb^{3+} energy transfer channel triggering the emission at 988 nm with ~50 nm fwhm (Figure 3.4c). This is also evidenced by time-resolved PL measurements showing a dramatic shortening of the band-edge emission lifetime (see Figure S3.5). In light of the above made considerations on Ln^{3+} doping effects in the removal of Cl vacancies and the very different NIR behavior between undoped and Yb^{3+} doped NCs (see Figure S3.6), it is reasonable to assume that the observed signal at 988 nm is entirely attributed to the Yb^{3+} $^2F_{5/2} \rightarrow {}^2F_{7/2}$ emissive transition. This peak becomes weaker upon increasing the Er^{3+} concentration, and is accompanied by the rise of a pronounced emission band centered at 1540 nm, corresponding to the Er^{3+} $^4I_{13/2} \rightarrow {}^4I_{15/2}$ transition (Figure 3.4c,d and Figure S3.7). Since the emission intensity at 988 nm in reference Yb^{3+} singly doped NCs increases slowly upon doping concentration increase (see Figure S3.6), the quenching of Yb^{3+} PL intensity in the codoped NCs can be ascribed to the energy transfer to Er^{3+}. The excitation spectrum monitored at 1540 nm closely resembles that retrieved for Yb^{3+} emission at 988 nm and the band-edge emission of the host (see Figure S3.8), likely evidencing a multistep energy transfer process from the host to Yb^{3+} and then to Er^{3+}.

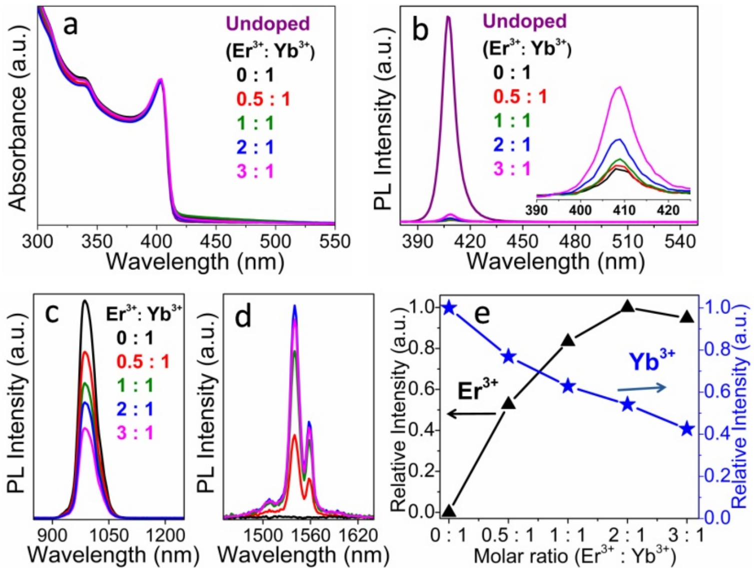

Figure 3.4 Optical absorption and corresponding PL spectra of undoped and Yb^{3+}/Er^{3+} codoped $CsPbCl_3$ NCs versus different relative ratios of the dopants (from Er^{3+}: Yb^{3+} = 0: 1 to 3: 1) (OD <0.3 at first exciton). (a) Absorption spectra. PL spectra of (b) band-edge emission, (c) Yb^{3+} emission ($^2F_{5/2} \rightarrow {}^2F_{7/2}$) and (d) Er^{3+} emission ($^4I_{13/2} \rightarrow {}^4I_{15/2}$). (e) PL intensity trend of Yb^{3+} emission and Er^{3+} emission as a function of the molar ratio. λ_{ex} = 365 nm.

Compared with the reported broad symmetric peak in Er^{3+} doped and Yb^{3+}/Er^{3+} codoped $CsPbCl_3$ NCs,[27,28] the Er^{3+} spectral shape here exhibits a well resolved structure resulting from the Stark splitting of J sublevels due to crystal field effects.[48] This suggests a homogeneous distribution of Er^{3+} ions within equivalent crystal sites in the $CsPbCl_3$ NCs. More importantly, the lifetime of the Er^{3+} $^4I_{13/2}$ level as displayed in Figure 3.5a is as long as ~3.0 ms, which is much longer than previously reported values of Er^{3+} in Yb^{3+}/Er^{3+} codoped $CsPbCl_3$ NCs (~7.1 μs and ~868.2 μs).[27,28] Such long lifetime and the monoexponential decay behavior provide further support to the hypothesis that Er^{3+} ions are effectively embedded within the NCs lattice and experience a homogeneous and well-defined low-phonon environment without the contamination of surface-adsorbed ions.[49] The different PL features of Er^{3+} with respect to literature reports are probably induced by the different synthetic protocols used, as previously discussed. Very recently, Nag et al. reported the Er^{3+} emission at 1540 nm in Bi^{3+}/Er^{3+} codoped double perovskite $Cs_2AgInCl_6$ in solid state experienced a monoexponential decay with an extremely long lifetime of 16.4 ms, which is desired for optical telecommunication.[50] This demonstration indicates that the Er^{3+} ions are well shielded from a high-phonon energy surroundings and most likely deeply buried into a low-phonon energy host, i.e. the perovskite host. In fact the surface ligands and the solvents contain several vibrational quenchers (i.e., C−H, N−H, and O−H groups)[51], which would dramatically shorten the NIR emission lifetime if the Er^{3+} ions were not embodied into the lattice.

Notably, the intensity of Er^{3+} emission is dependent on the Er^{3+}: Yb^{3+} relative molar ratio and is boosted by enriching the concentration of emitting Er^{3+} centers until it reaches an upper limit corresponding to a 2: 1 ratio beyond which it slightly decreases (Figure 3.4e). The maximum observed intensity is remarkably ~10^4 times higher than that of the Er^{3+} singly-doped NCs (see Figure S3.9). The above intensity trend of Er^{3+} emission is consistent with the observed intensity change of the residual band-edge emission (inset in Figure 3.4b), as discussed further. The PLQY at 1.5 μm measured for the sample with 2: 1 Er^{3+}: Yb^{3+} ratio under excitation of the LHP matrix reaches a relatively high value of ~6%. This value is comparable with the best performing materials showing sensitized Er^{3+} emission,[25] and much higher than in Yb^{3+}/Er^{3+} codoped double perovskite $Cs_2AgInCl_6$ (0.02%),[52] likely due to different energy transfer mechanism of the Yb^{3+} sensitization for Er^{3+} (QC *vs.* resonant Dexter-type transfer).

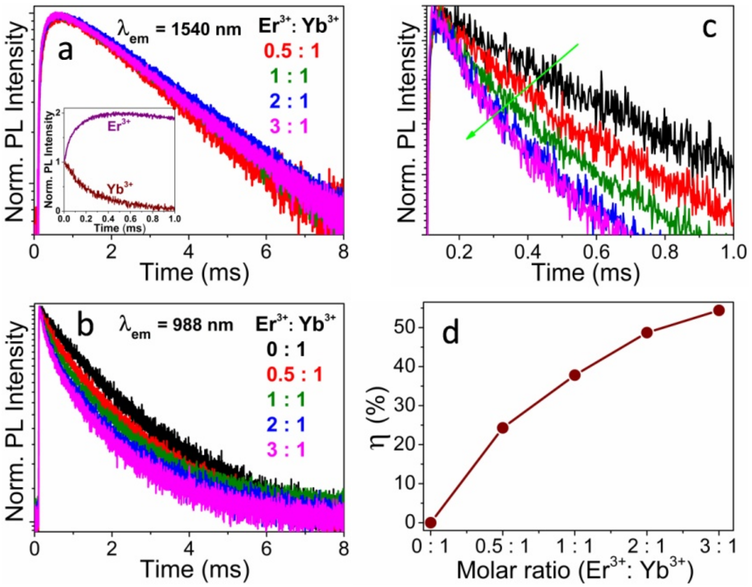

Figure 3.5 (a) PL decay curves of Yb^{3+}/Er^{3+} codoped CsPbCl$_3$ NCs with different relative ratios (from Er^{3+}: Yb^{3+} = 0: 1 to 3: 1) monitored at 1540 nm ($^4I_{13/2}$ level of Er^{3+}) upon excitation at 365 nm. Inset shows a close-up of the Yb^{3+} component and Er^{3+} signal rising. (b) PL decay curves monitored at 988 nm ($^2F_{5/2}$ level of Yb^{3+}). (c) Short time scale detail of (b). (d) Yb^{3+}-to-Er^{3+} energy transfer efficiency (η) as a function of the dopants molar ratio.

Time-resolved PL studies of the Yb^{3+} donor in the NIR can provide more detailed insights into the energy migration pathways inthe studied materials. As shown in Figure 3.5b, the decay kinetics of Yb^{3+} singly doped NCs at 988 nm is nearly monoexponential with a lifetime as long as ~1.7 ms, indicating the existence of only one population of equivalent emitting centers within the host. Upon introduction of Er^{3+} ions, the overall decay dynamics becomes significantly faster and exhibits a biexponential behavior. The retrieved time constants and calculated average lifetimes are summarized in Table 3.1. The Yb^{3+} lifetime shortening provides direct evidence that Yb^{3+} ions are acting as the energy transfer donors to Er^{3+} ions. In particular, the short decay component (τ_1) is associated to a fast time constant in the hundreds of μs range, which is indicative of highly efficient energy transfer most likely between donor and acceptor ions at a shorter separation than the Förster's radius (~1 nm).[48,53] The slow recovery component (τ_2) representing radiative energy depopulation becomes less predominant and faster at elevated Er^{3+} concentration, indicating that Er^{3+} incorporation changes the deexcitation pathway and the energy transfer probability from Yb^{3+} to Er^{3+} is boosted. Further observation evidences a matching between the rise-time of Er^{3+}-based emission and the decay of partially quenched Yb^{3+}-based emission (~200 μs, inset in Figure 3.5a), confirming that the Er^{3+} $^4I_{13/2}$ state is fed by energy transfer from the resonant $^2F_{5/2}$ level of Yb^{3+} in the co-doped NCs.

Table 3.1 PL decay parameters and energy transfer efficiency from Yb^{3+} to Er^{3+} in Yb^{3+}/Er^{3+} codoped $CsPbCl_3$ NCs with varying relative doping concentrations.

Sample	τ_1/ms (A_1)	τ_2/ms (A_2)	τ_{Yb}/ms[a]	τ_{Er}/ms	η(%)[a]
Er^{3+}: Yb^{3+} = 0: 1	—	1.7	1.7	—	—
Er^{3+}: Yb^{3+}= 0.5: 1	0.3 (0.28)	1.7 (0.72)	1.3	2.5	23.5
Er^{3+}: Yb^{3+}= 1: 1	0.3 (0.39)	1.6 (0.61)	1.1	2.8	35.3
Er^{3+}: Yb^{3+}= 2: 1	0.3 (0.49)	1.5 (0.51)	0.9	3.0	47.1
Er^{3+}: Yb^{3+}= 3: 1	0.2 (0.52)	1.4 (0.48)	0.8	2.8	52.9

[a] $\tau = \sum A_i\tau_i / \sum A_i$; $\eta = 1 - \tau_{Yb\text{-}Er}/\tau_{Yb}$, where $\tau_{Yb\text{-}Er}$ and τ_{Yb} are Yb^{3+} lifetimes in the presence and absence of Er^{3+} ions, respectively.

3.3.4 Sensitization Pathways in Yb^{3+}/Er^{3+} Codoped NCs

The efficiency (η) of the Yb^{3+}-to-Er^{3+} energy transfer process calculated on the basis of time-resolved Yb^{3+} data (Table 3.1 and Figure 3.5d) increases with increasing Er^{3+} load reaching 52.9% for the 3: 1 ratio of Er^{3+}: Yb^{3+}. However, despite the higher energy transfer probability and the increased number of emitters, the Er^{3+} emission intensity does not boost upon concentration increase above the 2: 1 ratio of Er^{3+}: Yb^{3+} (Figure 3.4e). Ruling out relevant quenching phenomena affecting Er^{3+} luminescence (from the similar values of the observed decay times, see Table 3.1) and observing that the band-edge emission intensity slightly increases upon further Er^{3+} incorporation (inset in Figure 3.4b), this effect can be attributed to a less effective injection of excitations from the host to the Yb^{3+}-to-Er^{3+} pathway. This behavior can be explained by considering the probability of conduction band (CB) electrons to populate localized shallow trap states induced by Yb^{3+} or Er^{3+} depends on the ratio between the dopants. The Yb^{3+}-induced shallow traps can effectively feed the multistep energy transfer pathway to Er^{3+}, possibly through a transient internal redox process followed by nonradiative Förster's coupling between excited Yb^{3+} and Er^{3+} ions. As depicted in Scheme 3.1, in this system, the photoexcited electron is firstly transferred from the LHP conduction band to the Ln^{3+}-induced shallow traps (1). Next, the electron is scavenged by Yb^{3+} to produce Yb^{2+} (2), and then Yb^{2+} is oxidized to Yb^{3+} through electron transfer to the valence band (VB) of LHP (3), as discussed before. This electron transfer process (3) will provide the energy to generate two excited Yb^{3+} ions (4), which are able to sensitize Er^{3+} luminescence following energy transfer to the resonant Er^{3+} $^4I_{11/2}$ level (5) and subsequent relaxation to the emissive $^4I_{13/2}$ level, as shown in Scheme 3.1a. On the other hand, shallow traps localized in the vicinity of Er^{3+} lead to poor sensitization, owing to the fact that the process (2) in Scheme 3.1a is blocked (Scheme 3.1b). Hence, an increasing fraction of excitations is lost through Er^{3+}-induced shallow traps as the doping concentration of this ion is increased, establishing the 2: 1 ratio of Er^{3+}: Yb^{3+} as optimal to achieve the highest emission intensity at 1.5 μm.

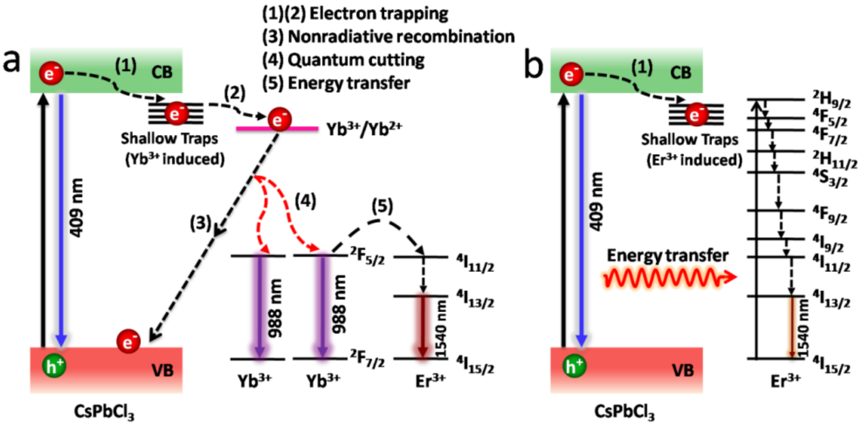

Scheme 3.1 Proposed energy transfer processes for (a) Yb^{3+}-induced shallow trap states and (b) Er^{3+}-induced shallow trap states.

3.4 Conclusions

We have successfully synthesized and deeply investigated the optical properties of NIR luminescent Yb^{3+} and Er^{3+} singly doped and Yb^{3+}/Er^{3+} codoped CsPbCl$_3$ NCs showing unprecedented intense and long-lived emission at 1.5 μm. This study first disentangles the underlying mechanism accounting for the extremely intense Yb^{3+} luminescence at 1 μm compared to the weak emission output of the corresponding Er^{3+}-doped CsPbCl$_3$ NCs at 1.5 μm. We hypothesize that Yb^{3+} acts as an electron trapping center by virtue of its relatively high redox potential giving rise to a Horrocks-type internal redox process involving the transient formation of Yb^{2+}, and releasing sufficient energy to leave two Yb^{3+} ions in the excited state. This mechanism explains the apparent QC effect leading to a PLQY of 150% observed for Yb^{3+} emission at 1 μm. On the other hand, this sensitization pathway is not viable for Er^{3+} and for other Ln^{3+} ions, making Yb^{3+} a unique case among the Ln^{3+} luminescence activators. Nonetheless, through Yb^{3+}-mediated sensitization, reaching 53% efficiency, intense NIR Er^{3+} emission at 1.5 μm with long lifetime

(~3.0 ms) and a relatively high PLQY (~6%) are observed. Our findings shed light on the energy transfer pathways in luminescent Ln^{3+}-functionalized perovskite NCs, which are also expected to be applicable for other kinds of semiconductor nanomaterials. Beyond this, novel scenarios for the development of innovative materials for silicon integrated photonics and optical devices at telecommunication wavelengths are envisaged.

References

(1) Shamsi, J.; Urban, A. S.; Imran, M.; De Trizio, L.; Manna, L. Metal Halide Perovskite Nanocrystals: Synthesis, Post-Synthesis Modifications, and Their Optical Properties. *Chem. Rev*. **2019**, *119*, 3296-3348.

(2) Akkerman, Q. A.; Rainò, G.; Kovalenko, M. V.; Manna, L. Genesis, Challenges and Opportunities for Colloidal Lead Halide Perovskite Nanocrystals. *Nat. Mater*. **2018**, *17*, 394-405.

(3) Wang, Y.; Dar, M. I.; Ono, L. K.; Zhang, T.; Kan, M.; Li, Y.; Zhang, L.; Wang, X.; Yang, Y.; Gao, X.; Qi, Y.; Grätzel, M.; Zhao, Y. Thermodynamically Stabilized β-$CsPbI_3$-Based Perovskite Solar Cells with Efficiencies >18%, *Science*. **2019**, *365*, 591-595.

(4) Duan, J.; Zhao, Y.; Wang, Y.; Yang, X.; Tang, Q. Hole-Boosted Cu(Cr, M)O_2 Nanocrystals for All-Inorganic $CsPbBr_3$ Perovskite Solar Cells. *Angew. Chem. Int. Ed*. **2019**, *58*, 16147-16151.

(5) Shoaib, M.; Zhang, X.; Wang, X.; Zhou, H.; Xu, T.; Wang, X.; Hu, X.; Liu, H.; Fan, X.; Zheng, W.; Yang, T.; Yang, S.; Zhang, Q.; Zhu, X.; Sun, L.; Pan, A. Directional Growth of Ultralong $CsPbBr_3$ Perovskite Nanowires for High-Performance Photodetectors. *J. Am. Chem. Soc*. **2017**, *139*, 15592-15595.

(6) Wang, Y.; Song, L.; Chen, Y.; Huang, W. Emerging New-Generation Photodetectors Based on Low-Dimensional Halide Perovskites. *ACS Photonics* **2020**, *7*, 10-28.

(7) Yuan, S.; Wang, Z.-K.; Zhuo, M.-P.; Tian, Q.-S.; Jin, Y.; Liao, L.-S. Self-Assembled High Quality $CsPbBr_3$ Quantum Dot Films toward Highly Efficient Light-Emitting Diodes. *ACS Nano* **2018**, *12*, 9541-9548.

(8) Yao, J.; Ge, J.; Han, B.-N.; Wang, K.-H.; Yao, H.-B.; Yu, H.-L.; Li, J.-H.; Zhu, B.-S.; Song, J.; Chen, C.; Zhang, Q.; Zeng, H.; Luo, Y.; Yu, S.-H. Ce^{3+}-Doping to Modulate Photoluminescence Kinetics for Efficient $CsPbBr_3$ Nanocrystals Based Light-Emitting Diodes. *J. Am. Chem. Soc*. **2018**, *140*, 3626-3634.

(9) Wang, X.; Chen, H.; Zhou, H.; Wang, X.; Yuan, S.; Yang, Z.; Zhu, X.; Ma, R.; Pan, A. Room-Temperature High-Performance $CsPbBr_3$ Perovskite Tetrahedral Microlasers. *Nanoscale* **2019**, *11*, 2393-2400.

(10) Song, Z.; Zhao, J.; Liu, Q. Luminescent Perovskites: Recent Advances in Theory and Experiments. *Inorg. Chem. Front*. **2019**, *6*, 2969-3011.

(11) Protesescu, L.; Yakunin, S.; Bodnarchuk, M. I.; Krieg, F.; Caputo, R.; Hendon, C. H.; Yang, R. X.; Walsh, A.; Kovalenko, M. V. Nanocrystals of Cesium Lead Halide Perovskites ($CsPbX_3$, X= Cl, Br, and I): Novel Optoelectronic Materials Showing Bright Emission with Wide Color Gamut. *Nano Lett.* **2015,** *15*, 3692-3696.

(12) Erickson, C. S.; Crane, M. J.; Milstein, T. J.; Gamelin, D. R. Photoluminescence Saturation in Quantum-Cutting Yb^{3+}-Doped $CsPb(Cl_{1-x}Br_x)_3$ Perovskite Nanocrystals: Implications for Solar Downconversion. *J. Phys. Chem. C* **2019**, *123*, 12474-12484.

(13) Mir, W. J.; Mahor, Y.; Lohar, A.; Jagadeeswararao, M.; Das, S.; Mahamuni, S.; Nag, A. Postsynthesis Doping of Mn and Yb into $CsPbX_3$ (X = Cl, Br, or I) Perovskite Nanocrystals for Downconversion Emission. *Chem. Mater*. **2018**, *30*, 8170-8178.

(14) Zhou, D.; Liu, D.; Pan, G.; Chen, X.; Li, D.; Xu, W.; Bai, X.; Song, H. Cerium and Ytterbium Codoped Halide Perovskite Quantum Dots: A Novel and Efficient

Downconverter for Improving the Performance of Silicon Solar Cells. *Adv. Mater.* **2017**, *29*, 1704149.

(15) Milstein, T. J.; Kroupa, D. M.; Gamelin, D. R. Picosecond Quantum Cutting Generates Photoluminescence Quantum Yields Over 100% in Ytterbium-Doped $CsPbCl_3$ Nanocrystals. *Nano Lett.* **2018**, *18*, 3792-3799.

(16) Pan, G.; Bai, X.; Yang, D.; Chen, X.; Jing, P.; Qu, S.; Zhang, L.; Zhou, D.; Zhu, J.; Xu, W.; Dong, B.; Song, H. Doping Lanthanide into Perovskite Nanocrystals: Highly Improved and Expanded Optical Properties. *Nano Lett.* **2017**, *17*, 8005 -8011.

(17) Hu, Q.; Li, Z.; Tan, Z.; Song, H.; Ge, C.; Niu, G.; Han, J.; Tang, J. Rare Earth Ion-Doped $CsPbBr_3$ Nanocrystals. *Adv. Opt. Mater.* **2018**, *6*, 1700864.

(18) Mir, W. J.; Sheikh, T.; Arfin, H.; Xia, Z.; Nag, A. Lanthanide Doping in Metal Halide Perovskite Nanocrystals: Spectral Shifting, Quantum Cutting and Optoelectronic Applications. *NPG Asia Mater*. **2020**, *12*, 9.

(19) Pinchetti, V.; Anand, A.; Akkerman, Q. A.; Sciacca, D.; Lorenzon, M.; Meinardi, F.; Fanciulli, M.; Manna, L.; Brovelli, S. Trap-Mediated Two-Step Sensitization of Manganese Dopants in Perovskite Nanocrystals. *ACS Energy Lett*. **2019**, *4*, 85-93.

(20) Rana, P. J. S.; Swetha, T.; Mandal, H.; Saeki, A.; Bangal, P. R.; Singh, S. P. Energy Transfer Dynamics of Highly Stable Fe^{3+} Doped $CsPbCl_3$ Perovskite Nanocrystals with Dual-Color Emission. *J. Phys. Chem. C* **2019**, *123*, 17026-17034.

(21) Cai, T.; Yang, H.; Hills-Kimball, K.; Song, J.-P.; Zhu, H.; Hofman, E.; Zheng, W.; Rubenstein, B. M.; Chen, O. Synthesis of All-Inorganic Cd-Doped $CsPbCl_3$ Perovskite Nanocrystals with Dual-Wavelength Emission. *J. Phys. Chem. Lett.* **2018**, *9*, 7079-7084.

(22) De Roo, J.; Ibáñez, M.; Geiregat, P.; Nedelcu, G.; Walravens, W.; Maes, J.; Martins, J. C.; Van Driessche, I.; Kovalenko, M. V.; Hens, Z. Highly Dynamic Ligand Binding and Light Absorption Coefficient of Cesium Lead Bromide Perovskite Nanocrystals. *ACS Nano* **2016**, *10*, 2071-2081.

(23) Duan, J.; Zhao, Y.; Yang, X.; Wang, Y.; He, B.; Tang, Q. Lanthanide Ions Doped $CsPbBr_3$ Halides for HTM-Free 10.14%-Efficiency Inorganic Perovskite Solar Cell with an Ultrahigh Open-Circuit Voltage of 1.594 V. *Adv. Energy Mater*. **2018,** *8*, 1802346.

(24) Geskus, D.; Aravazhi, S.; García-Blanco, S. M.; Pollnau, M. Giant Optical Gain in a Rare-Earth-Ion-Doped Microstructure. *Adv. Mater*. **2012**, *24*, OP19-OP22.

(25) Ye, H. Q.; Li, Z.; Peng, Y.; Wang, C. C.; Li, T. Y.; Zheng, Y. X.; Sapelkin, A.; Adamopoulos, G.; Hernández, I.; Wyatt, P. B.; Gillin, W. P. Organo-Erbium Systems for Optical Amplification at Telecommunications Wavelengths. *Nat. Mater*. **2014**, 13, 382-386.

(26) Zhou, J.; Teng, Y.; Liu, X.; Ye, S.; Ma, Z.; Qiu, J. Broadband Spectral Modification from Visible Light to Near-Infrared Radiation Using Ce^{3+}-Er^{3+} Codoped Yttrium Aluminium Garnet. *Phys. Chem. Chem. Phys.* **2010**, *12*, 13759-13762.

(27) Zhang, X.; Zhang, Y.; Zhang, X.; Yin, W.; Wang, Y.; Wang, H.; Lu, M.; Li, Z.; Gu, Z.; Yu, W. W. Yb^{3+} and Yb^{3+}/Er^{3+} Doping for Near-Infrared Emission and Improved Stability of $CsPbCl_3$ Nanocrystals. *J. Mater. Chem. C* **2018**, *6*, 10101-10105.

(28) Zhou, L.; Liu, T.; Zheng, J.; Yu, K.; Yang, F.; Wang, N.; Zuo, Y.; Liu, Z.; Xue, C.; Li, C.; Cheng, B.; Wang, Q. Dual-Emission and Two Charge-Transfer States in Ytterbium-doped Cesium Lead Halide Perovskite Solid Nanocrystals. *J. Phys. Chem. C* **2018**, *122*, 26825-26834.

(29) Dang, Z.; Shamsi, J.; Palazon, F.; Imran, M.; Akkerman, Q. A.; Park, S.; Bertoni, G.; Prato, M.; Brescia, R.; Manna, L. In Situ Transmission Electron Microscopy Study of

Electron Beam-Induced Transformations in Colloidal Cesium Lead Halide Perovskite Nanocrystals. *ACS Nano* **2017**, *11*, 2124-2132.
(30) Watanabe, K.; Koshimizu, M.; Yanagida, T.; Fujimoto, Y.; Asai, K. Luminescence and Scintillation Properties of La-and La, Ag-Doped $CsPbCl_3$ Single Crystals. *Jpn. J. Appl. Phys.* **2016**, *55*, 02BC20.
(31) Shi, H.; Du, M.-H. Shallow Halogen Vacancies in Halide Optoelectronic Materials. *Phys. Rev. B* **2014**, *90*, 174103.
(32) Zhou, Y.; Chen, J.; Bakr, O. M.; Sun, H.-T. Metal-Doped Lead Halide Perovskites: Synthesis, Properties, and Optoelectronic Applications. *Chem. Mater.* **2018**, *30*, 6589-6613.
(33) Muralidharan, M.; Thiyagarajan, R.; Sivakumar, K.; Sivaji, K. Near Infrared Emission and Enhanced Ferromagnetism in Fe Doped $SrSnO_3$ Perovskite Structured Nanorods. *J. Mater. Sci.: Mater. Electron.* **2019**, *30*, 4634-4643.
(34) Nenon, D. P.; Pressler, K.; Kang, J.; Koscher, B. A.; Olshansky, J. H.; Osowiecki, W. T.; Koc, M. A.; Wang, L.-W.; Alivisatos, A. P. Design Principles for Trap-Free $CsPbX_3$ Nanocrystals: Enumerating and Eliminating Surface Halide Vacancies with Softer Lewis Bases. *J. Am. Chem. Soc.* **2018**, *140*, 17760-17772.
(35) Buin, A.; Comin, R.; Xu, J.; Ip, A. H.; Sargent, E. H. Halide Dependent Electronic Structure of Organolead Perovskite Materials. *Chem. Mater.* **2015**, *27*, 4405-4412.
(36) Yong, Z.-J.; Guo, S.-Q.; Ma, J.-P.; Zhang, J.-Y.; Li, Z.-Y.; Chen, Y.-M.; Zhang, B.-B.; Zhou, Y.; Shu, J.; Gu, J.-L.; Zheng, L.-R.; Bakr, O. M.; Sun, H.-T. Doping-Enhanced Short-Range Order of Perovskite Nanocrystals for Near-Unity Violet Luminescence Quantum Yield. *J. Am. Chem. Soc.* **2018**, *140*, 9942-9951.
(37) Mondal, N.; De, A.; Samanta, A. Achieving Near-Unity Photoluminescence Efficiency for Blue-Violet-Emitting Perovskite Nanocrystals. *ACS Energy Lett.* **2019**, *4*, 32-39.
(38) Lau, C. F. J.; Zhang, M.; Deng, X.; Zheng, J.; Bing, J.; Ma, Q.; Kim, J.; Hu, L.; Green, M. A.; Huang, S.; Ho-Baillie, A. Strontium- Doped Low-Temperature-Processed $CsPbI_2Br$ Perovskite Solar Cells. *ACS Energy Lett.* **2017**, *2*, 2319-2325.
(39) Shannon, R. Revised Effective Ionic Radii and Systematic Studies of Interatomic Distances in Halides and Chalcogenides. *Acta. Cryst.* **1976**, *32*, 751-767.
(40) Imran, M.; Caligiuri, V.; Wang, M.; Goldoni, L.; Prato, M.; Krahne, R.; De Trizio, L.; Manna, L. Benzoyl Halides as Alternative Precursors for the Colloidal Synthesis of Lead-Based Halide Perovskite Nanocrystals. *J. Am. Chem. Soc.* **2018**, *140*, 2656-2664.
(41) Binnemans, K. Lanthanide-Based Luminescent Hybrid Materials. *Chem. Rev.* **2009,** *109*, 4283-4374.
(42) Li, X.; Duan, S.; Liu, H.; Chen, G.; Luo, Y.; Ågren, H. Mechanism for the Extremely Efficient Sensitization of Yb^{3+} Luminescence in $CsPbCl_3$ Nanocrystals. *J. Phys. Chem. Lett.* **2019**, *10*, 487-492.
(43) Vanýsek, P. Electrochemical Series. In *CRC Handbook of Chemistry and Physics*, 94th ed.; Haynes, W. M., Ed.; Taylor and Francis: Boca Raton, FL, **2014**, pp. 5-81-5-84.
(44) Ravi, V. K.; Markad, G. B.; Nag, A. Band Edge Energies and Excitonic Transition Probabilities of Colloidal $CsPbX_3$ (X = Cl, Br, I) Perovskite Nanocrystals. *ACS Energy Lett.* **2016**, *1*, 665-671.
(45) Horrocks, W. D.; Bolender, J. P.; Smith, W. D.; Supkowski, R. M. Photosensitized Near Infrared Luminescence of Ytterbium(III) in Proteins and Complexes Occurs via an Internal Redox Process. *J. Am. Chem. Soc.* **1997**, *119*, 5972-5973.

(46) Sim, K. M.; Swarnkar, A.; Nag, A.; Chung, D. S. Phase Stabilized α-$CsPbI_3$ Perovskite Nanocrystals for Photodiode Applications. *Laser Photonics Rev*. **2018**, *12*, 1700209.

(47) Gai, S. L.; Li, C. X.; Yang, P. P.; Lin, J. Recent Progress in Rare Earth Micro/Nanocrystals: Soft Chemical Synthesis, Luminescent Properties, and Biomedical Applications. *Chem. Rev*. **2014**, *114*, 2343-2389.

(48) Artizzu, F.; Quochi, F.; Marchiò, L.; Figus, C.; Loche, D.; Atzori, M.; Sarritzu, V.; Kaczmarek, A. M.; Van Deun, R.; Saba, M.; Serpe, A.; Mura, A.; Mercuri, M. L.; Bongiovanni, G.; Deplano, P. Light Conversion Control in NIR-Emissive Optical Materials Based on Heterolanthanide Er_xYb_{3-x} Quinolinolato Molecular Components. *Chem. Mater*. **2015**, *27*, 4082-4092.

(49) Xu, K.; Lin, C. C.; Xie, X.; Meijerink, A. Efficient and Stable Luminescence from Mn^{2+} in Core and Core-Isocrystalline Shell $CsPbCl_3$ Perovskite Nanocrystals. *Chem. Mater.* **2017**, *29*, 4265-4272.

(50) Arfin, H.; Kaur, J.; Sheikh, T.; Chakraborty, S.; Nag, A. Bi^{3+}-Er^{3+} and Bi^{3+}-Yb^{3+} Codoped $Cs_2AgInCl_6$ Double Perovskite Near Infrared Emitters. *Angew. Chem. Int. Ed*. **2020**, 59, 1-6.

(51) Mara, D.; Artizzu, F.; Smet, P. F.; Kaczmarek, A. M.; Van Hecke, K.; Van Deun, R. Vibrational Quenching in Near-Infrared Emitting Lanthanide Complexes: A Quantitative Experimental Study and Novel Insights. *Chem. – Eur. J.*, **2019**, *25*, 15944-15956.

(52) Lee, W.; Hong, S.; Kim, S. Colloidal Synthesis of Lead-Free Silver-Indium Double-Perovskite $Cs_2AgInCl_6$ Nanocrystals and Their Doping with Lanthanide Ions. *J. Phys. Chem. C* **2019**, *123*, 2665-2672.

(53) Deng, R.; Wang, J.; Chen, R.; Huang, W.; Liu, X. Enabling Förster Resonance Energy Transfer from Large Nanocrystals through Energy Migration. *J. Am. Chem. Soc.* **2016**, *138*, 15972-15979.

(54) Brouwer, A. M. Standards for Photoluminescence Quantum Yield Measurements in Solution. *Pure Appl. Chem.* **2011**, *83*, 2213-2228.

Supporting Information for Chapter 3

Synthetic Details, Analytical and Structural Characterization

Table S3.1. The starting amounts and X-ray fluorescence (XRF) data analysis for Er^{3+}-doped, Yb^{3+}-doped, and Yb^{3+}/Er^{3+} codoped $CsPbCl_3$ NCs with varying nominal concentrations. The amount of $Pb(CH_3CO_2)_2$ is fixed at 0.2 mmol. The lanthanide ions (Ln^{3+}) doping concentration with respect to Pb^{2+} is defined as [Ln]/([Ln] + [Pb]). It is worth noting that the actual ratio for Er^{3+}:Yb^{3+}corresponding to the 4: 1 nominal ratio is 3: 1.

Nominal ratio	**Starting amounts**		**XRF results**		
	$Er(CH_3CO_2)_3$ (mmol)	**$Yb(CH_3CO_2)_3$ (mmol)**	**Pb (%)**	**Er (%)**	**Yb (%)**
Er/Pb = 10%	0.02	—	99.4%	0.6%	—
Er/Pb = 40%	0.08	—	97.6%	2.4%	—
Er/Pb = 80%	0.16	—	96.5%	3.5%	—
Yb/Pb = 10%	—	0.02	99.1%	—	0.9%
Yb/Pb = 40% (Er^{3+}: Yb^{3+} = 0: 1)	—	0.08	97.3%	—	2.7%
Yb/Pb = 80%	—	0.16	96.0%	—	4.0%
Er^{3+}: Yb^{3+} = 0.5: 1	0.04	0.08	96.6%	1.1%	2.3%
Er^{3+}: Yb^{3+} = 1: 1	0.08	0.08	96.4%	1.8%	1.8%
Er^{3+}: Yb^{3+} = 2: 1	0.16	0.08	95.8%	2.7%	1.5%
Er^{3+}: Yb^{3+} = 4: 1	0.32	0.08	94.0%	4.6%	1.4%

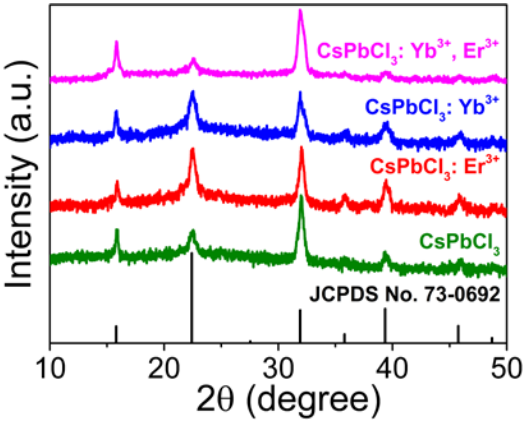

Figure S3.1 X-ray diffraction patterns of $CsPbCl_3$ NCs with and without dopants, along with the reference pattern of $CsPbCl_3$.

PL Properties of Ln^{3+}-Doped $CsPbCl_3$ NCs

Er^{3+} singly doped NCs

Table S3.2. Decay parameters of the band-edge emission (409 nm) in undoped and Er^{3+}-doped $CsPbCl_3$ NCs with varying doping concentrations. Average lifetimes: $\tau = \Sigma A_i\tau_i/\Sigma A_i$; radiative recombination rates: k_r = PLQY/τ; nonradiative recombination rates: k_{nr} = (1 – PLQY)/τ.[1]

Sample	**PLQY (%)**	**τ_1 (ns) (A_1)**	**τ_2 (ns) (A_2)**	**τ_3 (ns) (A_3)**	**τ (ns)**	**k_r (μs^{-1})**	**k_{nr} (μs^{-1})**
$CsPbCl_3$	1.2	2.0 (0.96)	16.1 (0.04)	—	2.6	4.6	380.0
0.6% Er^{3+}	6.8	3.0 (0.39)	11.4 (0.42)	39.4 (0.19)	13.4	5.1	69.5
2.4% Er^{3+}	2.9	2.4 (0.49)	8.9 (0.39)	27.8 (0.12)	8.0	3.6	121.4
3.5% Er^{3+}	1.7	2.3 (0.70)	9.6 (0.26)	32.0 (0.04)	5.4	3.1	182.0

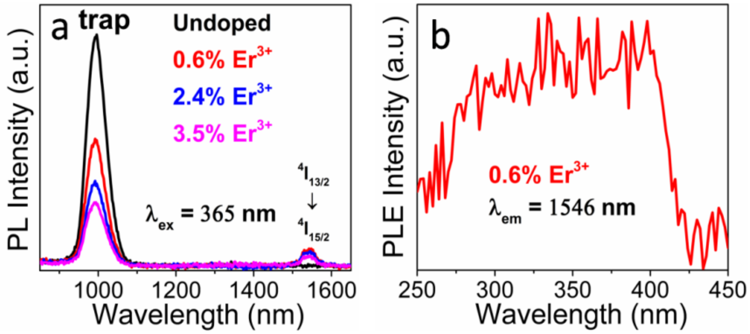

Figure S3.2 (a) PL spectra of concentrated undoped and Er^{3+}-doped CsPbCl$_3$ NCs (OD > 1 at first exciton) with varying doping concentrations under 365 nm illumination. (b) PL excitation spectrum of 0.6% Er^{3+}-doped NCs monitored at 1546 nm.

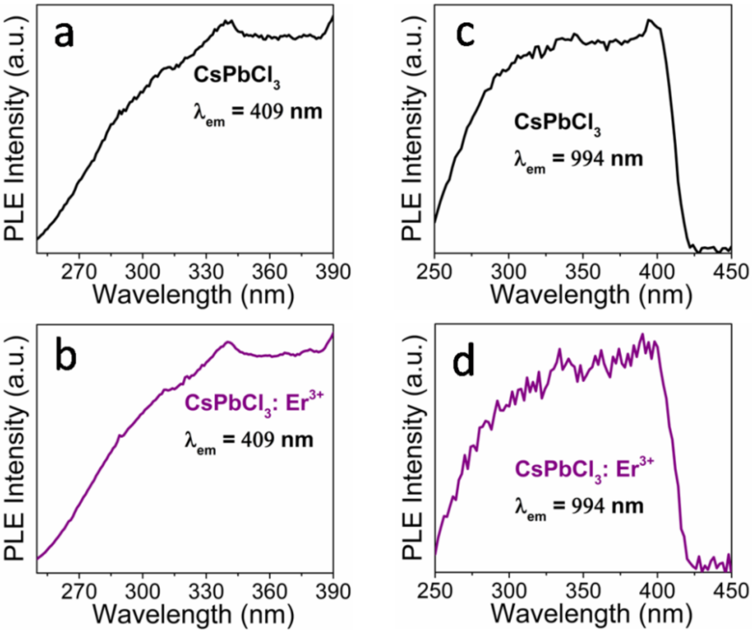

Figure S3.3 PL excitation spectra of undoped and 2.4% Er^{3+}-doped CsPbCl$_3$ NCs monitored at (a, b) 409 nm, and (c, d) 994 nm.

Lu^{3+} and Lu^{3+}/Er^{3+} codoped NCs

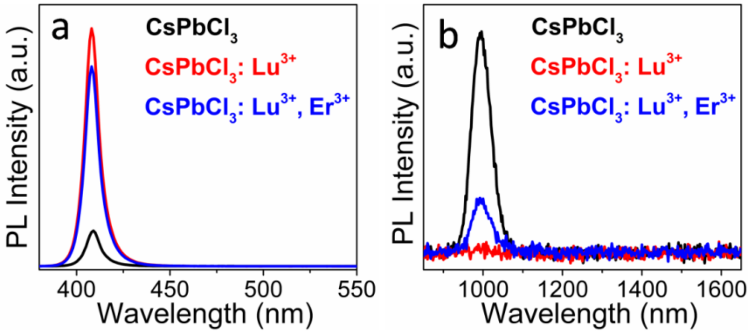

Figure S3.4 PL spectra of undoped, Lu^{3+}-doped (Lu/Pb = 1/10 nominal ratio) and Lu^{3+}/Er^{3+} codoped $CsPbCl_3$ NCs (with 1:1 nominal molar ratio) in the visible range (a), and NIR range (b) under 365 nm illumination.

Yb^{3+} and Yb^{3+}/Er^{3+} codoped NCs

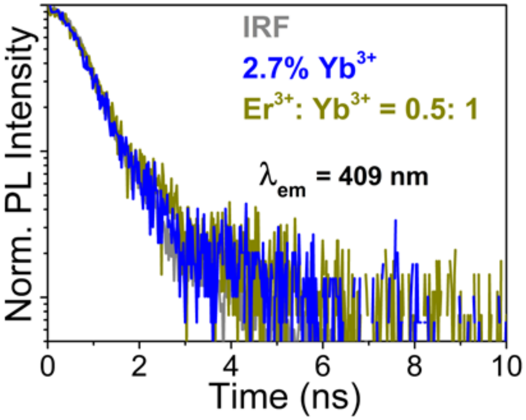

Figure S3.5. Decay curves of 2.7% Yb^{3+}-doped $CsPbCl_3$ NCs and 2.3%/1.1% Yb^{3+}/Er^{3+} codoped NCs(Er^{3+}: Yb^{3+} = 0.5: 1 ratio) monitored at 409 nm (λ_{ex} = 350 nm). The instrumental response function (IRF) was determined to be approximately 0.8 ns by measuring the scattering of a Ludox solution.

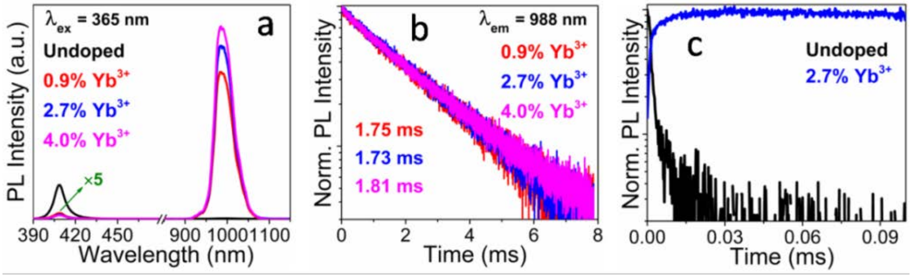

Figure S3.6 (a) PL spectra of undoped and Yb^{3+}-doped $CsPbCl_3$ NCs with varying doping concentrations under 365 nm illumination. For clarity, the intensity of the band-edge emission in Yb^{3+}-doped $CsPbCl_3$ NCs is multiplied by 5. (b) PL decay curves monitored at 988 nm ($^2F_{5/2}$ level of Yb^{3+}). (c) Comparison of PL decay curves between undoped and 2.7% Yb^{3+}-doped NCs monitored at 994 nm under the same measurement conditions. Compared to Yb^{3+}-doped NCs, the NIR emission at 994 nm from undoped NCs is negligible, suggesting that the NIR emission in Yb^{3+}-doped NCs originates from the Yb^{3+} $^2F_{5/2} \rightarrow {}^2F_{7/2}$ transition, which is further supported by the striking different decay lifetime monitored at 994 nm.

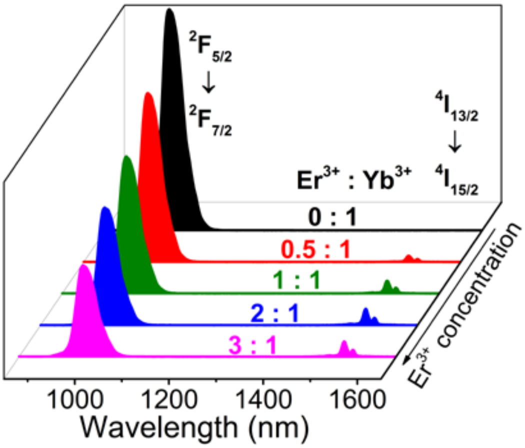

Figure S3.7. PL spectra of Yb^{3+}/Er^{3+} codoped $CsPbCl_3$ NCs versus different relative ratios (from Er^{3+}: Yb^{3+} = 0: 1 to 3: 1 ratio) under 365 nm illumination.

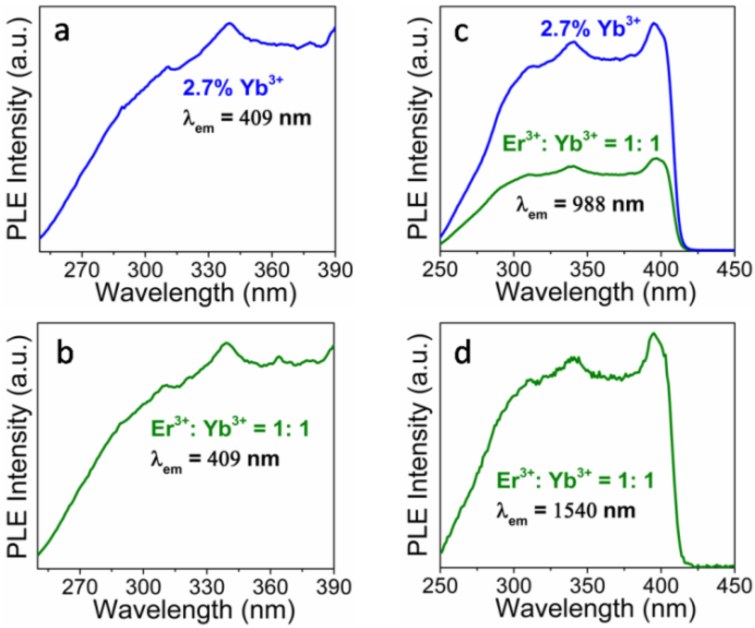

Figure S3.8 PL excitation spectra of 2.7% Yb^{3+}-doped $CsPbCl_3$ NCs and 1.8%/1.8% Yb^{3+}/Er^{3+} codoped NCs (Er^{3+}: Yb^{3+} = 1: 1 ratio) monitored at (a, b) 409 nm, (c) 988 nm and (d) 1540 nm, respectively.

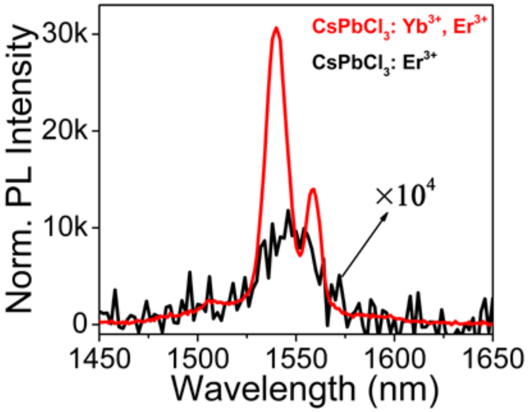

Figure S3.9 PL spectra of 1.5%/2.7% Yb^{3+}/Er^{3+} codoped $CsPbCl_3$ NCs (Er^{3+}: Yb^{3+} = 2: 1 ratio) and 0.6% Er^{3+}-doped NCs. The PL intensity is normalized by the NCs concentration.

Sensitization Mechanism

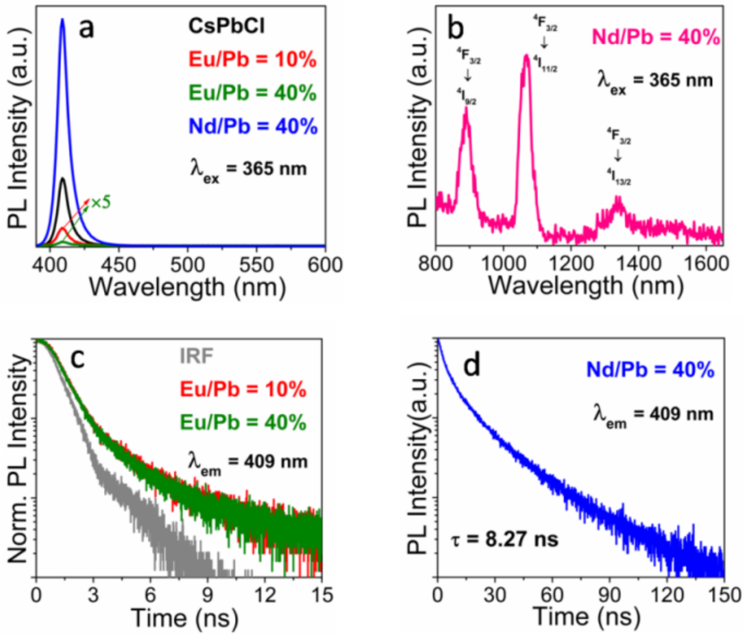

Figure S3.10 (a) PL spectra of undoped $CsPbCl_3$ NCs, Eu^{3+}-doped NCs with 10% and 40% Eu/Pb nominal ratio and Nd^{3+}-doped NCs with 40% Nd/Pb nominal ratio. (b) PL spectra of concentrated Nd^{3+}-doped $CsPbCl_3$ NCs (OD >1). (c, d) Decay curves of the Eu^{3+}-doped NCs and Nd^{3+}-doped NCs monitored at 409 nm (λ_{ex} = 350 nm).

As it can be seen from the band-edge emission decay profiles in Figure S3.10c,d, a dramatic shortening of the carriers lifetime, falling in the temporal resolution range of our PL setup (~0.8 ns), is observed in Eu^{3+}-doped NCs (Figure S3.10c) with respect to the Nd^{3+}-doped NCs (Figure S3.10d). The latter instead exhibits a multi-exponential decay with an average time constant similar to that found in 2.4% Er^{3+}-doped NCs (Table S3.2). These observations point out the role of Eu^{3+} as electron trapping center, similarly to Yb^{3+}.

The absence of a detectable emission from Eu^{3+} in contrast to the Yb^{3+} case, can be easily rationalized by taking into account some energy considerations. Previous literature reports have suggested that the halide-dependent band edge energies of $CsPbX_3$ NCs are not influenced by the particular media,[2] and Ln^{3+} doping cause only slight shift in the band gap of $CsPbCl_3$ (less than 0.1 eV) and almost unchanged conduction band (CB).[3] Hence, the conduction band values for undoped LHP taken from ref 2 are also applied for Ln^{3+}-doped LHP, and take 0.1 eV for the uncertainty of valence band. As shown in Figure 3.3 in the main text, the conduction band of $CsPbCl_3$ NCs is energetically located above the reduction potentials of the Yb^{3+}/Yb^{2+} and Eu^{3+}/Eu^{2+} couples,[4] thus Yb^{3+} and Eu^{3+} ions can undergo spontaneous reduction to divalent ions. It can be assumed that the reduction potential will shift to a more positive one (further below the LHP conduction band) in the case with the electron-donating LHP with respect to aqueous medium, leading to increased driving force for electron transfer from the conduction band of LHP to Yb^{3+} and Eu^{3+}, which are thus more easily reduced to divalent ions. These two Ln^{2+} ions are strong reducing agents, able to release the electron back to the LHP matrix. According to Horrocks,[5] the driving force of electron transfer from the Ln^{3+}/Ln^{2+} redox couple to the LHP valence band can be estimated by $-\Delta G_b = E(\mathrm{LHP}^+/\mathrm{LHP}) - E(\mathrm{Ln}^{3+}/\mathrm{Ln}^{2+})$.[6] Taking as indicative reference values the reduction potentials of Ln^{3+}/Ln^{2+} couples in aqueous medium,[4] we could roughly estimate $-\Delta G_b \approx +2.79 \pm 0.1$ eV for the Yb system, which is sufficient to leave two Yb^{3+} ions in the excited state (~1.26 eV). On the other hand, the $-\Delta G_b$ value for Eu system is estimated to be $+2.1 \pm 0.1$ eV (overestimated, attributed to a positive shift of the reduction potential as discussed before), which does not consent the excitation of the Eu^{3+} $^5D_0$ emissive state (~2.14 eV),[7] resulting in the absence of Eu^{3+} luminescence in $CsPbCl_3$ NCs.

Based on the above proposed transient internal redox mechanism for Yb^{3+} sensitization, we can predict whether the Ln^{3+} NIR emission can be obtained in the lower-band gap hosts like $CsPb(Cl/Br)_3$, $CsPbBr_3$ and $CsPbI_3$ NCs, which are more promising than $CsPbCl_3$ in optoelectronic applications due to the wider-range light aborption.[8] We notice that the proposed mechanism can also account for the intense Yb^{3+} emission in mixed halide $CsPb(Cl/Br)_3$ hosts.[9] As reported by Milstein et al., there is an energy threshold (E_g) for quantum cutting: $E_g > 2\times E_{f–f}$ (Yb^{3+} f–f transition ~980 nm). The Yb^{3+} PLQY drops rapidly when the E_g of the $CsPb(Cl/Br)_3$ host is below ~2.53 eV (~490 nm). For the pure $CsPbBr_3$ host, quantum cutting may be achieved by finely tuning the band gap through morphology/dimension or impurity doping unless the driving force $-\Delta G_b$ is sufficient (>+2.53 eV) to excite two Yb^{3+} ions. Liu et al. reported Al^{3+}-doped $CsPbBr_3$ NCs showed deep-blue emission at 456 nm (~2.72 eV).[10] Hence, Yb^{3+} codoping with another impurity (i.e., Al^{3+}) into $CsPbBr_3$ shifting the valence band below –5.98 eV as indicated by the red dotted line in Figure 3.3, could be an effective strategy to obtain quantum cutting. The prediction for $CsPbI_3$ is also consistent with the report by Nag et al.[11] In the narrowest-band gap $CsPbI_3$ host, Yb^{3+} 4f–4f transition may be highly weak, due to the negligible energy difference between the conduction band of $CsPbI_3$ (~3.45 eV below vacuum level) and Yb^{3+}/Yb^{2+} redox potential (~3.45 eV below vacuum level). Furthermore, as shown in Figure 3.3, the valence band of $CsPbI_3$ is clearly locating above the red dotted line, so quantum cutting would not take place.

References

(S1) Imran, M.; Caligiuri, V.; Wang, M.; Goldoni, L.; Prato, M.; Krahne, R.; De Trizio, L.; Manna, L. Benzoyl Halides as Alternative Precursors for the Colloidal Synthesis of Lead-Based Halide Perovskite Nanocrystals. *J. Am. Chem. Soc.* **2018**, *140*, 2656-2664.

(S2) Ravi, V. K.; Markad, G. B.; Nag, A. Band Edge Energies and Excitonic Transition Probabilities of Colloidal $CsPbX_3$ (X = Cl, Br, I) Perovskite Nanocrystals. *ACS Energy Lett.* **2016**, *1*, 665-671.

(S3) Li, X.; Duan, S.; Liu, H.; Chen, G.; Luo, Y.; Ågren, H. Mechanism for the Extremely Efficient Sensitization of Yb^{3+} Luminescence in $CsPbCl_3$ Nanocrystals. *J. Phys. Chem. Lett.* **2019**, *10*, 487-492.

(S4) Vanýsek, P. Electrochemical Series. In *CRC Handbook of Chemistry and Physics*, 94th ed.; Haynes, W. M., Ed.; Taylor and Francis: Boca Raton, FL, **2014**, pp. 5-81-5-84.

(S5) Horrocks, W. D.; Bolender, J. P.; Smith, W. D.; Supkowski, R. M. Photosensitized Near Infrared Luminescence of Ytterbium (III) in Proteins and Complexes Occurs via an Internal Redox Process. *J. Am. Chem. Soc.* **1997**, *119*, 5972-5973.

(S6) Rehm, D.; Weller, A. Kinetics of Fluorescence Quenching by Electron and H-Atom Transfer. *Isr. J. Chem*. **1970**, *8*, 259-271.

(S7) Dorenbos, P. Charge Transfer Bands in Optical Materials and Related Defect Level Location. *Opt. Mater*. **2017**, *69*, 8−22.

(S8) Sim, K. M.; Swarnkar, A.; Nag, A.; Chung, D. S. Phase Stabilized α-$CsPbI_3$ Perovskite Nanocrystals for Photodiode Applications. *Laser Photonics Rev*. **2018**, *12*, 1700209.

(S9) Milstein, T. J.; Kluherz, K. T.; Kroupa, D. M.; Erickson, C. S.; De Yoreo, J. J.; Gamelin, D. R. Anion Exchange and the Quantum-Cutting Energy Threshold in Ytterbium-Doped $CsPb(Cl_{1-x}Br_x)_3$ Perovskite Nanocrystals. *Nano Lett*. **2019**, *19*, 1931-1937.

(S10) Liu, M.; Zhong, G.; Yin, Y.; Miao, J.; Li, K.; Wang, C.; Xu, X.; Shen, C.; Meng, H. Aluminum-Doped Cesium Lead Bromide Perovskite Nanocrystals with Stable Blue Photoluminescence Used for Display Backlight. *Adv. Sci*. **2017**, *4*, 1700335.

(S11) Mir, W. J.; Mahor, Y.; Lohar, A.; Jagadeeswararao, M.; Das, S.; Mahamuni, S.; Nag, A. Postsynthesis Doping of Mn and Yb into $CsPbX_3$ (X = Cl, Br, or I) Perovskite Nanocrystals for Downconversion Emission. *Chem. Mater*. **2018**, *30*, 8170-8178.

Chapter 4 Mn^{2+}-Assisted Er^{3+} Luminescence at 1.5 µm Telecommunication Wavelength in $CsPbCl_3$ Perovskite Nanocrystals

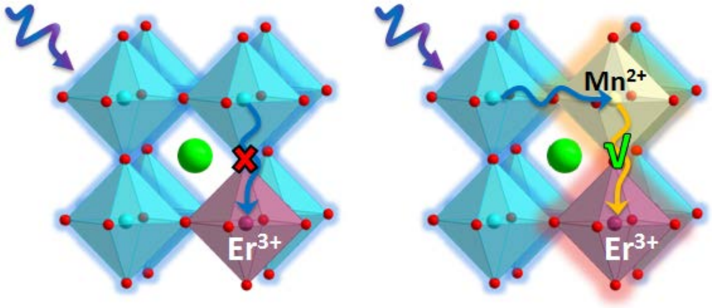

The results of this chapter are the subject of a submitted manuscript.

Abstract: The photoluminescence tuning of lead halide perovskites (LHPs) $CsPbX_3$ nanocrystals (NCs) can be achieved by varying the halide composition or introducing dopant ions. The emission wavelength of pure LHPs can not be extended to the near-infrared (NIR) spectral range beyond 750 nm by halide exchange. Consequently, enormous effort has been made to expand the LHPs emission wavelength to the NIR up to 1.0 μm. However, doping studies to achieve the very interesting NIR light above 1.5 μm, corresponding to the optical telecommunication window, are still rare, greatly impeding broader applications and further fundamental research. Herein, we present a strategy to enable intense NIR Er^{3+} emission at ~1.5 μm through a Mn^{2+}-mediated energy-transfer pathway. Steady-state and time-resolved photoluminescence studies show that the energy-transfer efficiencies of about 39% from Mn^{2+} to Er^{3+} is obtained, leading to the photoluminescence quantum yield of ~0.8%. This work provides guidance on constructing energy-transfer pathways in semiconductors opening new perspectives for the development of Er-functionalized LHPs as promising materials for optoelectronic devices operating at telecommunication wavelengths.

4.1 Introduction

Cesium lead halide perovskites (LHPs) $CsPbX_3$ ($X=Cl^-$, Br^-, I^-) nanocrytals (NCs) have attracted extensive interests due to their fascinating optical and electrical properties, which can find promising applications in photovoltaics and optoelectronics.[1-5] However, the $CsPbX_3$ LHPs are direct bandgap semiconductors with bandgaps ranging between ~3.1 – 1.7 eV (410 – 700 nm) yielding photoluminescence (PL) properties limited to the visible region.[6-9] It has been shown that introducing intermediate states in the mid bandgap of the host by metal ions doping, particularly for Yb^{3+} ions, is an efficient strategy to tune the emission of the LHP hosts to the near-infrared (NIR) region.[10-16] Nonetheless, the upper bound of the emission wavelength still remains below 1.0 μm, which restricts applications to some extent, such as photonic integrated devices and telecommunications. Therefore, it is highly desired to find a proper dopant to further expand the emission of LHP hosts. In contrast to Yb^{3+} with emission at ~ 1.0 μm in LHP, Er^{3+} with a transition $^4I_{13/2} \rightarrow {}^4I_{15/2}$ at ~1.5 μm[17,18] has been less explored as optically active dopant in LHPs.[19-22] However, unlike Yb^{3+}-doped $CsPbCl_3$ exhibiting extremely intense Yb^{3+} NIR emission at ~1.0 μm through a quantum-cutting effect,[13,15,23] the Er^{3+} analogs unexpectedly show negligible Er^{3+} emission at ~1.5 μm, likely due to an inefficient sensitization through the LHP matrix. These anomalous phenomena make Yb^{3+} a special case among the NIR lanthanide emitters, which is likely related to the much higher redox potential of the Yb^{3+}/Yb^{2+} pair than the Er^{3+} case. Therefore, the photoinduced electrons can be swiftly transferred from the $CsPbCl_3$ conduction band to the Yb^{3+} ions but this mechanism is not viable for Er^{3+} and other lanthanide ions such as Nd^{3+}. The weak PL properties displayed by Er^{3+} have motivated researchers to utilize Yb^{3+} as a suitable sensitizer for Er^{3+} thanks to the resonance of its $^2F_{5/2}$ level with the Er^{3+} $^4I_{11/2}$ one in the $CsPbCl_3$ NC host. Few inspired works have been reported on the enhancement of Er^{3+} emission at ~1.5 μm by the introduction of Yb^{3+} in the $CsPbCl_3$ NC.[19,20] Very recently, the PL performance of Er^{3+} has been further improved by adopting an optimized synthesis and more insights have been given into the intrinsic energy sensitization mechanism as described in Chapter 3.

Until now, Yb^{3+} is the only reported sensitizer for Er^{3+} emitter in $CsPbCl_3$ NCs. Recently, Nag et al. investigated Bi^{3+} as a new sensitizer for Er^{3+} in $Cs_2AgInCl_6$ double perovskites, and obtained a dramatically enhanced Er^{3+} 1540 nm emission and lifetime.[24] It is highly desired and significant to explore more abundant alternative sensitizers and disentangle the sensitization mechanism in the excellent $CsPbCl_3$ host, which is the main motive for this study. The proper selection of a sensitizer for Er^{3+} should consider the spectral overlap (energy matching) between the sensitizer (donor) emission and the Er^{3+} (acceptor) absorption. Er^{3+} has multiple absorption bands at ~520 nm, 540 nm, 650 nm and 980 nm, corresponding to transitions which originate from the ground state $^4I_{15/2}$ to the upper states $^2H_{11/2}$, $^4S_{3/2}$, $^4F_{9/2}$ and $^4I_{11/2}$, respectively.[25] Among the various metal cation dopants so far explored in the $CsPbCl_3$ matrix, Mn^{2+} is the most investigated one, and Yb^{3+} is the most efficiently sensitized exhibiting extraordinary high photoluminescence quantum yield (PLQY). Mn^{2+}- and Yb^{3+}-doped $CsPbCl_3$ LHPs show intense emissions at ~600 nm with broad band of ~90 nm fwhm (full width at half-maximum) originating from the $^4T_1 \rightarrow {}^6A_1$ transition and $^2F_{5/2} \rightarrow {}^2F_{7/2}$ transition at ~1000 nm (fwhm ≈ 50 nm), respectively.[8,20,26-32] Notably, these two emission spectra overlap with the above mentioned Er^{3+} absorption lines. Indeed, Yb^{3+} ion has been reported to be a good sensitizer for Er^{3+} due to the resonance between the Yb^{3+} $^2F_{5/2}$ level and Er^{3+} $^4I_{11/2}$ level.[33] Energy transfer in the Mn^{2+}–Er^{3+} pairs has also been well investigated in the other materials hosts, such as fluorides,[33] phosphors[34] and ceramics,[35] but not in LHPs. Compared to these insulating materials for the lanthanide hosting, the LHPs show large molar extinction coefficient, high excitation densities and semiconducting properties, which will be beneficial for the development of photonic devices working at telecom wavelengths.

Here, we demonstrate the viability of Mn^{2+} as an alternative sensitizer to enhance the Er^{3+} luminescence at ~1540 nm in $CsPbCl_3$ NCs owing to an efficient multistep energy-transfer pathway. The advantages of replacing Yb^{3+} with Mn^{2+} are: i) lower cost, ii) doping feasibility, iii) wider emission spectrum, i.e. higher probability for spectral overlap with lanthanide acceptors (Figure S4.1). In Mn^{2+}–Er^{3+} codoped NCs, the broad emission band of Mn^{2+} peaked at 600 nm is largely quenched by efficient energy transfer to Er^{3+}, giving rise to an intense NIR emission at ~1542 nm with ~0.8% of PLQY. In this system, Mn^{2+} serves as a long-lived intermediate energy-transfer donor (τ_{Mn} ~1.30 ms) for the sequential energy transfer. These findings can inspire future research on the tunability of the optical properties of semiconductors, making them attractive for applications in different fields.

4.2 Experimental Section

4.2.1 Sample Preparation

Synthesis of undoped $CsPbCl_3$ NCs: Undoped $CsPbCl_3$ NCs were synthesized based on the procedure reported in literature.[22] Briefly, 0.2 mmol of $Pb(CH_3CO_2)_2·3H_2O$ and 0.28 mL of 0.1 M $CsCH_3CO_2$ ethanol solution, 5 mL of ODE, 1 mL of OA and 0.5 mL of OLA were mixed in a three-neck flask. The reaction vessel was degassed under vacuum at 120 °C for 1 h under continuous stirring. Then the reaction mixture was heated to 240 °C and a mixture of 0.2 mL of TMS-Cl and 0.5 mL of ODE is swiftly injected under N_2 flow. The reaction was then immediately quenched by immersion in a room-temperature water bath. The crude solution was centrifuged for 15 min and the supernatant was discarded. The obtained pellet was dispersed in hexane, washed with ethyl acetate twice, then redispersed in hexane and allowed to settle down overnight. The NCs were obtained by separating the upper layer of the solution and then stored in a glass vial under ambient conditions for further characterization.

Synthesis of Mn^{2+} doped $CsPbCl_3$ NCs: The synthetic procedure was very similar to that for the above undoped $CsPbCl_3$ NCs, except for the addition of $Mn(CH_3CO_2)_2{\cdot}4H_2O$. For 1.41% Mn^{2+} -doped $CsPbCl_3$ NCs, 0.01 mmol of $Mn(CH_3CO_2)_2{\cdot}4H_2O$ precursor was added.

Synthesis of Er^{3+} doped $CsPbCl_3$ NCs: The synthetic procedure was very similar to that for the undoped $CsPbCl_3$ NCs, except for the addition of $Er(CH_3CO_2)_3{\cdot}4H_2O$ precursor.

Synthesis of Mn^{2+}/Er^{3+} codoped $CsPbCl_3$ NCs: The synthetic procedure was very similar to that for undoped $CsPbCl_3$ NCs, except for the addition of $Er(CH_3CO_2)_3{\cdot}4H_2O$ and $Mn(CH_3CO_2)_2{\cdot}4H_2O$ precursors with different relative amounts.

4.2.1 Characterization

Powder X-ray diffraction (XRD) investigation was carried out on a Thermo Scientific ARL X'TRA diffractometer with Cu K_α ($\lambda = 1.5406$ Å) radiation over the range of $2\theta = 10 - 50°$. Doping concentrations with respect to Pb in the sample were determined using an X-ray fluorescence (XRF) spectrometer (Rigaku NEX-CG). Transmission electron microscopy (TEM) images were collected on a Cs-corrected JEOL 2200FS microscope operated at 200 kV. UV-vis absorption spectra were recorded with a Perkin Elmer Lambda 950 spectrometer. Steady-state and time-resolved photoluminescence (PL) were measured by a FLS920 spectrofluorometer (Edinburgh Instruments) equipped with a 450 W xenon lamp.

The luminescence signals in the visible and NIR spectral range were detected using a photomultiplier (PMT) (Hamamatsu, R928P) and a liquid N_2 cooled PMT (Hamamatsu, R5509-72), respectively. A pulsed xenon microsecond flash lamp μF900H (pulse frequency 100 Hz, 60 W) and a hydrogen-filled nanosecond flash lamp nF900 (pulse frequency 40 kHz, 150 W) were employed as the excitation sources for slow decay process and fast decay process, respectively. The instrument response function (IRF) was obtained from a nonfluorescing suspension of colloidal silica LUDOX.

Absolute PLQYs of the NCs band-edge emission and Mn^{2+} emission were measured using an integrating sphere (Edinburgh Instruments) connected to the FLSP920 spectrofluorometer. Relative NIR PLQYs of Er^{3+} emission were measured using $[Ru(bpy)_3]^{2+}$ ($C_{30}H_{24}Cl_2N_6Ru\cdot 6H_2O$) dissolved in water as reference standard ($\Phi = 0.04$), according to the protocol described in ref 36. An uncertainty of 10% is estimated on the retrieved values.

4.3 Results and Discussion

Mn^{2+}-doped $CsPbCl_3$ NCs with different doping concentrations were firstly synthesized using manganese acetate as the dopant precursor. The PL measurement results reveal that the $CsPbCl_3$ NCs doped with 1.41% Mn^{2+} doping concentration (relative to Pb^{2+}), as determined from X-ray fluorescence (XRF) measurement show the highest PLQY of about 28% for Mn^{2+} emission (Figure S4.2), similarly to previous reports.[8,27-29] A series of Mn^{2+}–Er^{3+} codoped NCs with different Er^{3+} contents while keeping the nominal Mn^{2+} contents fixed were synthesized. The actual Mn^{2+}–Er^{3+} concentrations with 1/2 Mn^{2+}/Er^{3+} nominal ratio in the codoped sample were measured to be 1.03%/0.24% by XRF analysis. The much higher doping efficiency of Mn^{2+} relative to Er^{3+} in the codoped NCs is likely due to the favorable isovalent substitution of Pb^{2+} by Mn^{2+}. Moreover, Mn^{2+} is softer than Er^{3+}, which suggests that the Mn^{2+} preferentially binds to the soft LHP matrix based on the hard and soft acid base (HSAB) principle.[37] The introduction of low amount of Er^{3+} (0.24%) dopant does not alter the morphology and crystal structure of the Mn^{2+}-doped $CsPbCl_3$ NCs. As shown in Figure 4.1a,b, the 1.41% Mn^{2+} singly doped and 1.03% Mn^{2+}–0.24% Er^{3+} codoped $CsPbCl_3$ NCs exhibit quasi-cubic shapes with the average edge length of ~13 nm. Figure 4.1c depicts the X-ray diffraction (XRD) patterns of undoped and doped $CsPbCl_3$ NCs. No obvious extra diffraction peaks were detected after low-amount of dopants addition, suggesting the formation of highly crystalline $CsPbCl_3$ NCs. A close inspection of the XRD patterns reveals that the peaks at ~32° shift slightly toward higher angles upon dopant incorporation, likely resulting from the successful substitution of larger Pb^{2+} ions by smaller Mn^{2+} and Ln^{3+} ions, which has also been observed in earlier reports.[38]

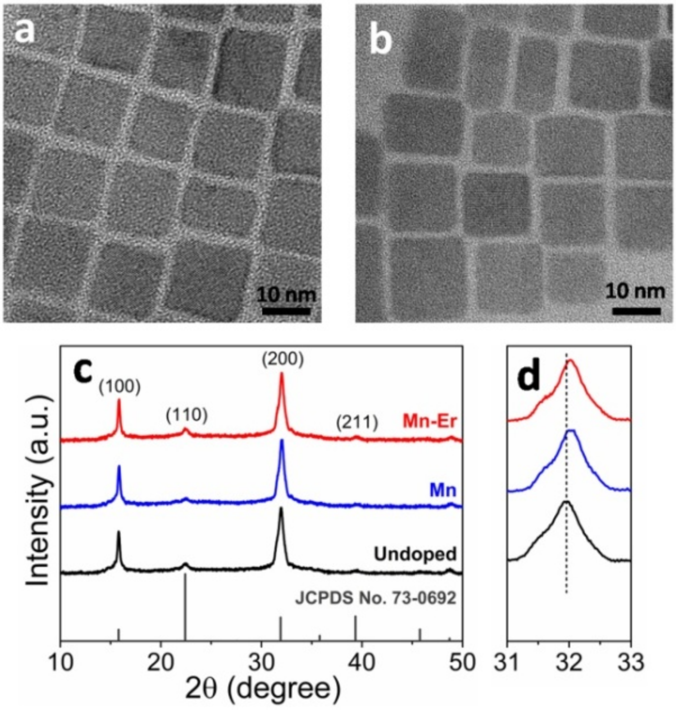

Figure 4.1 TEM images of $CsPbCl_3$ NCs doped with (a) 1.41% Mn^{2+}, (b) 1.03% Mn^{2+}–0.24% Er^{3+}. (c) XRD patterns of undoped and doped NCs, along with the reference bulk patterns for cubic $CsPbCl_3$. (d) Magnified view of the XRD patterns.

Figure 4.2a shows the absorption spectra of undoped and doped $CsPbCl_3$ NCs. The undoped and Er^{3+} singly doped $CsPbCl_3$ NCs show similar absorption spectra, displaying the band-edge absorption peak at ~403 nm. Upon Mn^{2+} and Ln^{3+} codoping, the band-edge absorption peak shows a slight blue-shift, which is probably attributed to the contraction of the perovskite cubic unit cell due to the substitution of Pb^{2+} mainly by Mn^{2+}, consistent with the XRD results and previous reports.[38] Interestingly, the absorption spectral profile of Mn^{2+}–Er^{3+} codoped NCs shows an additional peak around 380 nm with respect to the undoped NCs. The origin of this peak is not clarified, but from a comparison of the spectral shapes of the different samples we may tentatively suggest that it stems from a Mn^{2+}

absorption feature which is significantly blue shifted in the presence of the Er^{3+} codopants.

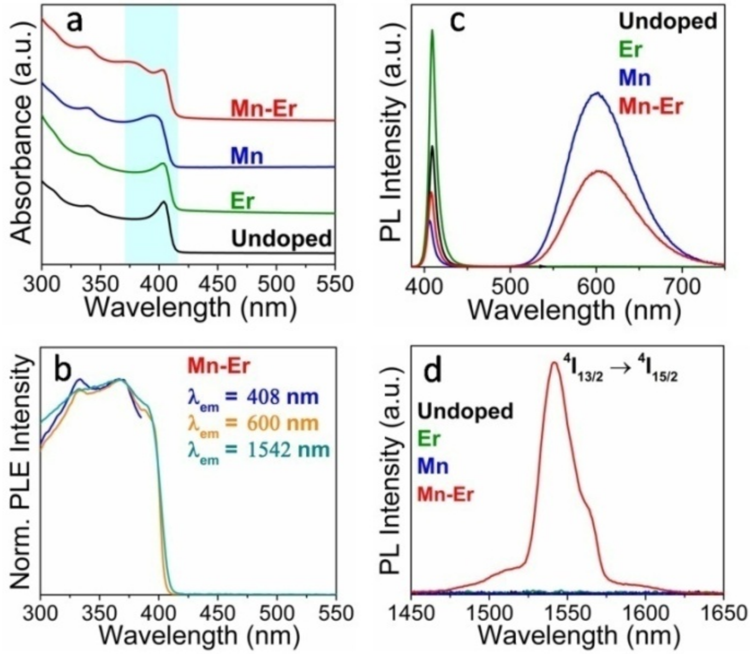

Figure 4.2 Optical properties of undoped and doped CsPbCl$_3$ NCs with Er^{3+}, Mn^{2+}, and Mn^{2+}–Er^{3+}. (a) Absorption spectra. (b) Normalized PL excitation spectra of the codoped NCs monitored at 408 nm, 600 nm and 1542 nm, respectively. (c) PL spectra in the visible range. (d) PL spectra in the NIR range under 365 nm excitation.

Figure 4.2c compares the Mn^{2+} luminescence intensity change after Er^{3+} codoping under excitation at 365 nm. The band-edge emission intensity of the LHPs host is significantly quenched after Mn^{2+} doping; however, it becomes more intense after single Er^{3+} doping. This trend is also reflected by the change of the decay dynamics of the band-edge charge carriers reported in Figure S4.3. The remarkable shortening of the band-edge carrier lifetime in the presence of Mn^{2+} with respect to the undoped NCs is in fact consistent with the efficient energy de-excitation of the CsPbCl$_3$ matrix by the activation of Mn^{2+} higher energy states, giving rise to the characteristic broad (fwhm ≈ 90 nm) Mn^{2+} emission band centered at ~600 nm, corresponding to the $^4T_1 \rightarrow {}^6A_1$ transition.[30,39] On the other hand, the negligible Er^{3+} emission peak in the NIR range (Figures 4.2d) and the increased PL intensity and lifetime of the band-edge carrier lifetime are indicative of a very inefficient Er^{3+} sensitization in the $CsPbCl_3$ host containing no Mn^{2+} but only Er^{3+}. The introduction of Er^{3+} in the $CsPbCl_3$ matrix is likely to induce a removal of deep trap states related to Cl^- vacancies[22] or enhanced lattice order through host relaxation,[40] thus leading to band-edge emission improvement. In turn, the PL intensity of Mn^{2+} emission is reduced upon the introduction of Er^{3+}. Importantly, an intense NIR emission at ~1542 nm ascribed to the Er^{3+} typical 4f–4f transition $^4I_{13/2} \rightarrow {}^4I_{15/2}$ is emerging in the Mn^{2+}–Er^{3+} codoped NCs (Figure 4.2d). This newly emerged NIR emission indicates efficient energy transfer from Mn^{2+} to Er^{3+} in the codoped NCs. The excitation spectra collected by monitoring the host band-edge emission at 408 nm, Mn^{2+} emission at 600 nm and Er^{3+} emission at 1542 nm closely follow the absorption profiles (Figure 4.2a,b), resembling a sequential energy transfer route: $CsPbCl_3$ host → Mn^{2+}→ Er^{3+}.

A systematic study on the Er^{3+} concentration effect on the PL properties of Mn^{2+}–Er^{3+} codoped NCs shows that the PL intensity of the Er^{3+} NIR emission at 1542 nm increases slightly with increasing the Er^{3+} concentration and then decreases when further elevating the concentration over 0.24% (Figure S4.4a). It is noteworthy that the Er^{3+} PL intensity quenching is not attributed to concentration quenching, which is supported by the fact that the lifetime of the $^4I_{13/2} \rightarrow {}^4I_{15/2}$ transition remains almost the same (~2.2 ms) even in doped NCs with the highest Er^{3+} concentration (Figure S4.4b). As already observed in Yb^{3+}–Er^{3+} codoped $CsPbCl_3$ NCs in previous work,[22] this behavior can be possibly ascribed to a competing nonradiative decay channel through Er^{3+}-induced shallow trap states depleting electrons from the host conduction band (*vide infra*). In addition, the

Mn^{2+} concentration is slightly decreased when the Er^{3+} concentration is further increased. Hence, less excitations are injected to Mn^{2+} resulting in less sensitized Er^{3+} centers. The PLQY of Er^{3+} emission is measured to be ~0.8% for the most intensely emitting sample of 1.03% Mn^{2+}–0.24% Er^{3+} codoped NCs. These PLQYs of NIR emission are not high but reasonable due to the strong susceptibility to nonradiative deactivation of the luminescence by oscillators in surrounding ligands or solvent molecules.[41,42] The PLQY here remains lower than that in Yb^{3+}/Er^{3+} codoped analogs (6%).[22] A more in-depth insight into the possible sensitization mechanism is then necessary to account for the lower efficiency with respect to Yb^{3+} case.

To evaluate the energy-transfer efficiency from Mn^{2+} to Er^{3+}, the PL decay dynamics of the Mn^{2+} d–d transition at 600 nm was measured upon excitation at 365 nm (Figure 4.3a). The Mn^{2+} singly doped NCs exhibit a nearly monoexponential decay behavior with an average lifetime of 1.30 ms, consistent with the forbidden nature of the Mn^{2+} $^4T_1 \rightarrow {}^6A_1$ transition. Upon Er^{3+} introduction, the Mn^{2+} PL decay becomes faster and displays a biexponential dynamics. The short Mn^{2+} decay component (τ_1 = 0.27 ms) is likely attributed to the energy transfer channel to the Er^{3+}, whereas the longer one (τ_2 = 1.19 ms), nearly consistent with that observed in singly doped NCs, is ascribed to a population (almost half of the total) of Mn^{2+} ions not transferring to the emitters. The average Mn^{2+} lifetime of codoped NCs monitored at 600 nm is estimated to be 0.79 ms, yielding 39.2% of energy transfer efficiency (See Table S4.1 for details).

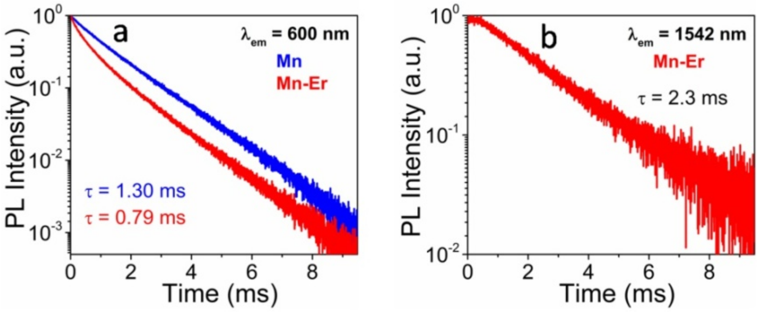

Figure 4.3 PL decay profiles of (a) Mn^{2+}-doped and Mn^{2+}–Er^{3+} codoped NCs monitored at 600 nm (Mn^{2+} emission), (b) Mn^{2+}–Er^{3+} codoped NCs monitored at 1542 nm (Er^{3+} emission). The excitation wavelength was 365 nm.

Figure 4.3b shows the PL decay dynamics of Er^{3+} emission at 1542 nm for Mn^{2+}–Er^{3+} codoped $CsPbCl_3$ NCs. The decay curve exhibits a nearly monoexponential dynamics with an average lifetime of 2.3 ms, which is consistent with the parity-forbidden nature of 4f–4f transitions. It is worth underlining that the long lifetime and monoexponential trend are indicative of a population of Er^{3+} emitters on a single doping site, presumably in the bulk of the LHP matrix. Surface Er^{3+} ions are in fact expected to yield a much faster decay due to severe quenching phenomena related to the environment (e.g., vibrational quenching, surface defect quenching).[43]

The possible energy-transfer mechanism in the Mn^{2+}–Er^{3+} codoped $CsPbCl_3$ NCs is illustrated in Scheme 4.1. Under UV excitation, the electrons in the LHP valence band are excited into the conduction band, a process followed by the radiative recombination with the holes in the valence band. The excitation energy is then transferred to the d-state of Mn^{2+}, promoting the $^4T_1 \rightarrow {}^6A_1$ transition. As shown in Scheme 4.1, the $^4F_{9/2}$ energy level of Er^{3+} is located below the $^4T_1$ level of Mn^{2+}, signifying that it can be populated by nonradiative energy transfer from Mn^{2+}. Excited Er^{3+} ions will then undergo a cascade relaxation to the lower $^4I_{11/2}$ level and then to the $^4I_{13/2}$ level, which will release a photon, corresponding to the 1542 nm emission. At higher Er^{3+} doping concentration, the population of Er^{3+}-induced trap states, only giving rise to nonradiative decay, becomes more competitive, as previously observed in Er^{3+} singly doped NCs presented in Chapter 3. This results in the reduction of radiative band-edge electron-hole recombination. Therefore, the sequential energy-transfer pathway of $CsPbCl_3$ host → Mn^{2+} → Er^{3+} is hampered. Instead, in the absence of Mn^{2+}, excitons are depleted by lanthanide ions (Ln^{3+}) induced shallow traps which can solely undergo electron transfer to Ln^{3+} ions with a lower redox potential such as Yb^{3+} or give rise to nonradiative charge carriers recombination.[22] Therefore, Mn^{2+} is key to activate NIR emission from Ln^{3+} ions that do not satisfy the requirement for redox-mediated energy transfer. This work will open up the opportunity to trigger LHP emission throughout the NIR spectral range.

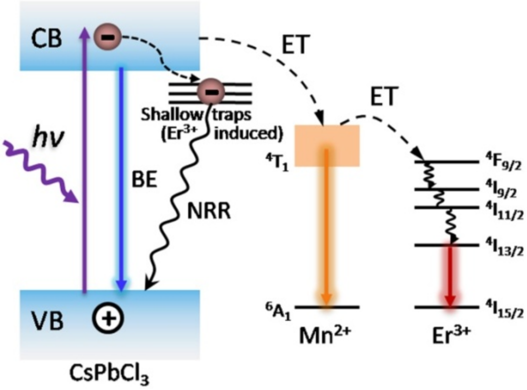

Scheme 4.1 Schematic energy-level diagram illustrating the possible energy-transfer mechanism in Mn^{2+}–Er^{3+} codoped $CsPbCl_3$ NCs under UV excitation. The blue vertical arrow represents the host band-edge (BE) emission, the orange vertical arrow corresponds to the Mn^{2+} d–d transition, the red vertical arrow to the Er^{3+} f–f transition, and the black zigzag arrow depicts the nonradiative recombination (NRR). Energy transfer (ET) processes are indicated by black dashed arrows.

4.4 Conclusions

In summary, we have designed a facile strategy to extend and boost the emission output of $CsPbCl_3$ NCs to the NIR range. The co-incorporation of Mn^{2+}, with broad emission at 600 nm, enables the efficient sensitization of Er^{3+}, emitters, so far inaccessible in LHPs hosts, through a bridged energy-transfer pathway: $CsPbCl_3$ host → Mn^{2+} → Er^{3+}. As a result, the NIR emission intensity of Er^{3+} at 1542 nm is dramatically enhanced, reaching up ~0.8% PLQY thanks to the 39% energy transfer efficiency. This work not only possesses great significance in regard to the fundamental understanding of the doping and optical properties of LHPs, but also shows promising potential for the development of a novel class of materials for applications in lasers and optical telecommunication technology.

References

(1) Kovalenko, M. V.; Protesescu, L.; Bodnarchuk, M. I. Properties and Potential Optoelectronic Applications of Lead Halide Perovskite Nanocrystals. *Science* **2017**, *358*, 745-750.

(2) Shamsi, J.; Urban, A. S.; Imran, M.; De Trizio, L.; Manna, L. Metal Halide Perovskite Nanocrystals: Synthesis, Post-Synthesis Modifications, and Their Optical Properties. *Chem. Rev.* **2019**, *119*, 3296-3348.

(3) Quan, L. N.; Rand, B. P.; Friend, R. H.; Mhaisalkar, S. G.; Lee, T.-W.; Sargent, E. H. Perovskites for Next-Generation Optical Sources. *Chem. Rev.* **2019**, *119*, 7444-7477.

(4) Dong, H.; Zhang, C.; Liu, X.; Yao, J.; Zhao, Y. S. Materials Chemistry and Engineering in Metal Halide Perovskite Lasers. *Chem. Soc. Rev.* **2020**, *49*, 951-982.

(5) Faheem, M. B.; Khan, B.; Feng, C.; Farooq, M. U.; Raziq, F.; Xiao, Y.; Li, Y. All-Inorganic Perovskite Solar Cells: Energetics, Key Challenges, and Strategies toward Commercialization. *ACS Energy Lett.* **2020**, *5*, 290-320.

(6) Protesescu, L.; Yakunin, S.; Bodnarchuk, M. I.; Krieg, F.; Caputo, R.; Hendon, C. H.; Yang, R. X.; Walsh, A.; Kovalenko, M. V. Nanocrystals of Cesium Lead Halide Perovskites ($CsPbX_3$, X= Cl, Br, and I): Novel Optoelectronic Materials Showing Bright Emission with Wide Color Gamut. *Nano Lett.* **2015**, *15*, 3692-3696.

(7) Ravi, V. K.; Markad, G. B.; Nag, A. Band Edge Energies and Excitonic Transition Probabilities of Colloidal $CsPbX_3$ (X = Cl, Br, I) Perovskite Nanocrystals. *ACS Energy Lett.* **2016**, *1*, 665-671.

(8) Liu, W.; Lin, Q.; Li, H.; Wu, K.; Robel, I.; Pietryga, J. M.; Klimov, V. I. Mn^{2+}-Doped Lead Halide Perovskite Nanocrystals with Dual-Color Emission Controlled by Halide Content. *J. Am. Chem. Soc.* **2016**, *138*, 14954-14961.

(9) Imran, M.; Caligiuri, V.; Wang, M.; Goldoni, L.; Prato, M.; Krahne, R.; De Trizio, L.; Manna, L. Benzoyl Halides as Alternative Precursors for the Colloidal Synthesis of Lead-Based Halide Perovskite Nanocrystals. *J. Am. Chem. Soc.* **2018**, *140*, 2656-2664.

(10) Mir, W. J.; Sheikh, T.; Arfin, H.; Xia, Z.; Nag, A. Lanthanide Doping in Metal Halide Perovskite Nanocrystals: Spectral Shifting, Quantum Cutting and Optoelectronic Applications. *NPG Asia Materials* **2020**, *12*, 9.

(11) Song, Z.; Zhao, J.; Liu, Q. Luminescent Perovskites: Recent Advances in Theory and Experiments. *Inorg. Chem. Front.* **2019**, *6*, 2969-3011.

(12) Zhou, D.; Sun, R.; Xu, W.; Ding, N.; Li, D.; Chen, X.; Pan, G.; Bai, X.; Song, H. Impact of Host Composition, Codoping, or Tridoping on Quantum-Cutting Emission of Ytterbium in Halide Perovskite Quantum Dots and Solar Cell Applications. *Nano Lett.* **2019**, *19*, 6904-6913.

(13) Pan, G.; Bai, X.; Yang, D.; Chen, X.; Jing, P.; Qu, S.; Zhang, L.; Zhou, D.; Zhu, J.; Xu, W.; Dong, B.; Song, H. Doping Lanthanide into Perovskite Nanocrystals: Highly Improved and Expanded Optical Properties. *Nano Lett.* **2017**, *17*, 8005-8011.

(14) Zhou, D.; Liu, D.; Pan, G.; Chen, X.; Li, D.; Xu, W.; Bai, X.; Song, H. Cerium and Ytterbium Codoped Halide Perovskite Quantum Dots: A Novel and Efficient Downconverter for Improving the Performance of Silicon Solar Cells. *Adv. Mater.* **2017**, *29*.

(15) Milstein, T. J.; Kroupa, D. M.; Gamelin, D. R. Picosecond Quantum Cutting Generates Photoluminescence Quantum Yields over 100% in Ytterbium-Doped $CsPbCl_3$ Nanocrystals. *Nano Lett.* **2018**, *18*, 3792-3799.

(16) Milstein, T. J.; Kluherz, K. T.; Kroupa, D. M.; Erickson, C. S.; De Yoreo, J. J.; Gamelin, D. R. Anion Exchange and the Quantum-Cutting Energy Threshold in Ytterbium-Doped $Cspb(Cl_{1-x}Br_x)_3$ Perovskite Nanocrystals. *Nano Lett.* **2019**, *19*, 1931-1937.

(17) Tan, M.; Li, F.; Wang, X.; Fan, R.; Chen, G. Temporal Multilevel Luminescence Anticounterfeiting through Scattering Media. *ACS Nano* **2020,** *14*, 6532–6538

(18) Xu, J.; Gulzar, A.; Yang, P.; Bi, H.; Yang, D.; Gai, S.; He, F.; Lin, J.; Xing, B.; Jin, D. Recent Advances in Near-Infrared Emitting Lanthanide-Doped Nanoconstructs: Mechanism, Design and Application for Bioimaging. *Coord. Chem. Rev.* **2019**, *381*, 104-134.

(19) Zhou, L.; Liu, T.; Zheng, J.; Yu, K.; Yang, F.; Wang, N.; Zuo, Y.; Liu, Z.; Xue, C.; Li, C.; Cheng, B.; Wang, Q. Dual-Emission and Two Charge-Transfer States in Ytterbium-Doped Cesium Lead Halide Perovskite Solid Nanocrystals. *J. Phys. Chem. C* **2018**, *122*, 26825-26834.

(20) Zhang, X.; Zhang, Y.; Zhang, X.; Yin, W.; Wang, Y.; Wang, H.; Lu, M.; Li, Z.; Gu, Z.; Yu, W. W. Yb^{3+} and Yb^{3+}/Er^{3+} Doping for Near-Infrared Emission and Improved Stability of $CsPbCl_3$ Nanocrystals. *J. Mater. Chem. C* **2018**, *6*, 10101-10105.

(21) Zhu, Y.; Pan, G.; Shao, L.; Yang, G.; Xu, X.; Zhao, J.; Mao, Y. Effective Infrared Emission of Erbium Ions Doped Inorganic Lead Halide Perovskite Quantum Dots by Sensitization of Ytterbium Ions. *J. Alloy. Comp.* **2020**, 155390.

(22) Zeng, M.; Artizzu, F.; Liu, J.; Singh, S.; Locardi, F.; Mara, D.; Hens, Z.; Van Deun, R. Boosting the Er^{3+} 1.5 μm Luminescence in $CsPbCl_3$ Perovskite Nanocrystals for Photonic Devices Operating at Telecommunication Wavelengths. *ACS Appl. Nano Mater*. **2020**, *3*, 4699-4707.

(23) Li, X.; Duan, S.; Liu, H.; Chen, G.; Luo, Y.; Ågren, H. Mechanism for the Extremely Efficient Sensitization of Yb^{3+} Luminescence in $CsPbCl_3$ Nanocrystals. *J. Phys. Chem. Lett.* **2019**, *10*, 487-492.

(24) Arfin, H.; Kaur, J.; Sheikh, T.; Chakraborty, S.; Nag, A. Bi^{3+}-Er^{3+} and Bi^{3+}-Yb^{3+} Codoped $Cs_2AgInCl_6$ Double Perovskite Near Infrared Emitters. *Angew. Chem. Int. Ed*. **2020**, *59*, 1-6.

(25) Loiko, P. A.; Vilejshikova, E. V.; Khaidukov, N. M.; Méndez-Ramos, J.; Mateos, X.; Yumashev, K. V. Judd-Ofelt Modeling, Emission Lifetimes and Non-Radiative Relaxation for Er^{3+} Doped Cs_2NaYF_6 Elpasolite Crystals. *J. Lumin.* **2017**, *185*, 279-285.

(26) Guria, A. K.; Dutta, S. K.; Adhikari, S. D.; Pradhan, N. Doping Mn^{2+} in Lead Halide Perovskite Nanocrystals: Successes and Challenges. *ACS Energy Lett.* **2017**, *2*, 1014-1021.

(27) Li, Z.-J.; Hofman, E.; Davis, A. H.; Khammang, A.; Wright, J. T.; Dzikovski, B.; Meulenberg, R. W.; Zheng, W. Complete Dopant Substitution by Spinodal Decomposition in Mn-Doped Two-Dimensional $CsPbCl_3$ Nanoplatelets. *Chem. Mater.* **2018**, *30*, 6400-6409.

(28) Paul, S.; Bladt, E.; Richter, A. F.; Döblinger, M.; Tong, Y.; Huang, H.; Dey, A.; Bals, S.; Debnath, T.; Polavarapu, L.; Feldmann, J. Manganese-Doping-Induced Quantum Confinement within Host Perovskite Nanocrystals through Ruddlesden-Popper Defects. *Angew. Chem. Int. Ed*. **2020**, *59*, 6794-6799.

(29) Das Adhikari, S.; Dutta, S. K.; Dutta, A.; Guria, A. K.; Pradhan, N. Chemically Tailoring the Dopant Emission in Manganese-Doped $CsPbCl_3$ Perovskite Nanocrystals. *Angew. Chem. Int. Ed*. **2017**, *56*, 8746-8750.

(30) Mir, W. J.; Jagadeeswararao, M.; Das, S.; Nag, A. Colloidal Mn-Doped Cesium Lead Halide Perovskite Nanoplatelets. *ACS Energy Lett.* **2017**, *2*, 537-543.

(31) Fei, L.; Zhiguo, X.; Caofeng, P.; Yue, G.; Lin, G.; Quanlin, L.; Z., Z. J. High Br^- Content $CsPb(Cl_yBr_{1-y})_3$ Perovskite Nanocrystals with Strong Mn^{2+} Emission through Diverse Cation/Anion Exchange Engineering. *ACS Appl. Mat. Interfaces* **2018**, *10*, 11739-11746.

(32) Xu, K.; Meijerink, A. Tuning Exciton-Mn^{2+} Energy Transfer in Mixed Halide Perovskite Nanocrystals. *Chem. Mater.* **2018**, *30*, 5346-5352.

(33) Tian, G.; Gu, Z.; Zhou, L.; Yin, W.; Liu, X.; Yan, L.; Jin, S.; Ren, W.; Xing, G.; Li, S.; Zhao, Y. Mn^{2+} Dopant-Controlled Synthesis of $NaYF_4$:Yb/Er Upconversion Nanoparticles for in Vivo Imaging and Drug Delivery. *Adv. Mater.* **2012**, *24*, 1226-1231.

(34) de Herval, L. K. S.; Tuncer Arslanlar, Y.; Ayvacikli, M.; Iikawa, F.; Nobrega, J. A.; Pizani, P. S.; Galvão Gobato, Y.; Can, N.; Henini, M.; de Godoy, M. P. F. Enhancement of the Luminescence Intensity by Co-Doping Mn^{2+} into Er^{3+}-Doped $SrAl_2O_4$. *J. Lumin.* **2015**, *163*, 17-20.

(35) Dan, H. K.; Thai, N. L.; Tin, L. D.; Qiu, J.; Zhou, D.; Jiao, Q. Enhanced Near/Mid-Infrared Emission Bands Centered at ∼1.54 and ∼2.73 μm of Er^{3+}-Doped in Transparent Silicate Glass-Ceramics via Mn^{2+}-Yb^{3+} Dimer. *Infrared Phys. Technol.* **2018**, *95*, 33-38.

(36) Brouwer, A. M. Standards for Photoluminescence Quantum Yield Measurements in Solution (IUPAC Technical Report). *Pure Appl. Chem.* **2011**, *83*, 2213-2228.

(37) Ghosh, S.; Manna, L. The Many “Facets” of Halide Ions in the Chemistry of Colloidal Inorganic Nanocrystals. *Chem. Rev.* **2018**, *118*, 7804-7864.

(38) van der Stam, W.; Geuchies, J. J.; Altantzis, T.; van den Bos, K. H. W.; Meeldijk, J. D.; Van Aert, S.; Bals, S.; Vanmaekelbergh, D.; de Mello Donega, C. Highly Emissive Divalent-Ion-Doped Colloidal $CsPb_{1-x}M_xBr_3$ Perovskite Nanocrystals through Cation Exchange. *J. Am. Chem. Soc.* **2017**, *139*, 4087-4097.

(39) Zou, S.; Liu, Y.; Li, J.; Liu, C.; Feng, R.; Jiang, F.; Li, Y.; Song, J.; Zeng, H.; Hong, M.; Chen, X. Stabilizing Cesium Lead Halide Perovskite Lattice through Mn (II) Substitution for Air-Stable Light-Emitting Diodes. *J. Am. Chem. Soc.* **2017**, *139*, 11443-11450.

(40) Yin, J.; Ahmed, G. H.; Bakr, O. M.; Brédas, J.-L.; Mohammed, O. F. Unlocking the Effect of Trivalent Metal Doping in All-Inorganic $CsPbBr_3$ Perovskite. *ACS Energy Lett.* **2019**, *4*, 789-795.

(41) Dorn, M.; Kalmbach, J.; Boden, P.; Päpcke, A.; Gómez, S.; Förster, C.; Kuczelinis, F.; Carrella, L. M.; Büldt, L. A.; Bings, N. H.; Rentschler, E.; Lochbrunner, S.; González, L.; Gerhards, M.; Seitz, M.; Heinze, K. A Vanadium (III) Complex with Blue and NIR-II Spin-Flip Luminescence in Solution. *J. Am. Chem. Soc.* **2020**, *142*, 7947-7955.

(42) Kreidt, E.; Kruck, C.; Seitz, M., Chapter 300 - Nonradiative Deactivation of Lanthanoid Luminescence by Multiphonon Relaxation in Molecular Complexes. In *Handbook on the Physics and Chemistry of Rare Earths*, Bünzli, J.-C. G.; Pecharsky, V. K., Eds. Elsevier: **2018**; Vol. *53*, pp 35-79.

(43) Xu, K.; Lin, C. C.; Xie, X.; Meijerink, A. Efficient and Stable Luminescence from

Mn^{2+} in Core and Core–Isocrystalline Shell $CsPbCl_3$ Perovskite Nanocrystals. *Chem. Mater.* **2017**, *29*, 4265-4272.

Supporting Information for Chapter 4

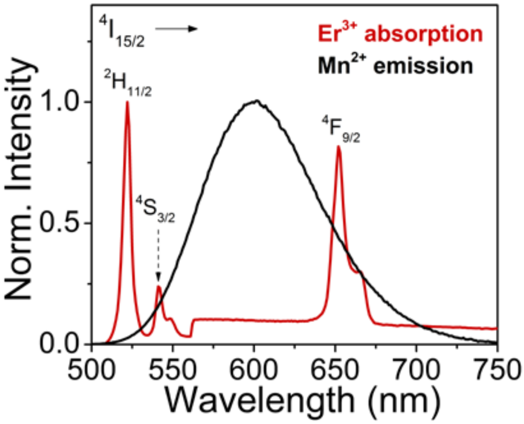

Figure S4.1 Spectral overlaps between Mn^{2+} emission and Er^{3+} absorption. The Er^{3+} absorption spectrum was obtained from a 0.05 M Er^{3+} chloride salts aqueous solution.

The Mn^{2+} doping concentrations relative to Pb^{2+} in the $CsPbCl_3$ host determined by XRF measurements are 0.58%, 1.41%, 2.67% and 3.43%, corresponding to 0.025/1, 0.05/1, 0.1/1 and 0.15/1 nominal ratios of Mn/Pb, respectively.

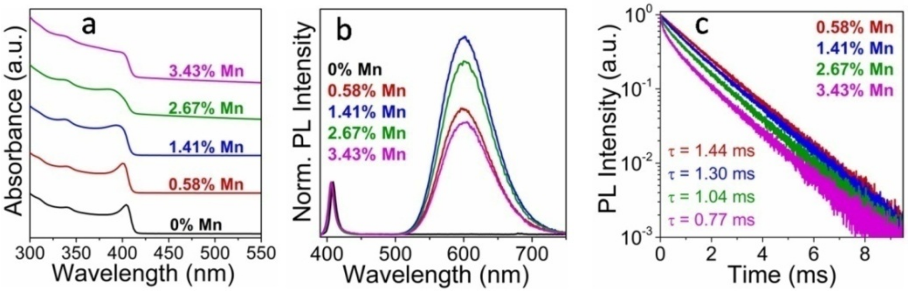

Figure S4.2 Optical properties of $CsPbCl_3$ NCs without and with different doping concentrations of Mn^{2+} ions. (a) Absorption spectra, (b) PL spectra normalized at the band-edge emission, (c) decay curves monitored by the Mn^{2+} $^4T_1 \rightarrow {}^6A_1$ transition at 600 nm. The decrease in PL intensity and the shortening of the decay dynamics of Mn^{2+} emission in Mn^{2+}-doped NCs with increasing Mn^{2+} content (>1.4%) may be attributed to the Mn^{2+}–Mn^{2+} coupling interactions and formed defects/traps near the Mn^{2+} ions.

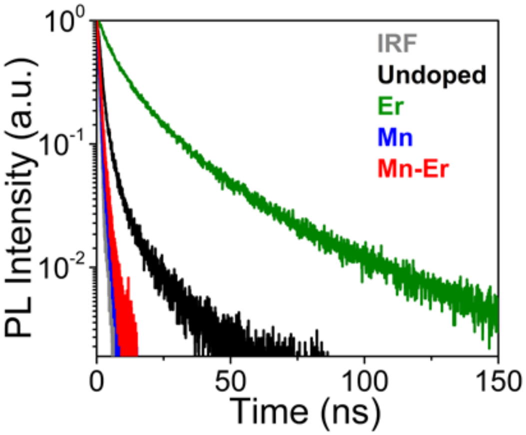

Figure S4.3 PL decay curves of undoped and doped $CsPbCl_3$ NCs collected by monitoring the band-edge emission of the $CsPbCl_3$ host (λ_{ex} = 350 nm). The instrumental response function (IRF) was determined to be approximately 0.8 ns by measuring the scattering of a

Ludox solution. The lengthening of the decay dynamics upon Er^{3+} doping is attributed to the removal of deep-trap states, possibily related to Cl^- vancancies.

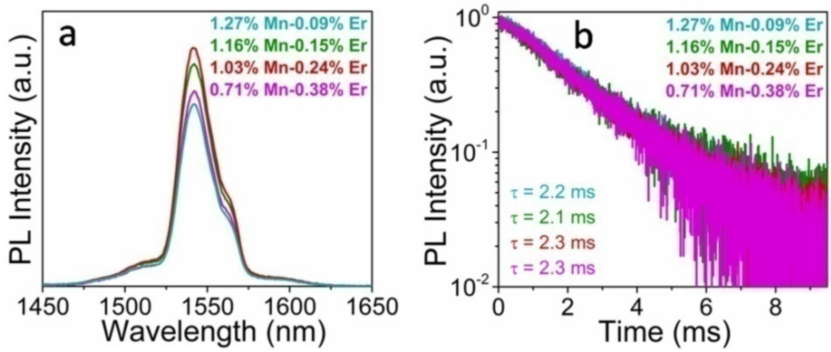

Figure S4.4 (a) PL spectra of Mn^{2+}–Er^{3+} codoped $CsPbCl_3$ NCs with different doping concentrations under excitation at 365 nm. It is worth noting that, while maintaining the same nominal amount, the actual Mn^{2+} concentration decreases as the Er^{3+} loading is increased, likely indicating a competition of the two ions for the doping sites. (b) Corresponding PL decay curves collected by monitoring Er^{3+} emission at 1542 nm.

Table S4.1. Decay parameters of the Mn^{2+} emission at 600 nm in Mn^{2+}-doped, Mn^{2+}–Er^{3+}, codoped $CsPbCl_3$ NCs. Average lifetimes: $\tau = \Sigma A_i\tau_i/\Sigma A_{i,}$, where A_i and τ_i represent the amplitude and the lifetime component of the multiple exponential functions by fitting the PL decay curve, respectively; energy transfer efficiency: $\eta = 1-\tau_{Mn–Er}/\tau_{Mn}$, where $\tau_{Mn–Er}$ and τ_{Mn} are the lifetimes of Mn^{2+} emission in the presence and absence of Er^{3+}, respectively.

Sample	**τ_1 (ms) (A_1)**	**τ_2 (ms) (A_2)**	**τ (ms)**	**η**
Mn^{2+}	—	1.30	1.30	
Mn^{2+}–Er^{3+}	0.27 (0.43)	1.19 (0.57)	0.79	39.2%

Chapter 5 Conclusions and Perspectives

5.1 Conclusions

The combination of luminescent Ln^{3+} ions with LHPs nanocrystals has proved a successful strategy to overcome the limits of both the poor absorption and the negligible emission in the NIR of these materials. Two different strategies have been pursued in this regard, the first one relying on the combination of Ln^{3+}-doped UCNPs with $CsPbBr_3$ NCs to achieve bright photon UCL from the LHPs after irradiation with NIR light and the second one consisting in the incorporation of NIR-emitting Ln^{3+} ions into the LHP matrix to obtain intense sensitized NIR emission.

In particular, as discussed in Chapter 2, three Ln^{3+}-doped UCNPs, $BaYF_5$:Yb,Tm, $BaYF_5$:Yb,Er and $BaYF_5$:Yb,Ho showing blue, green and yellow-green light under 975 nm excitation were integrated with $CsPbBr_3$ NCs by an *in situ* growth method to afford close-contact and highly homogeneous composites. The obtained UCNPs sensitized-$CsPbBr_3$ NCs exhibited bright green emission triggered by NIR irradiation thanks to the efficient sensitization from the Ln^{3+}-based UCNPs. The reason for the achieved high sensitization efficiency lies on the fact that ET largely occurs through FRET, favored by the short donor-acceptor distances in the material, as opposed to the simple and less effective long-range PR mechanism. Importantly, the investigated UCNP/$CsPbBr_3$ NCs assembly also showed improved thermal and photostability.

In Chapter 3, an innovative approach to extend the emission of $CsPbCl_3$ NCs to the 1.5 μm telecommunication wavelength is presented. First, it was found out that Er^{3+} singly doped $CsPbCl_3$ NCs unexpectedly did not show the characteristic 4f–4f transitions of Er^{3+}, unlike Yb^{3+} analogs. An alternative model mechanism of lanthanide sensitization as opposed to the accepted QC of the LHP exciton, was then proposed. Experimental evidence, on the basis of steady-state and time-resolved PL data, along with a comparative study on analogous materials doped with other Ln^{3+} ions (Eu^{3+} and Nd^{3+}), indicates that a transient internal redox mechanism was likely to play a key role in the extremely efficient Yb^{3+} emission at 1.0 μm. On the other hand, this pathway is unviable for Er^{3+} due to the fact that its redox potential is much higher in energy than the conduction band of $CsPbCl_3$ NCs. This observation leads to the key conclusion that Yb^{3+} represents a special case among the luminescent Ln^{3+} ions, as it is the only one which can be directly sensitized through the LHP excitation. Nonetheless, through Yb^{3+}-mediated sensitization, intense and long-lived NIR Er^{3+} emission at 1.5 μm was obtained, also thanks to an improved synthetic method.

Finally, in Chapter 4, it is demonstrated that cheaper and more readily available Mn^{2+} ions (relative to Yb^{3+}) work as excellent energy bridges from the excited donor LHP matrix to Er^{3+}. In Mn^{2+}–Er^{3+} codoped $CsPbCl_3$ NCs, intense NIR Er^{3+} emission at ~1.5 μm with similar figures of merits as in the analogous Yb^{3+}/Er^{3+} codoped system was also observed. As Mn^{2+} emission is much broader than Yb^{3+} so the system is less limited by the resonance of the donor-acceptor energy levels, this strategy could potentially enable the sensitization of other Ln^{3+} ions.

In conclusion, Ln^{3+} ions with special 4f–4f electron configurations can add important functionalities to $CsPbX_3$ perovskite materials. The Ln^{3+}-containing perovskites will be useful as spectral converters for applications in photovoltaic and photoelectric devices.

5.2 Perspectives

Since the first colloidal synthesis of $CsPbX_3$ NCs in 2015, massive progress has been made in achieving new emerging functionalities and improving phase stability.

Despite rapid developments, there are still some unresolved issues that need to be addressed.

For UCNPs sensitized-$CsPbX_3$ perovskites, the PLQY of energy transfer donor, such as the popular Ln^{3+}-doped fluorides, is very low <5%. In order to improve the UCL of $CsPbX_3$ perovskites, more efficient energy transfer donor are highly desired, such as dye-sensitized UCNPs. The important factor that determines the energy transfer mechanism (PR and FRET) is the separation-distance between the energy donor (UCNPs) and acceptor ($CsPbX_3$). The distance-dependent FRET mechanism can overcome the concentration quenching effect that commonly exists in PR-mediated energy-transfer system. In this regard, new synthetic methods allowing for intense interactions between UCNPs and $CsPbX_3$ are highly demanding, such as replacing the long-chain organic ligands with shorter ones and using smaller LHPs nanocubes or nanoplatelets with strong quantum confinement. The above strategy may be also applied to lead-free perovskites, which also exhibit poor NIR absorption performance.

Ln^{3+} doping imparts high flexibility to the optical properties tailoring of $CsPbX_3$. Several synthetic protocols have been developed to prepare either Ln^{3+}-doped NCs or films. However, some contrary results (e.g., size change, doping efficiency, Ln^{3+} luminescence) of Ln^{3+}-doped $CsPbX_3$ perovskites have been reported by different research groups even same doping approaches were employed. Such phenomena indicates that Ln^{3+} doping is very sensitive to the synthetic conditions, including precursor source and concentration, ligand source and amounts, reaction temperature, etc. However, it remains unclear how these parameters govern the Ln^{3+} doping, i.e., doping mechanism needs to be discovered for finely tuning the doping concentration and position in the perovskite structures. Compared to visible-emitting Ln^{3+} ions, NIR-emitting Ln^{3+} ions, such Er^{3+}, Nd^{3+}, Pr^{3+}, Sm^{3+}, Dy^{3+}, Ho^{3+}, and Tm^{3+} are rarely doped into $CsPbX_3$ perovskites. It should be noted that Yb^{3+}-doped $CsPbCl_3$ with PLQYs >100% is a special case among all of the existing Ln^{3+}-doped analogs. Meanwhile, more fundamental knowledge of the $CsPbX_3$ perovskites can be discovered through Ln^{3+} doping. It has been found that high-temperature HI approach with air-free is still the most popular one for Ln^{3+} doping, in which only small-scale output of the sample (milligram) can be obtained. Therefore, low-temperature facile synthetic protocols for producing large-scale products are highly desired for further commercialization.

In both cases, long-chain organic ligands are employed for stabilizing the perovskite phase. Such ligand disfavors charge carrier immigration, thus shorter ligand or ligand-free will be helpful for improving the photovoltaic and photoelectric devices.

Appendix

Appendix A: Application for UCNPs Sensitized-LHPs (Chapter 2)

On the basis of nonlinear and linear optical properties of the UCNPs-sensitized LHPs system, a dual-modal emission feature can be applied for anti-counterfeiting (Figure A1a-c).[1-3] The UCNPs-sensitized LHPs system can also take advantage of its optical feature of multi-color UCL emissions consisting of characteristic 4f–4f transitions of Ln^{3+} ions and band-edge emission of LHPs for temperature detection (Figure A1d).[3]

The outstanding UC optical properties of LHPs in the UCNPs-sensitized LHPs system can also find applications in photodetection, photocatalysis, solar cells. Unlike the case for traditional semiconductors (e.g., TiO_2, ZnO, $BiVO_4$, CdS),[4-8] the application of UCNPs-sensitized LHPs system in photoelectronics and photovoltaics is scarcely investigated, and only few literature reports can be found.[7] Zhang et al. fabricated photodetectors based on air-stable α-$CsPbI_3$ NCs and $NaYF_4$:Yb,Er UCNPs using a spin-coating technique (Figure A1e,f).[9] The UCNPs-modified LHPs photodetectors were capable of broad-bandwidth photodetection from the deep UV to the NIR region (260 – 1100 nm) with good photoresponsivity, high on/off ratio and very short rise/decay time. Moreover, they found that the device showed excellent stability when exposed at 30% relative humility and 25 °C over two months.

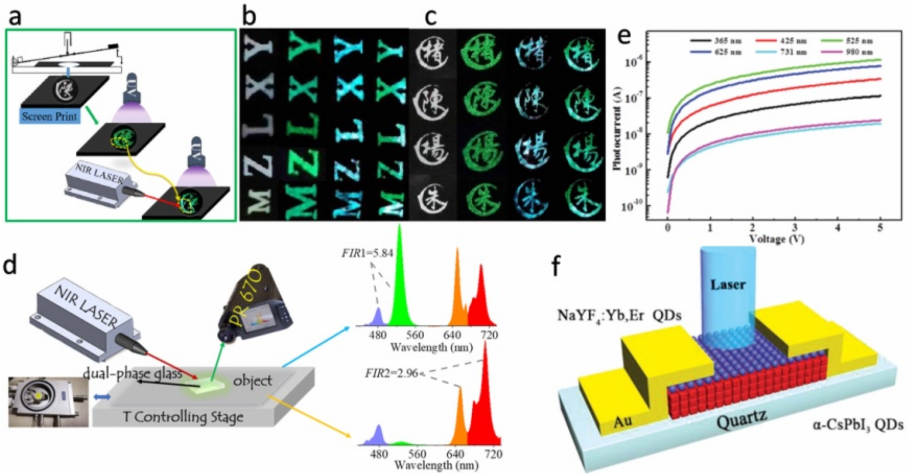

Figure A1 (a) Schematic illustration of anti-counterfeiting via a screen-printing technique and a single-modal or dual-modal excitation strategy. (b, c) Anti-counterfeiting luminescent patterns fabricated from dual-phase glass inks upon different excitation modes (column 1: daylight, column 2: UV light, column 3: NIR laser, column 4: UV light, and NIR laser). (d) Real-time temperature-measuring system to determine the actual temperature of an object coated with the dual-phase glass. UC emission spectra are directly read out from the emitting region via a spectroradiometer to obtain fluorescence intensity ratio (FIR) values. Adapted from ref 3. (e) I–V curves of the photodetectors with different excited light (10 mW cm^{-2}). (f) Schematic of the photodetector device configuration. Adapted from ref 9.

References

(1) Rao, M.; Fu, J.; Wen, X.; Sun, B.; Wu, J.; Liu, X.-H.; Dong, X. Near-Infrared-Excitable Perovskite Quantum Dots via Coupling with Upconversion Nanoparticles for Dual-Model Anti-Counterfeiting. *New J. Chem.* **2018**, *42*, 12353-12356.
(2) Lin, J.; Yang, C.; Huang, P.; Wang, S.; Liu, M.; Jiang, N.; Chen, D. Photoluminescence Tuning from Glass-Stabilized $CsPbX_3$ (X = Cl, Br, I) Perovskite Nanocrystals Triggered by Upconverting Tm:KYb_2F_7 Nanoparticles for High-Level Anti-Counterfeiting. *Chem. Eng. J.* **2020**, *395*, 125214.
(3) Li, X.; Yang, C.; Yu, Y.; Li, Z.; Lin, J.; Guan, X.; Zheng, Z.; Chen, D. Dual-Modal Photon Upconverting and Downshifting Emissions from Ultra-Stable $CsPbBr_3$ Perovskite Nanocrystals Triggered by Co-Growth of Tm:$NaYbF_4$ Nanocrystals in Glass. *ACS Appl. Mat. Interfaces* **2020,** *12*, 18705-18714.
(4) Li, C.; Wang, F.; Zhu, J.; Yu, J. C. $NaYF_4$:Yb,Tm/CdS Composite as a Novel Near-Infrared-Driven Photocatalyst. *Appl. Catal., B* **2010**, *100*, 433-439.

(5) Guo, X.; Song, W.; Chen, C.; Di, W.; Qin, W. Near-Infrared Photocatalysis of β-$NaYF_4$:Yb^{3+},Tm^{3+}@ZnO Composites. *Phys. Chem. Chem. Phys.* **2013**, *15*, 14681-14688.
(6) Tang, Y.; Di, W.; Zhai, X.; Yang, R.; Qin, W. NIR-Responsive Photocatalytic Activity and Mechanism of $NaYF_4$:Yb,Tm@TiO_2 Core-Shell Nanoparticles. *ACS Catal.* **2013**, *3*, 405-412.
(7) Roh, J.; Yu, H.; Jang, J. Hexagonal β-$NaYF_4$:Yb^{3+},Er^{3+} Nanoprism-Incorporated Upconverting Layer in Perovskite Solar Cells for Near-Infrared Sunlight Harvesting. *ACS Appl. Mat. Interfaces* **2016**, *8*, 19847-19852.
(8) Ullah, S.; Ferreira-Neto, E. P.; Hazra, C.; Parveen, R.; Rojas-Mantilla, H. D.; Calegaro, M. L.; Serge-Correales, Y. E.; Rodrigues-Filho, U. P.; Ribeiro, S. J. L. Broad Spectrum Photocatalytic System Based on $BiVO_4$ and $NaYbF_4$:Tm^{3+} Upconversion Particles for Environmental Remediation under UV-vis-NIR Illumination. *Appl. Catal., B* **2019**, *243*, 121-135.
(9) Zhang, X.; Wang, Q.; Jin, Z.; Zhang, J.; Liu, S. Stable Ultra-Fast Broad-Bandwidth Photodetectors Based on α-$CsPbI_3$ Perovskite and $NaYF_4$:Yb,Er Quantum Dots. *Nanoscale* **2017**, *9*, 6278-6285.

Appendix B: Application for Ln^{3+}-Doped LHPs (Chapter 3 and 4)

In the past three years, Ln^{3+} doping into LHPs has been recognized as a promising approach to tailor and modulate the electronic and optical performance and improve the stability of the LHP host.[1-5] The new and fascinating features, such as new emission centers, enhanced PLQYs and stability endowed by Ln^{3+} doping, particularly for NIR-emitting Yb^{3+} and Er^{3+} ions, can improve the photovoltaic and optoelectronic performance for potential applications in commercial solar cells, LEDs, lasers, luminescent solar concentrators (LSCs), and optical telecommunications.

On the other hand, the narrowest-bandgap $CsPbI_3$ perovskite has a bandgap of 1.7 eV and absorbs only a small portion of incident light in the visible light spectrum (up to 700 nm), thus resulting in energy loss in NIR light spectrum. NIR photons harvesting below the absorption threshold of perovskite has been regarded as a promising way to overcome the Shockley-Queisser efficiency limit of 32% of a single-junction solar cell.[6] It has been reported that introduction of Ln^{3+}-doped UC materials to LHPs can expand the absorption range of the LHPs via upconversion photoluminescence, resulting in an performance enhancement of the device.

Solar cells

All-inorganic $CsPbX_3$ perovskite solar cells have attracted enormous attention owing to their outstanding stability in comparison with organic-inorganic hybrid perovskite solar cells. The narrowest-bandgap $CsPbI_3$ perovskite (1.7 eV) is the most promising candidate for applications in optoelectrics and photovoltaic among $CsPbX_3$ perovskites. However, up to now, only few literature report on NIR-emitting Ln^{3+}-doped $CsPbI_3$ NCs exists,[7] whereas it was not integrated to solar cell. $CsPbBr_3$ perovskite (2.4 eV) exhibits the best phase stability compared to its chloride and iodide analogs. However, the greatest shortcoming of $CsPbBr_3$ perovskite solar cell device is their lower power conversion efficiencies (PCEs), mainly arising from narrow light-absorbance range (<550 nm) and serious charge recombination at interfaces or within perovskite films.[8] Duan et al. doped a series of Ln^{3+} (La^{3+}, Ce^{3+}, Nd^{3+}, Sm^{3+}, Eu^{3+}, Gd^{3+}, Tb^{3+}, Ho^{3+}, Er^{3+}, Yb^{3+}, and Lu^{3+}) into $CsPbBr_3$ films by a multi-step spin-coating technique.[9] The results showed that all of the above Ln^{3+} ions doping could enlarge grain size and thus reduced the defect state. The authors believed that lanthanide bromide served as a passivating layer for enhanced efficiency in corresponding solar cells. Among all the Ln^{3+}-doped $CsPbBr_3$ solar cell devices, 3% Sm^{3+}-doped device exhibited the highest PCE of 10.14%, and slightly enhanced phase thermal stability with over 90% initial efficiency than 80% initial efficiency of control device over 60 days (Figure B1a,c). However, not all Ln^{3+} ions had the same effect on perovskite quality and cell properties. Ce^{3+}, Nd^{3+}, and Eu^{3+} tailored devices displayed inferior performances comparing to control device (Figure B1b). The authors assumed that there may be other reasons in promoting photovoltaic performances by doping Ln^{3+} into $CsPbBr_3$ perovskite, arising from the optical properties of Ln^{3+} ions.

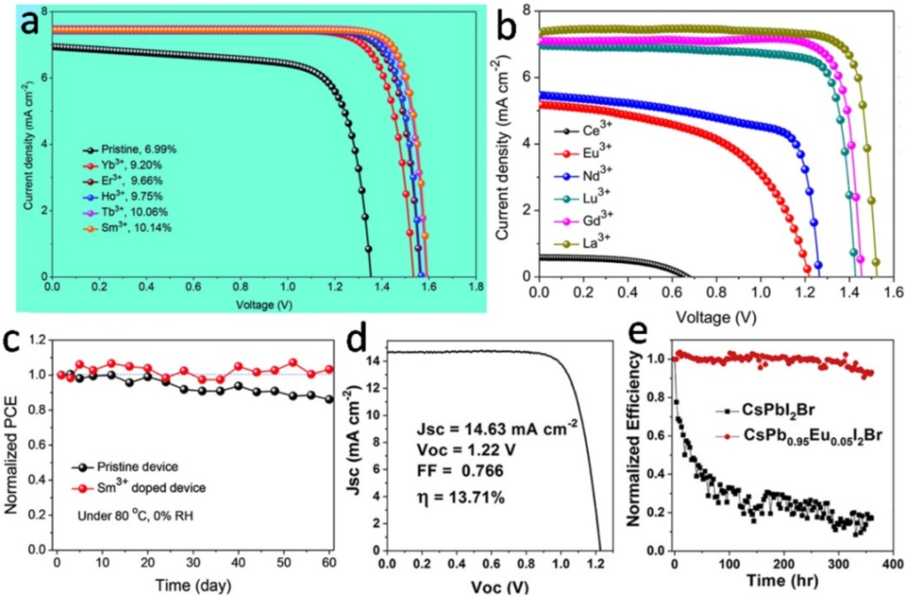

Figure B1 (a, b) The characteristic J–V curves of various Ln^{3+}-doped $CsPbBr_3$ perovskite solar cells. (c) Long-term stability of the pristine and 3% Sm^{3+}-doped devices without encapsulation under 80 °C and 0% RH. Adapted from ref 9. (d) J–V curve of the champion 5% Eu-doped $CsPbI_2Br$ device. (e) Normalized PCE of undoped and 5% Eu-doped $CsPbI_2Br$ devices monitored under continuous white light exposure as a function of time. Adapted from ref 10.

However, opposite results of Eu-doped LHPs solar cell were reported by Xiang et al.[10] The authors demonstrated that the PCE of perovskite solar cell could be enhanced from 10.21% to 13.71% upon Eu doping into $CsPbI_2Br$ lattice and the Eu-doped device retained 93% of the initial efficiency under 100 mW cm^{-2} continuous illumination for 370 hours, showing higher thermodynamic stability than the Eu-free device. The authors argued that the enhanced stability may be due to the increase of tolerance factor after Eu doping and increase of surface energy induced by increased surface-to-volume ratio. The different Eu doping effect on perovskite solar cell is likely arising from synthesis disparities, which lead to different growth rate (grain size). In addition, it is not clear about the oxidation state of Eu in ref 10.

The carrier thermalization resulted from high-energy photons absorption of single-junction solar cells is one of the major loss mechanisms, leading to lower PCE than the theoretical maximum value of ~31% (Schockley-Queisser).[11-13] The conversion of incident high-energy photons with energies larger than twice the solar cell bandgap into two or more lower energy photons by a luminescent down-converter can improve the theoretical maximum PCE of solar cell with 1.05 eV bandgap energies from ~31% to ~40%.[13] Fortunately, Yb^{3+}-doped $CsPbCl_3$ or $CsPb(Cl/Br)_3$ LHPs have been reported to be suitable quantum-cutters candidates with absorption below 450 nm and emission at ~1000 nm at an energy that is well-matched to the absorption onset of silicon and $CuIn_{1-X}Ga_XSe_2$ (CIGS) solar cells. Zhou et al. employed Yb^{3+}/Ce^{3+} codoped $CsPbCl_{1.5}Br_{1.5}$ NCs with 146% PLQY as the down-converter for commercial SSCs, and obtained 18.8% enhancement of PCE from 18.1% to 21.5%.[14] Two years later, the same group further improved the PCE of SSCs as well as CIGS solar cells by the application of $Yb^{3+}/Pr^{3+}/Ce^{3+}$ tridoped $CsPbClBr_2$ NCs (173%) as down-converter.[15] The modified SSCs and CIGS solar cells showed 20% enhancement from 15.9 to 19.1% and 18.1 to 21.9%, respectively (Figure B2). Furthermore, the charging time of smart mobile phone charged by the modified CIGS solar cells was shortened from 180 to 150 min.

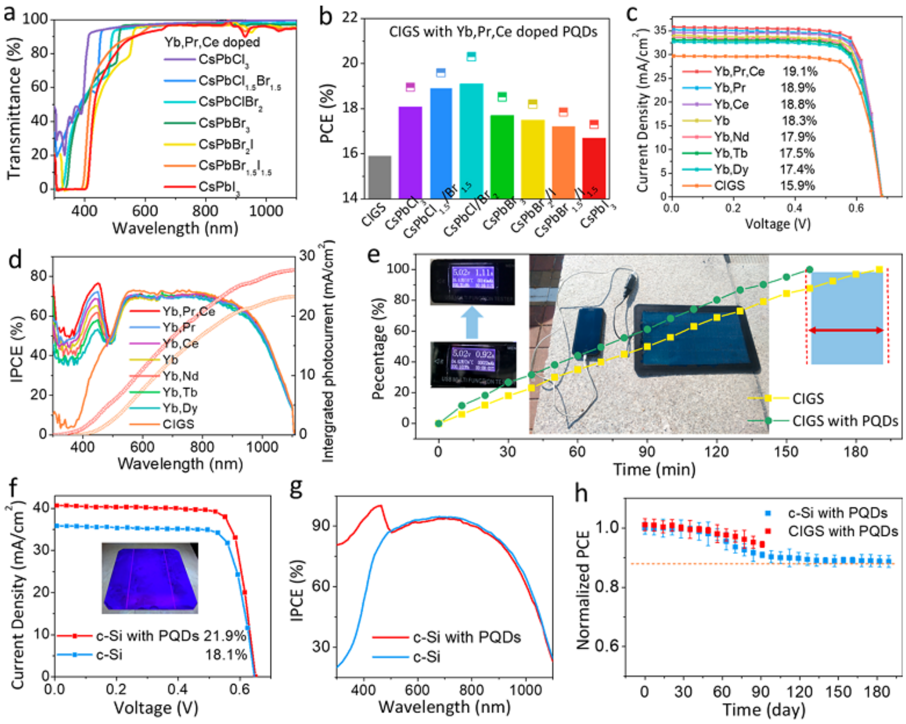

Figure B2 (a) Transmittance spectra of $Yb^{3+}/Pr^{3+}/Ce^{3+}$ tridoped $CsPb(Cl/Br/I)_3$ perovskite films. (b) PCEs of CIGS solar cells coated with 230 nm $Yb^{3+}/Pr^{3+}/Ce^{3+}$ tridoped perovskite films and the theoretical maximum PCEs induced by the perovskite films. (c) J−V curves of CIGS solar cells coated with different Yb^{3+}/Ln^{3+} (Ln = Nd, Dy, Tb, Pr, Ce) quantum-cutting couple-doped $CsPbClBr_2$ perovskite films. (d) IPCE curves of CIGS solar cells coated with Yb^{3+}/Ln^{3+} codoped $CsPbClBr_2$ and calculated short currents of the $Yb^{3+}/Pr^{3+}/Ce^{3+}$ tridoped $CsPbClBr_2$ coated CIGS solar cell and the single CIGS solar cell by convolution of the IPCE spectra with the photoflux density distribution for 1 sun. (e) Comparison of time for fully charging a mobile phone with a CIGS solar cell coated with $Yb^{3+}/Pr^{3+}/Ce^{3+}$ tridoped $CsPbClBr_2$ and a CIGS solar cell alone under the irradiation of sunlight. (Inset) Display of charging power and charging scene arrangement. (f) J−V curves and (g) IPCE curves of a single crystal SSC coated with $Yb^{3+}/Pr^{3+}/Ce^{3+}$ tridoped $CsPbClBr_2$ NCs and a SSC alone. (h) PCEs of a single crystal SSC and a CIGS solar cell coated with $Yb^{3+}/Pr^{3+}/Ce^{3+}$ tridoped $CsPbClBr_2$ NCs as a function of time. Adapted from ref 15.

Luminescent solar concentrators

A typical luminescent solar concentrators (LSC) is a semi-transparent plastic or glass optical waveguide doped or coated with highly emissive chromophores.[16,17] Upon sunlight illumination, chromophores absorb the incident light and reemit photons which are then waveguided to the edges of the LSC, where the attached solar cells absorb the concentrated photon and convert it into electrical power. The ratio between edge-emitted photons and absorbed solar photons defines the internal optical efficiency (η_{int}) of an LSC, while the external optical efficiency (η_{ext}) is defined as the ratio of edge-emitted photons to incident solar photons; that is, $\eta_{ext} = \eta_{int} \times \eta_{abs}$, with η_{abs} being the LSC absorption efficiency for solar photons.[18] Luo et al. employed Yb^{3+}-doped $CsPbCl_3$ NCs as chromophores in LSC in view of the ultrahigh PLQY (164%) and reabsorption-free features.[19] They achieved a very high η_{int} (118.1%) in a 25 cm^2 sized LSC, which was more than 2-fold higher than that of the Mn^{2+}-doped quantum dot LSC (Figure B3). Meinardi et al. highlighted that $CsPbCl_3$-based perovskites are not suitable for the highly efficient large-area LSCs due to both their relatively low PLQY (<15%) and their wide energy gap (only absorb sunlight less than 400 nm).[20] Although the low PLQY of $CsPbCl_3$ can be overcome by Yb^{3+} doping, the maximum solar photon absorption efficiency (η_{abs}) is only 3.1%, leading to a η_{ext} of 3.7% from a 5 cm^2 LSC. This η_{ext} is not high compared with previous QD-LSCs with similar sizes.[18,21] They further made projections for the scenario of improved solar photon absorption efficiency. In the case of Yb^{3+}-doped $CsPb(Cl/Br)_3$ NCs with a higher η_{abs} of 7.6%, ηext could be improved to 9.0% for a 5 cm^2 LSC. However, the improved solar photon absorption efficiency will reduce the visible light transmittance of LSCs.

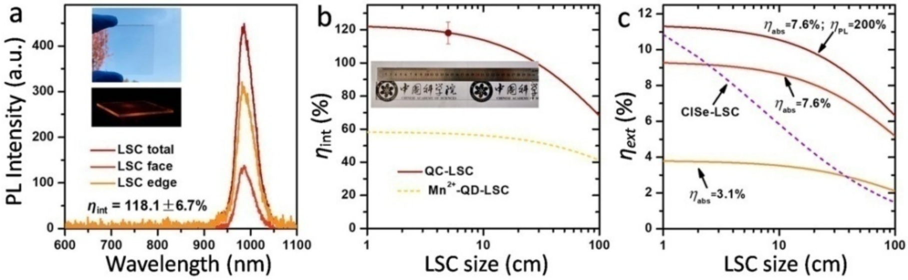

Figure B3 (a) Emissions measured for a 5 cm × 5 cm QC-LSC using Yb^{3+}-doped $CsPbCl_3$ NCs. The top inset is the picture of the LSC under sunlight; the bottom inset shows the edge emission from the LSC under UV illumination. (b) Extrapolated ηint for square-shaped QC-LSCs with edge lengths from 1 to 100 cm and the same thickness of 0.2 cm (dark red solid line). η_{int} for Mn^{2+}-doped QD-LSCs (yellow dashed line).The inset is a 30 cm long QC-LSC slab. (c) Extrapolated η_{ext} for square-shaped QC-LSCs with edge lengths from 1 to 100 cm for solar photon absorption efficiency (η_{abs}) of 3.1% (orange solid line), 7.6% (light red solid line) and for η_{abs} of 7.6% and η_{PL} of 200% (dark red solid line). The purple dashed line shows the η_{ext} of $CuInSe_2$ QD-LSCs (purple dashed line). Adapted from ref 19.

LEDs

White LEDs Phosphor-converted white light-emitting diodes (W-LEDs) have been considered as the next-generation lighting sources, owing to their advantages such as environmental protection, energy conservation, device miniaturization, , long operation life and high efficiency, compared to conventional incandescent and fluorescent lamps.[22-24] $CsPbX_3$ LHPs with tunable emission, narrow emission width, and high PLQYs, are highly desirable LEDs. However, owing to the inevitable PL emission shift induced by fast anion exchange in mixed-halide LHPs, it remains challenging to make W-LEDs by mixing the pure LHPs serving as the down-converting layer pumped by a blue InGaN chip. Ln^{3+} doping into LHPs has been regarded as an effective strategy to make LHPs-based W-LEDs, because of the multicolor luminescence from Ln^{3+}. Meanwhile, the device stability can also be improved by Ln^{3+} doping. Cheng et al. fabricated W-LEDs by regulating green-emitting Tb^{3+} ions and red-emitting Eu^{3+} ions in a $CsPbBr_3$ glass matrix with luminous efficiency of 63.21 lm/W.[5] The Commission Internationale de L'Eclairage (CIE) color coordinates of the obtained W-LEDs working under the forward bias voltage of 20 mA were (0.3335, 0.3413) (Figure B4a,b). Pan et al. fabricated W-LEDs by coating Ce^{3+}/Eu^{3+} codoped $CsPbCl_3$ NCs on a 365 nm LED chip. The W-LEDs exhibited cool white emission with a color coordinate of (0.32, 0.26), and a luminous efficiency of 24 lm/W. Meanwhile, the W-LEDs showed excellent stability. Later, the same group further prepared W-LEDs based on Ce^{3+}/Mn^{2+} codoped CsPbCl1.8$Br_{1.2}$ nanophosphor. The W-LEDs showed a color coordinate of (0.33, 0.29), a luminous efficiency of 51 lm/W, and robust stability under UV excitation and ambient environment. (Figure B4c,d).[25]

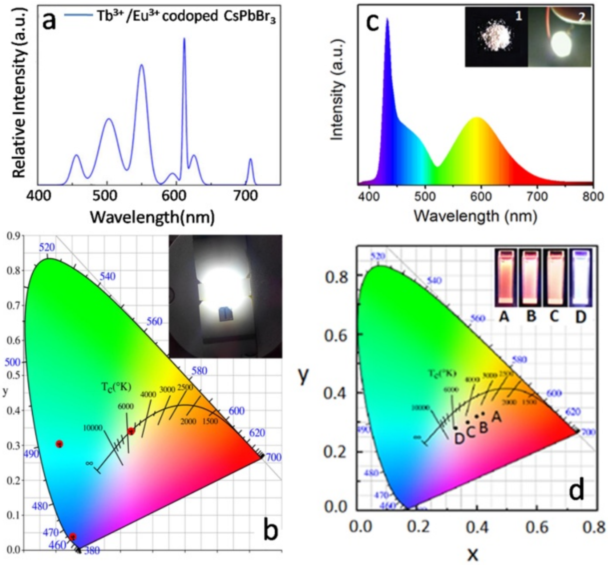

Figure B4 (a) Tb^{3+}/Eu^{3+} codoped $CsPbBr_3$ QDs glass-based LEDs. (b) CIE Chromaticity diagram of the corresponding LEDs (inset: photograph of operating W-LEDs). Adapted from ref 5. (c) PL spectra of the WLED. Inset 1 is white phosphor powder of 2.7% Ce^{3+}/9.1% Mn^{2+} codoped $CsPbCl_{1.8}Br_{1.2}$ NCs with polystyrene. Inset 2 is the photograph of the device operated at 3.0 V (the WLED is fabricated by coating Ce^{3+}/Mn^{2+} codoped $CsPbCl_{1.8}Br_{1.2}$ NC-mixed polystyrene composites on a 365 nm chip). (d) CIE chromaticity coordinate of the LED from Ce^{3+}/Mn^{2+} codoped $CsPb(Cl/Br)_3$ NCs [A(0.42, 0.33), B(0.39, 0.32), C(0.37, 0.30), and D(0.33, 0.29)]. The inset is PL images of codoped $CsPb(Cl/Br)_3$ NCs under a 365 nm UV lamp. Adapted from ref 25.

NIR LEDs NIR LEDs with the emission wavelength over 900 nm are highly desirable for applications in night-vision devices, biomedical imaging, remote sensing and optical communication.[26-28] The NIR LEDs based on narrow-bandgap organic compounds and colloidal lead chalcogenide QDs have been widely investigated.[26,27,29,30] However, LEDs using these materials suffer from low external quantum efficiency (EQE), because of the low carrier mobility and luminescence efficiency in the materials.[26,31] Therefore, organic NIR LEDs emit above 900 nm exhibit poor performance with EQE less than 0.5%, far from practical applications.[32] LHPs are emerging as promising candidates for next-generation LEDs, in view of its sharp emission peak, high PLQYs, and solution processability.[33] Nevertheless, despite the great potential of NIR LEDs based on Ln^{3+} doped LHPs, there is only one example of Yb^{3+}-doped $CsPbCl_3$ LHP LEDs emitting at ~1000 nm.[31] Ishii et al. demonstrated a highly efficient NIR LED based on Yb^{3+}-doped crystalline film, which exhibited a high EQE of 5.9% (Figure B5). They claimed that this EQE value was the highest ever reported for thin film type NIR LEDs with emission beyond 900 nm.

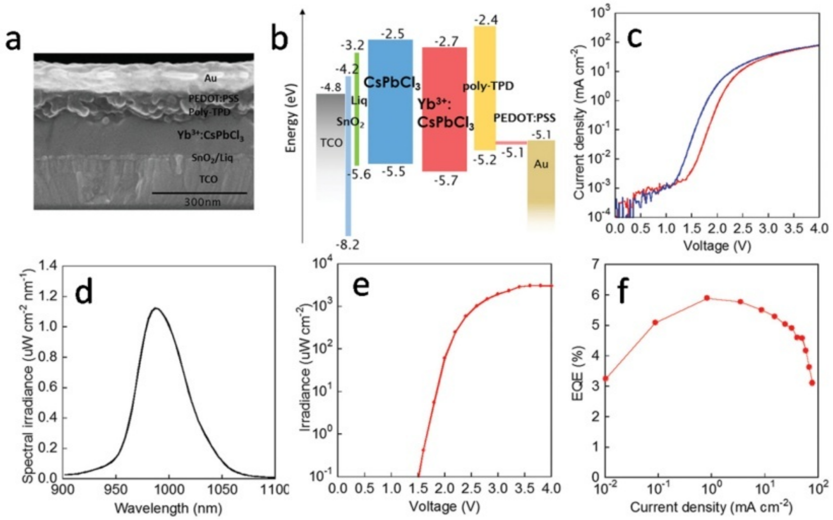

Figure B5 (a) Cross-sectional SEM image of the Yb^{3+}-doped $CsPbCl_3$ based LED. (b) Energy diagram of the charge transfer materials in LED. (c) Current density–voltage curves for $CsPbCl_3$ (blue) and Yb^{3+}-doped $CsPbCl_3$ (red) based LEDs. (d) NIR electroluminescence spectrum (applied voltage, 2 V). (e) Irradiance–voltage. (F) EQE–current density characteristics of the Yb^{3+}-doped $CsPbCl_3$ based LED. Adapted from ref 31.

References

(1) Yao, J.; Ge, J.; Han, B.-N.; Wang, K.-H.; Yao, H.-B.; Yu, H.-L.; Li, J.-H.; Zhu, B.-S.; Song, J.; Chen, C.; Zhang, Q.; Zeng, H.; Luo, Y.; Yu, S.-H. Ce^{3+}-Doping to Modulate Photoluminescence Kinetics for Efficient $CsPbBr_3$ Nanocrystals Based Light-Emitting Diodes. *J. Am. Chem. Soc.* **2018**, 140, 3626-3634.

(2) Wei, Y.; Cheng, Z.; Lin, J. An Overview on Enhancing the Stability of Lead Halide Perovskite Quantum Dots and Their Applications in Phosphor-Converted Leds. *Chem. Soc. Rev.* **2019**, *48*, 310-350.

(3) Guvenc, C. M.; Yalcinkaya, Y.; Ozen, S.; Sahin, H.; Demir, M. M. Gd^{3+}-Doped α-$CsPbI_3$ Nanocrystals with Better Phase Stability and Optical Properties. *J. Phys. Chem. C* **2019**, *123*, 24865-24872.

(4) Zhou, Y.; Zhao, Y. Chemical Stability and Instability of Inorganic Halide Perovskites. *Energy Environ. Sci.* **2019**, *12*, 1495-1511.

(5) Cheng, Y.; Shen, C.; Shen, L.; Xiang, W.; Liang, X. Tb^{3+}, Eu^{3+} Co-Doped $CsPbBr_3$ QDs Glass with Highly Stable and Luminous Adjustable for White LEDs. *ACS Appl. Mat. Interfaces* **2018**, *10*, 21434-21444.

(6) Shao, W.; Chen, G.; Kuzmin, A.; Kutscher, H. L.; Pliss, A.; Ohulchanskyy, T. Y.; Prasad, P. N. Tunable Narrow Band Emissions from Dye-Sensitized Core/Shell/Shell Nanocrystals in the Second Near-Infrared Biological Window. *J. Am. Chem. Soc.* **2016**, *138*, 16192-16195.

(7) Mir, W. J.; Mahor, Y.; Lohar, A.; Jagadeeswararao, M.; Das, S.; Mahamuni, S.; Nag, A. Postsynthesis Doping of Mn and Yb into $CsPbX_3$ (X = Cl, Br, or I) Perovskite Nanocrystals for Downconversion Emission. *Chem. Mater.* **2018**, *30*, 8170-8178.

(8) Duan, J.; Zhao, Y.; He, B.; Tang, Q. High-Purity Inorganic Perovskite Films for Solar Cells with 9.72% Efficiency. *Angew. Chem. Int. Ed.* **2018**, *130*, 3849-3853.

(9) Duan, J.; Zhao, Y.; Yang, X.; Wang, Y.; He, B.; Tang, Q. Lanthanide Ions Doped $CsPbBr_3$ Halides for HTM-Free 10.14%-Efficiency Inorganic Perovskite Solar Cell with an Ultrahigh Open-Circuit Voltage of 1.594 V. *Adv. Energy Mater.* **2018**, *8*, 1802346.

(10) Xiang, W.; Wang, Z.; Kubicki, D. J.; Tress, W.; Luo, J.; Prochowicz, D.; Akin, S.; Emsley, L.; Zhou, J.; Dietler, G.; Grätzel, M.; Hagfeldt, A. Europium-Doped $CsPbI_2Br$ for Stable and Highly Efficient Inorganic Perovskite Solar Cells. *Joule* **2019**, *3*, 205-214.

(11) Nayak, P. K.; Mahesh, S.; Snaith, H. J.; Cahen, D. Photovoltaic Solar Cell Technologies: Analysing the State of the Art. *Nat. Rev. Mater.* **2019**, *4*, 269-285.

(12) Leijtens, T.; Bush, K. A.; Prasanna, R.; McGehee, M. D. Opportunities and Challenges for Tandem Solar Cells Using Metal Halide Perovskite Semiconductors. *Nat. Energy* **2018,** *3*, 828-838.

(13) Trupke, T.; Green, M. A.; Würfel, P. Improving Solar Cell Efficiencies by Down-Conversion of High-Energy Photons. *J. Appl. Phys.* **2002**, *92*, 1668-1674.

(14) Zhou, D.; Liu, D.; Pan, G.; Chen, X.; Li, D.; Xu, W.; Bai, X.; Song, H. Cerium and Ytterbium Codoped Halide Perovskite Quantum Dots: A Novel and Efficient Downconverter for Improving the Performance of Silicon Solar Cells. *Adv. Mater.* **2017**, *29*, 1704149.

(15) Zhou, D.; Sun, R.; Xu, W.; Ding, N.; Li, D.; Chen, X.; Pan, G.; Bai, X.; Song, H. Impact of Host Composition, Codoping, or Tridoping on Quantum-Cutting Emission of Ytterbium in Halide Perovskite Quantum Dots and Solar Cell Applications. *Nano Lett.* **2019**, *19*, 6904-6913.

(16) Zhao, H.; Sun, R.; Wang, Z.; Fu, K.; Hu, X.; Zhang, Y. Zero-Dimensional Perovskite Nanocrystals for Efficient Luminescent Solar Concentrators. *Adv. Funct. Mater.* **2019**, *29*, 1902262.

(17) Li, Z.; Johnston, A.; Wei, M.; Saidaminov, M. I.; Martins de Pina, J.; Zheng, X.; Liu, J.; Liu, Y.; Bakr, O. M.; Sargent, E. H. Solvent-Solute Coordination Engineering for Efficient Perovskite Luminescent Solar Concentrators. *Joule* **2020**, *4*, 631-643.

(18) Wu, K.; Li, H.; Klimov, V. I. Tandem Luminescent Solar Concentrators Based on Engineered Quantum Dots. *Nat. Photonics* **2018**, *12*, 105-110.

(19) Luo, X.; Ding, T.; Liu, X.; Liu, Y.; Wu, K. Quantum-Cutting Luminescent Solar Concentrators Using Ytterbium-Doped Perovskite Nanocrystals. *Nano Lett.* **2019**, *19*, 338-341.

(20) Meinardi, F.; Bruni, F.; Brovelli, S. Luminescent Solar Concentrators for Building-Integrated Photovoltaics. *Nat. Rev. Mater.* **2017**, *2*, 17072.

(21) Meinardi, F.; Ehrenberg, S.; Dhamo, L.; Carulli, F.; Mauri, M.; Bruni, F.; Simonutti, R.; Kortshagen, U.; Brovelli, S. Highly Efficient Luminescent Solar Concentrators Based on Earth-Abundant Indirect-Bandgap Silicon Quantum Dots. *Nat. Photonics* **2017**, *11*, 177-185.

(22) Li, G.; Tian, Y.; Zhao, Y.; Lin, J. Recent Progress in Luminescence Tuning of Ce^{3+} and Eu^{2+}-Activated Phosphors for pc-WLEDs. *Chem. Soc. Rev.* **2015**, *44*, 8688-8713.

(23) Pan, M.; Liao, W.-M.; Yin, S.-Y.; Sun, S.-S.; Su, C.-Y. Single-Phase White-Light-Emitting and Photoluminescent Color-Tuning Coordination Assemblies. *Chem. Rev.* **2018**, *118*, 8889-8935.

(24) Kimura, N.; Sakuma, K.; Hirafune, S.; Asano, K.; Hirosaki, N.; Xie, R.-J. Extrahigh Color Rendering White Light-Emitting Diode Lamps Using Oxynitride and Nitride Phosphors Excited by Blue Light-Emitting Diode. *Appl. Phys. Lett.* **2007**, *90*, 051109.

(25) Pan, G.; Bai, X.; Xu, W.; Chen, X.; Zhou, D.; Zhu, J.; Shao, H.; Zhai, Y.; Dong, B.; Xu, L.; Song, H. Impurity Ions Codoped Cesium Lead Halide Perovskite Nanocrystals with Bright White Light Emission toward Ultraviolet–White Light-Emitting Diode. *ACS Appl. Mat. Interfaces* **2018**, *10*, 39040-39048.

(26) Vasilopoulou, M.; Kim, H. P.; Kim, B. S.; Papadakis, M.; Ximim Gavim, A. E.; Macedo, A. G.; Jose da Silva, W.; Schneider, F. K.; Mat Teridi, M. A.; Coutsolelos, A. G.; bin Mohd Yusoff, A. R. Efficient Colloidal Quantum Dot Light-Emitting Diodes Operating in the Second Near-Infrared Biological Window. *Nat. Photonics* **2020**, *14*, 50-56.

(27) Qian, G.; Zhong, Z.; Luo, M.; Yu, D.; Zhang, Z.; Wang, Z. Y.; Ma, D. Simple and Efficient Near-Infrared Organic Chromophores for Light-Emitting Diodes with Single Electroluminescent Emission above 1000 nm. *Adv. Mater.* **2009**, *21*, 111-116.

(28) Pradhan, S.; Di Stasio, F.; Bi, Y.; Gupta, S.; Christodoulou, S.; Stavrinadis, A.; Konstantatos, G. High-Efficiency Colloidal Quantum Dot Infrared Light-Emitting Diodes via Engineering at the Supra-Nanocrystalline Level. *Nat. Nanotechnol.* **2019**, *14*, 72-79.

(29) Wang, S.; Yan, X.; Cheng, Z.; Zhang, H.; Liu, Y.; Wang, Y. Highly Efficient Near-Infrared Delayed Fluorescence Organic Light Emitting Diodes Using a Phenanthrene-Based Charge-Transfer Compound. *Angew. Chem. Int. Ed.* **2015**, *54*, 13068-13072.

(30) Gong, X.; Yang, Z.; Walters, G.; Comin, R.; Ning, Z.; Beauregard, E.; Adinolfi, V.; Voznyy, O.; Sargent, E. H. Highly Efficient Quantum Dot Near-Infrared Light-Emitting Diodes. *Nat. Photonics* **2016**, *10*, 253-257.

(31) Ishii, A.; Miyasaka, T. Sensitized Yb^{3+} Luminescence in $CsPbCl_3$ Film for Highly Efficient Near-Infrared Light-Emitting Diodes. *Adv. Sci.* **2020**, *7*, 1903142.

(32) Qiu, W.; Xiao, Z.; Roh, K.; Noel, N. K.; Shapiro, A.; Heremans, P.; Rand, B. P. Mixed Lead-Tin Halide Perovskites for Efficient and Wavelength-Tunable Near-Infrared Light-Emitting Diodes. *Adv. Mater.* **2019**, *31*, 1806105.

(33) Shang, Y.; Liao, Y.; Wei, Q.; Wang, Z.; Xiang, B.; Ke, Y.; Liu, W.; Ning, Z. Highly Stable Hybrid Perovskite Light-Emitting Diodes Based on Dion-Jacobson Structure. *Sci. Adv.* **2019**, *5*, eaaw8072.

Publications

Peer-reviewed journals

Zeng, M.; Artizzu, F.; Liu, J.; Singh, S.; Locardi, F.; Mara, D.; Hens, Z.; Van Deun, R. Boosting the Er^{3+} 1.5 μm Luminescence in $CsPbCl_3$ Perovskite Nanocrystals for Photonic Devices Operating at Telecommunication Wavelengths. *ACS Appl. Nano Mater*. **2020**, *3*, 4699-4707.

Zeng, M.; Singh, S.; Hens, Z.; Liu, J.; Artizzu, F.; Van Deun, R. Strong Upconversion Emission in $CsPbBr_3$ Perovskite Quantum Dots through Efficient $BaYF_5$:Yb,Ln Sensitization. *J. Mater. Chem. C* **2019**, *7*, 2014-2021.

Liu, J.; Rijckaert, H.; **Zeng, M**.; Haustraete, K.; Laforce, B.; Vincze, L.; Van Driessche, I.; Kaczmarek, A. M.; Van Deun, R. Simultaneously Excited Downshifting/Upconversion Luminescence from Lanthanide-Doped Core/Shell Fluoride Nanoparticles for Multimode Anticounterfeiting. *Adv. Funct. Mater.* **2018**, *28*, 1707365.

Presenations on conferences

Zeng, M.; Singh, S.; Hens, Z.; Van Deun, R. Fast Synthesis of CdS/CdS Host-Shell Quantum Dots. ChemCYS 2018, the Chemistry Conference for Young Scientists, February 21st-23rd, 2018, Blankenberge, Belgium, Poster presentation.

Zeng, M.; Liu, J.; Singh, S.; Hens, Z.; Van Deun, R. Highly Efficient FRET System of $BaYF_5$:Yb,Ln/QDs Nanoheterostructures. The 10th International Conference on f-Elements (ICFE10), September 3rd-6th, 2018, Lausanne, Switzerland, Poster presentation.

Zeng, M.; Singh, S.; Hens, Z.; Liu, J.; Artizzu, F.; Van Deun, R. Strong Upconversion Emission in $CsPbBr_3$ Perovskite Quantum Dots through Efficient $BaYF_5$:Yb,Ln Sensitization. "Chemical Research in Flanders - CRF" (CRF-2), October 14th-16th, 2019. Blankenberge, Belgium, Oral presentation.